STUDIES ON VISIBLE-BLIND ULTRAVIOLET PHOTODETECTORS WITH LOW VOLTAGE OPERATION USING ZINC OXIDE NANOSTRUCTURES

by

HANNA B

10PP16J39007

A Thesis Submitted to the
Academy of Scientific & Innovative Research
for the Award of the Degree of
DOCTOR OF PHILOSOPHY
in
Science

Under the supervision of
Dr. K. N. NARAYANAN UNNI

CSIR-National Institute for Interdisciplinary Science and Technology (CSIR-NIIST) Thiruvananthapuram – 695 019

Academy of Scientific and Innovative Research
AcSIR Headquarters, CSIR-HRDC campus
Sector 19, Kamla Nehru Nagar,
Ghaziabad, U.P. – 201 002, India

May– 2022

CERTIFICATE

This is to certify that the work incorporated in this Ph.D. thesis entitled, **"*Studies on visible-blind ultraviolet photodetectors with low voltage operation using zinc oxide nanostructures*"**, submitted by *Ms. Hanna B.* to the Academy of Scientific and Innovative Research (AcSIR), in partial fulfilment of the requirements for the award of the Degree of *Doctor of Philosophy in Science*, embodies original research work carried out by the student. We further certify that this work has not been submitted to any other University or Institution in part or full for the award of any degree or diploma. Research materials obtained from other sources and used in this research work have been duly acknowledged in the thesis. Images, illustrations, figures, tables etc., used in the thesis from other sources, have also been duly cited and acknowledged.

Hanna B

Dr. K. P. Surendran

(Co-supervisor)

Dr. K. N. Narayanan Unni

(Supervisor)

STATEMENTS OF ACADEMIC INTEGRITY

I, Hanna B., a Ph.D. student of the Academy of Scientific and Innovative Research (AcSIR) with Registration No. 10PP16J39007 hereby undertake that, the thesis entitled **"Studies on visible-blind ultraviolet photodetectors with low voltage operation using zinc oxide nanostructures"** has been prepared by me and that the document reports original work carried out by me and is free of any plagiarism in compliance with the UGC Regulations on "*Promotion of Academic Integrity and Prevention of Plagiarism in Higher Educational Institutions (2018)*" and the CSIR Guidelines for "*Ethics in Research and in Governance (2020)*".

Hanna B
May 18th, 2022
Thiruvananthapuram

It is hereby certified that the work done by the student, under our supervision, is plagiarism free in accordance with the UGC Regulations on "*Promotion of Academic Integrity and Prevention of Plagiarism in Higher Educational Institutions (2018)*" and the CSIR Guidelines for "*Ethics in Research and in Governance (2020)*".

Dr. K. P. Surendran
(Co-supervisor)
May 18th, 2022
Thiruvananthapuram

Dr. K. N. Narayanan Unni
(Supervisor)
May 18th, 2022
Thiruvananthapuram

DECLARATION

I, Hanna B., bearing AcSIR Registration No. 10PP16J39007 declare: that my thesis entitled, "**Studies on visible-blind ultraviolet photodetectors with low voltage operation using zinc oxide nanostructures**" is plagiarism free in accordance with the UGC Regulations on "*Promotion of Academic Integrity and Prevention of Plagiarism in Higher Educational Institutions (2018)*" and the CSIR Guidelines for "*Ethics in Research and in Governance (2020)*".

I would be solely held responsible if any plagiarized content in my thesis is detected, which is violative of the UGC regulations 2018.

Hanna B

May 18th, 2022

Thiruvananthapuram

ACKNOWLEDGEMENTS

Hareesh, Mr. J. S. Kiran, Mr. Merin Santhosh, Mr. Aswin, Mr. Vibhu Darshan, Ms. Anjali K Sajeev, Ms. Sumitha, Dr. Swetha, and Mr. Lingamoorthy, for all their help and support in various matters throughout my research career at CSIR-NIIST.

Words are inadequate to express my gratitude to my family members who constantly stood as a source of encouragement and confidence. I take this opportunity to pay respect to all my teachers who taught me from childhood.

I thank UGC and DST, Government of India for the financial support.

<div align="right">Hanna B.</div>

TABLE OF CONTENTS

List of figures

List of tables

List of abbreviations

A	Ampere
Å	Angstrom
AC	Alternating current
AFM	Atomic force microscopy
Ag	Silver
Al	Aluminium
Al_2O_3	Aluminium oxide
ALD	Atomic layer deposition
AlGaN	Aluminium gallium nitride
AlN	Aluminium nitride
Ar	Argon
As	Arsenic
Au	Gold
B	Boron
BN	Boron nitride
CBD	Chemical bath deposition
CCD	Charge coupled device
CdS	Cadmium sulphide
CdSe	Cadmium selenide
CdSe	Cadmium selenide
CdTe	Cadmium telluride
CF_2	Difluorocarbene
CH_2	Methylene
Cu	Copper
CuO	Copper oxide
CuPC	Copper (II) phthalocyanine
CVD	Chemical vapour deposition
D	Crystallite size
D	Detectivity

DC	Direct current
DLS	Dynamic light scattering
e	Electron charge
ECD	Electrochemical deposition
E_g	Energy band gap
EQE	External quantum efficiency
E_u	Urbach energy
FeS_2	Iron (II) disulphide
FRET	Fluorescence resonance energy transfer
FTIR	Fourier transform infrared
G	Generation rate
Ga	Gallium
Ga_2O_3	Gallium oxide
GaAs	Gallium arsenide
GaN	Gallium nitride
GaP	Gallium phosphide
H	Hydrogen
h	Plank's constant
H_2O	Water
H_2O_2	Hydrogen peroxide
HMTA	Hexamethylenetetramine
HRTEM	High resolution transmission electron microscope
I	Current
I_d	Dark current
In	Indium
I_n	Total noise current
In_2O_3	Indium oxide
In_2Se_3	Indium (III) selenide
InAlGaN	Indium aluminium gallium nitride
InGaN	Indium gallium nitride
InN	Indium nitride

IPA	Isopropyl alcohol
IPCE	Incident photon to current efficiency
I_{ph}	Photocurrent
IQE	Internal quantum efficiency
I_s	Saturation current
ITO	Indium tin oxide
J_d	Dark current density
K	Boltzmann constant
K	Potassium
KOH	Potassium hydroxide
LCVD	Laser chemical vapour deposition
LDR	Linear dynamic range
LED	Light emitting diode
Li	Lithium
$LiNO_3$	Lithium nitrate
LPCVD	Low pressure chemical vapour deposition
MBE	Molecular beam epitaxy
Mg	Magnesium
MgO	Magnesium oxide
MOCVD	Metal organic chemical vapour deposition
MSM	Metal semiconductor metal
n	Ideality factor
N	Nitrogen
Na	Sodium
NaOH	Sodium hydroxide
Nb_2O_3	Niobium oxide
NBE	Near band edge emission
η_c	Collection efficiency
NEP	Noise equivalent power
η_{ext}	External quantum efficiency
NH_4	Ammonium

η_i	Internal quantum efficiency
Ni	Nickel
NiO	Nickel (II) oxide
NIR	Near infrared
NPB	N,N′-Di(1-naphthyl)-N,N′-diphenyl-(1,1′-biphenyl)-4,4′-diamine
η_t	Transmission efficiency
O	Oxygen
OH	Hydroxide
P	Phosphorus
P(VDF-TrFE)	Poly(vinylidene difluoride-trifluoroethylene
P3HT	Poly(3-hexylthiophene)
PANI	Polyaniline
Pd	Palladium
PECVD	Plasma enhanced chemical vapour deposition
PEDOT:PSS	Poly(3,4-ethylenedioxythiophene) polystyrene sulfonate
PFH	Poly(9,9-dihexylfluorene)
PFO	Polydioctylfluorene
PL	Photoluminescence
PLD	Pulsed laser deposition
PMMA	Poly(methyl methacrylate)
PMT	Photomultiplier tube
P_o	Incident optical power
PPC	Persistent photoconductivity
PS	Polystyrene
Pt	Platinum
PTFE	Polytetrafluoroethylene
Pt-Ru	Platinum-Ruthenium
PVA	Polyvinyl alcohol
PVD	Physical vapour deposition
PVK	Polyvinylcarbazole

PVP	Poly(4-vinylphenol)
q	Charge of an electron
QDs	Quantum dots
R	Responsivity
RF	Radio frequency
RMS	Root mean square
Sb	Antimony
Sb_2Se_3	Antimony triselenide
SEM	Scanning electron microscope
Si	Silicon
SiC	Silicon carbide
SnO_2	Tin (IV) oxide
SNR	Signal to noise ratio
T	absolute temperature
TAPC	1,1-Bis[(di-4-tolylamino)phenyl]cyclohexane
TCO	Transparent conducting oxide
TiO_2	Titanium dioxide
TMA	Tri methyl aluminium
UV	Ultraviolet
V	Bias voltage
VO_2	Vanadium (IV) oxide
W	Watt
XRD	X-ray diffraction
Zn	Zinc
ZnO	Zinc oxide
ZnS	Zinc sulphide
ZnSe	Zinc selenide
α	Absorption coefficient
β	Full width at half maximum intensity
λ	Wavelength
ν	Frequency

$\triangle f$	band width
0D	0-Dimensional
1D	1-Dimensional
2D	2-Dimensional
2-TNATA	4,4',4"-Tris[2-naphthyl(phenyl)amino]triphenylamine
3D	3-Dimensional
8HQ	8-hydroxyquinoline

PREFACE

Ultraviolet (UV) detectors are having great importance in the very survival and development of mankind. They find applications in various civilian and military fields. All these applications need devices with "5S" requirements such as high signal to noise ratio, spectral selectivity, sensitivity, speed and stability. UV detectors based on wide band gap semiconductors have received more attention due to their intrinsic visible-blind property and they provide secure and reliable operation. Among various wide band gap semiconductors, zinc oxide (ZnO) is a most promising material for UV detector application due to its attractive properties such as direct band gap, low cost, non-toxicity, abundance, high thermal and mechanical stability, high electron mobility, etc. Although UV photodetectors with reasonable performance have been reported by many researchers, the current demands are exceeding the characteristics of the conventional UV photodetectors. So, it is necessary to develop a novel UV photodetector with high performance to meet practical applications.

This thesis comprises four chapters. In the first chapter, an overview of UV photodetectors with the necessary fundamentals has been given. The chapter discusses the basic ideas and significant research problems existing in the fabrication of self-powered, flexible and wearable UV photodetectors and our approach to address some of them. In the following working chapters, the fabrication and characterization of visible-blind UV photodetectors with low voltage operation using ZnO nanostructures have been discussed.

The first working chapter discusses the fabrication of the organic-inorganic hybrid heterojunction based low temperature-processed self-powered UV photodetectors. Due to the defects present in ZnO thin film the device based on ZnO/NPB heterojunction exhibited poor performance. The defects in ZnO thin film were passivated by depositing a thin layer of TiO_2 as surface passivation layer. We have optimized the device performance by varying the

thickness of NPB. Then we studied the role of the organic layer on the spectral response properties of the device. We have tuned the spectral response of the device from UV to visible region by using different organic layers such as 2-TNATA, CuPC, TAPC and rubrene. The device with NPB exhibited best performance for a UV detector.

The morphology of ZnO plays an important role on the device performance. The second working chapter discusses the fabrication of UV photodetectors based on vertically aligned ZnO nanorods. The defects, surface states and traps present in ZnO nanorods affect device performance. The defects in ZnO nanorods can be passivated by surface passivation layers. Here, we have optimized the device performance by suitable choice of surface passivation layer. The device with ZnO thin film as surface passivation layer exhibited better performance with fast response. Then we studied the effect of growth time on device performance by changing the growth time from 5 h to 7 h and 9 h. Preferentially oriented nanorods were obtained for a 5 h grown sample. The performance of face-down ZnO nanorods were improved by depositing ZnO nanorods in interdigitated ITO coated substrates. The device exhibited an on-off ratio of 1.50×10^3, rise and fall times of 1.88 s and 6.39 s, detectivity of 4.20×10^{11} Jones responsivity of 55.60 mA/W and LDR of 62.01 dB at 1 V under 365 nm light illumination.

Polymer covering on ZnO nanoparticles can passivate the defects in ZnO nanoparticles. The third working chapter gives the details of fabrication and characterization of UV photodetector based on polymer/ZnO nanocomposite. The properties of nanocomposite can be varied by changing the concentration and morphology of ZnO nanoparticles. The choice of polymer also has an important role on the device performance. Here, we studied the role of polymers on device performance by using three different polymers such as PMMA, PS and P(VDF-TrFE). P(VDF-TrFE)/ZnO nanocomposite-based device exhibited better performance due to the ferroelectric nature of P(VDF-TrFE). Further, the device performance is optimized by varying the concentration and morphology of ZnO nanostructures. Top electrode material

plays an important role in device performance. We fabricated UV photodetectors based on polymer/ZnO nanocomposite with different top electrode materials. Due to the difference in the work function of the metals, the device with Ag as the top electrode material exhibited better performance.

ZnO-based devices always face problems associated with surface states and defects present in the ZnO film as these affect the device performance. Many fabrication techniques require a high temperature annealing step which makes them inappropriate for flexible or plastic substrates. Flexible and wearable UV photodetectors can be fabricated by high quality ZnO thin films formed from vapour deposition techniques. However, this will increase the cost of the device. Hence a fabrication protocol for ZnO thin films devoid of a high temperature annealing step, suitable for device fabrication, should be developed. Effect of morphology of ZnO on the UV detector performance is not well understood in spite of its critical role. In fact, there is versatility in nanostructure of ZnO which may have ramifications in the device performance which needs to be understood. It is very desirable for UV detectors to be either self-powered or having a low voltage operation. However, these aspects are not well explored in literature. In addition, the UV detector needs to be visible-blind in order to have a UV-selective response. . In this thesis, we tried to address some of these challenges in the UV photodetector fabrication.

Introduction to UV photodetectors

1.1 Photodetectors

Photodetectors are optoelectronic devices that convert light signals into electrical signals. They are vital components in many devices and find applications in optical communication systems, optical imaging, instrumentation, material processing, environmental monitoring, biomedical imaging, sensing, food technologies and manufacturing process monitoring, spectrometry etc.[1,2]

Photodetectors are commonly classified into two main classes such as thermal detectors and photon detectors.[3] Thermal detectors convert optical energy into heat energy by photothermal effect. The light falls on the device, raises its temperature and changes electrical properties of the device. They are comparatively slow, not efficient and mostly wavelength independent.[4] Photon detector works by generating electron-hole pairs on the absorption of incident radiation by the principle of photoelectric effect and they are wavelength dependent.[5,6]

The light can be detected if,

$$\frac{hc}{\lambda} \geq E_g$$

where λ is the wavelength of the incident radiation and E_g is the energy band gap of the material. The energy conversion process consists of four steps,

1. Light incident on the semiconductor material generates electron-hole pairs

2. Dissociation of the electron-hole pair

3. The generated electron and hole get transported through the semiconductor to the respective electrodes

4. Extraction of generated electron and hole by the respective electrodes

The energy band diagram of a p-n junction photodiode is shown in Figure 1.1. The electron-hole pairs are generated in the depletion region upon absorption of the incident radiation. These charge carriers are separated by the built-in potential or the applied reverse bias voltage, and a photocurrent is generated.

Space charge region

$h\nu > E_g$

p

Conduction band (E_c)
Fermi level (E_f)

n

Valence band (E_v)

Hole diffusion   Drift space   Electron diffusion
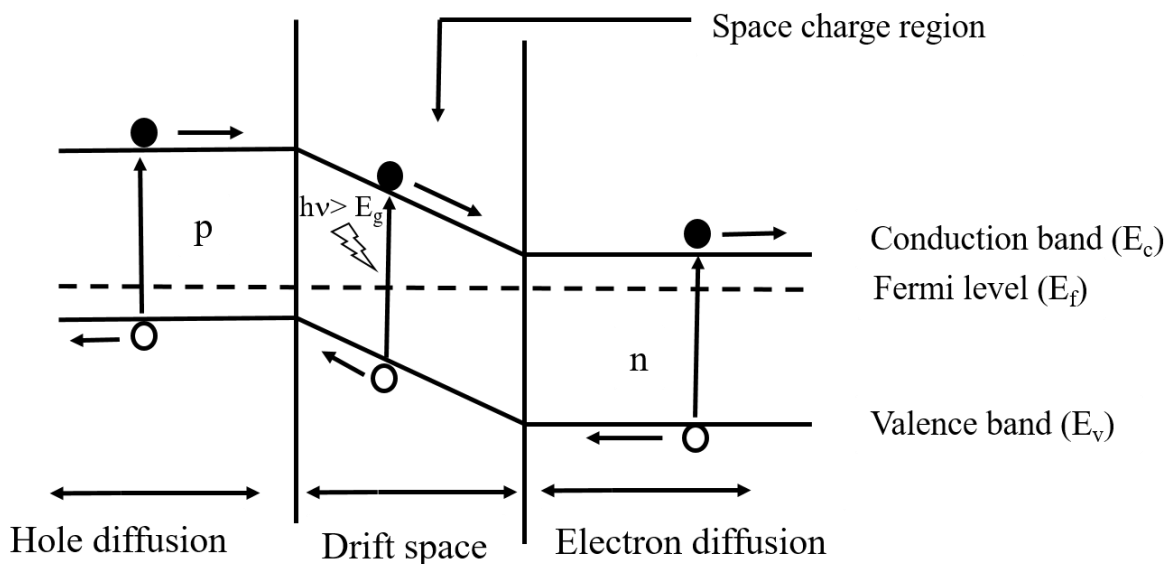
Figure 1.1. Energy band diagram of p-n junction photodiode.

Photodetection principle is based on internal photoelectric effect and external photoelectric effect. In internal photoelectric effect, the photogenerated carriers remain within the semiconductor and increase the conductivity. The most important of internal photoelectric effect is the photoconductivity. The external photoelectric effect involves photoelectric emission, in which the photogenerated carriers escape from the semiconductor. [7] Photoemissive detectors such as photomultiplier tubes and vacuum diodes are based on external photoelectric effect. [8] Photoconductive detectors have broad spectral responsivity, excellent linearity, high quantum

2

efficiency and high dynamic range of operation. Photoemissive detectors are easy to operate and they have high sensitivity. They have low quantum efficiency and they are sensitive to surface contaminants.

1.2 Performance parameters of photodetectors

The performance of a photodetector can be explained by certain parameters and they are discussed below.

1.2.1 On-off ratio

It is defined as the ratio of photocurrent to dark current. It is given by,

$$On - off\ ratio = \frac{I_{ph}}{I_d} \qquad (1.1)$$

where, I_{ph} is the photocurrent and I_d is the dark current.

1.2.2 Responsivity

It is defined as the ratio of the photocurrent to the incident optical power at a specific wavelength.[9] It is given by the equation (1.2) and expressed in A/W.

$$R = \frac{I_{ph}}{P_o} \qquad\qquad (1.2)$$

where P_o is the incident optical power.

1.2.3 Quantum efficiency

A photodetector is not able to collect all the photons incident on it and to convert them to electron-hole pairs. Quantum efficiency measures the ability of the photodetector to convert light signal to electrical signal. Internal quantum efficiency (IQE), η_i is the ratio of the number of electron-hole pairs generated to the total number of incident photons[10] and it is given by,

$$\eta_i = \frac{No.\,of\ electron-hole\ pairs\ generated}{No.\,of\ incident\ photons}\ 100\ \% \qquad (1.3)$$

It is similar to the quantum yield and for the materials with low dislocation densities and defects its value should be close to 100%. External quantum efficiency (EQE), η_{ext} is defined as the ratio of the number of photogenerated carriers collected at the electrode to the incident photons.[10] For a photodetector, the EQE is lower than the IQE. Due to Fresnel loss at semiconductor/air interface, reflection at the metal electrodes and absorption within non-active layers of the device, not all incident photons are absorbed within the active layer of the device.[10] These various processes constitute the transmission efficiency η_t. Second reason for the lower value of EQE is that not all the photogenerated electron-hole pairs are able to come out of the device as photocurrent. This constitutes the collection efficiency η_c of the photogenerated carriers in the device.[10] Thus EQE is given by,

$$\eta_{ext} = \eta_i \eta_t \eta_c \qquad (1.4)$$

$P_o/h\nu$ is the number of photons incident per unit time and I_{ph}/q is the number carriers collected at the electrode or coming out of the device as photocurrent.[11] Then EQE is given by,

$$\eta_{ext} = \frac{\frac{I_{ph}}{q}}{\frac{P_O}{h\nu}} \qquad (1.5)$$

using equation (1.5) in equation (1.2), we get Responsivity,

$$R = \frac{q\eta_{ext}}{h\nu} = \frac{q\eta_{ext}\lambda}{hc} \qquad (1.6)$$

4

1.2.4 Spectral response

It gives how the output signal of the photodetector changes with the variation in the wavelength of the incident radiation.[12] As the quantum efficiency depends on wavelength, the spectral response is not linear.

1.2.5 Noise equivalent power (NEP)

Thermal fluctuation is the source of noise in a photodetector. A small current of very low magnitude always exists in the device due to random motion of charge carriers by thermal fluctuation even in the absence of radiation. This is known as dark current. A detector must be able to differentiate this random noise and the incoming signal. The power of the incident signal must be higher than the noise signal. Signal to noise ratio,

$$SNR = \frac{Signal\ power}{Noise\ power} \tag{1.7}$$

NEP is the measure of the sensitivity of the photodetector. It is defined as the signal power that gives a signal to noise ratio of 1 in 1Hz output bandwidth at a particular wavelength and temperature.[13] It is given by,

$$NEP = \frac{I_n}{R\sqrt{\triangle f}} \tag{1.8}$$

where, I_n is the total noise current and $\triangle f$ is the band width.[14] NEP within the bandwidth $\triangle f$ is proportional to $\triangle f$ itself. Since the current is proportional to square root of the power, noise current is proportional to $\triangle f^{1/2}$.

1.2.6 Detectivity

Detectivity which is expressed in units of *Jones*, is used to characterize the sensitivity of the device. It is defined as the reciprocal of NEP normalized to the band width $\varDelta f$ and detector area A of the device. Higher the detectivity, more sensitive will be the device to the particular wavelength range. Detectivity is given by,

$$D = \frac{\sqrt{A}}{NEP} = \frac{\sqrt{A \triangle f}\, R}{I_n} \qquad (1.9)$$

Shot noise from dark current, Johnson noise and flicker noise contribute to the noise that limits the detectivity. If the Shot noise from dark current is the main contribution, then detectivity can be expressed as,[14]

$$D = \frac{R}{\sqrt{2qJ_d}} \qquad (1.10)$$

where, R is the responsivity, J_d is the dark current density and q is the charge of an electron.[15]

1.2.7 Linear dynamic range (LDR)

It is the range of current over which the response is linear which is given by,

$$LDR = 20 \, log(\frac{I_{ph}}{I_d}) \qquad (1.11)$$

where, I_{ph} is the photocurrent and I_d is the dark current.[16]

1.2.8 Rise and fall time

Rise time is defined as the time required to reach from 10% to 90% of the maximum value of the photocurrent. Similarly, fall time is the time required to reach from 90% to the 10% of the maximum value of the photocurrent.[17] Response time depends on drift of electron-hole

6

pairs generated in the depletion layer and diffusion of electron-hole pairs generated in the diffusion regions.

1.3 Different types of photodetectors

Photodetectors can be categorized into conductive mode and depletion mode devices. p-n junction photodiodes, p-i-n photodiodes, avalanche photodiodes and phototransistors are depletion mode devices and photoconductors, metal semiconductor metal (MSM) photodiodes, schottky photodiodes are conductive mode devices.
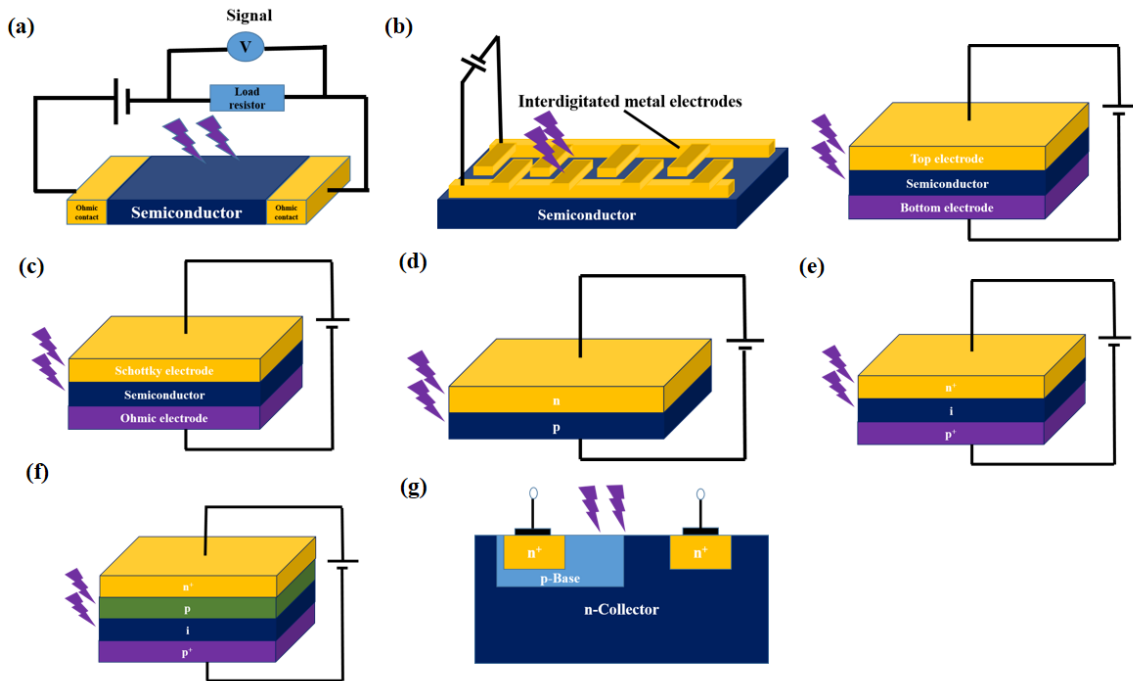
Figure 1.2. Different configurations of photodetector (a) Photoconductor (b) MSM photodiode in planar and vertical configuration (c) Schottky photodiode (d) p-n junction photodiode (e) p-i-n photodiode (f) Avalanche photodiode and (g) Phototransistor.

1.3.1 Photoconductors

The schematic diagram of a photoconductor is shown in Figure 1.2a. It consists of a semiconductor with two ohmic contacts.[18] Electron-hole pairs are generated upon the absorption of photons of energy higher than the band gap of the material. These charge carriers are

transported through the material under the influence of a bias voltage and a current is produced. It behaves like a resistor and the conductivity increases with the number of incident photons. Photoconductors have high internal gain at room temperature and high photoresponsivity. But persistent photoconductivity (PPC) effect and poor UV/Visible contrast affect their performance.[19]

1.3.2 MSM photodiodes

Simple structure, ease of fabrication and integration and low capacitance per unit area are the advantages of a metal semiconductor metal (MSM) photodiode. It comprises two back to back schottky diodes by using an interdigitated electrode configuration on top of an active light collection region.[20] Disadvantage of this type of configuration is that it cannot operate at zero bias. Also, it has relatively low responsivity. The schematic diagram of the MSM photodiode is shown in Figure 1.2b.

1.3.3 Schottky photodiodes

Figure 1.2c. shows the schematic diagram of a schottky photodiode. Compared to photoconductors and MSM photodiodes, schottky photodiodes have the advantages of high quantum efficiency, fast response, very low dark current, high UV/visible contrast and they operate at zero bias. It consists of a semiconductor with metal contact. The semiconductor-metal junction shows a rectifying behaviour which arises from the presence of an electrostatic barrier between metal and semiconductor due to the difference in the work functions of the metal and semiconductor.[21,22]

1.3.4 p-n junction photodiodes

A p-n junction photodiode is a p-n junction diode and it exhibits fast responding speed, low dark current and it can work without any applied bias. The schematic diagram of the p-n junction photodiode is shown in Figure 1.2d. They work under reverse bias conditions. Electron-

hole pairs are generated by the incident light in the depletion region and these charge carriers are separated and collected at the respective electrodes by the built in potential produced at the p-n junction and a current flows through the device.[23,24] The resulting photocurrent is proportional to the intensity of the incident radiation. The presence of diffusive components in the photocurrent due to the diffusion of charge carriers outside the depletion layer plays a major role in the device performance. This diffusion current distorts the temporal response of the device. It can be overcome by decreasing the width of the p and n regions and increasing the width of the depletion layer, such that most of the incident photons are absorbed inside it. This principle is used in p-i-n photodiodes.

1.3.5 p-i-n photodiodes

p-i-n photodiode consists of an intrinsic layer between p and n type materials. It operates in reverse biased conditions. The working principle of the p-i-n photodiode is similar to the p-n junction photodiode. The schematic diagram is shown in Figure 1.2e. The width of the depletion layer can be controlled by the thickness of the intrinsic layer. Compared to the p-n junction diode, the drift component of the photocurrent dominates over the diffusive component in the p-i-n photodiode because most of the incident radiation is absorbed inside the depletion region. Low noise, low dark current, low bias voltage, fast response and low junction capacitance are the advantages of p-i-n photodiodes. But they have low sensitivity and no internal gain.[25,26]

1.3.6 Avalanche photodiodes

The diagram of Avalanche photodiode is shown in Figure 1.2f. It is a p-n junction diode which operates under reverse bias near breakdown voltage. Advantages of Avalanche photodiodes are high signal to noise ratio, fast response, low dark current and high sensitivity. Much higher voltage is required for their operation and output is not linear.[27]

1.3.7 Phototransistors

Figure 1.2g shows the schematic diagram of a phototransistor. Phototransistors are semiconductor devices with a base region exposed to light. The light falling on the base region leads to the generation of electron-hole pairs and gives base current. This results in the flow of emitter current through the device. The magnitude of the generated photocurrent is proportional to the intensity of the incident radiation and will be amplified by the gain of the transistor. This leads to the generation of larger collector current.[28] Phototransistors are simple, compact and less expensive. High current gain, fast response, low noise and high stability are the advantages. But they are sensitive to electric spikes and surges. Compared to other two-terminal photodetectors, the third electrode in the phototransistor helps to control the photoresponse of the device without any noise associated problems.[29]

1.4 UV photodetectors

Ultraviolet (UV) radiation is part of the electromagnetic spectrum with wavelengths between 10 nm and 400 nm and has a very important role in human life. It is an important component in solar radiation and accounts for less than 10% of the total radiation. Research on UV radiation began in the 19th century after its discovery by Johann Ritter in 1801.[30] Moderate skin exposure to UV light is useful for human health, *i.e,* to facilitate the synthesis of vitamin D, to kill germs and for the treatment of rickets. Also, the UV radiation is useful for water sterilization and UV imaging of cancerous tissues in diagnosis. On the other hand, intensive exposure to UV radiation can cause skin cancer, sunburn and can damage the immune system and eyes.[31,32] It will also affect the life time of buildings and output of crops. Most of the UV radiation is absorbed by the stratospheric ozone. The decrease in stratospheric ozone produced by anthropogenic activities increases the intensity of UV radiation reaching the surface of earth. According to a report, a decrease of 1% in the stratospheric ozone will lead to an increase of 2%

in UV radiation coming to earth and will cause a 3% increase in the occurrence of UV induced skin cancer.[30]

UV radiation can be divided into three spectral regions. UV-A (400-320 nm), UV-B (320-280 nm) and UV-C (280-100 nm) regions.[33] UV radiation with wavelength less than 280 nm cannot reach the Earth's surface as it is absorbed by the ozone layer and the radiation with wavelength greater than 280 nm reaches the Earth's atmosphere. UV-A radiation stimulates photosynthesis and is useful for the synthesis of some vitamins and biochemical compounds. Overexposure to UV-A radiation causes erythema and premature ageing. Exposure to UV-B radiation causes skin cancer, cataracts, burns and erythema but it is useful for the activation of Vitamin D. UV-C radiation is important in inter satellite communications. Therefore, the detection of UV radiation becomes important in human life.[34–37]

UV detectors are having great importance on the survival and development of mankind. They find applications in various fields like radiation detection, UV imaging, pollution monitoring, space to space communications, flame detection, water sterilization, aerospace UV monitoring, environmental monitoring, lithography, ozone monitoring, missile early warning, chemical and biological agent detection etc.[38–40] All these applications require highly sensitive devices with high signal to noise ratio, high spectral selectivity, high sensitivity, high speed and stability. Due to high sensitivity, high signal-to-noise ratio and high response speed during the detection, low noise and high gain characteristics photomultiplier tube (PMT), charge coupled devices (CCDs) and silicon based UV detectors have dominated the main market.[41] However PMTs need ultra-high vacuum environment and high operating voltage for their operation. Also, fragile vacuum tube construction, large size and magnetic field sensitivity limit their applications in UV detection systems. Silicon based detectors need costly extra filters and phosphors to stop low energy photons. CCDs have poor spectral selectivity.[42,43] In the efforts to overcome these limitations, UV detectors based on wide band gap semiconductors have received more attention

due to their intrinsic visible-blind property. Since they are thermally and chemically stable, they can operate in harsh environments. UV photodetectors based on wide band gap semiconductors provide secure and reliable operation.[44,45] They are small and light weight and respond to light rapidly. They meet "5S" requirements of UV detectors such as high speed, high signal to noise ratio, high sensitivity, high spectral selectivity and high stability. They show high dynamic range of operation, excellent linearity and high quantum efficiency.[46]

1.5 Materials for UV detector fabrication

Si is the most commonly used material for the fabrication of UV detectors due to the well-established manufacturing process and easy circuit integration.[47] But there are some limitations in UV detection with Si technology due to its narrow band gap. The energy band gap of Si is 1.1 eV. So optical filters and phosphors are needed to stop low energy photons. Also, the performance of the device is degraded with increasing dark currents and lower efficiency upon aging. At high temperatures the intrinsic carrier concentration will overcome the doping concentration and the device will no longer operate as intended.[48] Wide band gap semiconductors such as, SiC, diamond, GaP, GaAs, III-Nitrides, ZnS, ZnO, TiO_2, CdS, GaP, GaO_3, In_2O_3, SnO_2, In_2Se_3, ZnSe, CdSe, Nb_2O_3, Sb_2Se_3 etc. have received much attention for the fabrication of high temperature and high power UV detectors and they can operate in harsh environments.[49,50]

Group III-Nitrides such as, GaN, AlN, InN, BN etc. and alloys of these compounds, such as InGaN, AlGaN, InAlGaN are used for the fabrication of photodetectors with high spectral selectivity, radiation hardness and high thermal stability.[51–54] The energy band gap of the material can be varied by varying the concentration of the alloy. They are direct band gap materials with wurtzite structure. High density dislocations and structural defects limit their use in UV detector fabrication. GaN is the most promising material in the III-Nitride group due to its high chemical and thermal stability.[55] Due to the PPC effect, the photocurrent response remains in GaN even

after the illumination source has been removed. PPC arises due to the presence of negatively charged surface states, metastable states defects, gallium vacancies and nitrogen antisites.[50] The very large photocurrent decay time and trapped charge carriers affect the quantum efficiency. BN is visible-blind and can be synthesized in different morphologies. It exhibited high thermal stability and large photocurrent and suitable for high temperature UV detector applications.[56]

SiC is the most mature wide band gap semiconductor used for high power, high temperature, high frequency and radiation hardened applications with fast response.[57] However, high pass optical filters are needed to select the appropriate spectral range. The operating temperature is higher than that of GaN based devices and the values of responsivity are less than that of GaN. The device photoresponse depends on temperature and PPC effect is not observed in these devices and the devices exhibited fast response.[50]

Diamond is another wide band gap semiconductor with high thermal conductivity, high carrier mobility suitable for the fabrication of deep UV detectors.[58] But the grain boundaries and the presence of non-diamond impurities affect the device performance. The performance of the diamond-based UV detectors can be enhanced by doping it with sulphur. Sulphur doped diamond based UV detectors exhibited high sensitivity, high speed and visible-blindness.[59]

Metal oxides are the main focus of the current research. Metal oxides such as ZnO, TiO_2, SnO_2 etc.[60,61] are commonly used for the fabrication of UV photodetectors. Other metal oxides such as VO_2, Ga_2O_3, In_2O_3 etc. are also used for the fabrication of UV detectors.[62–64] Among the above candidates, ZnO is a most promising material for UV detector application due to its attractive properties.[65] It is a II-VI group wide band gap semiconductor having properties comparable with GaN. Most of the commercial photodetectors are fabricated based on Si, GaN and SiC. However, their responsivity is low and the fabrication process is complex. The lack of high quality lattice-matched substrates leads to the materials with defects and grain boundaries.

These defects affect the device performance and increase leakage current and affect its visible-blindness.[50] So, photodetectors based on these materials require high quality and high cost fabrication processes such as metal organic chemical vapour deposition (MOCVD), and molecular beam epitaxy (MBE). This leads to the high cost of the device. ZnO has similar crystal structure and optical properties comparable with GaN and it is a best alternative material for UV detector applications. The energy band gap of ZnO is the same as that of GaN and ZnO shows better radiation resistance than GaN. ZnO is also of low cost comparable to GaN.[66]

1.6 Properties of ZnO

Transparent conducting oxides (TCOs) find applications in various optoelectronic devices such as solar cells, UV detectors, flat panel displays, plasma display panels, light emitting diodes, electronic paper displays, touch panels etc.[67] They show good electrical conductivity and high optical transparency in visible range. Among all TCOs indium tin oxide (ITO) is the material of choice for various transparent electrode applications. However, for the fabrication of flexible devices ITO is not suitable due to its conductivity instability with stretching and bending forces. Due to scarcity and high cost of indium it is necessary to develop non-indium based TCOs.[68] ITO can be replaced by ZnO due to its low cost, non-toxicity and stability against hydrogen plasma treatment and comparable electrical and optical properties with ITO.[69]

ZnO has attracted great attention in semiconductor device applications due to its peculiar electrical, optical, and chemical properties. It is a II-VI group semiconductor with direct band gap of 3.37 eV at room temperature. It is easily available, non-toxic and an inexpensive material. It shows high thermal and chemical stability, high electron mobility and crystallizes in hexagonal wurtzite structure. It has high mechanical strength, high thermal conductivity and is highly durable against hydrogen plasma. It exhibits piezoelectric and luminescent properties. It shows second and third order non-linear optical behaviour. The conductivity of ZnO varies when

exposed to various gases. It exhibits higher radiation hardness compared to GaN. It can be easily prepared by various synthetic methods.[70–73] ZnO nanoparticles have high antibacterial properties at lower concentrations.[74] So it is a promising functional material for the fabrication UV detector,[75] bio-molecule sensor,[76] optical waveguides,[77] surface acoustic wave devices,[78] nano generators,[79] thin film transistors,[80] light emitting diodes,[81] solar cells,[82] chemical and gas sensors,[83] varistors[84] etc. and it is used in photocatalytic[85] applications also. The properties of ZnO can be tuned by doping it with Al, Ga, In, As, P, N, B, Ag etc.[86]

ZnO can be crystallized in hexagonal wurtzite, zinc blende and rock salt structure.[87] Thermodynamically stable phase is the hexagonal wurtzite structure, in which Zn^{2+} ion is tetrahedrally bonded to four O^{2-} ions and vice versa. The zinc blende structure of ZnO is metastable and can be made stable by growing ZnO nanostructures on substrates with cubic lattice. The rock salt structure of ZnO is stable at high pressures.[88] The stable hexagonal wurtzite structure of ZnO is shown in Figure 1.3. In the structure, polar faces are Zn terminal face (0001) and O terminal face $(000\bar{1})$ and $(11\bar{2}0)$ and $(10\bar{1}0)$ are the non-polar faces.[89] Non-polar faces contain an equal number of Zn and O atoms. The polar symmetry along the hexagonal axis gives rise to the piezoelectric property of ZnO. The tetrahedral coordination of Zn and O atoms shows the presence of sp^3 hybridized covalent bonding and Zn-O bond shows ionic character. So, ZnO behaves like both ionic and covalent compounds. The lattice parameters of hexagonal unit cell of ZnO are a=3.2455 Å and c=5.2069 Å.[87]

The electronic band diagram of ZnO is shown in Figure 1.4. The valence band maxima and conduction band minima lie at k=0 indicating the direct band gap property of ZnO. The electronic configuration of Zn is $1s^2\ 2s^2\ 2p^6\ 3s^2\ 3p^6\ 4s^2\ 3d^{10}$ and O is $1s^2\ 2s^2\ 2p^4$. The occupied 2p states of O^{2-} form the bottom of the conduction band and the empty 4s states of Zn^{2+} form the top of the valence band. Due to crystal field and spin-orbit interaction, the valence band of ZnO is split into three sub bands such as A, B and C. The A and C sub bands possess Γ_7 symmetry

and the sub band B possesses Γ_9 symmetry.[90] The reported value of band gap is 3.43 eV at 4.2 K and 3.37 eV at room temperature. Some of the basic properties of ZnO are summarized in table 1.1.[91]
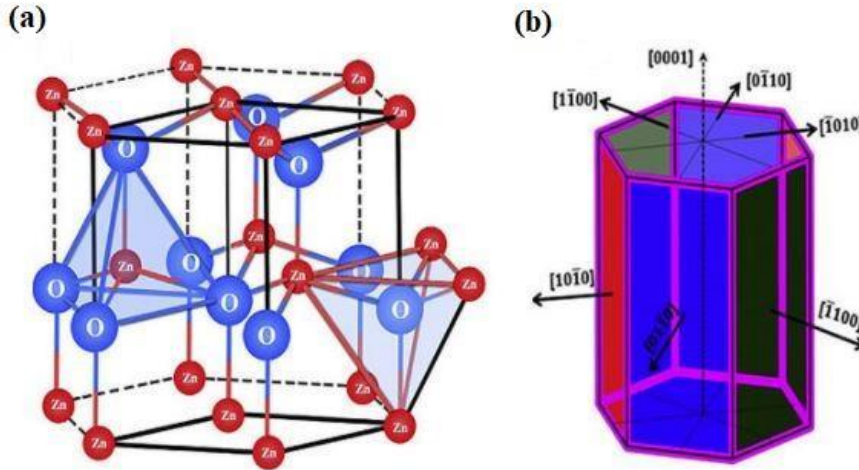
Figure 1.3. (a) Hexagonal wurtzite structure of ZnO (b) Hexagonal prism of ZnO crystal showing different crystallographic faces (adapted from reference 89).

The presence of defects and impurities affect the optical and electrical properties of ZnO. ZnO is an n-type semiconductor. The interstitial H which is present in all growth and processing environments forms a strong bond with O in ZnO and forms a shallow donor level. The H can also substitute for O in ZnO and acts as a shallow donor level. The presence of native point defects such as O vacancy, Zn antisites and Zn interstitials form deep donor level and contributes to the n-type conductivity.[92] Also, the unsaturated bonds present in ZnO attract chemical species such as OH, H_2O, O_2 etc. and affect chemical stoichiometry. This leads to the formation of surface states on the surface of ZnO and act as recombination centres and reduce the performance of ZnO-based optoelectronic devices. It can be overcome by suitable surface passivation techniques such as heat treatment, plasma treatment, hydrogen peroxide treatment, polymer coating, TiO_2, Al_2O_3 coating, UV ozone treatment etc.[93] The surface modification treatments enhance the near band edge emission and suppress the defect emission. Choosing the

suitable surface modification treatment is a major challenge because it will affect the chemical

stoichiometry of ZnO, form interfaces, affect morphology and get contaminated due to chemical

impurities. It is very difficult to obtain p-type conductivity in ZnO. It can be attained by doping

ZnO with materials such as Li, Na, K, P, As, Sb and N.[94]
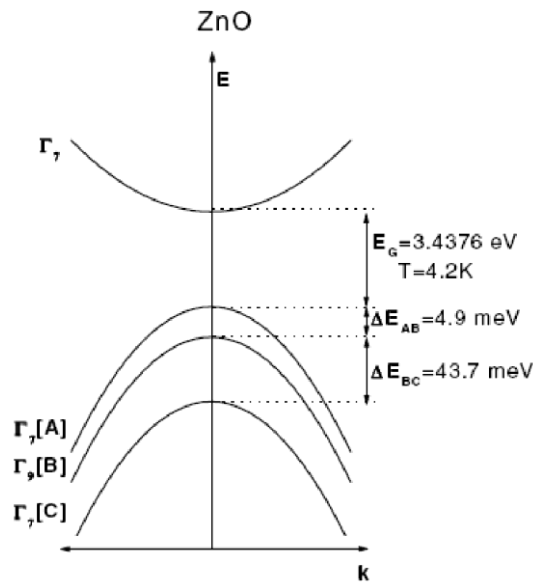
Figure 1.4. Electronic band diagram of ZnO (adapted from reference 90).

Energy band gap	3.37 eV
Stable structure	Hexagonal wurtzite
Lattice parameters	a=3.2455 Å c=5.206 Å
Density	5.606 g/cm^3
Refractive index	2.008, 2.029
Thermal conductivity	1-1.2 W/m.K
Melting point	1975 ^{0}C
Exciton binding energy	60 meV
Static dielectric constant	8.656
Intrinsic carrier concentration	<10^6 cm^{-3}
Electron effective mass	0.24 m$_o$
Hole effective mass	0.59 m$_o$

Table 1.1. Properties of ZnO at 300 K.

1.7 Different morphologies of ZnO

ZnO nanostructures have received great attention in many applications due to their exceptional chemical and thermal stability. Studies on ZnO growth processing techniques and its properties started in the 1900s. ZnO nanostructures of different morphologies can be easily obtained by different synthetic methods, by controlling the growth kinetics, by varying the growth temperature and chemical composition of precursor materials. The electrical, optical, structural and chemical properties of ZnO vary with morphology.[95] The ZnO nanostructures can be classified into 0-dimension (0D), 1-dimension (1D), 2-dimension (2D) and 3-dimension (3D) nanomaterials.

The 0D ZnO nanomaterials consist of quantum dots (QDs), nanoparticles and core-shell spheres. Compared to CdS, CdSe and CdTe QDs ZnO QDs have long term environmental stability, bio-compatibility and low-cost.[96] Also, due to their unique physical and chemical properties, they find a wide range of applications in optoelectronic devices. Due to the quantum size effect and large absorption coefficient of ZnO QDs, visible-blind and selective spectral response-UV photodetectors can be easily fabricated. In ZnO QDs based photodetectors, due to quantum confinement, more charge trapping states are introduced. Upon UV illumination in addition to the desorption of oxygen molecules, the quantum tunnelling of the photogenerated carriers, inter-band transitions and the surface charge trapping states cause drastic increase in photocurrent.[97] The ZnO QDs based devices exhibited good performance compared to nanoparticle based devices. [98–100]

Recently 1D ZnO nanomaterials like, Nanorods,[101] nanowires,[102] nanobelts,[103] nanotubes,[104] nanoneedles,[105] nanorings,[106] nanoribbons,[107] nanohelices/springs,[108] nanopropellers[109] etc. have attracted much attention for optoelectronic applications due to their high surface to volume ratio and long conduction path. Compared to other nanostructured

materials, 1D nanomaterials are the favourites for the fabrication of UV photodetectors with high sensitivity, quantum efficiency and fast response speed. The length, diameter and orientation affect the optical and electrical properties of the 1D nanomaterials.[110] Controlled 1D crystal growth can be easily obtained by several synthesis methods.

The performance of the QD based UV photodetector is limited due to the scattering of light from a large number of nanoscale grain boundaries within the QD and the performance of the 1D nanomaterials based photodetector is limited due to the incomplete surface coverage.[110] So, ultrathin 2D ZnO nanostructures like, nanosheets,[111] nanoplates,[112] nanoflakes,[113] nanocombs,[114] nanopellets,[115] nanowalls,[116] nanodisks[117] etc. are better suited for fabrication of high performance optoelectronic devices. The grain boundary recombination can be overcome by high quality ZnO nanosheets which enhance carrier transport and provide large active area of charge carriers.[118] Compared to other 0D and 1D nanostructures, 2D nanostructures can be easily transformed into more complex structures. The surface area of the 2D nanostructure could be larger than the wavelength of the incident radiation. So, the reflection of light occurs on top layer in planar structure. But in 1D nanostructure i.e, in nanorods, the diameter of the individual nanorods is smaller than the wavelength of the incident radiation that causes the scattering of light from nanorods. But in 2D nanostructures like nanoflakes multiple reflection of radiation occurs instead of scattering, due to its large surface area, which induces the high optical field intensity in the cavity of nanoflakes. The induced high optical fields in the cavity of nanoflakes increase light harvesting efficiency through absorption.[119] To further increase the light absorption efficiency of ZnO-based materials and optoelectronic devices, many researchers are working on engineering ZnO nanomaterials with even higher surface area. ZnO nanocomb with dense array of teeth has larger surface-to-volume ratio. The accumulation of electrons by adsorption of oxygen molecules at the teeth part reduces dark current of the backbone of the nanocomb and leads to an increase in the photoconductive gain of the UV detector.[120]

Compared to 0D, 1D and 2D ZnO nanomaterials, 3D ZnO nanomaterials exhibit high surface-to-volume ratio, large surface area and better permeability.[121] Also, the 3D ZnO structures like, nanotetrapod,[122] nanocone,[123] nanoballs,[124] nanopillar,[125] nanoflower[126] etc. can increase the light travelling path and thereby increase the light absorption efficiency. The significant advances in the development of different morphologies of ZnO lead to the fabrication of ultrafast low-cost, self-powered and flexible photodetectors.

1.8 ZnO film fabrication techniques

Highly transparent and conductive ZnO films can be prepared by a variety of techniques.[127] The synthesis techniques for the different morphologies of ZnO nanostructures can be classified into solid, liquid and vapour phase method.[128] The different synthesis methods are shown in Figure 1.5. Solid state method consists of grinding, mixing and heat treatment of precursor materials.[129] Inhomogeneity, poor stoichiometry, larger crystallites, difficulty in controlling the particle size and phase impurities are the disadvantages of this technique. Liquid phase methods are classified into hydrothermal, chemical bath deposition (CBD), electrochemical deposition (ECD), spray pyrolysis, sol-gel process, co-precipitation method, combustion, microwave assisted and polyol synthesis routes.[130–133] The advantages of liquid phase methods are the low growth temperature, simple and low cost processes and ease of controlling the composition.[128] Among liquid phase methods, sol-gel process is simple and inexpensive.[134] Other advantages are its reliability and repeatability. Highly crystalline films can be achieved at low temperature and it is easy to control the composition of ZnO films. The electrical, chemical, structural and optical properties of ZnO films prepared by sol-gel process depend on the precursors, solvents, annealing temperature and time.

Physical vapour deposition method (PVD) and chemical vapour deposition method (CVD) are the two sub-classes in the vapour phase methods. PVD is further divided into thermal

evaporation, sputtering and pulsed laser deposition (PLD). CVD method is classified into atomic layer deposition (ALD), thermal CVD, low pressure CVD (LPCVD), plasma enhanced CVD (PECVD), metal organic CVD (MOCVD), laser CVD (LCVD) and molecular beam epitaxy (MBE). Vapour phase methods are suitable for the production of high quality and single crystal ZnO nanostructures. But these processes require high temperature, vacuum conditions and costly gases for their operation. This leads to the high cost of film fabrication. [135–139]
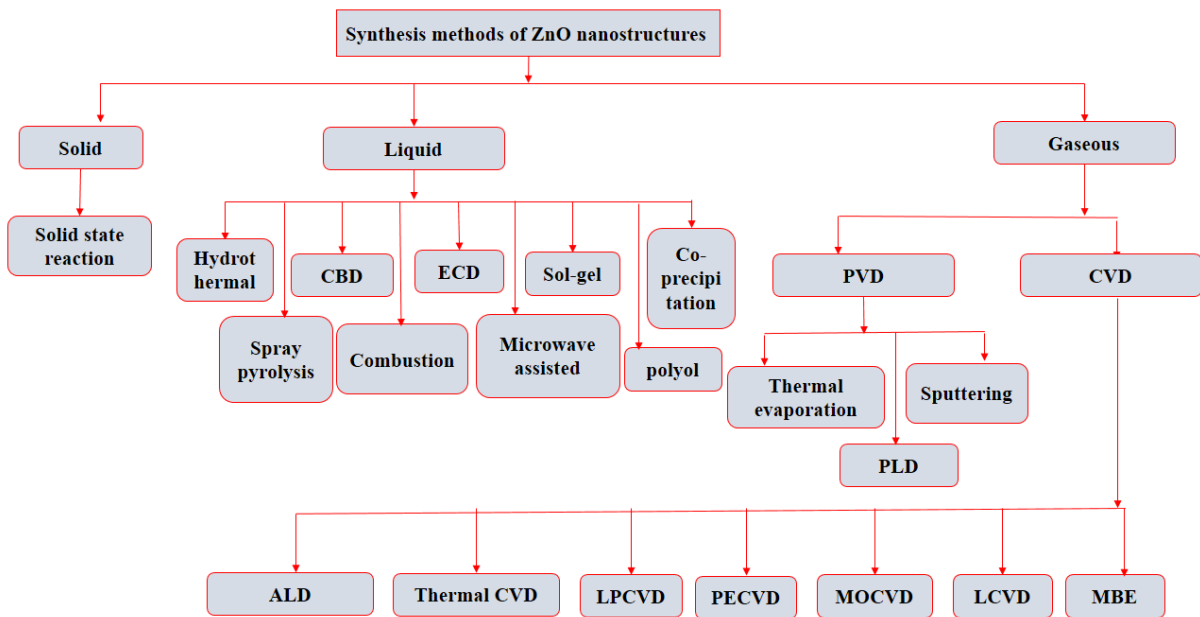
Figure 1.5. Synthesis methods of ZnO nanostructures.

1.9 ZnO-based UV photodetectors

The UV photoresponse property in ZnO thin films was first observed in 1940 by Mollow.[140] However, the research on ZnO-based UV detectors started only in the 1980s. Initially the devices were fabricated with simple structure and device performance was not good. Then with the improvement in the ZnO film fabrication techniques, development of different morphologies of ZnO nanostructures and different architectures, UV detectors with reasonable performance were reported.

1.9.1 ZnO-based UV Photoconductors

ZnO-based UV photoconductors have been reported by a number of research groups. UV photoconductors based on sol-gel synthesized ZnO films exhibited EQE of 14% and response time of 160 s at 5 V under 350 nm light.[141] In 2008, Jin et al. fabricated UV photodetectors based on colloidal ZnO nanoparticles. The device exhibited fast response with a responsivity of 61 A/W and photoconductive gain of 203 under 370 nm light illumination.[142] The oxygen molecules adsorbed on the ZnO surface form a depletion layer by trapping the free electrons from the n-type ZnO. Upon UV illumination, electron-hole pairs are generated and the ionized oxygen molecules combine with the photogenerated hole and desorb from the surface of the ZnO by releasing trapped electrons, which increases the photocurrent of the device. UV photodetectors based on PVA coated ZnO colloidal nanoparticles grown on GaN substrates were fabricated by Qin et al.[143] The colloidal nanoparticles were synthesized by top down wet chemistry synthesis process. The PVA coated ZnO nanoparticles showed better performance compared to ZnO without PVA because, PVA surface passivates the defects in ZnO. The device exhibited on-off ratio of 10^5 and responsivity of 0.8 A/W under 375 nm light at -20 V. UV photoconductor based on ZnO nanowire synthesized by hydrothermal method exhibited an on-off ratio of 892 at 30 V under 365 nm light.[144] The device exhibited slow response with fall time of 78 s due to the defects present in the sample. The surface defects present in ZnO lead to large rise and fall times. It can be overcome by passivating the defects using a surface passivation layer. Wang et al. fabricated flexible UV photoconductors based on ZnO nanorods coated with 8-hydroxyquinoline (8HQ).[145] The device without 8HQ exhibited too long rise and fall times of few hundred seconds because the adsorption and desorption of O_2 on ZnO nanorod surface need a long time to balance. In order to overcome this problem, they modified the surface of the ZnO nanorod by coating it with 8HQ. The role of this organic semiconductor is to prevent the reaction of O_2 with ZnO and to improve response speed. The device coated with 8HQ showed a responsivity of 484 A/W and rise and

decay times of 10 s and 27 s respectively. Fan et al. fabricated 3D periodic nanocone ZnO films by thermal nanoimprinting technology with different height and pitch values to improve their light capturing property.[146] Then these nanocone ZnO films were decorated by Au to further improve their device response. The on-off ratio of photoconductors with Au decorated ZnO nanocone films is 3.8 times higher than the device without Au. The schottky junction in the semiconductor metal contact also contributes to the light absorbing ability. The photocurrent varies with different height/pitch values of nanocones and the highest photocurrent was observed for ZnO nanocone with height/pitch values of 40 nm/860 nm. Photoresist coated ZnO nanowire synthesized by catalyst-free solid vapour process based photodetector exhibited fast response with rise time of 3 s and fall time of 20 s under 365 nm light.[147] UV photoconductors based on epitaxial ZnO thin films deposited by RF magnetron sputtering exhibited fast response with high responsivity under 325 nm light illumination.[148] Ni/Cu codoped ZnO nanorods exhibited high performance with a responsivity of 123 A/W and rise and fall times of 8 s and 3 s respectively.[149] Doping with Ni/Cu improves the crystallinity and reduces the defect states in ZnO nanorods.

1.9.2 ZnO-based MSM UV detectors

ZnO-based MSM UV detectors have attracted more attention due to their fast response, low capacitance per unit area, high responsivity and ease of fabrication.[150] They can be fabricated in planar and vertical configurations. In planar structure, the interdigitated electrodes are co-planar on the same side of the ZnO and in vertical configuration ZnO is sandwiched between the two metal electrodes.[151] MSM photodetectors fabricated based on ZnO films synthesized by sol-gel method generated a photocurrent of 44.89 μA at 6 V under 365 nm light illumination.[152] Liu et al. fabricated MSM detectors with high visible rejection and fast response based on c-axis preferred oriented ZnO film deposited by magnetron sputtering with Au contacts.[153] The device exhibited responsivity of 30 A/W and rise and fall times of 20 ns and 10 μs respectively at 3 V under 360 nm. The UV detectors fabricated on sapphire substrates with Au contacts of various

finger width and pitches showed responsivity of 0.135 A/W and detectivity of 2.23×10^{12} Jones at 1 V.[154] Jandow et al. fabricated detectors with on-off ratio of 159 based on ZnO deposited by DC sputtering on poly propylene carbonate (PPC) substrates with Pt contacts.[155] He et al. fabricated low cost MSM detectors based on electrically floated ZnO nanowire array. Ar ion bombardment and polymer coating were used for surface passivation and the device with polymer coating exhibited excellent photoconductive properties with repeatability. The electrical and optical properties of ZnO can be varied by doping. Ga doped ZnO-based fast response-MSM photodetectors with high responsivity of 1187 A/W at 5 V were reported by Shinde et al.[156] In the same year they reported fast response N doped ZnO-based MSM detectors with responsivity of 580 A/W at 5 V.[157] Singh et al. reported UV detectors based on Al doped ZnO nanorods with better performance under 372 nm.[158] 2D In doped ZnO nanostructures exhibited on-off ratio of 740, responsivity of 0.074 A/W and rise and fall times of 3.02 s and 1.53 s respectively at 1 V under 365 nm light illumination.[159] MSM detectors based on hydrothermally grown ZnO nanorod with Pd contacts showed responsivity of 0.199 A/W at 1.8 V.[160] Al-Khalli et al. theoretically studied the influence of structural parameters on the MSM device performance by drift diffusion model.[161] They found that the device with thicker active layer and wider finger spacing exhibited superior performance with high responsivity. The responsivity increases with increase in the thickness of the active layer and after a certain thickness it saturates around 0.085 A/W. Fall time increases with increase in finger spacing regardless of the thickness of the active layer. Widening the finger spacing worsens the temporal response characteristics of devices. The bipolar photoresponse of MSM photodetectors based on ZnO nanowires was studied by Zarezadeh et al in 2020.[162] In dc mode, photoconductivity increases with illumination. However, in ac mode the device exhibited a frequency modulated response to UV radiation. It provides the platform for the fabrication of bipolar photoresponse-UV photodetectors with high technological importance. Jezeh et al. reported MSM detectors with RF sputtered porous ZnO.[163] The porous nature can

improve the photodetector performance. They studied the effect of asymmetry of photodetector electrodes and the difference in the schottky barrier height in the device performance.

1.9.3 ZnO-based p-n junction UV photodiodes

The adsorption and re-adsorption of oxygen molecules on ZnO nanostructures play a major role in the response speed of the UV detector. p-n junction is an appropriate choice to avoid this problem as it can enhance the transportation efficiency of charge carriers. p-n junction UV photodiodes composed of ZnO nanostructures appear to be more promising due to its stability, fast response, zero bias operation and excellent sensitivity. So, they find applications in portable and wearable sensing devices without any external power supply. The photovoltaic effect produced by the built-in field of the p-n junction helps to separate the photogenerated electron-hole pairs without any applied bias. ZnO is one of the most suitable materials to make p-n homojunction devices due to its intrinsic n-type conductivity. Liu et al. reported p-n homojunction detector formed by Sb-doped p-type ZnO films grown on n-type Ga-doped ZnO layer and heterojunction with p-type Sb-doped ZnO film grown on n-Si.[164] Both homo and heterojunction exhibited better photoresponse properties. ZnO p-n homojunction photodetector with p-type As-doped ZnO and ZnO exhibited good rectifying behaviour with responsivity of 0.91 A/W at 6 V.[165] Leung et al. fabricated visible-blind UV detector by p-n homojunction formed by p-type Al-N codoped ZnO and n-type ZnO nanowire.[166] The device showed high rectification ratio with good photoresponse characteristics when illuminated with 384 nm at 3 V. The UV detector with Sb-doped p-type nanowire array and n-type ZnO film homojunction showed visible response at 570 nm due to the presence of deep levels in ZnO.[167] ZnO is a good choice to make p-n homojunction devices. But it is very difficult to synthesize stable and reproducible p-type ZnO due to the self-compensating effect from native defects. So, employing p-n heterojunction formed by ZnO and other p-type materials is a good way to produce high performance photodetectors. Park et al. reported high efficiency NiO/ZnO heterojunction UV

photodiode by sol-gel method with an EQE of 88%.[168] The device exhibited narrowband response from 300-450 nm with responsivity of 21.8 A/W and detectivity of 1.6×10^{12} Jones at 5 V. Due to lack of sharp junction interface, they did not observe any photovoltaic effect and the device cannot operate at zero bias. In 2015, Hasan et al. produced self-powered p-NiO/n-ZnO heterojunction UV photodetectors on plastic substrates.[169] Photovoltaic effect is produced by the built-in field at the junction and the photogenerated electron-hole pairs are separated by the built-in field. The device exhibited fast response with a responsivity of 0.14 A/W and EQE of 63% at 370 nm. Organic-inorganic hybrid heterojunction UV detectors have the advantages of low cost, flexibility, selective spectral response and broad absorption band width[170] because it possesses the properties of both organic and inorganic semiconductors. Srivastava et al. reported polyvinylcarbazole (PVK)/ZnO-based organic-inorganic hybrid heterojunction device with good performance.[171] Poly(9,9-dihexylfluorene)/ZnO heterojunction UV detector with good performance was reported by Xiaoyun.[172] Organic-inorganic hybrid heterojunction photodiode with PVK insertion layer exhibited better performance compared to the device without the same.[173] For the device without PVK, the poor rectifying behaviour is due to the large barrier existing at the p-NiO/n-ZnO interface and the defects of interface. PVK reduces the barrier height at the interface and improves the current transport. ALD-deposited ZnO thin films on laser micro structured silicon shows enhanced broadband responsivity across the UV-visible-NIR range.[174] The micro structured silicon helps to enhance the responsivity by increasing the heterojunction area and extending the spectral response region. Zhang et al. reported a high performance 3C-SiC/ZnO heterostructure UV photodetector based on piezo-phototronic effect.[175] The strain induced piezo-potential in ZnO nanorod array significantly improve the photodetector performance by modulating the charge carrier transport, separation and recombination process at the interface. The device exhibited a high responsivity of 1.01×10^6 A/W and fast response of 20 ms by applying an external compressive strain of -0.381%. Bulk heterojunction is suitable for

creating donor-acceptor interfaces throughout the active layer. The blending of the donor acceptor materials improves the efficiency of the photodetector by changing the structural, optical and electrical properties of the active layer. Srivastava et al. reported a bulk heterojunction photodetector based on pentacene:ZnO as the active layer.[176] The spectral response can extend from UV to visible region by changing the composition of pentacene:ZnO films. The device with blend film ratio of 1:2 exhibited optimum performance with a responsivity of 9.26 A/W and detectivity of 1.74×10^{13} Jones under 302 nm.

1.9.4 ZnO-based avalanche UV photodetectors

UV photodetectors with high photoresponsivity are required for solar-blind applications. ZnO-based avalanche photodetectors have the advantages of large photocurrent and high responsivity. The high responsivity is due to the carrier multiplication induced by ionization impact. For ZnO, the ratio between impact ionization coefficient of holes and electrons is low. This is one of the advantages of ZnO to achieve high responsivity UV photodetectors. Yu et al. reported ZnO-based avalanche UV photodetectors with high responsivity of 1.7×10^4 A/W at 367 nm and avalanche gain of 294 at 73 V.[177] The rise and fall times were 98.9 ns and 9.9 μs respectively. Solar-blind avalanche photodetectors based on single ZnO-Ga_2O_3 core shell microwire were fabricated by Zhao et al. The device exhibited fast response with high sensitivity and stability at 254 nm. The heterojunction formed between Ga_2O_3 and ZnO is good choice to fabricate avalanche photodetectors due to the difference in conduction band and valence band offsets.[178] MgO/MgZnO heterostructure based photodetector with high responsivity is reported by Chen et al.[179] The MgO layers were deposited on the MgZnO layer in the device as barrier layers to induce ionization impact for avalanche gain. Single crystalline MgZnO thin films deposited on Ga:ZnO exhibited high performance with a responsivity of 2 A/W at 5 V under 278 nm.[180] Gaoming et al. used p-Si/i-ZnO/n AZO structure to realize avalanche multiplication.[181] Different thickness of ZnO was used to study the influence of thickness of i-ZnO layer on the

device performance. In 2021, Zhao et al. reported photodetectors with high quantum efficiency of 502780% at 90 V under 275 nm using MgZnO/Au/ZnO sandwich structure.[182] In the sandwich-structured photodetectors, the avalanche effect originates from the collision ionization process that occurs inside the MgZnO film.

1.9.5 ZnO-based p-i-n UV photodiodes

ZnO-based p-i-n UV photodiodes have the advantages of high breakdown voltage, fast response, low dark current etc. The increase in the depletion layer width enhances the light absorption efficiency, reduces the junction capacitance for faster response and increases the charge collection efficiency. Lin et al. reported ZnO-based p-i-n homojunction UV detectors with p-type $LiNO_3$ doped ZnO, n-type In-doped ZnO and i-ZnO deposited on sapphire substrates by vapour cooling condensation system.[183] The device exhibited better performance with detectivity of 5.53×10^{11} Jones at -1 V under 360 nm due to the better interface quality at the p-i-n homojunction. UV photodetector operating at room temperature based on n-ZnO nanorods/i-ZnO/p-GaN heterojunction was reported by Zhang et al. in 2015.[184] The device exhibited stable and reproducible performance with a responsivity of 138.9 mA/W at 0 V under 362 nm. ZnO/FeS_2/CuI based p-i-n heterojunction photodiodes with on-off ratio of 371 at 0 V was reported.[185] The high performance of the device is due to the excellent collection ability of photogenerated electron-hole pairs due to the increase in the depletion layer width of p-i-n structure. Ajith et al. reported n-ZnO/i-ZnO/p-GaN heterojunction UV photodiode with a responsivity of 138.9 mA/W at 0 V under 362 nm.[26] ZnO-based p-i-n homojunction can be used to detect UV light as well as to generate energy to self-power this UV detector.[186] Kumar et al. reported p-i-n homojunction device with peak sensitivity occurring at 330 nm.[187] The effect of thickness and reverse bias voltage on the sputter-grown ZnO-based p-i-n homojunction UV photodetector with Sb-doped p-type ZnO, undoped ZnO (i-ZnO) and Ga-doped n-type ZnO was studied by Ruchi et al.[188] They found that the responsivity reduces by 41.9% with the increase in

28

the thickness of top p layer from 50-200 nm while the responsivity increases by 108.6% with the increase in the thickness of i-ZnO layer from 20-80 nm.

1.9.6 ZnO-based schottky UV photodiodes

ZnO-based schottky photodiodes have the advantages of low dark current, fast response, simple fabrication, excellent photoresponse properties in both forward and reverse bias regions, possible zero bias operation and high UV/visible contrast ratio. Schottky photodetectors can be fabricated in vertical and planar configurations. Liang et al. reported schottky photodetectors based on n-type ZnO epitaxial films grown on sapphire substrates by MOCVD.[189] The device showed fast response with a responsivity of 1.5 A/W at 5 V. Schottky photodiode with metal alloy electrodes for schottky barrier was reported by Nagata et al.[190] They used Pt-Ru alloy electrodes. UV photodetector with PEDOT:PSS as the transparent polymer schottky contact was reported.[191] The device exhibited best performance with 100% EQE and detectivity of 3.6×10^{14} Jones at 370 nm without applied bias. Ali et al. reported fabrication, characterization and testing of the thermal stability of sol-gel deposited ZnO-based schottky UV photodetectors with EQE of 72%, responsivity of 0.2137 A/W and detectivity of 1.4567×10^{9} Jones under 365 nm.[192] The changes in the electrical and photoresponse properties of the device with different annealing temperatures is due to the combined effects of interfacial reaction and phase transition during the annealing process. Schottky photodiodes with surface treated ZnO films deposited by sputtering were reported.[193] H_2O_2 and $(NH_4)S_x$ solutions were used for surface treatment. The device Cu-ZnO-Cu exhibited responsivity of 4.45 µA/W at 1 V under 365 nm.[194] Hwang et al. used the surface plasmon resonance of Au nanoparticles to enhance the photoresponse properties of ZnO nanorod based schottky barrier photodetectors.[195] The surface plasmon resonance of Au nanoparticles helps to cross the schottky barrier near ZnO/Au interface. This increases near band edge emission and reduces defect level emissions of ZnO nanorods and enhances photoresponse properties. Hydrothermally grown ZnO nanorod based low voltage detector showed responsivity

of 0.033 A/W at 1 V.[196] The comparison of photoresponse properties of ZnO nanorods and nanoflakes fabricated in schottky diode configuration is reported by Maurya et al.[197] The adsorption of H_2O/O_2 on the surface of ZnO results in the degradation of device performance. Zheng et al. used TiO_2 insertion layer between ZnO and Au in the device to enhance the photoresponse properties by weakening the surface state effects.[198] Planar schottky photodiodes based on ZnO thin films grown by three different techniques such as hydrothermal, RF sputtering and vacuum coating techniques were reported.[199] The detectivity, sensitivity and EQE varies with the deposition method and the device with hydrothermally grown ZnO films exhibited better performance with high sensitivity and EQE under 254 nm.

1.9.7 ZnO-based phototransistors

High optical gain and low operating voltages are the advantages of phototransistors. In phototransistors the channel current is controlled by the intensity of incident light and applied gate bias. They have the ability to solve the persistent photoconductivity problem associated with ZnO by applying a negative voltage at the gate terminal. Yakuphanoglu et al. studied the photosensitivity of sol-gel deposited n-channel ZnO-based phototransistor.[200] All transparent ZnO-based phototransistor exhibited better performance with a responsivity of 2520 A/W, photoconductive gain of 8682, detectivity of 1.57×10^{11} Jones.[201] The device is illuminated from both front side and back side and back side illumination exhibited better performance. The device performance was controlled by the applied gate bias. The phototransistor composed of ZnO nanoparticle embedded in the nanopore structure surrounded by gate electrode and connected to top and bottom electrode exhibited high performance with EQE of 5.6×10^7, responsivity of 1.39×10^6 A/W, detectivity of 8.69×10^{12} Jones and response time of 90 μs.[202] The embedded ZnO nanoparticles do not suffer any grain boundary scattering and showed high mobility values and excellent photoresponse properties. Yoo et al. reported phototransistor based on In-Ga-ZnO thin film with Se capping layer.[203] Hwang et al. reported all transparent high performance solar-blind

UV heterojunction bipolar phototransistor with ITO, NiO and ZnO as emitter, base and collector respectively. The device showed high UV/Visible rejection ratio with photoconductive gain of 7.4×10^4 at 4 V under 280 nm light.[204] H_2O_2 treated ultra-thin ZnO film based UV phototransistors exhibited responsivity of 1.99 A/W and detectivity of 3.35×10^{10} Jones.[205] Kumar et al. fabricated and compared the photoresponse properties of spray coated and sputter deposited ZnO film based UV phototransistors.[206] The spray coated ZnO-based device exhibited better performance with a responsivity of 3.65×10^4 A/W at 355 nm due to the large grain size of ZnO film.

Table 1.2 provides a representative list of ZnO-based photodetectors with the important device parameters.

Active layer/morphology	Wavelength with highest responsivity	On-off ratio	Photoconductive gain	Rise time	Fall time	Responsivity (A/W)	Detectivity (Jones)	Reference
ZnO nanoparticle	375 nm (5 V)	48		204 s	486 s	3.75		[98]
ZnO thin film	369 nm (2 V)		-	-	-	3000		[207]
ZnO nanocones	387 nm (10 V)			10 s	30 s			[208]
ZnO nanowire	370 nm (5 kV/cm)		10^6		120 min	10^5		[209]
ZnO bicones	370 nm (20 V)	154.67						[210]
ZnO nanorods	325 nm (3 V)			1.2 s	1.8 s	2.856		[211]
ZnO/ZnS core-shell nanorod arrays	340 nm (0 V)			40 ms		0.056		[212]
ZnO thin film	365 nm (5 V)			9 s	21 s	28.14		[213]
ZnO nanosheets	220 nm (10 V)	2.829×10^3		260 ms	1656 ms	3.424	2.581×10^{12}	[214]
ZnO quantum dots/ carbon nanodots hybrid films	375 nm (14 V)			2.97 ns	3.16 ns	1.7×10^6	3.1×10^{17}	[215]
ZnO thin film	365 nm (5 V)	23.2		100 ns	1.5 μs	18		[97]
ZnO films	360 nm (5 V)	14		5 min	7 min			[216]
ZnO/Si	350 nm (10 V)	6310				1.26		[217]
Ga-doped ZnO	360 nm (1 V)	570.2		89 s	106 s	4.6×10^{-2}		[218]
Fe-doped ZnO nanorods	380 nm (3 V)	471.1		46 s	37 s	0.758		[219]
Sb-doped ZnO/ZnO naowire	365 nm (0.1 V)	27.5		30 ms				[220]
Single walled carbon nanotube/ZnO	370 nm (2 V)	10^3		14 s	23 s		3.2×10^{15}	[221]
ZnO/GaN	325 nm (1 V)			20 ms		0.225	4.83×10^{13}	[222]

Device	Wavelength (Voltage)			Rise time	Fall time	Responsivity	Detectivity	Ref.
Al/PFO/ZnO/ITO	370 nm (2 V)					0.040	3×10^{10}	[223]
pn junction arrays of ZnO nanofibers	360 nm (2 V)	10^2		3.9 s	4.71 s	0.001		[224]
ZnO/PEDOT:PSS	380 nm (2 V)			200 ms		0.013		[225]
H:V ZnO/PEDOT:PSS	365 nm (0 V)			23 ms	26 ms	0.0026	5.25×10^{10}	[226]
n-ZnO nanorod/i-ZnO/p-GaN	362 nm (-4 V)	73.3		1 s		0.138		[184]
n-ZnO microwire/ p-GaN	380 nm (0 V)					0.450		[227]
n-ZnO/p-NiO	325 nm (-3.5 V)	21.3		18.1 s		2.050		[228]
ZnO/PANI	365 nm (3 V)			12 s				[229]
p-Si/n-ZnO	365 nm (2 V)	1115				0.075	6.44×10^{9}	[230]
Al-doped ZnO nanosheet	325 nm (1 V)	10^5		0.7 s	2.5 s	0.031		[231]
ZnO nanowire	370 nm (5 V)	10^3		12 s				[232]
ZnO film	370 nm (5 V)					0.04		[233]
ZnO film	370 nm (5 V)	3525		0.3 s				[234]
p-CuO nanosphere /n-ZnO	254 nm (-3 V)			1.8 s	0.26 s			[235]
n-ZnO/n-Si	365 nm (-5 V)	5.332×10^{3}				8.39	7.5×10^{12}	[236]
Au/ZnO quantum dots	365 nm (-5 V)	2.289×10^{4}		73.1 ms	17.85 ms	41.17	1.57×10^{14}	[237]
Pd/ZnO nanoparticle	365 nm (-5 V)	541.34				0.20	6.5×10^{9}	[238]
Graphene/ZnO	365 nm (0.1 V)	10^3	347	0.16 s	0.19 s	101		[239]
ZnO thin film	365 nm (-2 V)	7				0.17		[240]
ZnO thin film	365 nm (3 V)	12				0.056	1.28×10^{9}	[241]
Polymer/ZnO	300 nm (-2 V)					0.18		[242]
ZnO film	370 nm (5 V)	3.2×10^{4}				0.0083		[243]

N-doped ZnO films	365 nm (5 V)	1 μs	1.5 μs	400	[244]
Ga-doped ZnO films	374 nm (20 V)	95 s	2068 s	1.68	[245]

Table 1.2. Performance parameters of reported ZnO-based UV photodetectors

1.10 Remaining challenges

UV photodetectors with high stability, high sensitivity, high signal-to-noise ratio and high speed are reported by many researchers. However, with the development in science and technology, the performance demands are exceeding the characteristics of the conventional UV photodetectors. So, it is necessary to develop a novel UV photodetector with high performance to meet practical applications. Self-powered, flexible, smart and low-cost UV photodetectors are needed for several applications in civilian, medical, military and communication fields. One challenge in the field of UV detector fabrication is realization of low operating voltages. One way to make the device self-powered is to change the device structure and morphology of the active material. Another challenge is the need for flexible photodetectors for wearable applications. Flexible UV photodetectors can be fabricated by high quality ZnO thin films formed from vapour deposition techniques. However, this will increase the cost of the device. This challenge can be overcome by using low-cost solution process techniques. But these techniques face problems with quality of film formation, annealing temperature, difficulty in controlling the composition and morphology of the materials. ZnO-based devices always face problems associated with defects present in the sample. The surface states and defects present in the ZnO film affect device performance. It can be overcome by using suitable surface passivation layers. The structural and electrical problems also affect the device performance. Selecting an appropriate surface passivation layer for ZnO nanostructures is another challenge. Morphology of ZnO nanostructures plays an important role in the device performance and synthesizing stable

and reproducible ZnO nanostructures by simple and cost effective techniques is yet another problem faced by the researchers.

1.11 Theme of the thesis

The major challenges in the field of UV detectors are to develop self-powered, flexible, smart, low-cost and intelligent photodetectors. In this thesis, we tried to address these problems by fabricating UV photodetectors using ZnO nanostructures in different architectures. Here we fabricated self-powered, low temperature processable visible-blind UV photodetectors. Formation of surface states on ZnO surface is a major problem faced by the researchers in the fabrication of high performance photodetectors. In this work we tried to address this issue by using different surface passivation techniques to passivate the defects in ZnO nanostructures and fabricated UV detectors with high performance. Effect of morphology on device performance is studied by fabricating devices based on ZnO nanoparticles, nanorods and nanoflowers.

1.12 References

1.   Gupta, S. & Kedia, J. A Review on Silicon-Based Photodetectors. *Ijirset.* **5**, 1245–1252 (2016).

2.   Konstantatos, G. Current status and technological prospect of photodetectors based on two-dimensional materials. *Nat. Commun.* **9**, 5266 (2018).

3.   Jiang, W. *et al.* A versatile photodetector assisted by photovoltaic and bolometric effects. *Light Sci. Appl.* **9**, 160 (2020).

4.   Rogalski, A. Comparison of photon and thermal detector performance. in *Handbook of Infra-red Detection Technologies* 5–81 (Elsevier, 2002).

5.   Hadfield, R. H. Single-photon detectors for optical quantum information applications. *Nat. Photonics* **3**, 696–705 (2009).

6.   Rogalski, A. Infrared thermal detectors versus photon detectors: I. Pixel performance. in *Material Science and Material Properties for Infrared Optoelectronics* (eds. Sizov, F. F. & Tetyorkin, V. V.) 14–25 (1997).

7.   Yotter, R. A. & Wilson, D. M. A review of photodetectors for sensing light-emitting reporters in biological systems. *IEEE Sens. J.* **3**, 288–303 (2003).

8.   Razeghi, M. & Rogalski, A. Semiconductor ultraviolet detectors. *J. Appl. Phys.* **79**, 7433–7473 (1996).

9.   Shakir, M. *et al.* High-performance visible light photodetectors based on inorganic CZT and InCZT single crystals. *Sci. Rep.* **9**, 12436 (2019).

10.   Pratiyush, A. S., Krishnamoorthy, S., Muralidharan, R., Rajan, S. & Nath, D. N. Advances in Ga_2O_3 solar-blind UV photodetectors. in *Gallium Oxide* 369–399 (Elsevier, 2019).

11.   Jin, Z., Gao, L., Zhou, Q. & Wang, J. High-performance flexible ultraviolet photoconductors based on solution-processed ultrathin ZnO/Au nanoparticle composite films. *Sci. Rep.* **4**, 4268 (2015).

12.   Jansen-van Vuuren, R. D., Armin, A., Pandey, A. K., Burn, P. L. & Meredith, P. Organic Photodiodes: The Future of Full Color Detection and Image Sensing. *Adv. Mater.* **28**, 4766–4802 (2016).

13.   Zhou, W. *et al.* Electrode effect on high-detectivity ultraviolet photodetectors based on perovskite oxides. *J. Appl. Phys.* **114**, 224503 (2013).

14.   Ji, C. H., Kim, K. T. & Oh, S. Y. High-detectivity perovskite-based photodetector using a Zr-doped TiO_x cathode interlayer. *RSC Adv.* **8**, 8302–8309 (2018).

15.   Feng, W. *et al.* Ultrahigh photo-responsivity and detectivity in multilayer InSe nanosheets phototransistors with broadband response. *J. Mater. Chem. C* **3**, 7022–7028 (2015).

16.   Gong, X. *et al.* High-Detectivity Polymer Photodetectors with Spectral Response from 300 nm to 1450 nm. *Science.* **325**, 1665–1667 (2009).

17.   Lu, Y.-J., Lin, C.-N. & Shan, C.-X. Optoelectronic Diamond: Growth, Properties, and Photodetection Applications. *Adv. Opt. Mater.* **6**, 1800359 (2018).

18.   Gupta, M. C., Harrison, J. T. & Islam, M. T. Photoconductive PbSe thin films for infrared

imaging. *Mater. Adv.* **2**, 3133–3160 (2021).

19.   Yadav, H. K., Sreenivas, K. & Gupta, V. Persistent photoconductivity due to trapping of induced charges in Sn/ZnO thin film based UV photodetector. *Appl. Phys. Lett.* **96**, 223507 (2010).

20.   Berger, P. R. MSM photodiodes. *IEEE Potentials* **15**, 25–29 (1996).

21.   Dushaq, G. & Rasras, M. Planar Multilayered 2D GeAs Schottky Photodiode for High-Performance Visible–Near-Infrared Photodetection. *ACS Appl. Mater. Interfaces* **13**, 21499–21506 (2021).

22.   Wang, Y. *et al.* The fabrication of Schottky photodiode by monolayer graphene direct-transfer-on-silicon. *J. Appl. Phys.* **128**, 014501 (2020).

23.   Wang, Y. *et al.* All-Oxide NiO/Ga$_2$O$_3$ p–n Junction for Self-Powered UV Photodetector. *ACS Appl. Electron. Mater.* **2**, 2032–2038 (2020).

24.   Guo, D. *et al.* Self-Powered Ultraviolet Photodetector with Superhigh Photoresponsivity (3.05 A/W) Based on the GaN/Sn:Ga$_2$O$_3$ pn Junction. *ACS Nano* **12**, 12827–12835 (2018).

25.   Pernot, C. *et al.* Solar-Blind UV Photodetectors Based on GaN/AlGaN p-i-n Photodiodes. *Jpn. J. Appl. Phys.* **39**, L387–L389 (2000).

26.   Jitty Jose, Ajith Ravindran & Keerthi K Nair. A Highly Sensitive Heterojunction Photodetector for UV Application. *Int. J. Eng. Res.* **V5**, 671–675 (2016).

27.   Sood, A. K. *et al.* Development of high gain avalanche photodiodes for UV imaging applications. in *Infrared Sensors, Devices, and Applications V* (eds. LeVan, P. D., Sood, A. K., Wije Warnasuriya, P. & D'Souza, A. I.) **9609**, 96090X (2015).

28.   Di Bartolomeo, A. *et al.* Electrical transport and persistent photoconductivity in monolayer MoS$_2$ phototransistors. *Nanotechnology* **28**, 214002 (2017).

29.   Lee, S. *et al.* Impact of transparent electrode on photoresponse of ZnO-based phototransistor. *Appl. Phys. Lett.* **103**, 251111 (2013).

30.   Chen, H., Liu, K., Hu, L., Al-Ghamdi, A. A. & Fang, X. New concept ultraviolet photodetectors. *Mater. Today* **18**, 493–502 (2015).

31.   Wilson, B. D., Moon, S. & Armstrong, F. Comprehensive review of ultraviolet radiation and the current status on sunscreens. *Jclin Aesthet Dermatol.* **5**, 18-23 (2012).

32.   D'Orazio, J., Jarrett, S., Amaro-Ortiz, A. & Scott, T. UV Radiation and the Skin. *Int. J. Mol. Sci.* **14**, 12222–12248 (2013).

33.   Surjadinata, B., Jacobo-Velázquez, D. & Cisneros-Zevallos, L. UVA, UVB and UVC Light Enhances the Biosynthesis of Phenolic Antioxidants in Fresh-Cut Carrot through a Synergistic Effect with Wounding. *Molecules* **22**, 668 (2017).

34.   Juzeniene, A. & Moan, J. Beneficial effects of UV radiation other than via vitamin D production. *Dermatoendocrinol.* **4**, 109–117 (2012).

35.   Mamahlodi, M. T. Potential benefits and harms of the use of UV radiation in transmission of tuberculosis in South African health facilities. *J. Public Health Africa* **10**, 61–67 (2019).

36.   Moozhipurath, R. K., Kraft, L. & Skiera, B. Evidence of protective role of Ultraviolet-B (UVB) radiation in reducing COVID-19 deaths. *Sci. Rep.* **10**, 17705 (2020).

37. Vanhaelewyn, L., Van Der Straeten, D., De Coninck, B. & Vandenbussche, F. Ultraviolet Radiation From a Plant Perspective: The Plant-Microorganism Context. *Front. Plant Sci.* **11**, 1–18 (2020).

38. Liu, L.-Y. *et al.* The Fabrication and Characterization of Ni/4H-SiC Schottky Diode Radiation Detectors with a Sensitive Area of up to 4 cm^2. *Sensors* **17**, 2334 (2017).

39. Chen, Y.-C. *et al.* Ga 2 O 3 photodetector arrays for solar-blind imaging. *J. Mater. Chem. C* **7**, 2557–2562 (2019).

40. Shepelev, V. A. *et al.* Measuring the optical density of wastewater by means of a diamond UV photodetector. *Russ. Eng. Res.* **37**, 273–275 (2017).

41. Zou, Y., Zhang, Y., Hu, Y. & Gu, H. Ultraviolet Detectors Based on Wide Bandgap Semiconductor Nanowire: A Review. *Sensors* **18**, 2072 (2018).

42. Monroy, E., Omn s, F. & Calle, F. Wide-bandgap semiconductor ultraviolet photodetectors. *Semicond. Sci. Technol.* **18**, R33–R51 (2003).

43. Shi, L. & Nihtianov, S. Comparative Study of Silicon-Based Ultraviolet Photodetectors. *IEEE Sens. J.* **12**, 2453–2459 (2012).

44. Zhou, C. *et al.* Ultraviolet photodetectors based on wide bandgap oxide semiconductor films. *Chinese Phys. B* **28**, 048503 (2019).

45. Liao, M., Koide, Y. & Sang, L. Nanostructured Wide-bandgap Semiconductors for Ultraviolet Detection. *Austin J. Nanomed. Nanotechnol.* **2**, 1029 (2014).

46. Sang, L., Liao, M. & Sumiya, M. A Comprehensive Review of Semiconductor Ultraviolet Photodetectors: From Thin Film to One-Dimensional Nanostructures. *Sensors* **13**, 10482–10518 (2013).

47. Li, Y., Zheng, W. & Huang, F. All-silicon photovoltaic detectors with deep ultraviolet selectivity. *PhotoniX* **1**, 15 (2020).

48. Chen, L. Si-Based ZnO Ultraviolet Photodiodes. in *Photodiodes - From Fundamentals to Applications*, 13 (InTech, 2012).

49. Liu, K., Sakurai, M. & Aono, M. ZnO-Based Ultraviolet Photodetectors. *Sensors* **10**, 8604–8634 (2010).

50. Sang, L., Liao, M. & Sumiya, M. A Comprehensive Review of Semiconductor Ultraviolet Photodetectors: From Thin Film to One-Dimensional Nanostructures. *Sensors* **13**, 10482–10518 (2013).

51. Zheng, Y. *et al.* Self-Integrated Hybrid Ultraviolet Photodetectors Based on the Vertically Aligned InGaN Nanorod Array Assembly on Graphene. *ACS Appl. Mater. Interfaces* **11**, 13589–13597 (2019).

52. Cai, Q. *et al.* Progress on AlGaN-based solar-blind ultraviolet photodetectors and focal plane arrays. *Light Sci. Appl.* **10**, 94 (2021).

53. Li, J. *et al.* 200nm deep ultraviolet photodetectors based on AlN. *Appl. Phys. Lett.* **89**, 213510 (2006).

54. Wang, Y. *et al.* Deep Ultraviolet Photodetectors Based on Carbon-Doped Two-Dimensional Hexagonal Boron Nitride. *ACS Appl. Mater. Interfaces* **12**, 27361–27367

(2020).

55. Zhang, M. *et al.* A photoelectrochemical type self-powered ultraviolet photodetector based on GaN porous films. *Mater. Lett.* **162**, 117–120 (2016).

56. Zhang, N., Song, Y., Zhou, K. & Wang, W. Enhanced performance of solar-blind photodetector of hexagonal boron nitride with bottom-contact electrodes. *AIP Adv.* **10**, 085013 (2020).

57. Aldalbahi, A. *et al.* A new approach for fabrications of SiC based photodetectors. *Sci. Rep.* **6**, 23457 (2016).

58. Zhang, Z. *et al.* Solar-blind imaging based on 2-inch polycrystalline diamond photodetector linear array. *Carbon N. Y.* **173**, 427–432 (2021).

59. Mendoza, F., Makarov, V., Weiner, B. R. & Morell, G. Solar-blind field-emission diamond ultraviolet detector. *Appl. Phys. Lett.* **107**, 201605 (2015).

60. Fu, Q.-M. *et al.* Highly sensitive ultraviolet photodetectors based on ZnO/SnO2 core-shell nanorod arrays. *Appl. Surf. Sci.* **527**, 146923 (2020).

61. Wang, L. *et al.* Efficient ultraviolet photodetectors based on TiO₂ nanotube arrays with tailored structures. *RSC Adv.* **5**, 52388–52394 (2015).

62. Wu, J. M. & Chang, W. E. Ultrahigh Responsivity and External Quantum Efficiency of an Ultraviolet-Light Photodetector Based on a Single VO₂ Microwire. *ACS Appl. Mater. Interfaces* **6**, 14286–14292 (2014).

63. Chen, X. & Wei, Z. P. Single In₂O₃ Nanowire Ultraviolet Phototransistor with High Optical On-off Ratio and High Responsivity. *Faguang Xuebao/Chinese J. Lumin.* (2021).

64. Jia, M. *et al.* High-Performance Deep Ultraviolet Photodetector Based on NiO/β-Ga₂O₃ Heterojunction. *Nanoscale Res. Lett.* **15**, 47 (2020).

65. Ghasempour Ardakani, A., Pazoki, M., Mahdavi, S. M., Bahrampour, A. R. & Taghavinia, N. Ultraviolet photodetectors based on ZnO sheets: The effect of sheet size on photoresponse properties. *Appl. Surf. Sci.* **258**, 5405–5411 (2012).

66. Cheng, J., Fu, M., Zhang, Y. & Guo, R. Ultraviolet Photodetection Properties of ZnO Microtubes. *MRS Proc.* **957**, 0957-K01-07 (2006).

67. Stadler, A. Transparent Conducting Oxides—An Up-To-Date Overview. *Materials (Basel).* **5**, 661–683 (2012).

68. Peelaers, H., Kioupakis, E. & Van de Walle, C. G. Limitations of In₂O₃ as a transparent conducting oxide. *Appl. Phys. Lett.* **115**, 082105 (2019).

69. Liu, Y., Li, Y. & Zeng, H. ZnO-Based Transparent Conductive Thin Films: Doping, Performance, and Processing. *J. Nanomater.* **2013**, 1–9 (2013).

70. Foo, K. L., Kashif, M., Hashim, U. & Liu, W.-W. Effect of different solvents on the structural and optical properties of zinc oxide thin films for optoelectronic applications. *Ceram. Int.* **40**, 753–761 (2014).

71. Xue, S. W. *et al.* Effects of post-thermal annealing on the optical constants of ZnO thin film. *J. Alloys Compd.* **448**, 21–26 (2008).

72. Xiao, Z. Y., Liu, Y. C., Mu, R., Zhao, D. X. & Zhang, J. Y. Stability of p-type conductivity

in nitrogen-doped ZnO thin film. *Appl. Phys. Lett.* **92**, 052106 (2008).

73. R. Saleh, W., M. Saeed, N., A. Twej, W. & Alwan, M. Synthesis Sol-Gel Derived Highly Transparent ZnO Thin Films for Optoelectronic Applications. *Adv. Mater. Phys. Chem.* **02**, 11–16 (2012).

74. Gudkov, S. V. *et al.* A Mini Review of Antibacterial Properties of ZnO Nanoparticles. *Front. Phys.* **9**, 1–12 (2021).

75. Al-Salman, H. S. & Abdullah, M. J. Fabrication and Characterization of Undoped and Cobalt-doped ZnO Based UV Photodetector Prepared by RF-sputtering. *J. Mater. Sci. Technol.* **29**, 1139–1145 (2013)

76. Foo, K. L., Kashif, M., Hashim, U., Usman Ali, S. M. & Willander, M. Study of ZnO thin film on silicon substrate by sol-gel spin coating method for bio-medical application. in *2012 International Conference on Biomedical Engineering (ICoBE)* 223–226 (IEEE, 2012)

77. Struk, P. *et al.* Hybrid photonics structures with grating and prism couplers based on ZnO waveguides. *Opto-Electronics Rev.* **21**, 376–381 (2013)

78. Zhou, J. *et al.* Nebulization using ZnO/Si surface acoustic wave devices with focused interdigitated transducers. *Surf. Coatings Technol.* **367**, 127–134 (2019).

79. Le, A. T., Ahmadipour, M. & Pung, S.-Y. A review on ZnO-based piezoelectric nanogenerators: Synthesis, characterization techniques, performance enhancement and applications. *J. Alloys Compd.* **844**, 156172 (2020).

80. Kang, S. C. *et al.* Channel Defect Profiling and Passivation for ZnO Thin-Film Transistors. *Nanomaterials* **10**, 1186 (2020).

81. Choi, Y.-S., Kang, J.-W., Hwang, D.-K. & Park, S.-J. Recent Advances in ZnO-Based Light-Emitting Diodes. *IEEE Trans. Electron Devices* **57**, 26–41 (2010).

82. Kaphle, A., Echeverria, E., McIlroy, D. N. & Hari, P. Enhancement in the performance of nanostructured CuO–ZnO solar cells by band alignment. *RSC Adv.* **10**, 7839–7854 (2020)

83. Bhati, V. S., Hojamberdiev, M. & Kumar, M. Enhanced sensing performance of ZnO nanostructures-based gas sensors: A review. *Energy Reports* **6**, 46–62 (2020).

84. Jiang, F., Peng, Z., Zang, Y. & Fu, X. Progress on rare-earth doped ZnO-based varistor materials. *J. Adv. Ceram.* **2**, 201–212 (2013).

85. Liu, J., Wang, Y., Ma, J., Peng, Y. & Wang, A. A review on bidirectional analogies between the photocatalysis and antibacterial properties of ZnO. *J. Alloys Compd.* **783**, 898–918 (2019).

86. Bharat, T. C. *et al.* Synthesis of Doped Zinc Oxide Nanoparticles: A Review. *Mater. Today Proc.* **11**, 767–775 (2019).

87. Morkoc, H. & Ozgur, U. General Properties of ZnO. in *Zinc Oxide* 1–76 (Wiley, 2009).

88. Espitia, P. J. P. *et al.* Zinc Oxide Nanoparticles: Synthesis, Antimicrobial Activity and Food Packaging Applications. *Food Bioprocess Technol.* **5**, 1447–1464 (2012).

89. Adegoke, K. A. *et al.* Photocatalytic Conversion of CO_2 Using ZnO Semiconductor by Hydrothermal Method. *Pakistan J. Anal. Environ. Chem.* **19**, 1–27 (2018).

90. Meyer, B. K. *et al.* Bound exciton and donor–acceptor pair recombinations in ZnO. *Phys. status solidi* **241**, 231–260 (2004).

91. K. Pathak, T. & Swart, H. C. Structural and Luminescence Properties of ZnO Nanoparticles Synthesised by Mixture of Fuel Approach in Solution Combustion Method. in *Zinc Oxide Based Nanomaterials and Devices* (IntechOpen, 2019).

92. Oba, F., Choi, M., Togo, A. & Tanaka, I. Point defects in ZnO: an approach from first principles. *Sci. Technol. Adv. Mater.* **12**, 034302 (2011).

93. Nandanapalli, K. R. & Mudusu, D. Surface Passivated Zinc Oxide (ZnO) Nanorods by Atomic Layer Deposition of Ultrathin ZnO Layers for Energy Device Applications. *ACS Appl. Nano Mater.* **1**, 4083–4091 (2018).

94. Hjiri, M., Aida, M. S., Lemine, O. M. & El Mir, L. Study of defects in Li-doped ZnO thin films. *Mater. Sci. Semicond. Process.* **89**, 149–153 (2019).

95. Djurišić, A. B., Chen, X., Leung, Y. H. & Man Ching Ng, A. ZnO nanostructures: growth, properties and applications. *J. Mater. Chem.* **22**, 6526 (2012).

96. Patra, M. K. *et al.* Synthesis of stable dispersion of ZnO quantum dots in aqueous medium showing visible emission from bluish green to yellow. *J. Lumin.* **129**, 320–324 (2009).

97. Xu, X., Xu, C. & Hu, J. High-performance deep ultraviolet photodetectors based on ZnO quantum dot assemblies. *J. Appl. Phys.* **116**, 103105 (2014).

98. Chang, S.-P. & Chen, K.-J. Zinc Oxide Nanoparticle Photodetector. *J. Nanomater.* **2012**, 1–5 (2012).

99. Qin, L., Shing, C. & Sawyer, S. Ultraviolet Photodetection Based on ZnO Colloidal Nanoparticles Made by Top-Down Wet-Chemistry Synthesis Process. in *2010 Symposium on Photonics and Optoelectronics* 1–4 (IEEE, 2010).

100. Jin, Y., Wang, J., Sun, B., Blakesley, J. C. & Greenham, N. C. Solution-Processed Ultraviolet Photodetectors Based on Colloidal ZnO Nanoparticles. *Nano Lett.* **8**, 1649–1653 (2008).

101. Yang, J., Shao, S., Li, Y., Wang, Y. & Feng, C. The Parameters of the Field Emission Model and the Fabrication of Zinc Oxide Nanorod Arrays/Graphene Film. *Front. Phys.* **8**, 1–8 (2021).

102. Zhang, Y., Ram, M. K., Stefanakos, E. K. & Goswami, D. Y. Synthesis, Characterization, and Applications of ZnO Nanowires. *J. Nanomater.* **2012**, 1–22 (2012).

103. Rao, K. M., Suneetha, M., Zo, S., Duck, K. H. & Han, S. S. One-pot synthesis of ZnO nanobelt-like structures in hyaluronan hydrogels for wound dressing applications. *Carbohydr. Polym.* **223**, 115124 (2019).

104. Wang, H. *et al.* Surfactant-Assisted in situ Chemical Etching for the General Synthesis of ZnO Nanotubes Array. *Nanoscale Res. Lett.* **5**, 1102–1106 (2010).

105. Yuvaraj, D., Rao, K. N. & Nanda, K. K. Room temperature synthesis of ZnO nanoneedles by activated reactive evaporation. *J. Phys. D. Appl. Phys.* **42**, 035403 (2009).

106. Peng, Y. & Bao, L. Controlled-synthesis of ZnO nanorings. *Front. Chem. China* **3**, 458–463 (2008).

107. Wang, L., Chen, K. & Dong, L. Synthesis of Exotic Zigzag ZnO Nanoribbons and Their Optical, Electrical Properties. *J. Phys. Chem. C* **114**, 17358–17361 (2010).

108. Gao, P. X. & Wang, Z. L. High-Yield Synthesis of Single-Crystal Nanosprings of ZnO. *Small* **1**, 945–949 (2005).

109. Liu, J., Huang, X., Li, Y., Zhong, Q. & Ren, L. Preparation and photoluminescence of ZnO complex structures with controlled morphology. *Mater. Lett.* **60**, 1354–1359 (2006).

110. Nasiri, N., Jin, D. & Tricoli, A. Nanoarchitechtonics of Visible-Blind Ultraviolet Photodetector Materials: Critical Features and Nano-Microfabrication. *Adv. Opt. Mater.* **7**, 1800580 (2019).

111. Sahu, K. *et al.* Facile wet chemical synthesis of ZnO nanosheets: Effects of counter ions on the morphological, structural, optical and photocatalytic properties. *Ceram. Int.* **44**, 23094–23101 (2018).

112. Chen, Y., Wang, L., Wang, W. & Cao, M. Synthesis of Se-doped ZnO nanoplates with enhanced photoelectrochemical and photocatalytic properties. *Mater. Chem. Phys.* **199**, 416–423 (2017).

113. Kaneti, Y. V., Yue, J., Jiang, X. & Yu, A. Controllable Synthesis of ZnO Nanoflakes with Exposed (10$\bar{1}$0) for Enhanced Gas Sensing Performance. *J. Phys. Chem. C* **117**, 13153–13162 (2013).

114. Altintas Yildirim, O., Liu, Y. & Petford-Long, A. K. Synthesis of uniformly distributed single- and double-sided zinc oxide (ZnO) nanocombs. *J. Cryst. Growth* **430**, 34–40 (2015)

115. Chiu, W. S. *et al.* Synthesis of two-dimensional ZnO nanopellets by pyrolysis of zinc oleate. *Chem. Eng. J.* **142**, 337–343 (2008).

116. Kumar, B., Shin, K.-S., Yi, M.-S., Lee, S. Y. & Kim, S.-W. Synthesis of Functional ZnO Nanowall Networks Using Simple Solution Etching. *J. Nanosci. Nanotechnol.* **14**, 5207–5211 (2014).

117. Navaneethan, M., Archana, J., Arivanandhan, M. & Hayakawa, Y. Chemical synthesis of ZnO hexagonal thin nanodisks and dye-sensitized solar cell performance. *Phys. status solidi - Rapid Res. Lett.* **6**, 120–122 (2012).

118. Young, S.-J. *et al.* ZnO-Based Ultraviolet Photodetectors With Novel Nanosheet Structures. *IEEE Trans. Nanotechnol.* **13**, 238–244 (2014).

119. Deka Boruah, B. & Misra, A. Energy-Efficient Hydrogenated Zinc Oxide Nanoflakes for High-Performance Self-Powered Ultraviolet Photodetector. *ACS Appl. Mater. Interfaces* **8**, 18182–18188 (2016).

120. Li, Q., Chen, H. & Chu, S. Mg-alloyed ZnO nanocombs for self-gating photodetectors. *Opt. Express* **25**, 5091 (2017).

121. Shingange, K. *et al.* 0D to 3D ZnO nanostructures and their luminescence, magnetic and sensing properties: Influence of pH and annealing. *Mater. Res. Bull.* **85**, 52–63 (2017).

122. Chen, Z., Shan, Z., Cao, M. S., Lu, L. & Mao, S. X. Zinc oxide nanotetrapods. *Nanotechnology* **15**, 365–369 (2004).

123. Attanayake, S., Okuya, M. & Murakami, K. Synthesis and characterization of Al-doped

ZnO terrace-truncated nanocone structure by the advanced spray pyrolysis deposition technique. *Jpn. J. Appl. Phys.* **58**, 080904 (2019).

124. Chen, J. *et al.* Synthesis of reduced graphene oxide intercalated ZnO quantum dots nanoballs for selective biosensing detection. *Appl. Surf. Sci.* **376**, 133–137 (2016).

125. Li, X. *et al.* Direct Observation of the Layer-by-Layer Growth of ZnO Nanopillar by In situ High Resolution Transmission Electron Microscopy. *Sci. Rep.* **7**, 40911 (2017).

126. Ponnada, S. *et al.* A facile, cost-effective, rapid, single-step synthesis of Ag–Cu decorated ZnO nanoflower-like composites (NFLCs) for electrochemical sensing of dopamine. *Mater. Adv.* **2**, 5986–5996 (2021).

127. Kołodziejczak-Radzimska, A. & Jesionowski, T. Zinc Oxide—From Synthesis to Application: A Review. *Materials (Basel).* **7**, 2833–2881 (2014).

128. Naveed Ul Haq, A. *et al.* Synthesis Approaches of Zinc Oxide Nanoparticles: The Dilemma of Ecotoxicity. *J. Nanomater.* **2017**, 1–14 (2017).

129. Zhu, Y. & Zhou, Y. Preparation of pure ZnO nanoparticles by a simple solid-state reaction method. *Appl. Phys. A* **92**, 275–278 (2008).

130. Poornajar, M., Marashi, P., Haghshenas Fatmehsari, D. & Kolahdouz Esfahani, M. Synthesis of ZnO nanorods via chemical bath deposition method: The effects of physicochemical factors. *Ceram. Int.* **42**, 173–184 (2016).

131. Maryanti, E., Damayanti, D., Gustian, I. & Yudha S, S. Synthesis of ZnO nanoparticles by hydrothermal method in aqueous rinds extracts of Sapindus rarak DC. *Mater. Lett.* **118**, 96–98 (2014).

132. Akcan, D., Gungor, A. & Arda, L. Structural and optical properties of Na-doped ZnO films. *J. Mol. Struct.* **1161**, 299–305 (2018).

133. Narayanan, N. & Deepak, N. K. B-N Co Doped p Type ZnO Thin Films for Optoelectronic Applications. *Mater. Res.* **21**, 1–8 (2017).

134. Hanna, B., Manuraj, M., Surendran, K. P. & Unni, K. N. N. Opto-electronic properties of solution-processed zinc oxide thin films: role of solvents and doping. *J. Mater. Sci. Mater. Electron.* **31**, 13570–13577 (2020).

135. Park, S.-H., Park, J.-W., Yang, S.-M., Kim, K.-H. & Hwang, N.-M. Effect of Electric Bias on the Deposition Behavior of ZnO Nanostructures in the Chemical Vapour Deposition Process. *J. Phys. Chem. C* **119**, 25047–25052 (2015).

136. Girtan, M., Kompitas, M., Mallet, R. & Fasaki, I. On physical properties of undoped and Al and In doped zinc oxide films deposited on PET substrates by reactive pulsed laser deposition. *Eur. Phys. J. Appl. Phys.* **51**, 33212 (2010).

137. Suja, M., Bashar, S. B., Morshed, M. M. & Liu, J. Realization of Cu-Doped p-Type ZnO Thin Films by Molecular Beam Epitaxy. *ACS Appl. Mater. Interfaces* **7**, 8894–8899 (2015).

138. Li, X. *et al.* p-type ZnO thin films grown by MOCVD. in *Conference Record of the Thirty-first IEEE Photovoltaic Specialists Conference, 2005.* 152–154 (IEEE, 2005).

139. Jayaraj, M. K., Antony, A. & Ramachandran, M. Transparent conducting zinc oxide thin film prepared by off-axis rf magnetron sputtering. *Bull. Mater. Sci.* **25**, 227–230 (2002).

140. Mollow, E. Proceedings of the Photoconductivity Conference. *Wiley, New York, NY, USA* (1954).

141. Basak, D., Amin, G., Mallik, B., Paul, G. K. & Sen, S. K. Photoconductive UV detectors on sol–gel-synthesized ZnO films. *J. Cryst. Growth* **256**, 73–77 (2003).

142. Jin, Y., Wang, J., Sun, B., Blakesley, J. C. & Greenham, N. C. Solution-Processed Ultraviolet Photodetectors Based on Colloidal ZnO Nanoparticles. *Nano Lett.* **8**, 1649–1653 (2008).

143. Qin, L., Shing, C. & Sawyer, S. Low-Pass and Bandpass Alternative Ultraviolet Photoconductor Based on Zinc Oxide Nanoparticles on Intrinsic Gallium Nitride-Based Substrate. *IEEE Photonics Technol. Lett.* **23**, 414–416 (2011).

144. Bai, Z. *et al.* ZnO nanowire array ultraviolet photodetectors with self-powered properties. *Curr. Appl. Phys.* **13**, 165–169 (2013).

145. Jin, Z. & Wang, J. Flexible high-performance ultraviolet photoconductor with zinc oxide nanorods and 8-hydroxyquinoline. *J. Mater. Chem. C* **2**, 1966 (2014).

146. Fan, H. *et al.* UV photodetectors based on 3D periodic Au-decorated nanocone ZnO films. *Nanotechnology* **27**, 365303 (2016).

147. Yang, X. *et al.* Enhanced Response Speed of ZnO Nanowire Photodetector by Coating with Photoresist. *J. Nanomater.* **2016**, 1–6 (2016).

148. Mohammed Nahhas, A. High Responsivity Ultraviolet Photoconductors Based on Epitaxial ZnO Thin Films. *Am. J. Nano Res. Appl.* **7**, 6 (2019).

149. Ajmal, H. M. S. *et al.* High-Performance Flexible Ultraviolet Photodetectors with Ni/Cu-Codoped ZnO Nanorods Grown on PET Substrates. *Nanomaterials* **9**, 1067 (2019).

150. Jandow, N. N., Abu, H., Yam, F. K. & Ibrahim, K. ZnO Metal-Semiconductor-Metal UV Photodetectors on PPC Plastic with Various Metal Contacts. in *Photodetectors* (InTech, 2012).

151. Shi, L. *et al.* Status and Outlook of Metal–Inorganic Semiconductor–Metal Photodetectors. *Laser Photon. Rev.* **15**, 2000401 (2021).

152. Xu, Z. *et al.* Photoconductive UV Detectors Based on ZnO Films Prepared by Sol-Gel Method. *J. Sol-Gel Sci. Technol.* **36**, 223–226 (2005).

153. Liu, K. W. *et al.* Ultraviolet photoconductive detector with high visible rejection and fast photoresponse based on ZnO thin film. *Solid. State. Electron.* **51**, 757–761 (2007).

154. Young, S. J., Ji, L. W., Chang, S. J. & Du, X. L. ZnO Metal-Semiconductor-Metal Ultraviolet Photodiodes with Au Contacts. *J. Electrochem. Soc.* **154**, H26 (2007).

155. N. Jandow, N., Kamarul Azizi Ibrahim, Haslan Abu Hassan & M. Thahab, S. The electrical properties of ZnO MSM Photodetector with Pt Contact Electrodes on PPC Plastic. *J. Electron Devices* **7**, 225–229 (2010).

156. Shinde, S. S. & Rajpure, K. Y. Fast response ultraviolet Ga-doped ZnO-based photoconductive detector. *Mater. Res. Bull.* **46**, 1734–1737 (2011).

157. Shinde, S. S., Bhosale, C. H. & Rajpure, K. Y. N-doped ZnO-based fast response ultraviolet photoconductive detector. *Solid. State. Electron.* **68**, 22–26 (2012).

158. Singh, S. & Park, S.-H. Fabrication and characterization of Al:ZnO-based MSM ultraviolet photodetectors. *Superlattices Microstruct.* **86**, 412–417 (2015).

159. Young, S.-J. & Liu, Y.-H. Ultraviolet Photodetectors With 2-D Indium-Doped ZnO Nanostructures. *IEEE Trans. Electron Devices* **63**, 1–5 (2016).

160. Singh, S. *et al.* A study of hydrothermally grown ZnO nanorod-based metal-semiconductor-metal UV detectors on glass substrates. *Nanomater. Nanotechnol.* **7**, 184798041770214 (2017).

161. Al-Khalli, N. & Debbar, N. Performance enhancement of ZnO-based MSM photodiodes by optimizing structure parameters. *Int. J. Numer. Model. Electron. Networks, Devices Fields* **32**, e2519 (2019).

162. Zarezadeh, E. & Ghorbani, A. Bipolar photoresponse ultraviolet photodetectors based on ZnO nanowires. *Mater. Res. Express* **7**, 056203 (2020).

163. Jezeh, Z. A., Efafi, B. & Ghafary, B. The effect of electrode shape on Schottky barrier and electric field distribution of flexible ZnO photodiode. *Sci. Rep.* **11**, 15604 (2021).

164. Liu, J. L., Xiu, F. X., Mandalapu, L. J. & Yang, Z. P-type ZnO by Sb doping for PN-junction photodetectors. in *Zinc Oxide Materials and Devices* (eds. Hosseini Teherani, F. & Litton, C. W.) **6122**, 61220H (2006).

165. Li, L. *et al.* ZnO p-n Junction Photodetectors. in *2007 Conference on Lasers and Electro-Optics (CLEO)* 1–2 (IEEE, 2007).

166. Leung, Y. H. *et al.* ZnO nanowires array p-n homojunction and its application as a visible-blind ultraviolet photodetector. *Appl. Phys. Lett.* **96**, 053102 (2010).

167. Wang, G. *et al.* ZnO homojunction photodiodes based on Sb-doped p-type nanowire array and n-type film for ultraviolet detection. *Appl. Phys. Lett.* **98**, 041107 (2011).

168. Park, N., Sun, K., Sun, Z., Jing, Y. & Wang, D. High efficiency NiO/ZnO heterojunction UV photodiode by sol–gel processing. *J. Mater. Chem. C* **1**, 7333 (2013).

169. Hasan, M. R. *et al.* Self-powered p-NiO/n-ZnO heterojunction ultraviolet photodetectors fabricated on plastic substrates. *APL Mater.* **3**, 106101 (2015).

170. Yuan, Z., Fu, M. & Ren, Y. Optoelectronic Properties of ZnO Nanoparticle/Pentacene Heterojunction Photodiode. *J. Electron. Mater.* **43**, 3270–3275 (2014).

171. Srivastava, A. & Chakrabarti, P. Fabrication and electrical characterization of a polycarbazole/ZnO-based organic–inorganic hybrid heterojunction diode. *Superlattices Microstruct.* **88**, 723–730 (2015).

172. Li, X. *et al.* A self-powered nano-photodetector based on PFH/ZnO nanorods organic/inorganic heterojunction. *Results Phys.* **8**, 468–472 (2018).

173. Hwang, J. D. & Fan, C. W. High-performance organic/inorganic hybrid ultraviolet p-NiO/PVK/n-ZnO heterojunction photodiodes with a poly(N -vinylcarbazole) insertion layer. *J. Mater. Chem. C* **7**, 3529–3534 (2019).

174. Chatzigiannakis, G. *et al.* Laser-Microstructured ZnO/p-Si Photodetector with Enhanced and Broadband Responsivity across the Ultraviolet–Visible–Near-Infrared Range. *ACS Appl. Electron. Mater.* **2**, 2819–2828 (2020).

175. Zhang, X. *et al.* Enhanced optoelectronic performance of 3C–SiC/ZnO heterostructure photodetector based on Piezo-phototronic effect. *Nano Energy* **77**, 105119 (2020).

176. Srivastava, A. & Tripathi, S. Responsivity Spectrum Tailoring of Pentacene:ZnO Multi-Nano Film-Based Bulk Heterojunction Photodetector. *IEEE Trans. Nanotechnol.* **20**, 143–150 (2021).

177. Yu, J. *et al.* ZnO-based ultraviolet avalanche photodetectors. *J. Phys. D. Appl. Phys.* **46**, 305105 (2013).

178. Zhao, B. *et al.* Solar-Blind Avalanche Photodetector Based On Single ZnO–Ga_2O_3 Core–Shell Microwire. *Nano Lett.* **15**, 3988–3993 (2015).

179. Chen, H. *et al.* Avalanche solar blind photodetectors with high responsivity based on MgO/MgZnO heterostructures. *Opt. Mater. Express* **8**, 785 (2018).

180. Chen, H. *et al.* Avalanche solar blind photodetectors based on single crystalline $Mg_{0.47}$ $Zn_{0.53}O$ thin film on Ga:ZnO substrate. *J. Phys. D. Appl. Phys.* **51**, 175104 (2018).

181. Li, G., Zhao, X., Jia, X., Li, S. & He, Y. Characterization of Impact Ionization Coefficient of ZnO-based on a p-Si/i-ZnO/n-AZO Avalanche Photodiode. *Micromachines* **11**, 740 (2020).

182. Zhao, X., Jiang, D., Zhao, M. & Duan, Y. Avalanche Effect and High External Quantum Efficiency in MgZnO/Au/ZnO Sandwich Structure Photodetector. *Adv. Opt. Mater.* **9**, 2002023 (2021).

183. Lin, T.-S. & Lee, C.-T. Performance investigation of p-i-n ZnO-based thin film homojunction ultraviolet photodetectors. *Appl. Phys. Lett.* **101**, 221118 (2012).

184. Zhang, L. *et al.* Optoelectronic characteristics of UV photodetector based on GaN/ZnO nanorods p-i-n heterostructures. *Electron. Mater. Lett.* **11**, 682–686 (2015).

185. Yang, Z. *et al.* Developing Seedless Growth of ZnO Micro/Nanowire Arrays towards ZnO/FeS2/CuI P-I-N Photodiode Application. *Sci. Rep.* **5**, 11377 (2015).

186. Singh, K. J., Singh, C. A., Singh, T. J., Chettri, D. & Sarkar, S. K. ZnO-based homojunction p-i-n solar cell to self-power UV detector. in *2017 International Conference on Inventive Communication and Computational Technologies (ICICCT)* 304–307 (IEEE, 2017).

187. Kumar, R. R., Punetha, D. & Pandey, S. K. Performance Optimization and Analysis of ZnO-based Green Light Emitting Diode. in *Springer Proceedings in Physics* **215**, 1127–1135 (IEEE, 2019).

188. Singh, R., Bhardwaj, R., Siddharth, G., Kumar, P. & Mukherjee, S. Analytical Study of Sputter-Grown ZnO-Based p-i-n Homojunction UV Photodetector. *IEEE Sens. J.* **21**, 7515–7521 (2021).

189. Liang, S. *et al.* ZnO Schottky ultraviolet photodetectors. **225**, 110–113 (2001).

190. Nagata, T. *et al.* Schottky metal library for ZnO-based UV photodiode fabricated by the combinatorial ion beam-assisted deposition. *Appl. Surf. Sci.* **252**, 2503–2506 (2006).

191. Nakano, M. *et al.* Transparent polymer Schottky contact for a high performance visible-blind ultraviolet photodiode based on ZnO. *Appl. Phys. Lett.* **93**, 123309 (2008).

192. Ali, G. M. & Chakrabarti, P. Performance of ZnO-Based Ultraviolet Photodetectors Under Varying Thermal Treatment. *IEEE Photonics J.* **2**, 784–793 (2010).

193. Chang, R.-H. *et al.* Surface Modification on the Sputtering-Deposited ZnO Layer for ZnO-Based Schottky Diode. *J. Nanomater.* **2013**, 1–9 (2013).

194. Bedia, A., Bedia, F. Z., Benyoucef, B. & Hamzaoui, S. Electrical Characteristics of Ultraviolet Photodetector based on ZnO Nanostructures. *Phys. Procedia* **55**, 53–60 (2014).

195. Hwang, J. D., Wang, F. H., Kung, C. Y. & Chan, M. C. Using the Surface Plasmon Resonance of Au Nanoparticles to Enhance Ultraviolet Response of ZnO Nanorods-Based Schottky-Barrier Photodetectors. *IEEE Trans. Nanotechnol.* **14**, 318–321 (2015).

196. Singh, S., Jit, S. & Park, S.-H. Characterization of Ag/ZnO Nanorod Schottky Diode-Based Low-Voltage Ultraviolet Photodetector. *Nano* **12**, 1750063 (2017).

197. Maurya, M. R., Toutam, V. & Haranath, D. Comparative Study of Photoresponse from Vertically Grown ZnO Nanorod and Nanoflake Films. *ACS Omega* **2**, 5538–5544 (2017).

198. Zheng, X., Sun, Y., Qin, H., Ji, Z. & Chi, H. Interface engineering on ZnO/Au based Schottky junction for enhanced photoresponse of UV detector with TiO_2 inserting layer. *J. Alloys Compd.* **816**, 152537 (2020).

199. Ali, G. M. Performance analysis of planar Schottky photodiode based on nanostructured ZnO thin film grown by three different techniques. *J. Alloys Compd.* **831**, 154859 (2020).

200. Yakuphanoglu, F. & Mansouri, S. Photosensitivity n-channel ZnO phototransistor for optoelectronic applications: Modeling of ZnO TFT. *Microelectron. Reliab.* **51**, 2200–2204 (2011).

201. Liu, H.-Y. & Huang, R.-C. All-Transparent Zinc Oxide-Based Phototransistor by Mist Atmospheric Pressure Chemical Vapor Deposition. *IEEE Electron Device Lett.* **40**, 243–246 (2019).

202. Nguyen, L.-N., Chang, W.-H., Chen, C.-D. & Lan, Y.-W. Superior phototransistors based on a single ZnO nanoparticle with high mobility and ultrafast response time. *Nanoscale Horizons* **5**, 82–88 (2020).

203. Yoo, H. *et al.* High Photosensitive Indium–Gallium–Zinc Oxide Thin-Film Phototransistor with a Selenium Capping Layer for Visible-Light Detection. *ACS Appl. Mater. Interfaces* **12**, 10673–10680 (2020).

204. Hwang, J. D., Hwang, Y. E. & Chen, Y. A. All transparent high-performance solar-blind n-ITO/p-NiO/n-ZnO ultraviolet heterojunction bipolar phototransistor. *Appl. Phys. Lett.* **117**, 091104 (2020).

205. Sannakashappanavar, B. S., Yadav, A. B., Byrareddy, C. R. & Narasimha Murty, N. V. L. Synthesis of ZnO Ultra-Thin Film-Based Bottom-Gate Phototransistors for UV Detection. *J. Electron. Mater.* **49**, 5272–5280 (2020).

206. Kumar, D. *et al.* UV Phototransistors-Based Upon Spray Coated and Sputter Deposited ZnO TFTs. *IEEE Sens. J.* **20**, 7532–7539 (2020).

207. Acosta-Osorno, M. *et al.* Characterization of ZnO thin films obtained by ultrasonic spray pyrolysis for application in UV photoconductive detectors. *Mater. Res. Express* **6**, 116450

(2019).

208. Cheng, C. *et al.* Facile synthesis, optical and photoconductive properties of novel ZnO nanocones. *Mater. Res. Bull.* **43**, 3506–3513 (2008).

209. Mallampati, B., Nair, S. V., Ruda, H. E. & Philipose, U. Role of surface in high photoconductive gain measured in ZnO nanowire-based photodetector. *J. Nanoparticle Res.* **17**, 176 (2015).

210. Rajkumar, C. & Srivastava, R. K. UV–visible photoresponse properties of self-seeded and polymer mediated ZnO flower-like and biconical nanostructures. *Results Phys.* **15**, 102647 (2019).

211. Shabannia, R. & Hassan, H. A. Characteristics of photoconductive UV photodetector based on ZnO nanorods grown on polyethylene naphthalate substrate by chemical bath deposition method. *Electron. Mater. Lett.* **10**, 837–843 (2014).

212. Lin, H. *et al.* High-Performance Self-powered Photodetectors Based on ZnO/ZnS Core-Shell Nanorod Arrays. *Nanoscale Res. Lett.* **11**, 420 (2016).

213. Shaikh, S. K., Inamdar, S. I., Ganbavle, V. V. & Rajpure, K. Y. Chemical bath deposited ZnO thin film based UV photoconductive detector. *J. Alloys Compd.* **664**, 242–249 (2016).

214. Amini, E. *et al.* Solution-Processed Photoconductive UV Detectors Based on ZnO Nanosheets. *IEEE Photonics Technol. Lett.* **24**, 1995–1997 (2012).

215. Guo, D.-Y., Shan, C.-X., Qu, S.-N. & Shen, D.-Z. Highly Sensitive Ultraviolet Photodetectors Fabricated from ZnO Quantum Dots/Carbon Nanodots Hybrid Films. *Sci. Rep.* **4**, 7469 (2015).

216. Zheng, X. G. *et al.* Photoconductive ultraviolet detectors based on ZnO films. *Appl. Surf. Sci.* **253**, 2264–2267 (2006).

217. Yen, T., Yun, J., Kim, S. J., Cartwright, A. & Anderson, W. A. Photocurrent Enhancement in Nanocrystalline-ZnO/Si Heterojunction Metal-Semiconductor-Metal Photodetectors. *Electrochem. Solid-State Lett.* **14**, H415 (2011).

218. Young, S.-J. *et al.* Flexible Ultraviolet Photodetectors Based on One-Dimensional Gallium-Doped Zinc Oxide Nanostructures. *ACS Appl. Electron. Mater.* **2**, 3522–3529 (2020).

219. Chu, Y.-L., Young, S.-J., Ji, L.-W., Tang, I.-T. & Chu, T.-T. Fabrication of Ultraviolet Photodetectors Based on Fe-Doped ZnO Nanorod Structures. *Sensors* **20**, 3861 (2020).

220. Wang, Y. *et al.* A Self-Powered Fast-Response Ultraviolet Detector of p–n Homojunction Assembled from Two ZnO-Based Nanowires. *Nano-Micro Lett.* **9**, 11 (2017).

221. Li, G. *et al.* Visible-Blind UV Photodetector Based on Single-Walled Carbon Nanotube Thin Film/ZnO Vertical Heterostructures. *ACS Appl. Mater. Interfaces* **9**, 37094–37104 (2017).

222. Mishra, M. *et al.* ZnO/GaN heterojunction based self-powered photodetectors: Influence of interfacial states on UV sensing. *Appl. Surf. Sci.* **478**, 1081–1089 (2019).

223. Guo, X. *et al.* Solution processable organic/inorganic hybrid ultraviolet photovoltaic detector. *AIP Adv.* **6**, 055318 (2016).

224. Ning, Y., Zhang, Z., Teng, F. & Fang, X. Novel Transparent and Self-Powered UV Photodetector Based on Crossed ZnO Nanofiber Array Homojunction. *Small* **14**, 1703754 (2018).

225. Hernandez-Como, N. *et al.* Ultraviolet photodetectors based on low temperature processed ZnO/PEDOT:PSS Schottky barrier diodes. *Mater. Sci. Semicond. Process.* **37**, 14–18 (2015).

226. Deka Boruah, B. & Misra, A. Energy-Efficient Hydrogenated Zinc Oxide Nanoflakes for High-Performance Self-Powered Ultraviolet Photodetector. *ACS Appl. Mater. Interfaces* **8**, 18182–18188 (2016).

227. Ding, M., Zhao, D., Yao, B., Li, Z. & Xu, X. Ultraviolet photodetector based on heterojunction of n-ZnO microwire/p-GaN film. *RSC Adv.* **5**, 908–912 (2015).

228. Ko, Y. H., Nagaraju, G. & Yu, J. S. Wire-shaped ultraviolet photodetectors based on a nanostructured NiO/ZnO coaxial p–n heterojunction via thermal oxidation and hydrothermal growth processes. *Nanoscale* **7**, 2735–2742 (2015).

229. Wang, H. *et al.* Photoelectric characteristics of the p–n junction between ZnO nanorods and polyaniline nanowires and their application as a UV photodetector. *Mater. Lett.* **162**, 83–86 (2016).

230. Hazra, P., Singh, S. K. & Jit, S. Ultraviolet Photodetection Properties of ZnO/Si Heterojunction Diodes Fabricated by ALD Technique Without Using a Buffer Layer. *JSTSJournal Semicond. Technol. Sci.* **14**, 117–123 (2014).

231. Young, S.-J. & Liu, Y.-H. High Response of Ultraviolet Photodetector Based on Al-Doped ZnO Nanosheet Structures. *IEEE J. Sel. Top. Quantum Electron.* **23**, 1–5 (2017).

232. Nunez, C. G., Taube, W., Liu, F. & Dahiya, R. ZnO nanowires based flexible UV photodetectors for wearable dosimetry. in *2017 IEEE SENSORS* **2017**-**Decem**, 1–3 (IEEE, 2017).

233. Liu, R. *et al.* High-performance ultraviolet photodetectors based on ZnO/Au/ZnO sandwich structure. *J. Phys. D. Appl. Phys.* **48**, 275104 (2015).

234. Tran, V. T., Wei, Y., Yang, H., Zhan, Z. & Du, H. All-inkjet-printed flexible ZnO micro photodetector for a wearable UV monitoring device. *Nanotechnology* **28**, 1–10 (2017).

235. Ji, Y. *et al.* Ultraviolet photodetectors using hollow p-CuO nanospheres/n-ZnO nanorods with a pn junction structure. *Sensors Actuators A Phys.* **304**, 111876 (2020).

236. Yadav, A. B., Pandey, A., Somvanshi, D. & Jit, S. Sol-Gel-Based Highly Sensitive Pd/n-ZnO Thin Film/n-Si Schottky Ultraviolet Photodiodes. *IEEE Trans. Electron Devices* **62**, 1879–1884 (2015).

237. Kumar, Y. *et al.* Visible-Blind Au/ZnO Quantum Dots-Based Highly Sensitive and Spectrum Selective Schottky Photodiode. *IEEE Trans. Electron Devices* **64**, 2874–2880 (2017).

238. Somvanshi, D. & Jit, S. Pd/ZnO Nanoparticles Based Schottky Ultraviolet Photodiodes Grown on Sn-Coated n-Si Substrates by Thermal Evaporation Method. *IEEE J. Sel. Top. Quantum Electron.* **20**, 120–125 (2014).

239. Lee, Y., Kim, D. Y. & Lee, S. Low-Power Graphene/ZnO Schottky UV Photodiodes with

Enhanced Lateral Schottky Barrier Homogeneity. *Nanomaterials* **9**, 799 (2019).

240. Ali, G. M. & Chakrabarti, P. Fabrication and characterization of thin film ZnO Schottky contacts based UV photodetectors: A comparative study. *J. Vac. Sci. Technol. B, Nanotechnol. Microelectron. Mater. Process. Meas. Phenom.* **30**, 031206 (2012).

241. Ali, G. M. & Chakrabarti, P. ZnO-based interdigitated MSM and MISIM ultraviolet photodetectors. *J. Phys. D. Appl. Phys.* **43**, 415103 (2010).

242. Lin, Y.-Y. *et al.* Near-ultraviolet photodetector based on hybrid polymer/zinc oxide nanorods by low-temperature solution processes. *Appl. Phys. Lett.* **92**, 233301 (2008).

243. Young, S. J. *et al.* ZnO-based MIS photodetectors. *Sensors Actuators A Phys.* **141**, 225–229 (2008).

244. Liu, Y. *et al.* Ultraviolet detectors based on epitaxial ZnO films grown by MOCVD. *J. Electron. Mater.* **29**, 69–74 (2000).

245. Mandalapu, L. J., Xiu, F. X., Yang, Z. & Liu, J. L. Ultraviolet photoconductive detectors based on Ga-doped ZnO films grown by molecular-beam epitaxy. *Solid. State. Electron.* **51**, 1014–1017 (2007).

Low Temperature-Processed ZnO Thin Films for Organic-Inorganic Hybrid Visible-Blind Ultraviolet Photodetectors
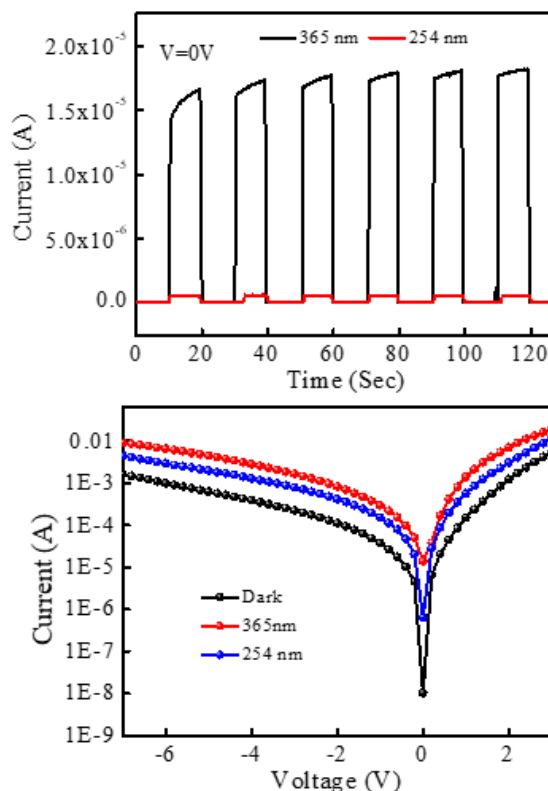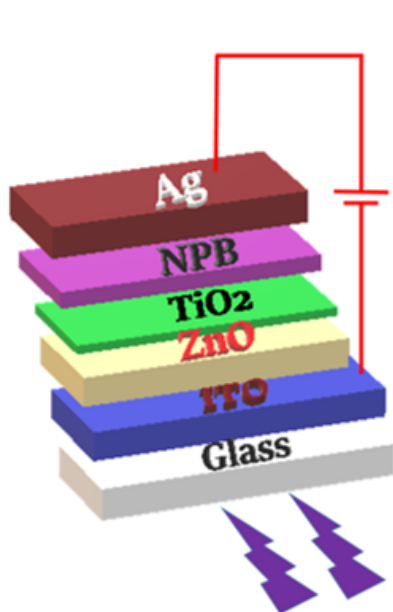
2.1 Abstract

Zinc oxide (ZnO) based UV-detectors have impressive performance but many of them are not visible-blind and the fabrication techniques mostly involve a high temperature annealing step. Here we fabricated a self-powered p-n junction photodiode based on annealing-free ZnO thin films prepared from ZnO nanoparticles and N,N′-Di(1-naphthyl)-N,N′-diphenyl-(1,1′-biphenyl)-4,4′-diamine (NPB). NPB was chosen due to its transparent nature in the visible and the relatively high hole mobility. The ZnO nanoparticles and thin films were characterized by UV-Visible absorption spectroscopy, atomic force microscopy (AFM), scanning electron microscope (SEM), dynamic light scattering (DLS) particle size analysis, Fourier transform

infrared (FTIR) spectroscopy, photoluminescence spectroscopy, XRD and profilometry. At zero bias, the device exhibited a responsivity of 0.017 A/W, external quantum efficiency (EQE) of 5.68%, an on-off ratio more than 10^3 and linear dynamic range (LDR) of 63 dB. A high built-in potential at ZnO/NPB interface could be the reason for this performance at zero bias. The rise and fall times were 156 ms and 319 ms respectively. The device performance was optimized by varying the thickness of NPB layer. The device with 30 nm thick NPB film exhibited better performance. Further, different organic materials such as copper(II) phthalocyanine (CuPC), 4,4',4"-Tris[2-naphthyl(phenyl)amino]triphenylamine (2-TNATA), rubrene and 1,1-Bis[(di-4-tolylamino)phenyl]cyclohexane (TAPC) were used for device fabrication. The properties of the organic layer influence the spectral response of the devices. The device with NPB as an organic layer exhibited better performance. The results suggest that a self-powered visible-blind UV photodetector with acceptable performance can be fabricated with annealing-free ZnO film which may lead to flexible detectors, due to the low temperature processes involved.

2.2 Introduction

Ultraviolet (UV) detectors are having great importance on the survival and development of mankind since excessive exposure to UV radiation causes skin cancer, damages the immune system and fastens the ageing process.[1,2] Zinc oxide (ZnO) based UV detectors are now getting greater attention over silicon, photomultiplier tube (PMT) based UV photodetectors and other wide band gap semiconductors due to its attractive properties such as strong radiation tolerance, high breakdown voltage, low toxicity, high transparency, low-cost, high electron mobility, large exciton binding energy (60 meV), high refractive index and versatile synthetic methods.[3,4] UV photodetectors can be fabricated in different configurations like p-n junction photodiode,[5] photoconductor,[6] avalanche photodiode,[7] phototransistor,[8] metal semiconductor metal (MSM) photodiode,[9] Schottky photodiode,[10] p-i-n photodiode[11] etc.

For desirable photoresponse properties, an external power supply is required to prevent the recombination of photogenerated electron-hole pairs in UV photodetectors. This limits their applications in large scale arrays and miniaturization of photodetectors.[12] So, self-powered UV detectors are now receiving greater attention due to their ability to operate continuously without any applied bias. It can be achieved by the UV detectors operating in the "photovoltaic" mode. Schottky junction and p-n junction photodetectors can operate at zero bias due to the built-in potential produced at the junction interface. The photogenerated electron-hole pairs can be separated by the built-in field generated at the interface and the same can be collected at respective electrodes.[13] p-n junction photodetector is a p-n junction diode in which the incident radiation can penetrate into the vicinity of the metallurgical junction.[3] Due to its fast response, low dark current, high impedance, ability to operate under high frequency conditions and high operational stability, p-n junction diode structure is promising for the fabrication of UV detectors. p-n junction detectors operate under reverse biased conditions. Under reverse biased conditions, the dark current, carrier transit time and diode capacitance are reduced and the difference between the dark current and photocurrent will reach maximum and improve the sensitivity of the device. The total current in a p-n junction photodiode can be expressed by the relation (2.1),

$$I(V) = I_s \exp[\left(\frac{eV}{nKT}\right) - 1] - eG \qquad (2.1)$$

where, I_s is the saturation current, e is the electron charge, V is the bias voltage, n is the ideality factor, K is Boltzmann constant, T is the absolute temperature and G is the generation rate. In the equation (2.1), $I_s[\exp(eV/nKT)-1]$ corresponds to dark current and eG corresponds to photocurrent.[14]

ZnO-based p-n homojunction UV detectors have exhibited relatively improved electrical performance. ZnO is an n-type semiconductor due to the presence of intrinsic defects such as O vacancies and interstitial H atoms.[15] It is very difficult to achieve high quality and stable p-type

ZnO due to the self-compensating effect from the defects in ZnO, deep acceptor levels and low solubility of the dopants.[16] P-type ZnO films can be obtained by doping it with N, Li, Na, K, As and P.[17–19] In 2005, Moon et al. prepared a ZnO p-n homojunction by As-doped ZnO and ZnO. The As-doped ZnO films deposited on GaAs substrates by RF magnetron sputtering showed p-type behaviour. The p-n homojunction exhibited rectifying IV characteristics and a photocurrent of 2 mA was observed under 325 nm light illumination.[20] Next year, Liu et al. studied the properties of Sb-doped p-type ZnO and Ga-doped n-type ZnO-based p-n homojunction photodiodes. The p-type ZnO film obtained by Sb doping by Molecular Beam Epitaxy (MBE) technique achieved a carrier concentration of 1.7×10^8 cm^{-3} and mobility of 20 cm^2/Vs. Rectifying IV curves were observed with better photodetection properties.[21] A p-n junction photodetector with high responsivity of 12.9 A/W under a reverse bias voltage of 3 V at 376 nm was fabricated by Agarwal et al. in 2020. The p-n homojunction was fabricated with RF sputtered n-type ZnO and Cu-doped p-type ZnO and the device showed a detectivity of 2.9×10^9 Jones at zero bias.[22]

Due to the difficulty in preparing stable, reliable, reproducible and high-quality p-type ZnO films, ZnO-based p-n heterojunction UV detectors are fabricated with different p-type materials such as, NiO,[23] GaN,[24] Si,[25], SiC[26] etc. Among them Si is receiving greater attention due to its low cost, compatibility with integrated circuit technology, low deposition temperature and comparable properties with GaN.[27] Shen et al. fabricated a self-powered UV photodetector based on p-NiO/ZnO nanorod array heterojunction. The photogenerated electron-hole pairs are separated by the built-in electric field between ZnO and NiO arising from the devices' aligned energy band structure at the heterojunction interface which transports these charge carriers to respective electrodes and thus produces photocurrent. The device exhibited a responsivity of 0.44 mA/W and an on-off ratio of 10^2 under 355 nm light illumination. The devices were fast responding with rise and fall times of 0.23 s and 0.21 s respectively.[28] Tahani et al. fabricated photodetectors with high stability and responsivity of 101.2 A/W at 5 V based on p-Si/n-ZnO

nanotube heterojunctions, ZnO nanotubes were deposited by PLD technique and they found that high photodetection performance was due to the optical confinement, the high surface-to-volume ratio, high structural quality of the nanotube and the high photoinduced carrier density. At 2 V, the device showed responsivity of 21.51 A/W, detectivity of 1.26×10^{12} Jones and rise and fall times of 0.44 s and 0.59 s respectively.[29] Enhanced photoresponse was observed in UV photodetectors based on ZnO nanorod array/p-GaN heterojunction devices fabricated by Fu et al. In their work, the nanorod arrays were coupled with coral like CuO nanostructures to improve the photodetector performance. The on-off ratio, responsivity and detectivity were improved by ~187, ~104 and ~153 times respectively when compared with the device without CuO nanostructures. This coral like CuO nanostructures also improved the responding speed of the device. The reason for the enhanced performance of the device with CuO nanostructures is that the separation efficiency of photogenerated electron-hole pairs is improved by the ZnO nanorod arrays coupled with CuO nanostructures.[30]

Most of the p-n junction photodiodes fabricated with inorganic semiconductors exhibit high performance due to its high carrier mobility and large absorption coefficients. But these materials have some drawbacks such as complex and high cost fabrication techniques, high temperature synthesis and low flexibility. The high cost fabrication techniques lead to the high cost of the device. However, organic semiconductors are solution processable, flexible, light weight and it is easy to tune their properties. But they have low values of carrier mobility, low carrier concentration and large density of defects.[31,32] In spite of the drawbacks, the heterojunction formed between organic-inorganic hybrid semiconductors is a suitable choice for the fabrication of high-performance UV detectors. The p-n junction formed between organic and inorganic materials have the advantages of low-cost, large optical absorption bandwidth, large area fabrication, low temperature processability, selective spectral response, mechanical

flexibility and high sensitivity, since they combine the unique properties of both organic and inorganic semiconductors.[33,34]

Li et al. fabricated UV photodetectors based on organic-inorganic hybrid by sandwiching ZnO nanoparticles and poly (9,9-dihexylfluorine) (PFH) between two electrodes.[35] The devices showed high on-off ratio at -1 V with relatively fast response. The devices exhibited narrow band spectral response from 300-320 nm, with its peak centered at 335 nm. The photoelectric performance of the device was improved by aging in air. In 2012, narrow band UV detectors based on MgZnO and NPB heterojunction were reported by Hu et al.[36] A narrow band photoresponse was observed from 300-400 nm with peak at 340 nm with a responsivity of 0.192 A/W at -1 V. In 2016, Cai et al. fabricated UV photodetectors based on ZnO nanoflakes/PVK heterojunction with PEDOT:PSS as anode layer. Here ZnO acts as electron acceptor and electron transport material and PVK acts as an electron donor and hole transport material. The device exhibited better performance with large responsivity and detectivity values such as 7.27×10^3 A/W and 6.20×10^{13} Jones at 2 V under 365 nm light illumination.[37] In the same year Ranjith et al. have reported ZnO nanorod/PEDOT:PSS hybrid heterojunction based and ZnO nanorod based UV photodetectors and compared the results.[38] They found that photocurrent, sensitivity and responsivity of ZnO nanorod/PEDOT:PSS hybrid devices are higher than that of ZnO nanorod based device. This was explained based on the fact that the photo-induced charge separation efficiency of the organic inorganic hybrid device was higher. A fast response self-powered UV photodetector with a responsivity 125 µA/W and detectivity 3.7×10^7 Jones based on P3HT/ZnO nanowire array heterojunction was reported in 2017.[39] They have also investigated the thermal effect on UV photoresponse properties. The performance enhancement in this device arises due to the thermo-phototronic effect. i.e., the applied temperature difference changes the band gap of the p-n junction by producing a thermoelectric field. High performance ZnO/pentacene

heterojunction based UV-visible photodetectors were reported by Anshika et al. The high performance of the device was explained by the trap-assisted photomultiplication process.[40]

Another important requisite for UV detectors is the ability to be visible-blind. n-ZnO/p-Si heterostructures are reported to be suitable for UV photodetectors.[41] But the photoresponse to visible light needs to be tackled. A photodetector based on n-ZnO/insulator-MgO/ p-Si MBE has been shown to be visible-blind.[42] However, simpler fabrication techniques are required for low-cost manufacturing.

Recently, flexible photodetectors gained considerable attention because of their peculiar applications in spacecrafts, future paper displays and wearable and portable devices.[43] ZnO thin films prepared by a low cost technique such as sol-gel process require high annealing temperature to produce high quality films with high electron mobility.[44] Hence, this technique is not suitable for the fabrication of flexible devices. ZnO thin film prepared from ZnO nanoparticles dispersion could be a good alternative to the sol-gel process.

The above discussion points to the need for developing a UV photodetector which can be self-powered, can be processed at low temperature and visible-blind. We have attempted to address these challenges in the present work.

Herein, we fabricated self-powered UV photodetectors based on organic inorganic heterojunction formed between ZnO nanoparticles and N,N′-Di(1-naphthyl)-N,N′-diphenyl-(1,1′-biphenyl)-4,4′-diamine (NPB). To address the issue of low temperature processability, we used a technique to deposit ZnO films at room temperature which do not require any annealing. However, the performance of ZnO/NPB heterojunction was poor due to the presence of defects in ZnO thin film. To circumvent this drawback, we deposited a thin layer of Titanium dioxide (TiO$_2$) on ZnO as a surface passivation layer to passivate the defects in ZnO which resulted in improved performance. Then different organic layers such as copper(II) phthalocyanine (CuPC),

4,4',4"-Tris[2-naphthyl(phenyl)amino]triphenylamine (2-TNATA), rubrene and 1,1-Bis[(di-4-tolylamino)phenyl]cyclohexane (TAPC) were used in the device structure to study the spectral response properties. The device with 30 nm thick NPB layer exhibited better performance due to its excellent film forming properties, high hole mobility and transparent nature in the visible region.[45] This technique is suitable for the fabrication of flexible UV photodetectors, as it avoids a high temperature annealing step.

2.3 Experimental

2.3.1 Annealing-free ZnO thin film preparation

Annealing-free ZnO thin films were prepared from ZnO nanoparticles dispersion by a method similar to the one reported by Alem et al.[46] 1.475g of zinc acetate dihydrate was dissolved in 62.5 ml of methanol at reflux. 0.74g of KOH was dissolved in 32.5 ml of methanol and then this solution was added to the first solution drop by drop by using a syringe. The resultant mixture was refluxed under Ar for 6 h and a white precipitate was formed. Subsequently, this precipitate was washed twice with methanol and the nanoparticles were separated through centrifugation. These nanoparticles were dispersed in chloroform and filtered through a 0.2µm PTFE filter. Then propylamine was added to keep the solution stable and homogeneous. This solution was spin coated at 3000 rpm and no further plasma treatment or thermal annealing was required. The ZnO film coated substrates were kept in low vacuum (10^{-1} Torr) overnight for the solvents to evaporate completely.

2.3.2 Characterization

Optical properties of the annealing-free ZnO thin films were studied by using Fluorolog Spectrofluorometer, HORIBA Jobin Yvon and PerkinElmer UV/VIS/NIR Spectrometer, Lambda 950. Surface morphology of the ZnO thin films before and after TiO_2 deposition were investigated by Bruker AFM. Surface morphology of annealing-free ZnO thin film and

synthesized ZnO nanoparticles were recorded by Carl Zeiss scanning electron microscope (SEM), Germany. Bruker Stylus Profilometer was used for the thickness measurements. The size of the nanoparticles were measured by dynamic light scattering (DLS) method at 25 $^{\circ}$C with Malvern Zetasizer Nano Zs. X-ray diffraction (XRD) patterns were recorded by XPert-PRO Scan Diffractometer with Cu Kα (λ=1.54060 Å) radiation from 20^0 to 70^0 scanning range. Fourier transform infrared (FTIR) spectra of ZnO nanoparticles were measured by IR prestige-21 FTIR Spectrophotometer, Shimadzu.

2.3.3 Device fabrication

The structure of the fabricated device is shown in Figure 2.1(a) and device fabrication procedure is shown in Figure 2.1(b). Annealing-free ZnO thin film was deposited by spin coating at 3000 rpm on ultrasonically cleaned and subsequently, UV-ozone treated ITO coated glass substrate. 0.15 M TiO$_2$ solution was prepared by dissolving 55 µl of titanium diisopropoxide bis(acetylacetonate) in 1 ml of isopropyl alcohol. This solution was deposited on the ZnO layer as a surface passivation layer and then the film was annealed at 125^0 C for 1 h. 30 nm thick NPB was thermally evaporated at the rate of 1 Å/s as hole transporting layer. Finally, Ag anode (100 nm) was thermally evaporated. Devices with and without TiO$_2$ were prepared and the device performance was compared. The device performance was optimized by fabricating devices with different thickness of NPB such as 20 nm, 50 nm and 70 nm. The role of the organic layer in the device was studied by varying the organic layer in the device structure. 30 nm thick CuPC, 2-TNATA, Rubrene and TAPC were used as organic layers in the device structure and the device performance was compared.
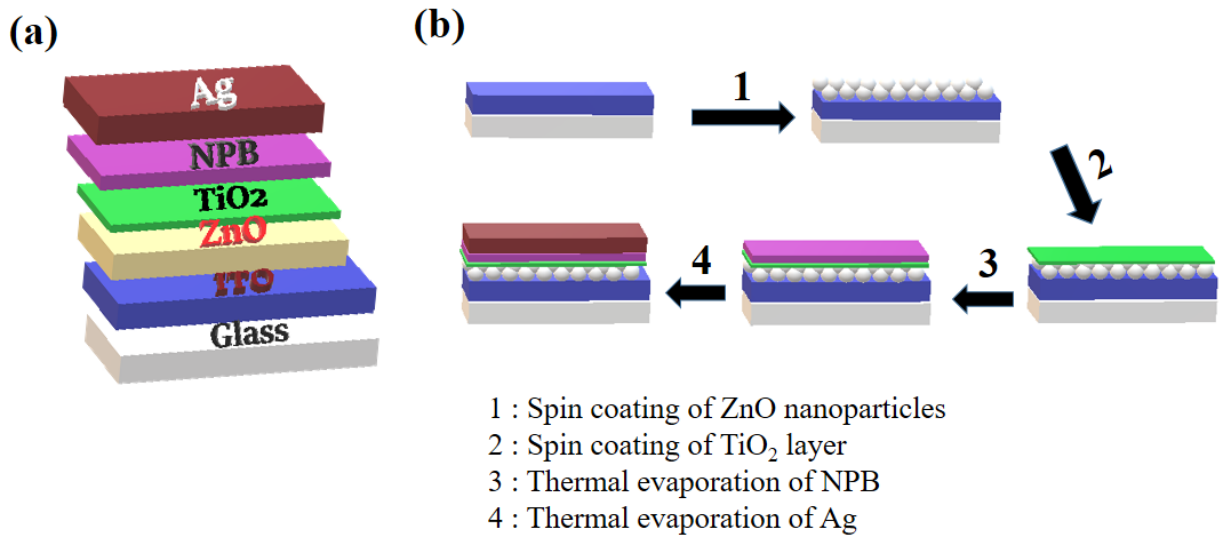
Figure 2.1. (a) Device structure of the photodetector (b) Schematic diagram depicting steps of device fabrication.

2.3.4 Characterization of UV photodetector

The current-voltage characteristics and transient photoresponse of the device were studied with Keithley 2400 source meter and 6 W ENF 260C spectroline UV Lamp with 365 nm and 254 nm wavelengths. Spectral response measurements were carried out by using a 250 W Xenon lamp coupled to a Newport monochromator and chopped at 40 Hz using a light chopper blade as a light source and a power meter to measure the intensity of light.

2.4 Results and discussion

2.4.1 Characterization of ZnO

Surface morphology of the annealing-free ZnO thin films were imaged by using atomic force microscopy (AFM). Figure 2.2 shows the AFM image of ZnO thin film obtained through tapping mode with 1μm and 500 nm scanning range before and after TiO_2 deposition. The nanoparticles were spherical in shape. The thickness of ZnO and TiO_2 thin films were determined using profilometry. The thickness values are 80 nm and 10 nm for ZnO and TiO_2 thin films respectively. The RMS surface roughness values of ZnO thin films before and after TiO_2

deposition are summarized in Table 2.1. RMS surface roughness of ZnO is low in areas where a compact ZnO layer is formed. But there are some areas where the depth is more and this probably is leading to a greater RMS roughness when we select a large area for the calculation. However, the RMS surface roughness was decreased with TiO_2 deposition due to the improvement in the film quality. The particle size of ZnO nanoparticles from the AFM image was less than 50 nm. The fact that the RMS surface roughness increases only incrementally for longer scan ranges is an indication of the quality and uniformity of the film.

Sample	RMS surface roughness (scanning range 500 nm)	RMS surface roughness (scanning range 1 μm)
ZnO	6.98 nm	7.07 nm
ZnO+TiO_2	3.66 nm	3.71 nm

Table 2.1. RMS surface roughness values of ZnO thin films before and after TiO_2 deposition.
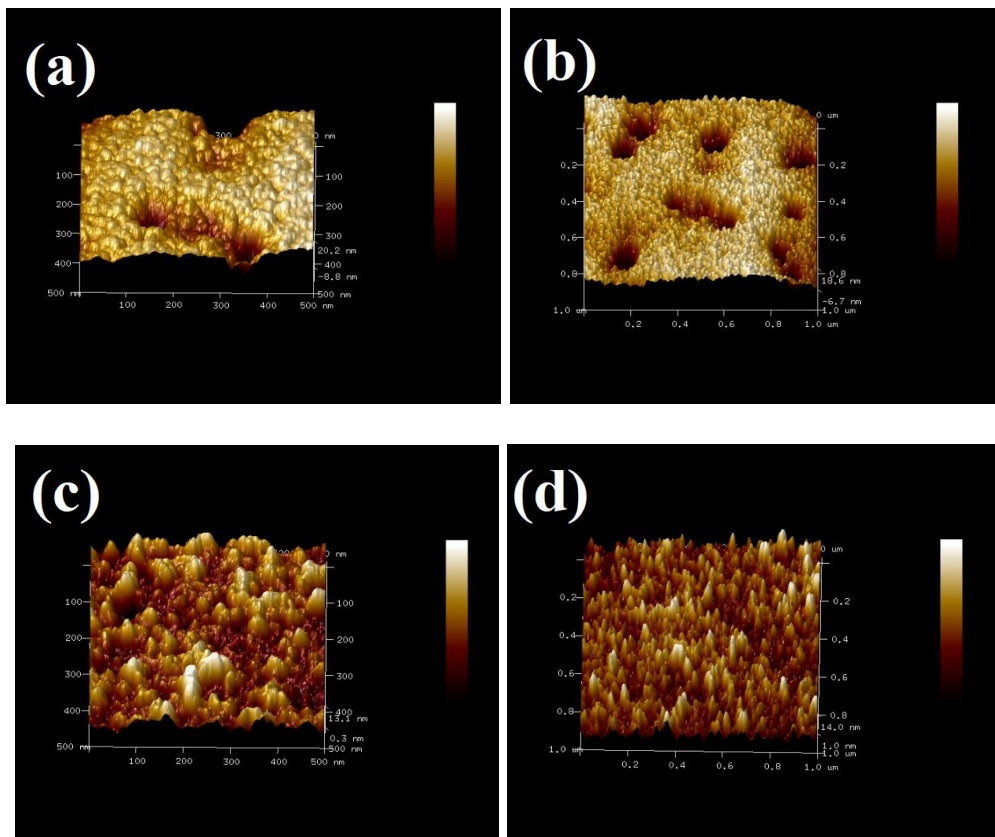
Figure 2.2. AFM images of annealing-free ZnO thin films before and after TiO_2 deposition (a), (b) before TiO_2 deposition (c), (d) after TiO_2 deposition.

The SEM images of the ZnO thin film and synthesized ZnO nanoparticles recorded with a magnification of x50k are shown in Figure 2.3.
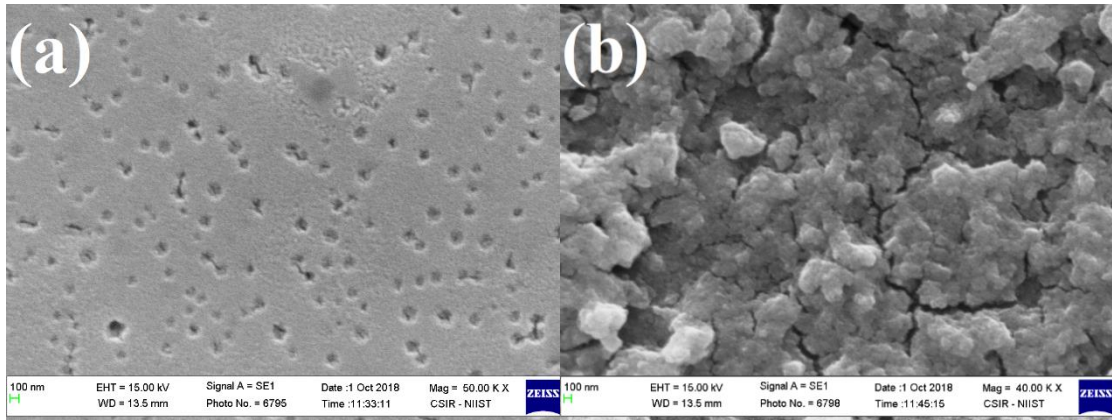
Figure 2.3. (a) SEM image of annealing-free ZnO thin film (b) SEM image of ZnO nanoparticles.

The structural properties of ZnO nanoparticles were studied by using XRD and FTIR spectroscopy. The XRD pattern of the ZnO nanoparticles is shown in Figure 2.4(a). (100), (002), (101) (102), (110), (103) and (112) peaks were observed. All the XRD peaks were identified with the standard card JCPDS 36-1451, in the recorded range of 2θ. It is confirmed that ZnO nanoparticles have hexagonal wurtzite structure. We calculated the crystallite size for the most intense peak by using Scherrer's formula,[47]

$$D = \frac{K\lambda}{\beta cos\theta} \qquad\qquad (2.2)$$

Where K is a constant, λ is the X-ray wavelength and β is the full width at half maximum intensity (FWHM). The crystallite size is found to be 15.1 nm. The XRD pattern of ZnO thin film with and without passivation layer is shown in Figure 2.4(b). It can be seen that there is hardly any change in the XRD data. This indicates that TiO_2 is amorphous and does not affect the crystallinity of ZnO in any manner. NPB thin film deposited by thermal evaporation is considered to be amorphous[48]. During the deposition of NPB, we did not anneal the film or give any substrate temperature. So, it will not affect the crystalline properties of ZnO.
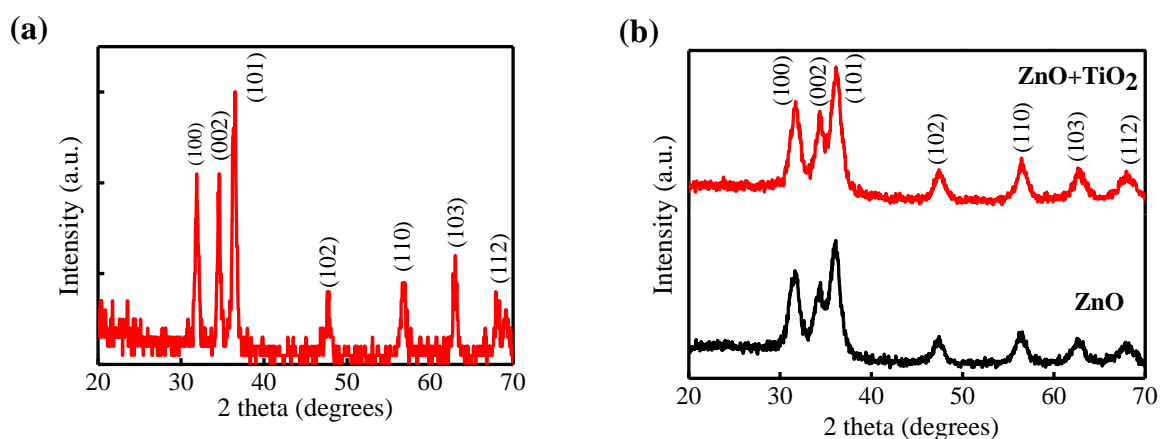
Figure 2.4. (a) XRD pattern of ZnO nanoparticles (b) XRD pattern of ZnO thin films before and after TiO$_2$ deposition.

To understand the presence of molecular species in the prepared samples, FTIR studies were done within the range of 400 cm^{-1} to 4000 cm^{-1} at room temperature. FTIR spectra of ZnO nanoparticles are shown in Figure 2.5. Absorption bands below 1000 cm^{-1} are due to interatomic vibrations of metal oxides.[49] The absorption bands observed between 480 cm^{-1} – 580 cm^{-1} correspond to Zn-O stretching mode.[50] The n-type conductivity of undoped ZnO is due to the presence of impurities, such as hydrogen (H). H is present in almost all growth environments. The interstitial H bonding with oxygen (O) and H substituted for O in ZnO act as shallow donor levels and contribute to the n-type conductivity. The substitutional H is more stable than the interstitial H. The peak near 900 cm^{-1} is related to the hydrogen substituted at the oxygen site bound to the lattice Zn site (ie, Zn-H).[51] The IR peaks around 1330 cm^{-1}, 1400 cm^{-1} and 1570 cm^{-1} were observed due to symmetric and asymmetric stretching vibrations of C=O group.[52] The absorption band near 3400 cm^{-1} corresponds to O-H stretching mode.[44]
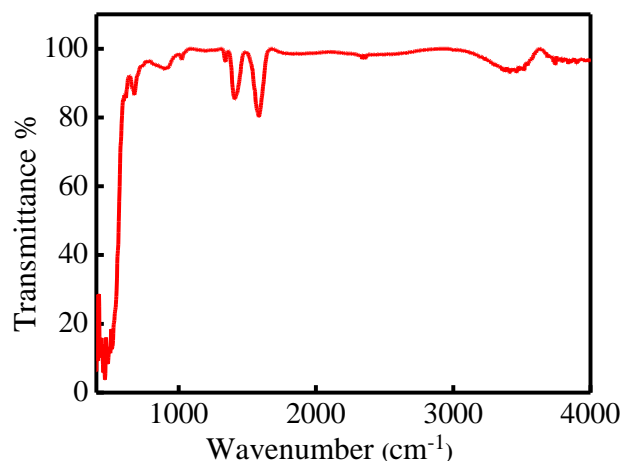
Figure 2.5. FTIR spectra of ZnO nanoparticles.

DLS measurements were carried out at 632.8 nm with a He-Ne gas laser at an angle of 175°. The mean diameter of the nanoparticles was around 50 nm.

The optical properties of ZnO thin films were studied by using photoluminescence (PL) and UV-Visible absorption spectroscopy. PL spectra of ZnO thin film excited at 320 nm is shown in Figure 2.6. The peak at 370 nm is due to the near band edge emission and the other one near 585 nm is due to the oxygen vacancy defect.[53] In order to passivate the defect, a very thin layer of TiO$_2$ was deposited as a surface passivation layer.[54] From the PL spectrum of ZnO after TiO$_2$ deposition it is clear that the intensity of UV emission is enhanced and visible emission is suppressed due to decrease in the defects density. The enhancement in the UV emission is due to the fluorescence resonance energy transfer (FRET) between TiO$_2$ and ZnO i.e, the energy is transferred from TiO$_2$ to ZnO thin film. The reduction in the intensity of visible emission is attributed to the surface passivation effect due to covered TiO$_2$ layer.[54]
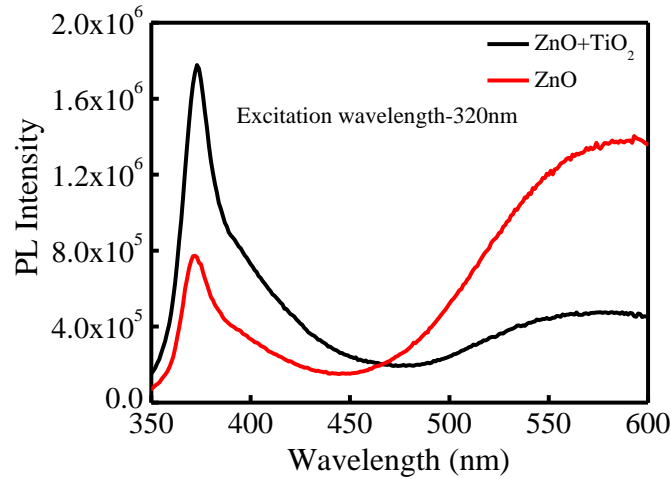
Figure 2.6. PL spectra of ZnO thin films before and after TiO$_2$ deposition.

The transmittance spectra of ZnO thin film before and after TiO$_2$ deposition are shown in Figure 2.7(a). The films yielded transmittance above 85% in the visible region before and after TiO$_2$ deposition. It can be seen that the transparent nature of ZnO is not affected by the TiO$_2$ deposition. This is highly desirable as the transparent nature of ZnO is very important for several optoelectronic applications. The value of energy band gap of ZnO thin film can be calculated from the Tauc's plot using the relation,

$$\alpha h\nu = A\left(h\nu - E_g\right)^n \qquad (2.3)$$

where α is absorption coefficient, A is the proportionality constant, $h\nu$ is the incident energy and E_g is the band gap of the material.[55] Since ZnO is reported to be a direct band gap semiconductor,[56] value of n is taken to be ½ and then the equation (2.3) becomes

$$\alpha h\nu = A\left(h\nu - E_g\right)^{1/2} \qquad (2.4)$$

Figure 2.7(b) shows the Tauc's plot of ZnO thin film and we estimated the band gap to be 3.34 eV. The relation between absorption coefficient and photon energy near band edge is given by

$$\alpha = \alpha_0 exp\left(\frac{h\nu}{E_u}\right) \qquad (2.5)$$

where α_0 is a constant and E_u is the width of the localized states known as Urbach energy.[57] The Urbach energy of the ZnO thin films can be calculated from the slope of the curve plotted between $\ln(\alpha)$ and $h\nu$. Figure 2.7(c) shows the plot of $\ln(\alpha)$ *Vs. $h\nu$.*[58] The values of Urbach energy of ZnO thin film before TiO_2 deposition is 0.877 eV and after TiO_2 deposition is 0.651 eV. We found that Urbach energy of annealing-free ZnO thin films decreases upon TiO_2 deposition. The decrease in the Urbach energy implies the reduction in the defect density after TiO_2 deposition.
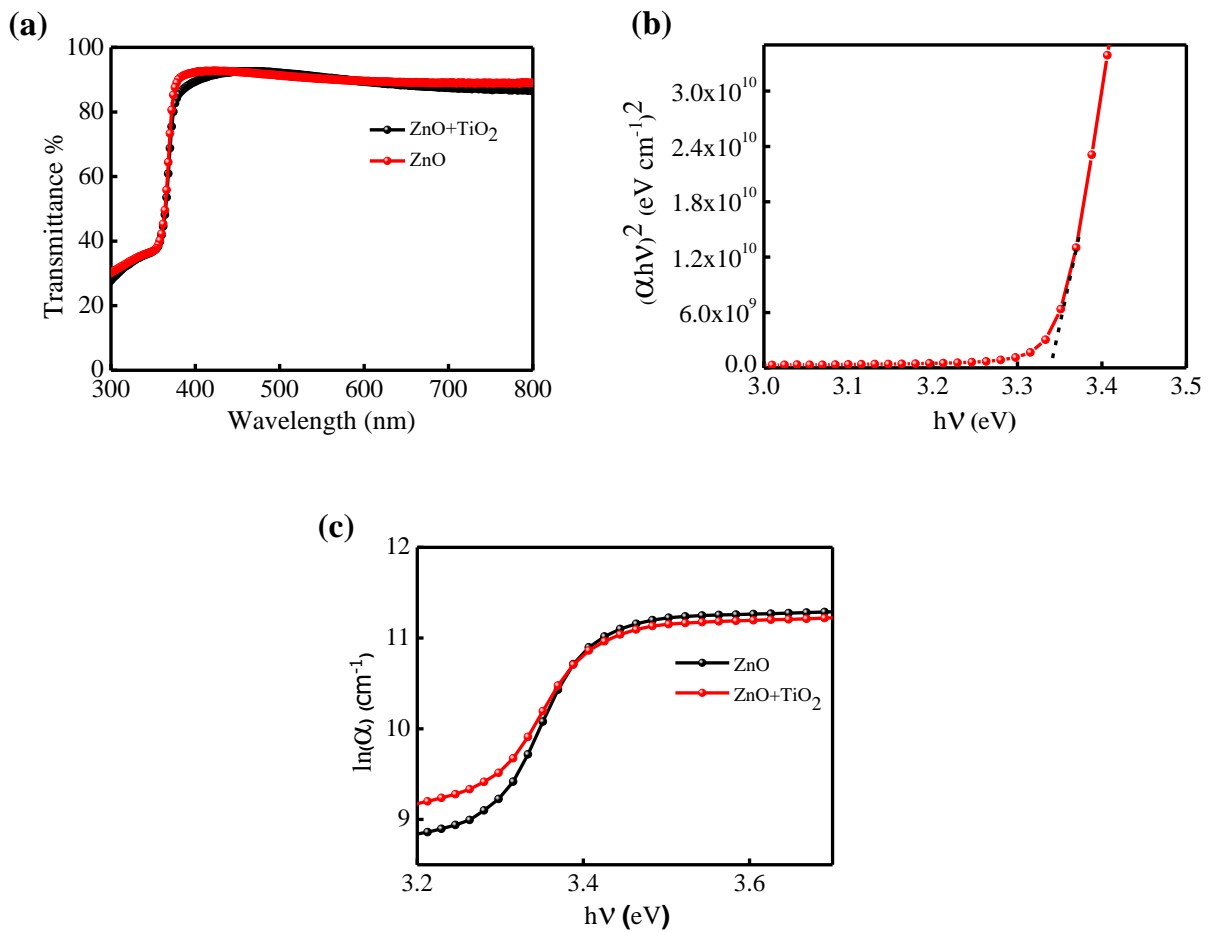
Figure 2.7. (a) Transmittance spectra (b) Tauc's plot and (c) Urbach Plot of ZnO thin film with and without a TiO_2 film.

2.4.2 Characterization of UV photodetector

IV characteristics of the device with and without TiO_2 under dark and 365 nm light illumination at an intensity of 1.24 mW/cm^2 and 254 nm light illumination at an intensity of 2.4 mW/cm^2 are shown in Figure 2.8. The device without TiO_2 exhibited poor performance due to the oxygen vacancy defect present in ZnO film. TiO_2 acts as a surface defects passivation layer and improves the device performance. The order of on-off ratio was improved from 10^2 to 10^3 under 365 nm light illumination. The performance parameters of the device are summarized in Table 2.2. Upon UV illumination, ZnO and NPB absorb UV light and generate electron-hole pairs. These electron-hole pairs will dissociate into electrons and holes by the built-in potential at the organic-inorganic heterojunction. These electrons and holes are collected by the electrodes and thus a photocurrent is produced. The photocurrent of the device without TiO_2 was 1.71 µA and it is increased to 15 µA upon TiO_2 deposition.
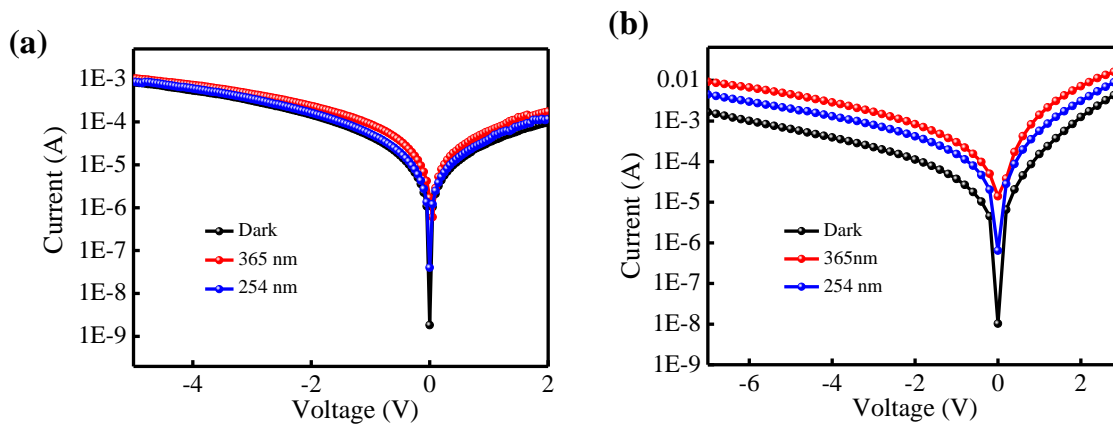
Figure 2.8. (a) I-V characteristics of the device without TiO_2 under dark, 365 nm and 254 nm light illumination (b) I-V characteristics of the device with TiO_2 under dark, 365 nm and 254 nm light illumination.

Figure 2.9 shows the transient photoresponse of the device under 365 nm and 254 nm light illumination at 0 V. From the transient photoresponse we calculated the rise time and fall time of the device. The device with TiO_2 layer showed a fast response with rise and fall times of 156 ms and 319 ms respectively. The rise time was reduced from 254 ms to 156 ms and fall

time was reduced from 416 ms to 319 ms under 365 nm light illumination due to the surface passivation of defects upon TiO_2 deposition. The rise and fall times were also reduced under 254 nm light illumination after TiO_2 deposition. The rise time and fall time values are summarized in table 2.2.
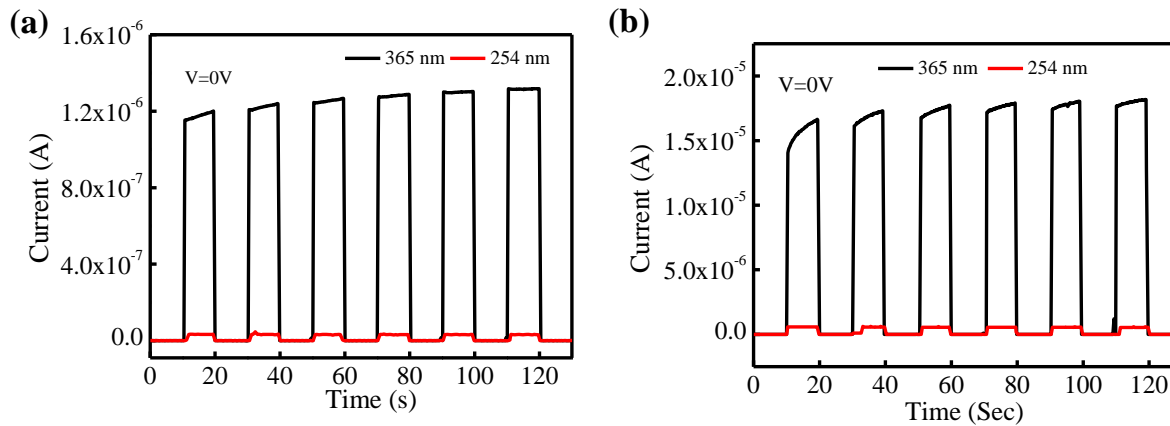
Figure 2.9. (a) Transient photoresponse of the device without TiO_2 under 365 nm and 254 nm light illumination (b) Transient photoresponse of the device with TiO_2 under 365 nm and 254 nm light illumination.

We measured the I-V characteristics and transient photoresponse with increase in the intensity of illumination at 365 nm. We observed an increase in the photocurrent with increase in the intensity of illumination. Figure 2.10(a) and Figure 2.10(b) show the IV characteristics and transient photoresponse with increase in the intensity of radiation and Figure 2.10(c) shows the transient photoresponse with increasing intensity.
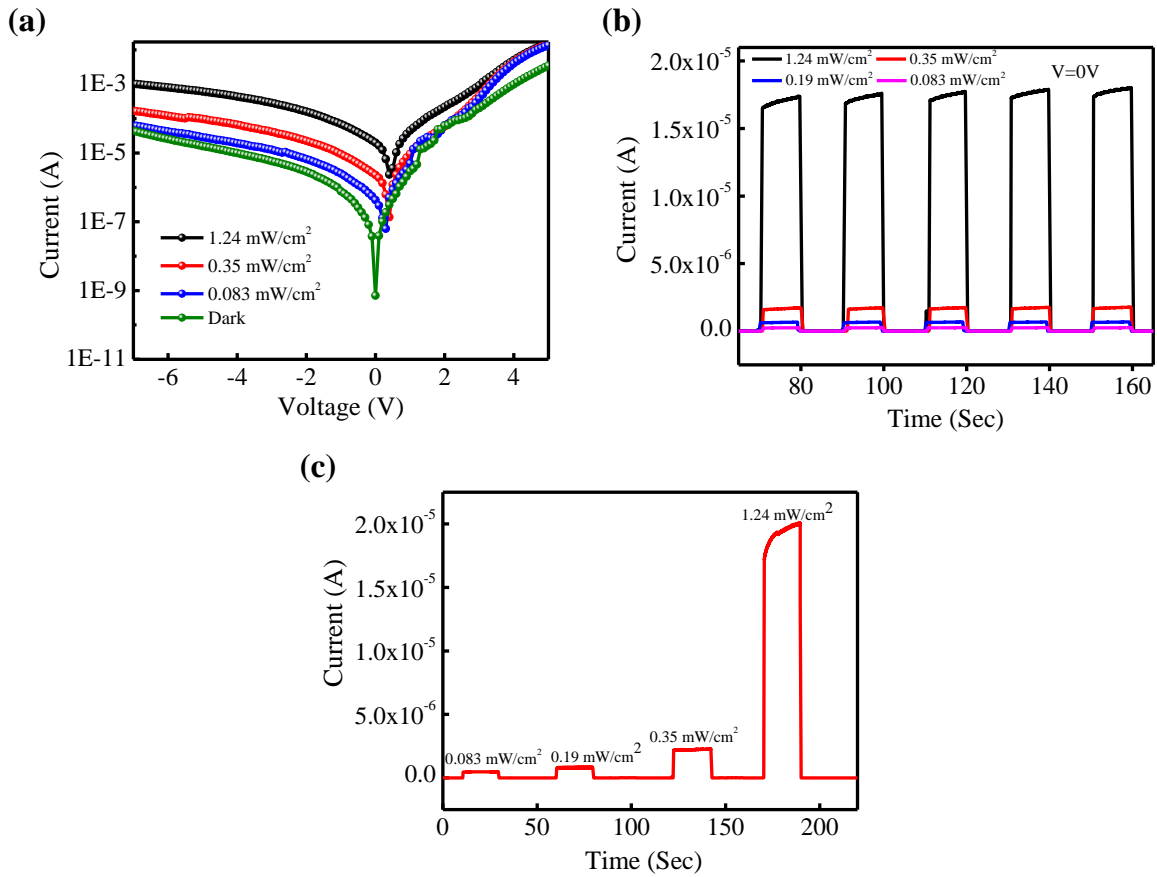
Figure 2.10. (a) I-V characteristics of the photodetector at different UV (365 nm) intensities (b) Transient photoresponse under 365 nm light illumination at different intensities and (c) Transient photoresponse with increasing intensity.

Spectral response measurements were carried out within the 300 nm to 800 nm wavelength range at 0 V by using the IPCE measurement system. The devices exhibited a narrow band response with peak centered at 360 nm. From spectral response measurement it is clear that the device is completely visible-blind and suitable for applications requiring selective UV detection. From spectral response measurements, responsivity, detectivity and EQE were calculated and are summarized in Table 2.2. Figure 2.11(a) shows variation of responsivity with wavelength, Figure 2.11(b) shows variation of detectivity with wavelength and Figure 2.11(c) shows the variation of EQE with wavelength of the device without TiO_2 layer. The device without TiO_2 exhibited responsivity of 0.80 mA/W and detectivity of 1.61×10^{10} Jones. The responsivity, detectivity and EQE values were enhanced upon TiO_2 deposition. The responsivity

is increased to 17 mA/W and detectivity is increased to 5.20×10^{10} under zero bias. Figure 2.12(a) shows variation of responsivity with wavelength, Figure 2.12(b) shows variation of detectivity with wavelength and Figure 2.12(c) shows the variation of EQE with wavelength of the device with TiO_2 layer at different bias voltages. The responsivity, detectivity and EQE values at different bias voltage under 360 nm light illumination is summarized in Table 2.3. It is found that the responsivity and EQE increases with the increase in the bias voltage. The device exhibited a maximum responsivity of 0.037 A/W and external quantum efficiency of 12.86% at 360 nm illumination at 5 V. The LDR of the device is increased from 59.44 to 63.52 dB with TiO_2 coating. This value is comparable with the LDR of UV photodetectors fabricated based on InGaAs (66 dB).[59] It is very interesting to note that a UV photodetector based on ZnO fabricated from a simple and cost effective fabrication technique is yielding a LDR value very similar to that of the one fabricated from energy intensive techniques. We believe that this is an important step in fabricating flexible photodetectors.
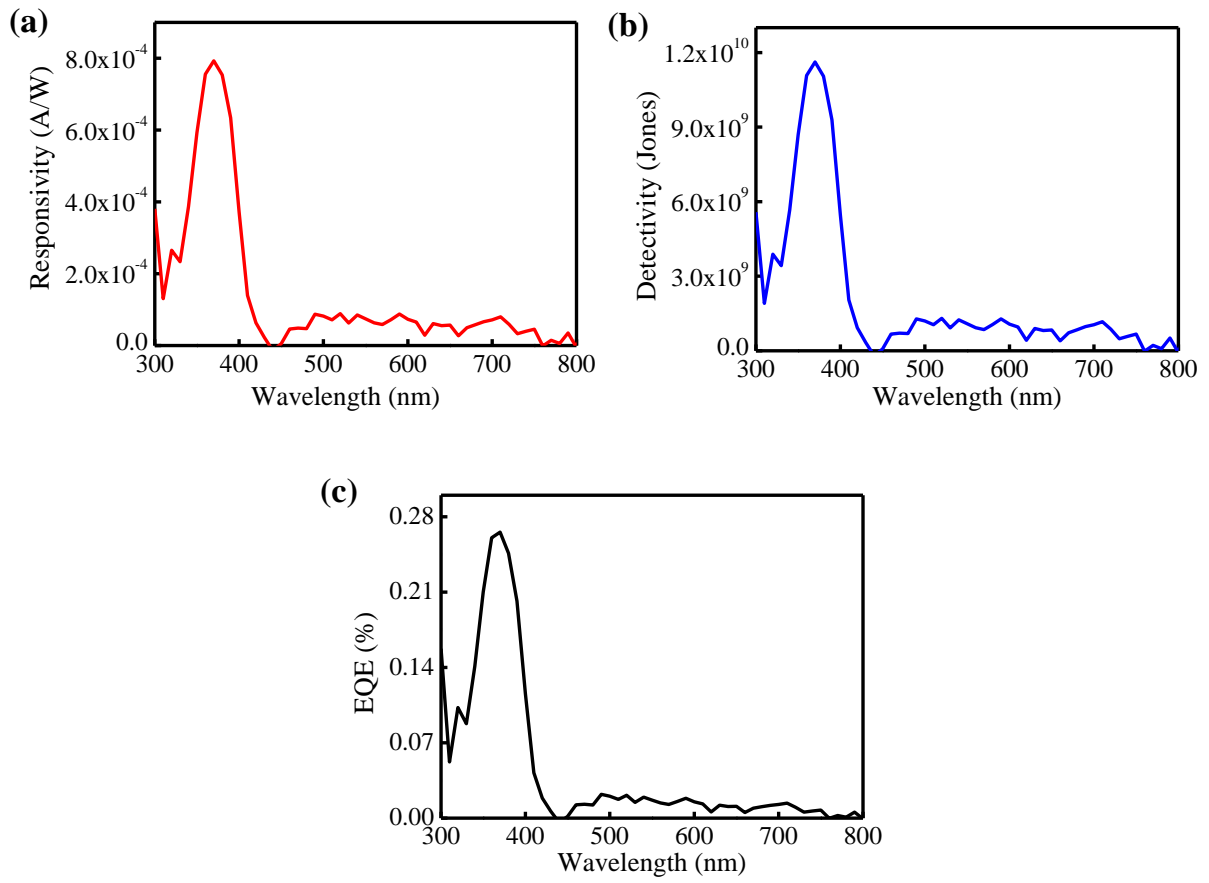
Figure 2.11. (a) Variation of responsivity with wavelength (b) Variation of detectivity with wavelength (c) Variation of EQE with wavelength of the device without TiO$_2$ layer.
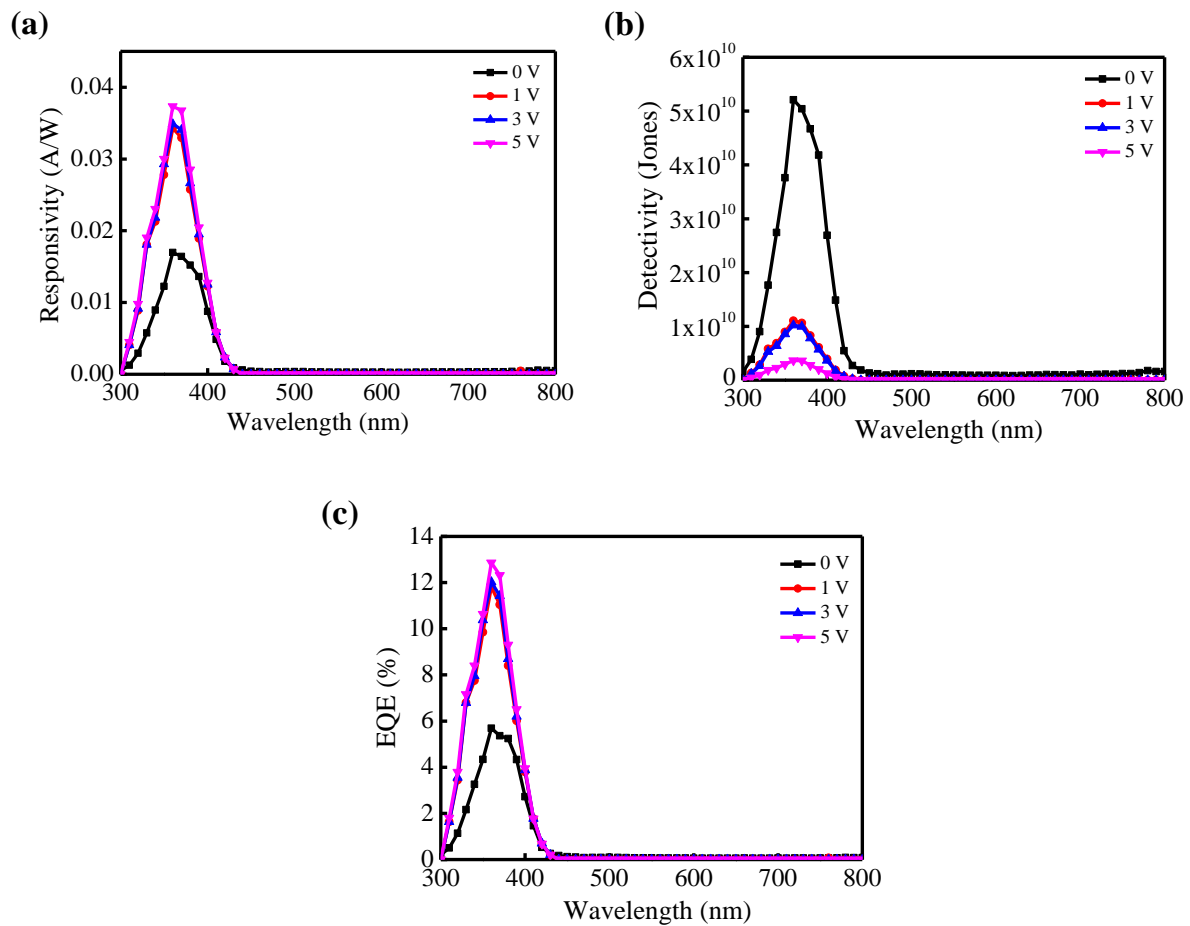
Figure 2.12. (a) Variation of responsivity with wavelength (b) Variation of detectivity with wavelength and (c) Variation of EQE with wavelength of the device withTiO$_2$ layer.

Device	On-off ratio		Rise time (ms)		Fall time (ms)		Responsivity (A/W)	Detectivity (Jones)	EQE (%)	LDR (dB)	
	365 nm	254 nm	365 nm	254 nm	365 nm	254 nm	360 nm	360 nm	360 nm	365 nm	254 nm
ITO/ZnO/ NPB/Ag	9.38×10^2	21.8	254	503	416	502	7.93×10^{-4}	1.61×10^{10}	0.26	59.44	26.76
ITO/ZnO/ TiO$_2$/NPB/ Ag	1.5×10^3	62	156	262	319	408	0.017	5.20×10^{10}	5.68	63.52	35.84

Table 2.2. Performance parameters of the devices with and without TiO$_2$ layer at 0 V.

72

Bias Voltage (V)	Responsivity (A/W)	EQE (%)	Detectivity (Jones)
0	0.017	5.68	5.20×10^{10}
1	0.034	11.81	2.43×10^{10}
3	0.035	12.02	2.28×10^{10}
5	0.037	12.86	8.18×10^{9}

Table 2.3. Performance parameters of the devices with TiO_2 layer at 0 V, 1 V, 3 V and 5 V.

To further study the effect of thickness on the device performance, self-powered UV photodetectors were fabricated with different thickness of NPB such as 20 nm, 50 nm and 70 nm. The performance parameters of the devices with different thickness of NPB are summarized in Table 2.4. It is found that first the device performance is improving from 20 nm thick NPB to 30 nm thick NPB. After that the device performance is diminishing. The device with 70 nm thick NPB exhibited poor performance and the device with 30 nm thick NPB exhibited better performance. The variation of responsivity wavelength and variation of detectivity with wavelength of the devices with different thickness of NPB layer is shown in Figure 2.13. First, responsivity, detectivity and EQE are increasing from 20 nm to 30 nm and then decreasing if we further increase the thickness of NPB. On-off ratio and LDR are also decreasing after 30 nm under 365 nm and 254 nm light illumination. The reason for this behaviour is that the diffusion of charge carriers in the organic layer is inversely related to the thickness of the layer.[60] As the thickness of NPB increases after 30 nm recombination increases and photocurrent decreases. A properly designed UV photodetector should be optically thick to absorb most of the incident photons and electronically thin to collect most of the photogenerated electron-hole pairs.[61] Here 30 nm is the optimized thickness for the organic layer to have the best performance.

Device	On-off ratio		Responsivity (A/W)	Detectivity (Jones)	EQE (%)	LDR (dB)	
	365 nm	254 nm	360 nm	360 nm	360 nm	365 nm	254 nm
ITO/ZnO/NPB (30 nm)/Ag	9.38×10^2	21.8	7.93×10^{-4}	1.61×10^{10}	0.26	59.44	26.76
ITO/ZnO/TiO$_2$/NPB (20 nm)/Ag	75.59	22.07	0.0043	8.09×10^9	1.43	37.56	26.87
ITO/ZnO/TiO$_2$/NPB (30 nm)/Ag	1.5×10^3	62	0.017	5.20×10^{10}	5.68	63.52	35.84
ITO/ZnO/TiO$_2$/NPB (50 nm)/Ag	33.24	1.71	2.98×10^{-4}	2.60×10^9	0.10	30.43	4.65
ITO/ZnO/TiO$_2$/NPB (70 nm)/Ag	30.51	1.15	2.50×10^{-4}	2.17×10^9	0.08	29.68	1.21

Table 2.4. Performance parameters of the devices with different thickness of NPB
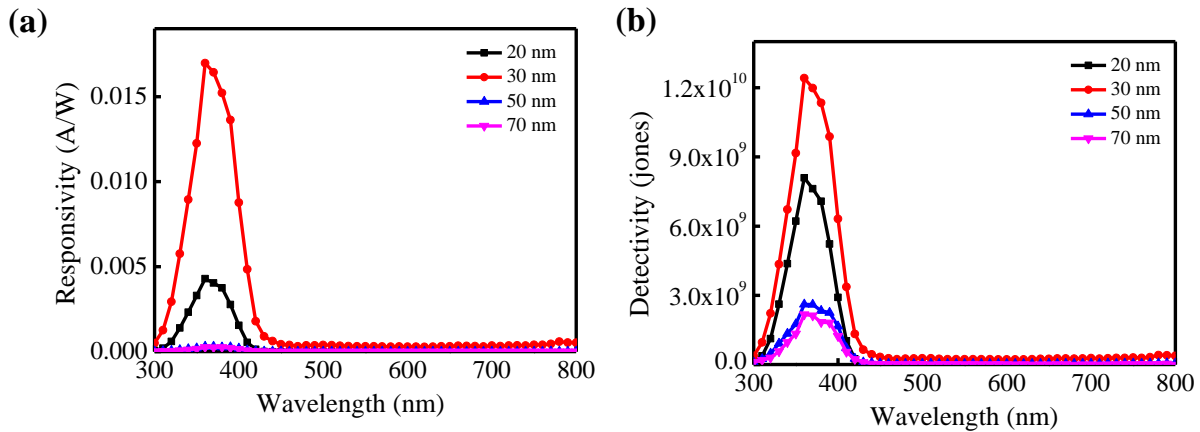
Figure 2.13. (a) Variation of responsivity with wavelength (b) Variation of detectivity with wavelength of the devices with different thickness of NPB layer.

To study the influence of different organic layers on the device performance, UV photodetectors with different organic layers as hole transporting layer was fabricated. We have used various hole transporting materials, 2-TNATA, TAPC, CuPc and rubrene. The results of the spectral response measurements of the devices are shown in Figure 2.14. The characteristics

of the device with 30 nm of NPB is also shown along with the other devices for comparison. The devices with NPB, 2-TNATA, and TAPC exhibited narrow band response with peak centered at 360 nm, 370 nm and 320 nm respectively. These devices are visible-blind and can be used for applications requiring selective spectral response performance. The devices with rubrene and CuPC have exhibited response in visible regions also. The bandgap of both organic and inorganic layers play a significant role in the photodetector device performance. The narrow band spectral response can be changed to different wavelengths by changing the organic layer in the ZnO-based organic-inorganic hybrid heterojunction devices. All the devices are self-powered. The device with NPB exhibited better performance compared to other devices due to its best hole transporting properties and transparency in the visible region. The performance parameters of the devices with different organic layers are summarized in Table 2.5.
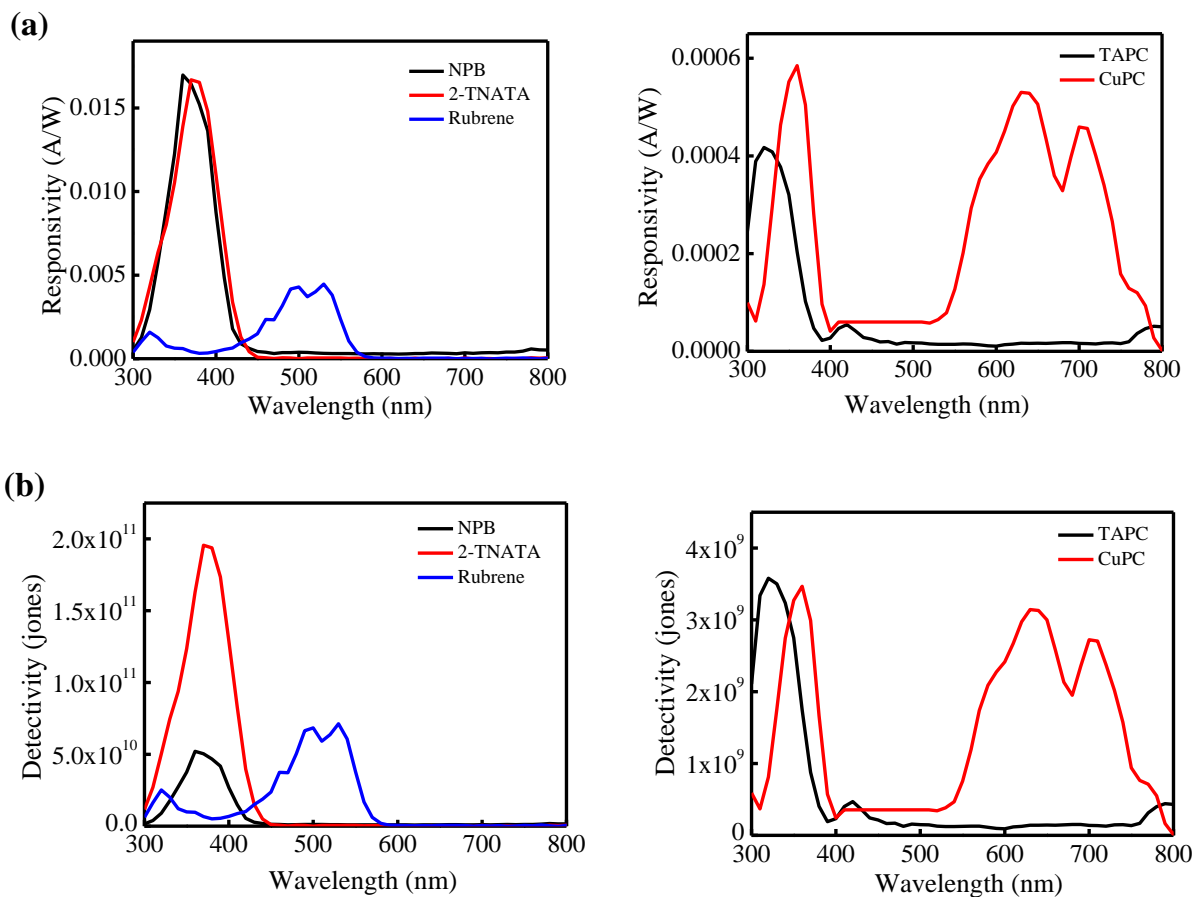
Figure 2.14. (a) Variation of responsivity with wavelength (b) Variation of detectivity with wavelength of the devices with different organic layers.

Device	On-off		Rise time (ms)		Fall time (ms)		R (A/W)	D (Jones)	EQE (%)	LDR (dB)	
	365 nm	254 nm	365 nm	254 nm	365 nm	254 nm				365 nm	254 nm
ITO/ZnO/ NPB/ TiO$_2$/Ag	1.50×10^3	62	156	262	319	408	0.017 (360 nm)	5.20×10^{10}	5.68	63.52	35.84
ITO/ZnO/ TiO$_2$/ 2 TNATA/ Ag	1.19×10^3	6.17	482	1605	251	514	0.016 (370 nm)	1.95×10^{11}	5.59	61.52	15.81
ITO/ZnO/ TiO$_2$/ TAPC/Ag	5.91	2.93	315	866	435	306	4.36×10^{-4} (320 nm)	3.74×10^9	0.17	15.43	9.36
ITO/ZnO/ TiO$_2$/ CuPC/Ag	24.09	2.24	326	-	244	-	5.93×10^{-4} (360 nm) 5.34×10^{-4} (630 nm) 4.79×10^{-4} (700 nm)	3.52×10^9 3.17×10^9 2.84×10^9	0.20 0.11 0.08	27.63	7.02
ITO/ZnO/ TiO$_2$/ Rubrene/ Ag	90.41	12.47	242	329	411	246	0.002 (320 nm) 0.004 (500 nm) 0.004 (530 nm)	2.52×10^{10} 6.84×10^{10} 7.12×10^{10}	0.61 1.06 1.04	39.12	21.91

Table 2.5. Performance parameters of the devices with different organic layers.

2.5 Conclusions

We fabricated a self-powered and visible-blind UV photodetector, processable at low temperature based on NPB/ZnO nanoparticle heterojunction. The ZnO thin films do not require any annealing and are transparent in the visible region. An additional passivation with TiO$_2$ layer, could control the defect emission from ZnO. The device showed narrow band response from 300-400 nm with the response peak centered at 360 nm. The device exhibited responsivity of 0.017 A/W and detectivity of 5.20×10^{10} at 0 V under 360 nm light illumination. The rise and fall times

were 156 ms and 319 ms respectively. We observed an increase in the photocurrent with increasing intensity of radiation. We also studied the influence of NPB thickness on the photoresponsive properties of NPB/ZnO UV detector. The thickness of NPB plays a significant role in the device performance. As the thickness of NPB increases after 30 nm, the device performance diminishes. Different organic layers were used in the device structure as hole transporting layer to study the effect of organic layers on the device performance. The spectral response properties depend on the optical properties of the organic layer and the devices can be used for spectral selective applications. The device with rubrene shows response to UV as well as green region with better performance for the latter. The device with CuPC exhibited response in UV, in the red region and in NIR. Thus, the choice of the organic layer decides the response windows of the photodetector in the visible. The results suggest that a visible-blind UV photodetector or a multi-band photodetector with promising performance can be fabricated with annealing-free ZnO film which may lead to the development of flexible detectors.

2.6 References

1. Sang, L., Liao, M. & Sumiya, M. A Comprehensive Review of Semiconductor Ultraviolet Photodetectors: From Thin Film to One-Dimensional Nanostructures. *Sensors* **13**, 10482–10518 (2013).

2. Deka Boruah, B. Zinc oxide ultraviolet photodetectors: rapid progress from conventional to self-powered photodetectors. *Nanoscale Adv.* **1**, 2059–2085 (2019).

3. Liu, K., Sakurai, M. & Aono, M. ZnO-Based Ultraviolet Photodetectors. *Sensors* **10**, 8604–8634 (2010).

4. Coleman, V. A. & Jagadish, C. Basic Properties and Applications of ZnO. in *Zinc Oxide Bulk, Thin Films and Nanostructures* 1–20 (Elsevier, 2006).

5. Chatzigiannakis, G. *et al.* Laser-Microstructured ZnO/p-Si Photodetector with Enhanced and Broadband Responsivity across the Ultraviolet–Visible–Near-Infrared Range. *ACS Appl. Electron. Mater.* **2**, 2819–2828 (2020).

6. Jin, Y., Wang, J., Sun, B., Blakesley, J. C. & Greenham, N. C. Solution-Processed Ultraviolet Photodetectors Based on Colloidal ZnO Nanoparticles. *Nano Lett.* **8**, 1649–1653 (2008).

7. Chen, H. *et al.* Avalanche solar blind photodetectors with high responsivity based on MgO/MgZnO heterostructures. *Opt. Mater. Express* **8**, 785 (2018).

8.   Yoo, H. *et al.* High Photosensitive Indium–Gallium–Zinc Oxide Thin-Film Phototransistor with a Selenium Capping Layer for Visible-Light Detection. *ACS Appl. Mater. Interfaces* **12**, 10673–10680 (2020).

9.   Singh, S. *et al.* A study of hydrothermally grown ZnO nanorod-based metal-semiconductor-metal UV detectors on glass substrates. *Nanomater. Nanotechnol.* **7**, 184798041770214 (2017).

10. Nagata, T. *et al.* Schottky metal library for ZNO-based UV photodiode fabricated by the combinatorial ion beam-assisted deposition. *Appl. Surf. Sci.* **252**, 2503–2506 (2006).

11. Lin, T. & Lee, C. Performance investigation of p-i-n ZnO-based thin film homojunction ultraviolet photodetectors. *Appl. Phys. Lett.* **101**, 221118 (2012).

12. Ning, Y., Zhang, Z., Teng, F. & Fang, X. Novel Transparent and Self-Powered UV Photodetector Based on Crossed ZnO Nanofiber Array Homojunction. *Small* **14**, 1703754 (2018).

13. Hasan, M. R. *et al.* Self-powered p-NiO/n-ZnO heterojunction ultraviolet photodetectors fabricated on plastic substrates. *APL Mater.* **3**, 106101 (2015).

14. Zou, Y., Zhang, Y., Hu, Y. & Gu, H. Ultraviolet Detectors Based on Wide Bandgap Semiconductor Nanowire: A Review. *Sensors* **18**, 2072 (2018).

15. Janotti, A. & Van de Walle, C. G. Fundamentals of zinc oxide as a semiconductor. *Reports Prog. Phys.* **72**, 126501 (2009).

16. Jannane, T. *et al.* Self-compensation reduction as first step of p-type ZnO synthesis. *Superlattices Microstruct.* **147**, 106689 (2020).

17. Hanna, B., Manuraj, M., Surendran, K. P. & Unni, K. N. N. Opto-electronic properties of solution-processed zinc oxide thin films: role of solvents and doping. *J. Mater. Sci. Mater. Electron.* **31**, 13570–13577 (2020).

18. Sáaedi, A. *et al.* Optical and electrical properties of p-type Li-doped ZnO nanowires. *Superlattices Microstruct.* **61**, 91–96 (2013).

19. Akcan, D., Gungor, A. & Arda, L. Structural and optical properties of Na-doped ZnO films. *J. Mol. Struct.* **1161**, 299–305 (2018).

20. Moon, T.-H., Jeong, M.-C., Lee, W. & Myoung, J.-M. The fabrication and characterization of ZnO UV detector. *Appl. Surf. Sci.* **240**, 280–285 (2005).

21. Liu, J. L., Xiu, F. X., Mandalapu, L. J. & Yang, Z. P-type ZnO by Sb doping for PN-junction photodetectors. in *Zinc Oxide Materials and Devices* (eds. Hosseini Teherani, F. & Litton, C. W.) **6122**, 61220H (2006).

22. Agarwal, L. & Tripathi, S. High responsivity ZnO-based p–n homojunction UV-photodetector with series Schottky barrier. *Semicond. Sci. Technol.* **35**, 065001 (2020).

23. Yin, B. *et al.* Enhancing performance of ZnO/NiO UV photodetector by piezo-phototronic effect. *RSC Adv.* **6**, 48319–48323 (2016).

24. Mishra, M. *et al.* Surface-Engineered Nanostructure-Based Efficient Nonpolar GaN Ultraviolet Photodetectors. *ACS Omega* **3**, 2304–2311 (2018).

25. Ismail, R. A., Al-Samarai, A.-M. E. & Mohammed, W. M. Preparation of n-ZnO/p-Si

heterojunction photodetector via rapid thermal oxidation technique: effect of oxidation time. *Appl. Phys. A* **124**, 527 (2018).

26. Lien, W.-C. *et al.* Low-Temperature, Ion Beam-Assisted SiC Thin Films With Antireflective ZnO Nanorod Arrays for High-Temperature Photodetection. *IEEE Electron Device Lett.* **32**, 1564–1566 (2011).

27. Jose, J., Ravindran, A. & K Nair, K. A Review on ZnO Heterojunction Photodetector for UV Application. *ICTACT J. Microelectron.* **02**, 305–310 (2017).

28. Shen, Y. *et al.* A self-powered ultraviolet photodetector based on solution-processed p-NiO/n-ZnO nanorod array heterojunction. *RSC Adv.* **5**, 5976–5981 (2015).

29. Flemban, T. H. *et al.* A Photodetector Based on p-Si/n-ZnO Nanotube Heterojunctions with High Ultraviolet Responsivity. *ACS Appl. Mater. Interfaces* **9**, 37120–37127 (2017).

30. Fu, Q.-M. *et al.* Enhanced photoresponse in ZnO nanorod array/p-GaN self-powered ultraviolet photodetectors via coupling with CuO nanostructures. *Mater. Res. Express* **7**, 015063 (2020).

31. Game, O., Singh, U., Kumari, T., Banpurkar, A. & Ogale, S. ZnO(N)–Spiro-MeOTAD hybrid photodiode: an efficient self-powered fast-response UV (visible) photosensor. *Nanoscale* **6**, 503–513 (2014).

32. Hwang, J. D. & Fan, C. W. High-performance organic/inorganic hybrid ultraviolet p-NiO/PVK/n-ZnO heterojunction photodiodes with a poly(N -vinylcarbazole) insertion layer. *J. Mater. Chem. C* **7**, 3529–3534 (2019).

33. Guo, B., Wu, G., Chen, H. & Wang, M. Solution-processed organic/inorganic hybrid photodetector with selective deep UV sensitivity. *Org. Electron.* **29**, 13–21 (2016).

34. Ha, J., Yoon, S., Lee, J. & Chung, D. S. Organic–inorganic hybrid inverted photodiode with planar heterojunction for achieving low dark current and high detectivity. *Nanotechnology* **27**, 095203 (2016).

35. Li, H.-G. *et al.* ZnO/poly(9,9-dihexylfluorene) based inorganic/organic hybrid ultraviolet photodetector. *Appl. Phys. Lett.* **93**, 153309 (2008).

36. Hu, Z. *et al.* Narrowband ultraviolet photodetector based on MgZnO and NPB heterojunction. *Opt. Lett.* **37**, 3072 (2012).

37. Cai, Y. *et al.* High performance ultraviolet photodetectors based on ZnO nanoflakes/PVK heterojunction. *Appl. Phys. Lett.* **109**, 073103 (2016).

38. Ranjith, K. S. & Rajendra Kumar, R. T. Facile construction of vertically aligned ZnO nanorod/PEDOT:PSS hybrid heterojunction-based ultraviolet light sensors: efficient performance and mechanism. *Nanotechnology* **27**, 095304 (2016).

39. Ouyang, B., Zhang, K. & Yang, Y. Self-Powered UV Photodetector Array Based on P3HT/ZnO Nanowire Array Heterojunction. *Adv. Mater. Technol.* **2**, 1700208 (2017).

40. Srivastava, A., Jit, S. & Tripathi, S. High-Performance Pentacene/ZnO UV-Visible Photodetector Using Solution Method. *IEEE Trans. Electron Devices* **68**, 3439–3445 (2021).

41. Chen, L.-C. & Pan, C.-N. Photoresponsivity enhancement of ZnO/Si photodiodes through use of an ultrathin oxide interlayer. *Eur. Phys. J. Appl. Phys.* **44**, 43–46 (2008).

42. Zhang, T. C., Guo, Y., Mei, Z. X., Gu, C. Z. & Du, X. L. Visible-blind ultraviolet photodetector based on double heterojunction of n-ZnO/insulator-MgO∕p-Si. *Appl. Phys. Lett.* **94**, 113508 (2009).

43. Trung, T. Q. *et al.* An Omnidirectionally Stretchable Photodetector Based on Organic–Inorganic Heterojunctions. *ACS Appl. Mater. Interfaces* **9**, 35958–35967 (2017).

44. Kamalasanan, M. N. & Chandra, S. Sol-gel synthesis of ZnO thin films. *Thin Solid Films* **288**, 112–115 (1996).

45. Wang, L. G., Zhu, J. J., Liu, X. L. & Cheng, L. F. Characterization of the Hole Transport and Electrical Properties in the Small-Molecule Organic Semiconductors. *J. Electron. Mater.* **46**, 5546–5552 (2017).

46. Alem, S. *et al.* Solution-processed annealing-free ZnO nanoparticles for stable inverted organic solar cells. *Org. Electron.* **15**, 1035–1042 (2014).

47. Holzwarth, U. & Gibson, N. The Scherrer equation versus the 'Debye-Scherrer equation'. *Nat. Nanotechnol.* **6**, 534–534 (2011).

48. Wang, Z. *et al.* Field Emission Properties of Amorphous NPB Nanostructures. *J. Nanosci. Nanotechnol.* **17**, 3829–3834 (2017).

49. Khan, M. I., Bhatti, K. A., Qindeel, R., Alonizan, N. & Althobaiti, H. S. Characterizations of multilayer ZnO thin films deposited by sol-gel spin coating technique. *Results Phys.* **7**, 651–655 (2017).

50. Kumari, R., Sahai, A. & Goswami, N. Effect of nitrogen doping on structural and optical properties of ZnO nanoparticles. *Prog. Nat. Sci. Mater. Int.* **25**, 300–309 (2015).

51. Senthilkumar, K., Tokunaga, M., Okamoto, H., Senthilkumar, O. & Fujita, Y. Hydrogen related defect complexes in ZnO nanoparticles. *Appl. Phys. Lett.* **97**, 091907 (2010).

52. Ghoreishi, F. S., Ahmadi, V. & Samadpour, M. Synthesis and Characterization of Graphene-ZnO Nanocomposite and its Application in Photovoltaic Cells. *J. nanostructures* **3**, 453–459 (2014).

53. Gadallah, A. & El-Nahass, M. M. Structural, Optical Constants and Photoluminescence of ZnO Thin Films Grown by Sol-Gel Spin Coating. *Adv. Condens. Matter Phys.* **2013**, 1–11 (2013).

54. Xu, L. Enhanced ultraviolet emission from ZnO thin film covered by TiO$_2$ nanoparticles ý. *Chinese Opt. Lett.* **7**, 953–955 (2009).

55. Pathak, T. K., Kumar, V. & Purohit, L. P. High quality nitrogen-doped zinc oxide thin films grown on ITO by sol–gel method. *Phys. E Low-dimensional Syst. Nanostructures* **74**, 551–555 (2015).

56. Raghu, P., Naveen, C. S., Shailaja, J. & Mahesh, H. M. Enhanced optical band-gap of ZnO thin films by sol-gel technique. in *AIP Conference Proceedings* **1728**, 020469 (2016).

57. Kim, Y. & Leem, J.-Y. Effects of Precursor Concentration on Structural and Optical Properties of ZnO Thin Films Grown on Muscovite Mica Substrates by Sol–Gel Spin-Coating. *J. Nanosci. Nanotechnol.* **16**, 5186–5189 (2016).

58. Rai, R. C. Analysis of the Urbach tails in absorption spectra of undoped ZnO thin films. *J. Appl. Phys.* **113**, 153508 (2013).

59. Gong, X. *et al.* High-Detectivity Polymer Photodetectors with Spectral Response from 300 nm to 1450 nm. *Science (80-.).* **325**, 1665–1667 (2009).

60. Javadi, M., Gholami, M., Torbatiyan, H. & Abdi, Y. Hybrid organic/inorganic position-sensitive detectors based on PEDOT:PSS/n-Si. *Appl. Phys. Lett.* **112**, 113302 (2018).

61. Andreani, L. C., Bozzola, A., Kowalczewski, P., Liscidini, M. & Redorici, L. Silicon solar cells: toward the efficiency limits. *Adv. Phys. X* **4**, 1548305 (2019).

Visible-Blind Ultraviolet Photodetectors Based on ZnO Nanorods
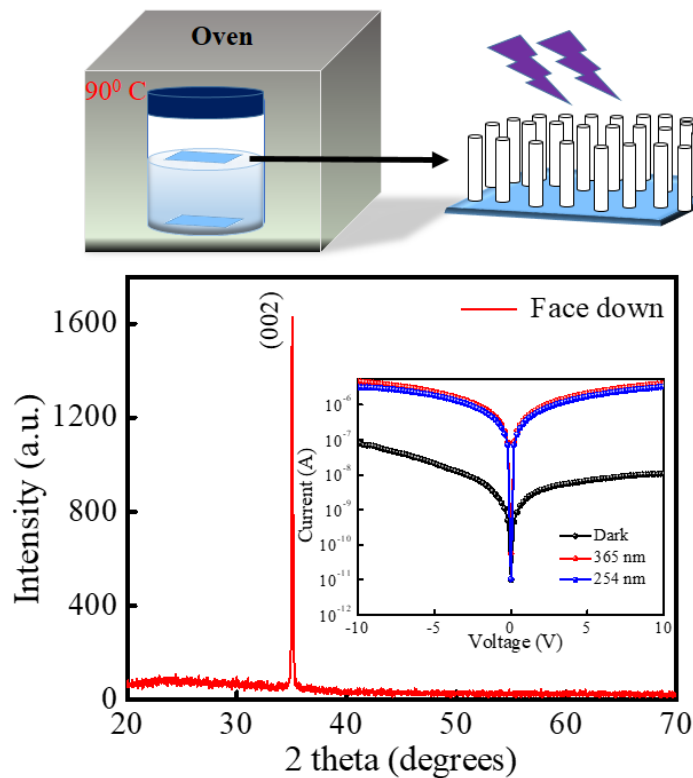
3.1 Abstract

Visible-blind ultraviolet (UV) photodetectors based on zinc oxide (ZnO) nanorods were fabricated on glass substrates in planar photoconductor configuration with Au electrodes. Nanorods of different morphologies were obtained by placing the seed layer coated substrate in the growth solution in face-up or face-down configurations during chemical bath deposition. The structural and morphological properties of ZnO nanorods were studied by X-ray diffraction (XRD) and scanning electron microscopy (SEM). For the face-up sample, the nanorods were randomly oriented, whereas for the face-down sample, they were vertically oriented. Face-down

configuration is seen to be a facile route to synthesize vertically oriented ZnO nanorods. The nanorods were crystallized in hexagonal wurtzite structure in both cases and were preferentially oriented along the c axis in the case of face-down sample. Optical properties were studied by UV-Visible absorption spectroscopy and photoluminescence (PL) spectroscopy. The intensity of defect emission due to surface states was higher than that of the near band edge emission (NBE) in both cases. The defect emission was substantially controlled by forming a homojunction of the nanorods with a thin layer of ZnO nanoparticles as a surface passivation layer deposited by spin coating. Nanorods were grown for different growth durations to study the effect of growth time on the structural and photoresponse properties of the device. The device having face-down ZnO nanorods with the passivation film exhibited the best transient photoresponse at 365 nm and 254 nm UV illumination. The rise and fall times of the face-down ZnO nanorods were improved by depositing the nanorods on the interdigitated ITO coated substrates.

3.2 Introduction

In recent years, visible-blind ultraviolet (UV) photodetectors have been receiving increased attention due to their multifaceted applications in scientific, engineering, medical and civilian areas.[1–4] UV radiation has a very important role in the existence and development of mankind. Due to versatile synthetic methods, low cost, large exciton binding energy and high electron mobility, zinc oxide (ZnO) has been regarded as a promising material for the fabrication of UV photodetectors.[5–7] The optical and electrical properties of ZnO depend on the morphology which, in turn, affects the photodetector performance.[8] UV photodetectors have been reported with different nanostructures of ZnO.[9] One dimensional (1D) ZnO nanostructures such as nanorods, nanowires, nanobelts, nanotubes, etc., have exceptional optoelectronic properties due to their high surface to volume ratio, quantum confinement, good crystallinity and long conduction path.[10–13] Compared to other nanostructured materials, 1D nanomaterials are the favourable materials for the fabrication of UV photodetectors with high sensitivity, quantum

efficiency and fast response speed[14]. The length, diameter and alignment affect the optical and electrical properties of the 1D nanomaterials. Controlled 1D crystal growth can be obtained by several synthesis methods like CVD, PLD, wet synthesis etc.

Guo et al. fabricated visible and UV light alternative photodetectors based on ZnO nanowire/n-Si heterojunction with rectification ratio of 1.6×10^2 at 4 V under UV illumination.[15] Self-powered near UV and visible photodetector based on ZnO nanorods/n-Si heterojunction was fabricated by Huang et al. After annealing at 900 ^{0}C in O_2 atmosphere for 1 h, the device exhibited responsivity of 0.3 A/W.[16] Sb-doped ZnO nanobelt based self-powered UV exhibited photoresponse sensitivity as high as 2200%.[17] Ji et al. fabricated metal-semiconductor-metal (MSM) UV photodetectors based on the selectively grown ZnO nanorod arrays with a responsivity of 41.22 A/W at 5 V under 370 nm light illumination.[18] The high photoresponse property of the device depends on the oxygen adsorption and desorption on the ZnO nanorod surface in the presence of trap states. Self-powered ZnO nanorod/p-Si heterojunction UV photodetectors exhibited fast response and high sensitivity of 8000% under 395 nm light illumination.[19] UV photodetectors based on high quality, well aligned ZnO nanorods by modified chemical bath deposition (CBD) have been fabricated.[20] In this method, air bubbles were added to the growth solution during the CBD process. The device exhibited high sensitivity of 3172.8% and responsivity of 2.28 A/W.

However, ZnO nanorod based UV photodetectors exhibit long response time due to the persistent photoconductivity (PPC) effect, presence of defects or traps and large electrode spacing.[21–23] In 2012, Ji et al. fabricated UV photodetectors based on selectively drawn ZnO nanorods in metal-semiconductor-metal (MSM) configuration with 17 s rise time and 85 s fall time.[24] ZnO nanowire-based flexible photodetectors with single-walled carbon nanotube thin film electrodes showed a recovery time of 16 s for the device with a nanowire density of 100 NW/μm^2.[25] UV detectors based on vertically aligned ZnO nanorod array synthesized by

hydrothermal method exhibited a recovery time of 26.1 s.[26] Lam et al. fabricated UV detectors based on ZnO nanorods with rise and fall times of 62.4 s and 44.9 s, respectively.[27] Shaik et al. fabricated ZnO nanorod-based highly selective UV photodetectors. Due to the possible presence of trap levels within the energy band gap of ZnO nanorods, the device exhibited a long decay time of 22 s and a rise time of 17 s.[28]

Therefore, the main focus has been to develop UV photodetectors with a fast response by passivating the defects in nanorods. Surface modification of ZnO nanorod array is one of the best ways to passivate the defects in the sample and to enhance the optical properties and device performance.[23] Deposition of Al_2O_3 layer on the ZnO nanorod array reduces the intensity of deep level emission due to defects and enhances the intensity of near band edge emission by flat-band effect and the reduction in the density of surface defects or traps.[29,30] Hydrogen plasma treatment can passivate the non-radiative recombination centers and can enhance the near band edge emission. Also, hydrogen ions diffuse into the ZnO lattice and combine with the surface defects and form a shallow donor level in ZnO and improve the conductivity of nanorods.[31] Zhong et al. used C_{60} pyrrolidine to passivate ZnO surface states and they found that it can improve ZnO nanorod/P3HT interface and improve the exciton dissociation.[32] Liu et al. suggest that deposition of a polymer layer such as PMMA on ZnO nanorod array can enhance the near band edge emission due to the reduction in the non-radiative recombination by surface modification.[33] A surface passivation layer of ZnS can also reduce the visible emission by passivating the defects.[34] Laser treatment and hydrogen peroxide treatment can also be used for surface passivation of ZnO nanorods.[35,36] Metal oxide film coatings such as ZnO and TiO_2 coatings on ZnO nanorod array can passivate the defects and traps and enhance the optical and electrical properties.[37,38]

ZnO-based UV photodetectors can be fabricated in photodiode,[39] photoconductor,[40] metal-semiconductor-metal (MSM) photodiode,[41] phototransistor,[42] and avalanche photodiode,[43] configurations. Photoconductor consists of a semiconductor with two ohmic contacts and the

advantages are high internal gain at room temperature and high photoresponsivity.[44,45] When photons of energy greater than the band gap of the material are incident on the photoconductor, electron-hole pairs are generated and these charge carriers are transported through the material under the influence of an applied bias voltage and a photocurrent is produced. The photocurrent increases with the intensity of the incident radiation. Ahn et al. studied the photoresponse properties of ZnO nanorods deposited on Si substrates by sol-gel process.[46] The device exhibited an on-off ratio of 22 and rise and fall times of 3.7 s and 63.6 s respectively. The UV light sensing mechanism in ZnO nanowires were studied by Gao et al. by fabricating ZnO nanowire based photoconductors.[47] The nanowires were deposited by the thermal evaporation of Zn powder. At 5 V the device showed rise and fall times of 8 s and 56 s and on-off ratio of 75. UV photoconductors were fabricated by modifying the surface of ZnO nanowires by coating ZnS by Bera et al.[48] The photocurrent gain of the device was 17 times higher than that of the device with ZnO nanowires without ZnS coating. The rise and fall times were 10 s and 62 s for the device with ZnO nanowires and 229 s and 547 s at 3 V for devices with ZnS coated nanowires. The slow response of the device is due to the surface modification of ZnO nanowires by ZnS. A lateral ZnO nanowire photodetector was prepared on glass substrates in photoconductor configuration using Au contacts by Weng et al.[49] The device exhibited responsivity of 3.1×10^{-2} A/W at 0.5 V and 3.9×10^{-1} A/W and detectivity of 1.9×10^{8} Jones at 2 V under 360 nm light illumination. The device showed slow response with a fall time of 100 s. Chitara et al. fabricated UV photodetectors based on ZnO nanorods in photoconductor configuration with a responsivity of 1.6 A/W at 5 V under 375 nm light illumination and studied the role of defect concentration on the device performance.[50] They found that the defects present in ZnO nanorods have strong influence on the electrical and optical properties. UV photoconductors fabricated based on hydrothermally grown Cu-doped ZnO nanorods exhibited photocurrent gain of 2.8×10^{5}, which is of 2 orders of magnitude higher than the device with undoped sample.[51] High photoconductive

gain is due to the trapping of carriers under dark and detrapping them under illumination by Cu related defects. The device exhibited slow decay with fall time of 118 s and rise time of 2.7 s. Visible-blind UV photodetectors based on Mg doped ZnO nanorods on glass substrates exhibited better performance with on-off ratio of 5.2×10^3 and rise and fall times of 24.5 s and 18.4 s respectively at 1 V.[52] UV photoconductors based on hierarchically structured arrays of network loaded ZnO nanorods showed improved sensitivity of 8000% and responsivity of 2 A/W at 5 V.[53] The device showed rise and fall times of 55 s and 44 s respectively.

ZnO nanostructures can be grown by (i) solid-state synthesis, (ii) vapour phase deposition and (iii) wet-chemical method. Though the first two routes generally give highly aligned nanorod structures, they are relatively more energy-intensive and costly. Hence wet chemical methods, among which chemical bath deposition [54] has gained greater attention due to its low-cost, good scalability, control over the deposition parameters and low deposition temperature.[55,56]

In this work, we report the performance of UV photodetectors based on ZnO nanorod array synthesized by chemical bath deposition method in photoconductor configuration. Two different morphologies of ZnO nanorods were synthesized by placing the face of the substrate in the upward (face-up) and downward (face-down) directions. The structural, electrical and photoresponse properties of ZnO nanorods were studied with various values of growth time such as 5 h, 7 h and 9 h. The response time of the device with face-down nanorods was improved by decorating the nanorods with a thin film of ZnO nanoparticles. The device performance of the face-up ZnO nanorods was improved by fabricating the device on interdigitated ITO coated substrates.

87

3.3 Experimental

3.3.1 ZnO nanorods synthesis

The ZnO seed layer was deposited on glass substrates by spin coating. Zinc acetate dihydrate was dissolved in 2-methoxyethanol and ethanolamine was used as the stabilizing agent. This solution was spin-coated on the substrates and annealed at 170° C for 1 h to get a thickness of 60 nm.[57] The experimental set up for the synthesis of ZnO nanorods is shown in Figure 3.1. The nanorod growth solution was prepared by using zinc nitrate hexahydrate and hexamethylenetetramine (HMTA) as the precursor materials. Zinc nitrate hexahydrate (25 mmol) was dissolved in DI water and HMTA (25 mmol) was dissolved in DI water. Both the solutions were mixed and stirred at room temperature for 30 minutes.[58] The seed layer coated substrates were placed in the growth solution in such a way that the face of the substrate is either in the face-up or in the face-down direction. The whole set up was placed in an oven at 90° C for 5 h. After 5 h, the solution was allowed to cool down to room temperature and the substrates were rinsed with DI water and annealed at 200° C for 2 h. Effect of growth time on morphology and photoresponse properties were studied by varying the growth time to 7 h and 9 h.

3.3.2 Characterization

Optical properties of the different morphologies of ZnO nanorods were studied by using Fluorolog Spectrofluorometer, HORIBA Jobin Yvon and PerkinElmer UV/VIS/NIR Spectrometer, Lambda 950. Surface morphology of the ZnO nanorods before and after ZnO surface passivation layer deposition was investigated by Carl Zeiss scanning electron microscope (SEM) Germany and surface morphology of ZnO seed layer prepared by the sol-gel process was investigated by BRUKER AFM. Crystalline properties were studied using X-ray diffraction (XRD) patterns measured by XPert-PRO Scan Diffractometer with Cu Kα (λ=1.54060 Å) radiation in a scanning range from 20° to 70°.

3.3.3 UV photodetector fabrication

The devices were fabricated in photoconductor configuration. The device structure is shown in Figure 3.2. Device 1 (D1) is the face-up sample and Device 2 (D2) is the face-down sample. In order to improve the device performance, different passivation layers viz. a thin layer of ZnO nanoparticles, TiO_2, Al_2O_3 and nafion were deposited on the ZnO nanorod array. ZnO thin film was prepared, as reported previously, by dissolving 5 wt% synthesized ZnO nanoparticles in chloroform and a stabilizing agent was added to make the solution stable.[59] Then the solution was spin-coated on the ZnO nanorod array and no post-deposition thermal treatment was required. Device 3 (D3) is the face-up sample with ZnO thin film and Device 4 (D4) is the face-down sample with ZnO thin film.

Al_2O_3 film was deposited by atomic layer deposition (ALD) technique. Tri methyl aluminium (TMA) was used as the aluminium precursor, and water was used as the oxidizing agent. Nitrogen was used as the carrier gas. The pulse times of TMA and water were 50 ms and the nitrogen purge time was 10 seconds between the TMA and water pulses. The deposition was done at $200^{\circ}C$. Growth rate of Al_2O_3 films in thermal ALD is 1.2 Angstrom/cycle. To ensure that the precursor molecules have sufficient time to diffuse over the nanoparticle samples, after every precursor pulse, a residence time of 5 seconds was given before purging. Such 9 cycles were applied to form 1 nm of Al_2O_3. Device 5 (D5) is the face-down sample with Al_2O_3 film. 0.15 M TiO_2 solution was prepared by dissolving 55 µl of titanium diisopropoxide bis(acetylacetonate) in 1 ml of isopropyl alcohol. This solution was deposited on face-down ZnO nanorods by spin-coating and dip coating methods and annealed at 125^0 C for 1 h.[59] Device 6 (D6) is the face-down sample with dip-coated TiO_2 film and Device 7 (D7) is the face-down sample with spin-coated TiO_2 film. Device 8 (D8) is the face-down sample with dip-coated nafion film. Nafion film was prepared by dissolving 5 wt% nafion in IPA and dip coated on face-down ZnO nanorods

and annealed at 80 °C for 2 h. Finally, 50 nm Au was thermally evaporated as the electrodes with channel length of 100 µm and channel width of 4 mm.

Face-down ZnO nanorods with ZnO thin film as surface passivation layer exhibited best performance. So, the growth time is changed from 5 h to 7 h and 9 h. Device 9 (D9) is the face-down sample with 7 h growth time, device (10) the face-down sample with 7 h growth time and ZnO film, device 11 (D11) is the face-down sample with 9 h growth time, device (12) the face-down sample with 9 h growth time and ZnO film.

The device performance of the face-up sample was improved by growing ZnO nanorods on seed layer deposited on interdigitated ITO coated glass substrates purchased from Ossilla. Device 13 (D13) is the device with 30 mm channel width and 150 µm channel length.
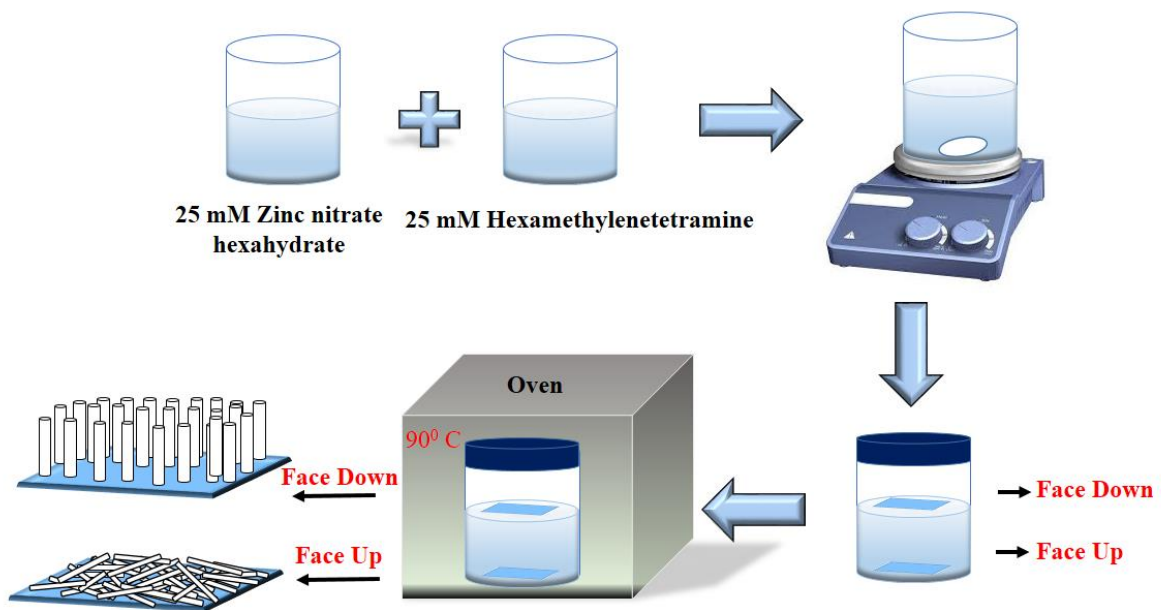
Figure 3.1. Experimental set up for ZnO nanorod synthesis.
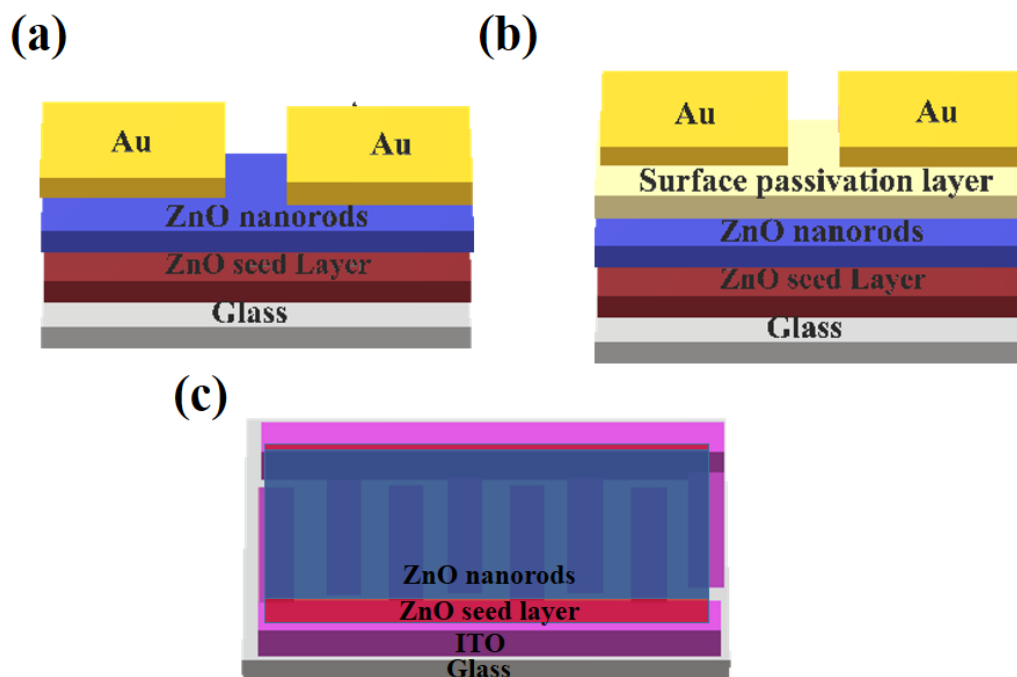
Figure 3.2. (a) Structure of D1, D2, D9, D11 (b) Structure of D3, D4, D5, D6, D7, D8, D10, D12 and (c) Structure of D13.

3.3.4 UV photodetector characterization

The current-voltage characteristics and transient photoresponse of the device were studied with Keithley 2400 source meter and 6 W ENF 260C spectroline UV Lamp with 365 nm and 254 nm wavelengths. The IV characteristics of the devices were measured under 470 nm (LDC470 Blue, 700 mA, 174 lm), 540 nm (LDC540-Green, 700mA, 369 lm) and White light (LDCCW-White, 700 mA, 540 lm) LEDs to study the response of the device under visible light.

3.4 Results and Discussion

3.4.1 Characterization of ZnO nanorods

The atomic force microscopy (AFM) image of the ZnO seed layer deposited on glass substrates by sol-gel process is shown in Figure 3.3a and 3.3b. The wrinkle structure formation in the thin film suggests that, for films synthesized by the sol-gel process, due to the evaporation of the solvent, compressive stress is generated. A volumetric strain is induced in the film due to this compressive stress and leading to the formation of wrinkles.[60] The surface morphology of

ZnO nanorods was imaged using scanning electron microscope (SEM). SEM images of face-up and face-down samples grown at 5 h are shown in Figure 3.3c to 3.3f. The morphology of ZnO nanorods is different for the samples. For face-up samples, the nanorods are randomly oriented with approximately 10 μm length and 1 μm width and for face-down samples the nanorods are vertically oriented. The reason for the difference in morphology is the nucleation mechanism.[61] The homogeneous nucleation mechanism is responsible for the randomly oriented nanorods and the heterogeneous nucleation mechanism is responsible for the preferentially oriented nanorods. The SEM images of nanorods after Al_2O_3, TiO_2, nafion and ZnO nanoparticle film deposition are shown in Figure 3.3g to 3.3l. It is found that the morphology of face-down ZnO nanorods is not affected by ZnO film and Al_2O_3 deposition. Uniform film of nafion and TiO_2 is not formed on the surface. For TiO_2 dip coated sample, a thick layer of TiO_2 is formed on the surface of the face-down sample. Uniform film of ZnO nanoparticles is not formed on face-up sample. SEM images of face-down ZnO nanorods grown at 7 h and 9 h with and without ZnO nanoparticle film are shown in Figure 3.3m to 3.3p. The morphology is changed after ZnO film deposition, i.e, the vertically grown nanorods fall upon the deposition of ZnO nanoparticle film.
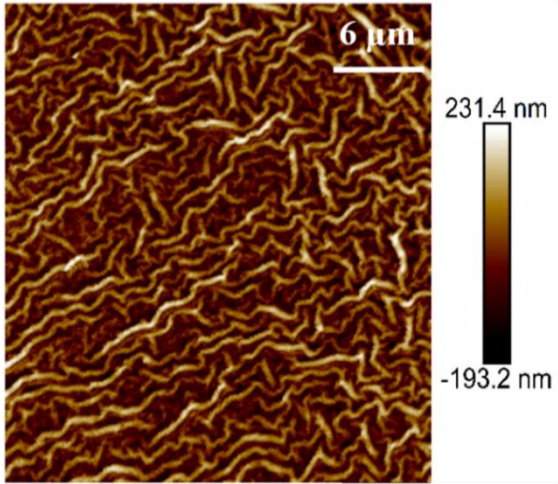
(a) Height
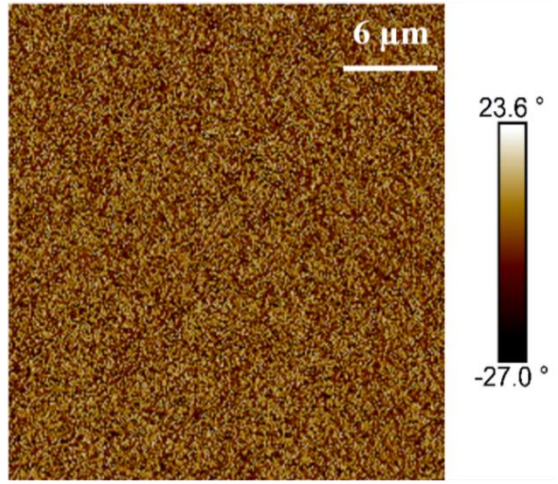
(b) Phase

(c)

(d)

(e)

(f)

(g)

(h)

(i)

(j)

(k)

(l)

(m)

(n)

(o)   **(p)**

200 nm   200 nm
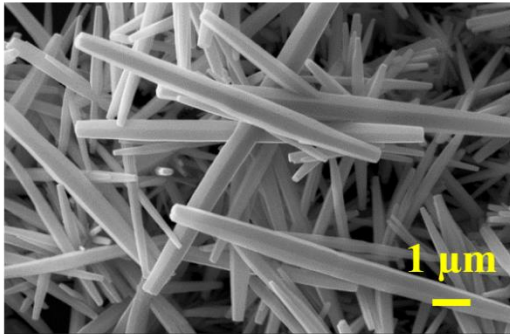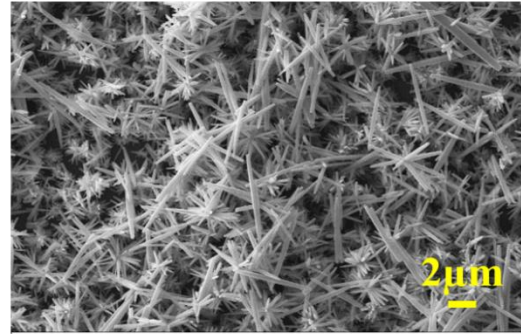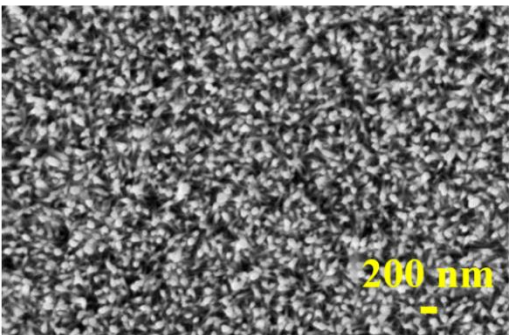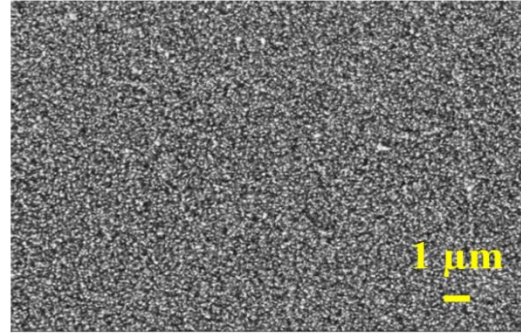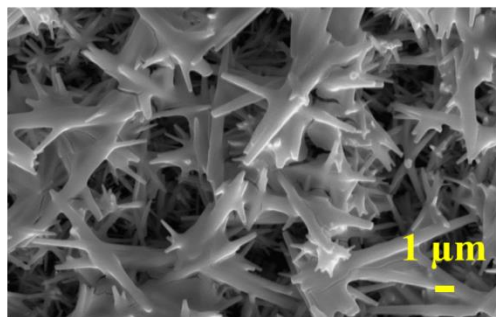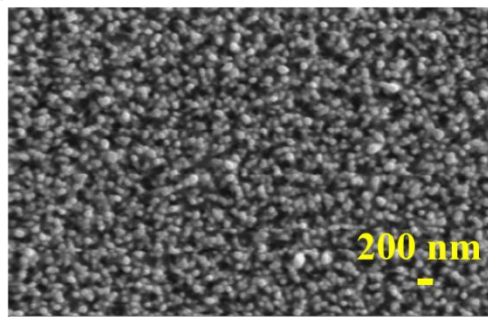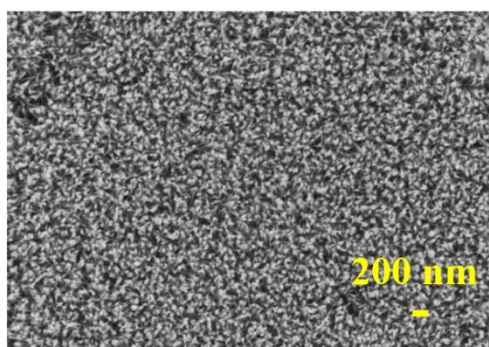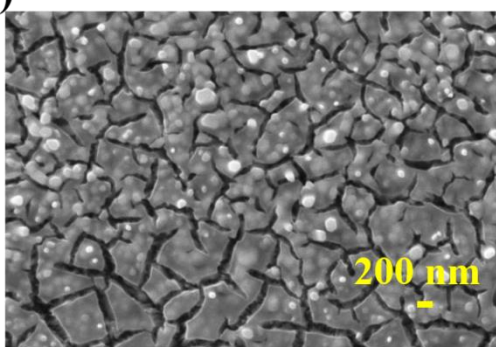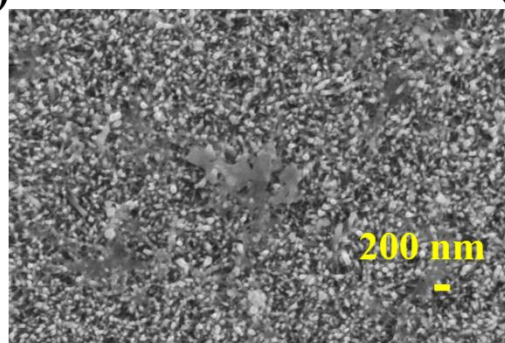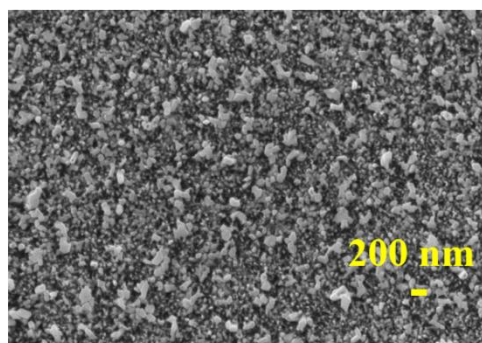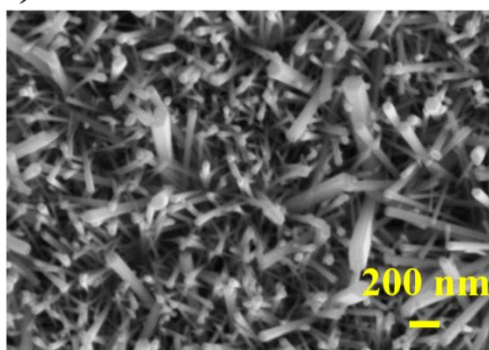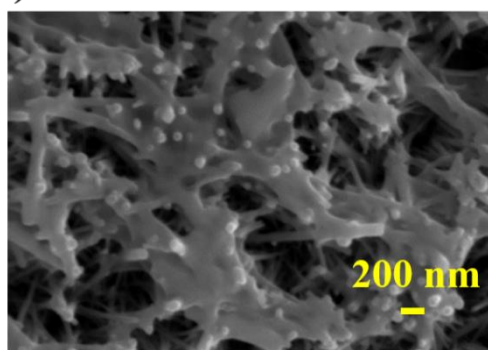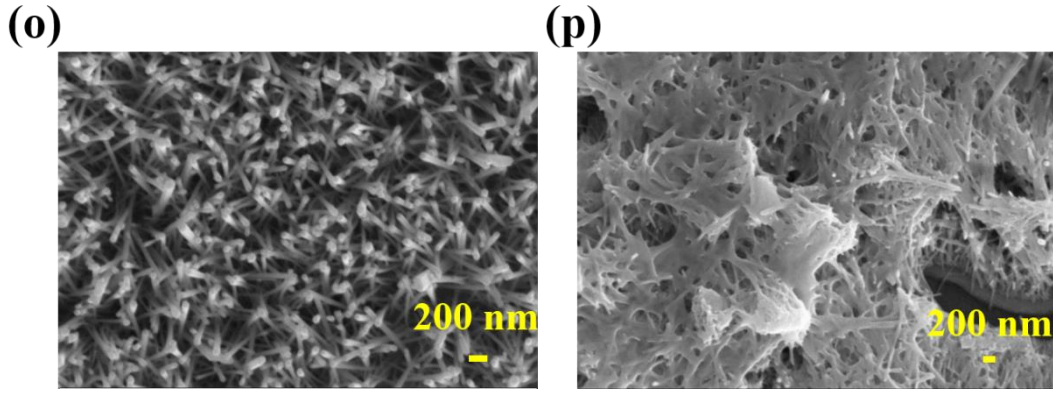
Figure 3.3. (a) and (b) Height and phase AFM images of ZnO seed layer (c),(d) SEM image of face-up ZnO nanorods (e), (f) SEM images of face-down ZnO nanorods (g) SEM image face-up ZnO nanorods with ZnO film (h) SEM image of face-down ZnO nanorods with ZnO film (i) SEM image of face-down ZnO nanorods with Al_2O_3 layer (j) SEM image of face-down ZnO nanorods with TiO_2 dip coated (k) SEM image of face-down ZnO nanorods with TiO_2 spin-coated (l) SEM image of face-down ZnO nanorods with nafion film (m) SEM image of 7 h grown face-down ZnO nanorods (n) SEM image of 7 h grown face-down ZnO nanorods with ZnO film (o) SEM image of 9 h grown face-down ZnO nanorods and (p) SEM image of 9 h grown face-down ZnO nanorods with ZnO film.

The crystalline properties of the nanorods were studied using XRD. XRD patterns of face-up and face-down ZnO nanorods are shown in Figure 3.4. All the XRD peaks were identified in the recorded range of 2θ with the standard card JCPDS 36-1451. The values of FWHM and d-spacing of the peaks are summarized in Table 3.1. From the XRD pattern, it is clear that the ZnO nanorods are crystallized in hexagonal wurtzite structure. It is found that crystallites are randomly oriented in the face-up sample and preferentially oriented along the (002) plane in the face-down sample. It indicates that for a face-down sample, the growth of ZnO nanorods is favoured along the c-axis. The crystallite size, *D,* is calculated for the most intense peak using Scherrer's formula given in Equation 1 and it is found to be 52.2 nm for face-up sample and 142.1 nm for face-down sample.

$$D = \frac{K\lambda}{\beta cos\theta} \qquad\qquad (3.1)$$

where K is Scherrer's constant, λ is the wavelength of X-ray radiation and β is the full width at half maximum intensity (FWHM).[62] The XRD pattern of nanorods is in agreement with SEM results.
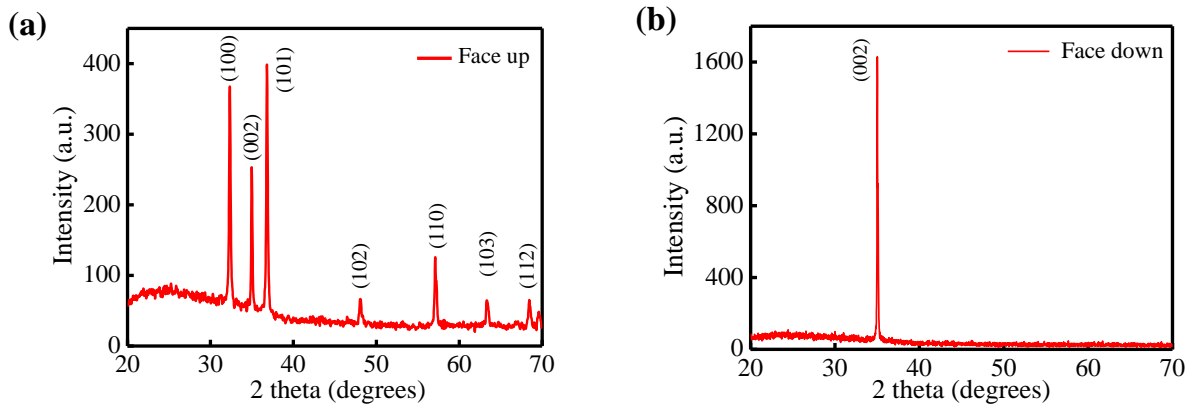
Figure 3.4. (a) XRD pattern of face-up ZnO nanorods (b) XRD pattern of face-down ZnO nanorods.

	2θ (°)	(hkl)	FWHM (°2θ)	d-spacing (Å)	Relative Intensity (%)
Face-up ZnO nanorods	32.2686	(100)	0.1673	2.77196	77.70
	34.9307	(002)	0.0669	2.56656	63.42
	36.7862	(101)	0.1673	2.44125	100.00
	47.9958	(102)	0.2007	1.89401	9.35
	57.0440	(110)	0.1004	1.61320	29.10
	63.2986	(103)	0.2676	1.46802	10.16
	68.4701	(112)	0.3264	1.36920	9.23
Face-down ZnO nanorods	35.0128	(002)	0.0612	2.56073	100.00

Table 3.1. Results of XRD measurements of face-up and face-down samples.

Optical properties of different morphologies of ZnO nanorods were investigated using UV-Visible absorption spectroscopy and photoluminescence (PL) spectroscopy. Absorption spectra of face-up and face-down samples grown for 5 h are shown in Figure 3.5a. From the graph, it is evident that the absorbance of the face-up sample is higher than that of the face-down sample. This is because the needle-like morphology makes the absorption cross-section smaller. This indicates that the face-down sample is more transparent than that of the face-up sample. Therefore, face-down sample is suitable for most optoelectronic applications like transparent photovoltaic cells and photodetectors, which require transparent conductors. From Tauc's plot using Equation 3.2, the energy band gap can be calculated.

$$\alpha h v = A\left(h v - E_g\right)^n \qquad (3.2)$$

wvere α is absorption coefficient, A is the proportionality constant, hv is the incident energy and E_g is the band gap of the material.[63] The value of n is assumed to be ½ since ZnO is reported to be a direct band gap semiconductor.[64] The values of the band gap of face-up and face-down samples are found to be 3.05 eV and 3.27 eV, respectively.
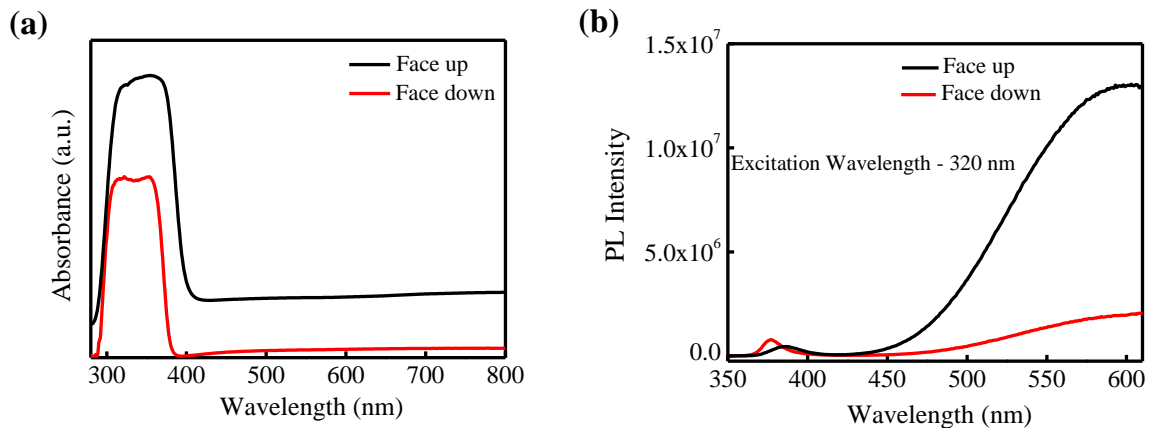
Figure 3.5. (a) Absorption spectra of face-up and face-down ZnO nanorods (b) PL spectra of face-up and face-down ZnO nanorods.

PL spectra of face-up and face-down ZnO nanorods are shown in Figure 3.5b. There are two emission peaks in the spectrum. The one observed near 380 nm is due to the near band edge emission. The other broad emission peak in the visible region is due to defect emission [65] originating from oxygen vacancies, zinc interstitials or zinc antisites (Zn ion located at the O site). The dangling bonds or unsaturated bonds present in the surface of the ZnO nanorods attract other chemical species such as OH, O_2, H_2O etc. and change the chemical stoichiometry. This will induce surface states on the ZnO nanorods. These surface states, in turn, affect the emission spectrum.[38] From the PL spectra, it is clear that the defect states present in the face-up sample is higher than that of face-down sample. However, this may be due to the increased absorption cross-section in the case of face-up samples. Using materials such as Al_2O_3, TiO_2, Polymers, etc. for surface passivation can suppress the defects and traps. Here we used a thin layer of TiO_2, Al_2O_3, nafion and ZnO nanoparticles to passivate the defects in ZnO nanorods. Absorption and PL spectra of face-down ZnO nanorods after the deposition of Al_2O_3, TiO_2, nafion and ZnO thin film are shown in Figure 3.6a and 3.6b. UV absorption of face-down ZnO nanorods increased upon the deposition of ZnO nanoparticle film. But UV absorption is reduced upon the deposition of Al_2O_3, TiO_2 and nafion films. This may be due to the reduced exposure of ZnO nanorods after the passivation with Al_2O_3, TiO_2 and nafion films. With Al_2O_3 deposition by ALD, ZnO nanoparticle film deposition by spin coating and TiO_2 film deposition by dip coating, near band edge emission is enhanced and defect emission is suppressed. Al_2O_3-deposited samples exhibited maximum intensity of near band edge emission and minimum intensity of defect emission. With TiO_2 and nafion deposition, intensities of both near band edge emission and defect emission are enhanced. Using heterogeneous materials such as Al_2O_3, TiO_2 and nafion for surface passivation can suppress the defects and traps but, the nanostructure or surface morphology of ZnO prevents the formation of conformal coatings. The lattice mismatch between

the nanorods and the surface passivating layer may lead to stress. So, ZnO thin film deposition seems to be the most suitable choice for surface passivation in ZnO nanorods.

Figures 3.7a and 3.7b show the absorption and PL spectra of face-up and face-down ZnO nanorods with ZnO thin film. It is found that after ZnO film deposition, the intensity of visible emission is suppressed and UV emission is enhanced in both cases. It is already reported that the deposition of ZnO thin film releases the physisorbed chemical species and improves the chemical stoichiometry of ZnO nanorods which, in turn, reduces the surface defects or surface states and enhances the optical and electrical properties of ZnO nanorods.[66]
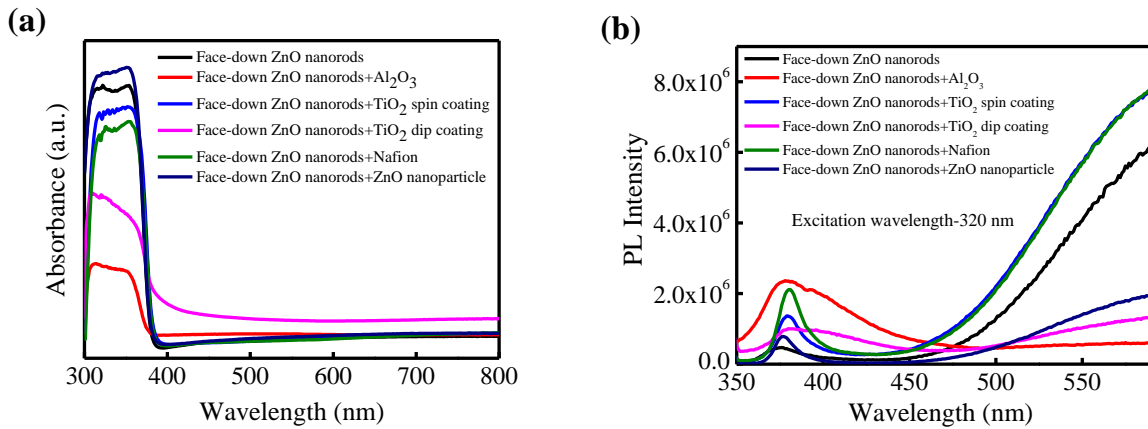
Figure 3.6. Absorption spectra of face-down ZnO nanorods with Al_2O_3, TiO_2, nafion and ZnO nanoparticle film (b) PL spectra of face-down ZnO nanorods with Al_2O_3, TiO_2, nafion and ZnO nanoparticle film.
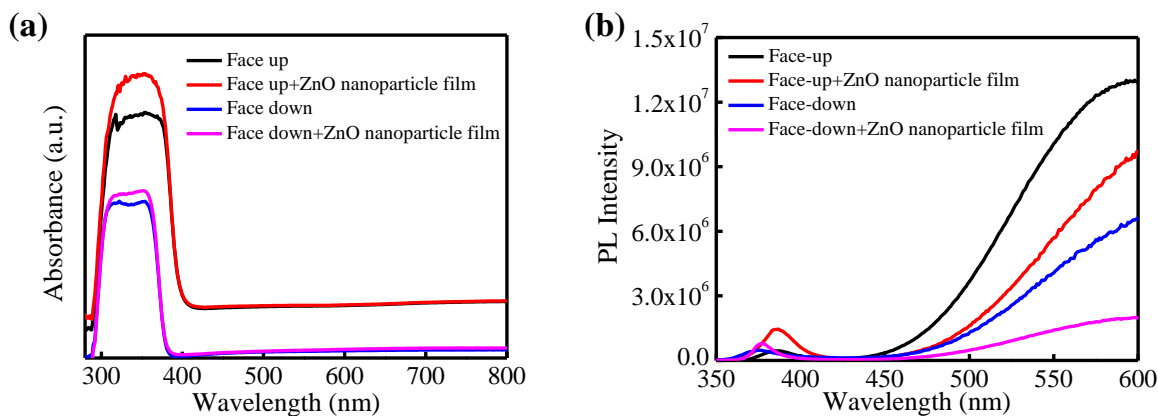
Figure 3.7. (a) Absorption spectra of face-up and face-down ZnO nanorods before and after ZnO nanoparticle film deposition (b) PL spectra of face-up and face-down ZnO nanorods before and after ZnO nanoparticle film deposition.

Figure 3.8a and 3.8b show the absorption and PL spectra of face-down ZnO nanorods grown at different growth times with and without ZnO film. It is found that 5 h grown face-down ZnO nanorods with ZnO film exhibited maximum absorbance. The decrease in absorbance of the 7 h and 9 h samples may be due to the reduced crystallinity or reduced absorption cross section. A reduction in band gap with increasing growth time has been reported for ZnO nanorods.[67] The intensity of defect emission increases with the increase in the growth time due to the increase in the surface defects and trap states. For the 5 h sample, the intensity of near band edge emission increases with ZnO nanoparticle film. This is matching with the observation of increased absorption (with ZnO nanoparticle film) in UV for the same sample. The defect emission also increases with ZnO nanoparticle film deposition except for the 5 h sample. But this effect becomes much weaker for a 9 h sample.
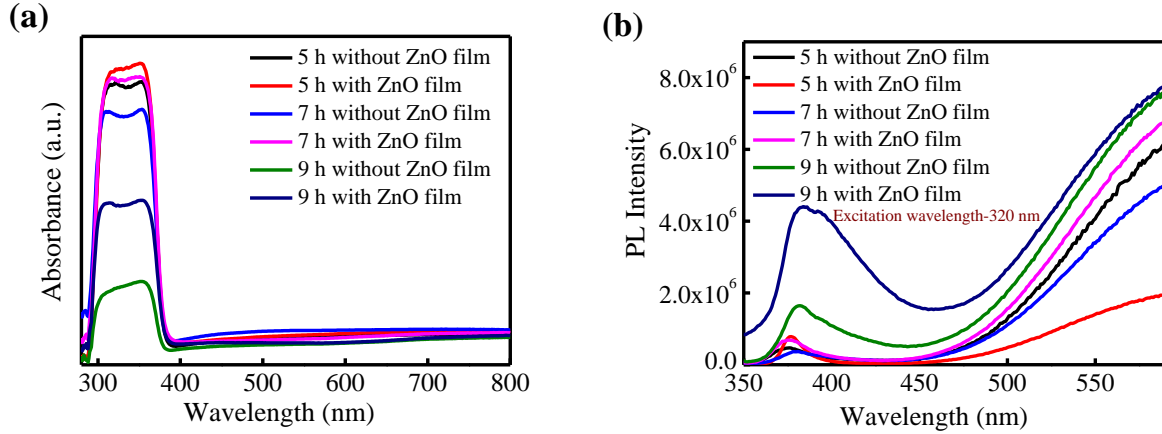
Figure 3.8. (a) Absorption spectra of face-down ZnO nanorods grown at different times with and without ZnO nanoparticle film (b) PL spectra of face-down ZnO nanorods grown at different times with and without ZnO nanoparticle film.

3.4.2 Characterization of device

The devices were fabricated in photoconductor configuration. The device structure is shown in Figure 3.2. IV characteristics and transient photoresponse of the devices from D1 to D8 under dark, 365 nm and 254 nm light illumination from front (device) side at an intensity of 1.24 mW/cm^2 and 2.4 mW/cm^2 respectively were measured. The values of device parameters are summarized in Table 3.2. It is found that in the case of devices without surface passivation layer, D2 exhibits better performance compared to D1 due to the higher crystalline quality and lesser defect states in the face-down sample. The value of photocurrent of D2 is higher than that of D1 due to the preferential vertical growth orientation of ZnO nanorods upon UV illumination. Films of Al$_2$O$_3$, TiO$_2$, nafion and ZnO nanoparticles were used as surface passivation layers to further improve the device performance of D2. The devices D2, D4, D5 and D8 exhibited on-off ratio of 10^2 and the on-off ratio of D6 and D7 were less than that of D2 under 365 nm light illumination. The on-off ratio of D2 under 254 nm light illumination is 48.70 and the devices D4 and D8 exhibited an on-off ratio of 10^2.

The oxygen molecules from the atmosphere get adsorbed on the surface of the ZnO nanorods under dark conditions. Then these oxygen molecules get ionized by trapping free

101

electrons from the conduction band of ZnO nanorods. This creates a depletion layer on the surface and decreases the conductivity of ZnO nanorods. Electron-hole pairs are generated upon UV illumination and the ionized oxygen molecule combines with the photogenerated hole and desorbs from the surface of the ZnO nanorods by releasing the trapped electron back to the conduction band of ZnO, which enhances the photoconductivity and increases the photocurrent of the device.[68] The reaction mechanism as proposed in [69] is shown below,

Under dark conditions

$$O_{2(g)} + e^- \longrightarrow O_{2(ad)}{}^-$$

Upon UV illumination,

$$h\nu \longrightarrow e^- + h^+$$

$$O_{2(ad)}{}^- + h^+ \longrightarrow O_{2(g)}$$
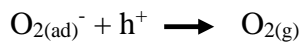
Transient photoresponse of the devices was measured at 1 V under 365 nm and 254 nm light illumination. The rise time and fall time of the devices were calculated from the transient photoresponse curves and the values are summarized in Table 3.2. The devices D1 and D2 exhibited long response times due to the surface defects and traps on the surface. The time taken for the desorption of oxygen molecules is higher than that of the adsorption of oxygen molecules due to the persistent photoconductivity (PPC) effect.[70] So, the devices exhibit longer fall times. The effect of UV light on ZnO nanostructures is more complex and a steady increase in electrical conductivity is induced, which lasts for a longer period of time after UV exposure. There are two assumptions for PPC in ZnO.[70] One is that the origin of the PPC effect is due to the presence of surface defects located between shallow and deep energy levels. These surface defects form a metastable charge state. The oxygen vacancies in the sample can be excited to this metastable state. In the metastable state, there is a thermally activated barrier to prevent the recapture of electrons. The other theory is that PPC is a surface effect and the surface charges produce a built-

in potential on the surface of ZnO nanorods.[70] Upon UV illumination, the electron-hole pairs are separated by this built-in potential and cause the hole to accumulate at the surface. When the UV light is switched off, the accumulated charges are not immediately drained off as recombination centers are not available, and as a result, the PPC effect takes place. The PPC effect can be overcome by surface passivation.

For D4, the rise and fall times are less than that of D2 due to surface passivation of defects and surface states. After ZnO film deposition, the rise time of D4 is reduced from 12.50 s to 10.42 s and fall time is reduced from 14.06 s to 11.98 s under 365 nm light illumination and rise time is reduced from 16.45 s to 12.50 s and fall time is reduced from 24.67 s to 16.45 s under 254 nm light illumination. D5 takes too long to decay the photocurrent compared to all other devices. Al_2O_3 is a good surface passivation layer but, due to its insulating property carrier transport properties are affected and leads to longer rise and fall times. D6 exhibited very fast response with lower values of rise and fall times compared to all other devices under both 365 nm and 254 nm light illumination. For D7 the rise times under 365 nm and 254 nm light illumination were less than 10 s but fall times were higher than D2. The fall times of D8 is also higher than that of D2. This may be because for both TiO_2 spin-coated and nafion coated face-down ZnO nanorods the intensity of both near band edge emission and defect emission is higher than that of ZnO nanorods alone. So TiO_2 thin layer and nafion are not suitable choices for surface passivation.

Since, D4 exhibited better performance, ZnO nanoparticle film was used to passivate the defects in face-up ZnO nanorods. D3 exhibited better performance than D1. The photocurrent increased after the ZnO film deposition under both 365 nm and 254 nm light illumination. But for D3, fall time is less than that of D1 and rise time is higher than that of D1. This is due to the non-uniform size and random orientation of ZnO nanorods and the passivation layer being not uniformly coated on the surface of ZnO nanorods.

Responsivity (R) and Detectivity (D) values were calculated and are summarized in Table 3.2. D2 exhibited better performance with R and D values higher than that of D1 due to its preferential growth and less defects. D4 and D5 showed higher R and D values compared to D2 and D3 showed better performance than D1. It is found that D of D6 and D7 is less than that of D2 under 365 nm and 254 nm light illumination. D8 showed better performance with highest value of R and D. When comparing all the parameters such as on-off ratio, rise time, fall time, R and D under 365 nm and 254 nm light illumination, D4 exhibited better performance. So, ZnO nanoparticle film is the best choice for the fabrication of fast response UV photodetectors. IV characteristics of the devices D1, D2, D3 and D4 under dark, 365 nm and 254 nm light illumination from front (device) side is shown in Figure 3.9. To further know the response of devices in the visible region, IV characteristics of the devices were measured under 470 nm, 540 nm and white light LEDs. IV characteristics are shown in Figure 3.10. It is evident that the devices are indeed visible-blind, which is an attractive pre-requisite for a UV detector.

Device	On-off ratio	Rise time (s)	Fall time (s)	Responsivity (mA/W)	Detectivity (Jones)
365 nm					
D1-Face-up ZnO nanorod	34.28	14.67	33.77	2.64	1.48×10^{10}
D2-Face-down ZnO nanorod	2.35×10^{2}	12.50	14.06	7.92	6.83×10^{10}
D3-Face-up ZnO nanorod+ZnO film	1.05×10^{2}	19.30	30.16	119.46	2.00×10^{11}
D4-Face-down ZnO nanorod +ZnO film	2.13×10^{2}	10.42	11.98	88.48	2.17×10^{11}
D5- Face-down ZnO nanorod+Al_2O_3	3.34×10^{2}	22.40	180.94	141.70	3.45×10^{11}
D6- Face-down ZnO nanorod+TiO_2 dip coated	28.20	8.31	4.84	1.10	8.70×10^{9}
D7- Face-down ZnO nanorod+TiO_2 spin-coated	59.46	5.37	27.38	20.40	5.48×10^{10}
D8- Face-down ZnO nanorod+Nafion	1.39×10^{2}	15.48	30.97	2040	8.46×10^{16}
254 nm					
D1-Face-up ZnO nanorod	8.58	20.15	66.22	0.31	1.70×10^{9}
D2-Face-down ZnO nanorod	48.70	16.45	24.67	0.83	7.20×10^{9}
D3-Face-up ZnO nanorod+ZnO film	60.34	19.96	46.78	35.01	5.86×10^{10}
D4-Face-down ZnO nanorod +ZnO film	1.72×10^{2}	12.50	16.15	36.88	9.07×10^{10}
D5- Face-down ZnO nanorod+Al_2O_3	52.05	21.19	116.55	11.20	2.72×10^{10}
D6- Face-down ZnO nanorod+TiO_2 dip coated	12.66	10.32	5.97	0.24	1.92×10^{9}
D7- Face-down ZnO nanorod+TiO_2 spin-coated	74.01	8.80	32.27	13.10	3.53×10^{10}
D8- Face-down ZnO nanorod+Nafion	1.74×10^{2}	13.85	30.15	1320	5.46×10^{16}

Table 3.2. Performance parameters of D1 to D8

Transient photoresponse of the devices under 365 nm and 254 nm light illumination at 1 V is shown in Figure 3.11. Then we measured the transient photoresponse at different bias voltages and found that photocurrent increases with an increase in the bias voltage. Transient photoresponse of the devices at 1 V, 3 V and 5 V under 365 nm and 254 nm light illumination are shown in Figure 3.12. From the IV characteristics and transient photoresponse, it is evident that D4 exhibited better performance.
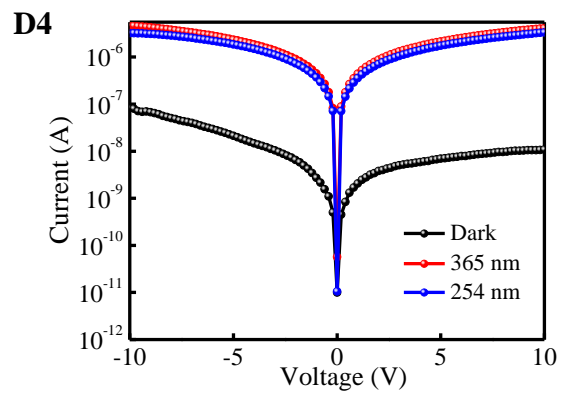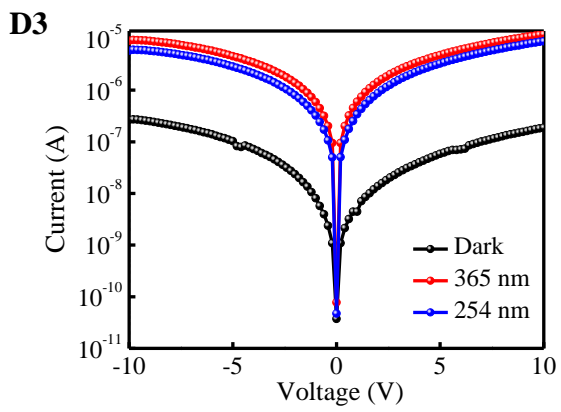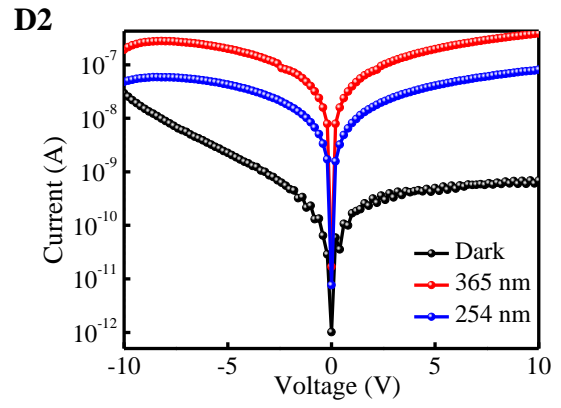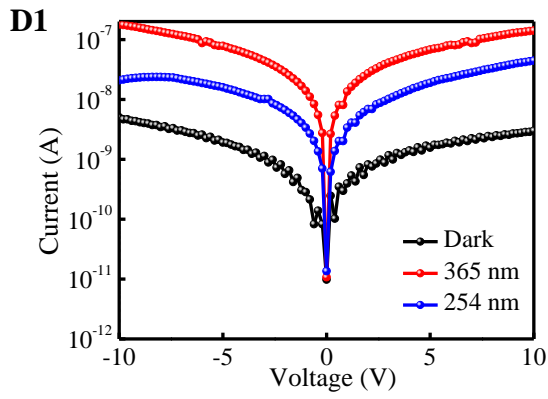
Figure 3.9. IV characteristics of the devices D1, D2, D3, D4 under dark, 365 nm and 254 nm light illumination.
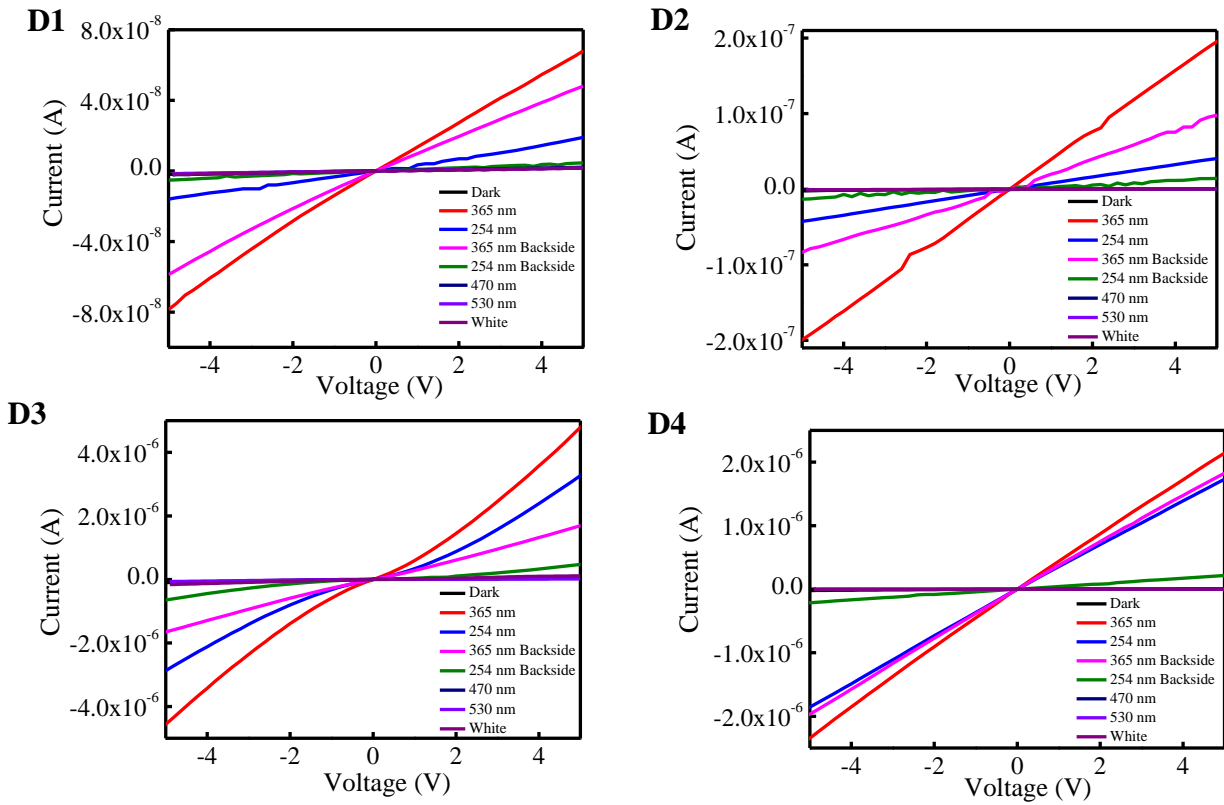
Figure 3.10. IV characteristics of the devices D1, D2, D3, D4 under dark, 365 nm, 254 nm, 470 nm, 540 nm and white light illumination.
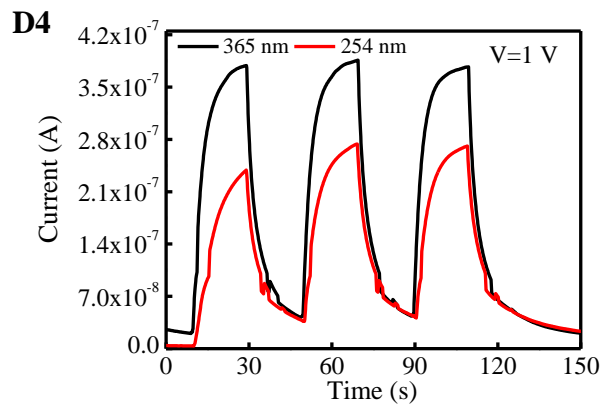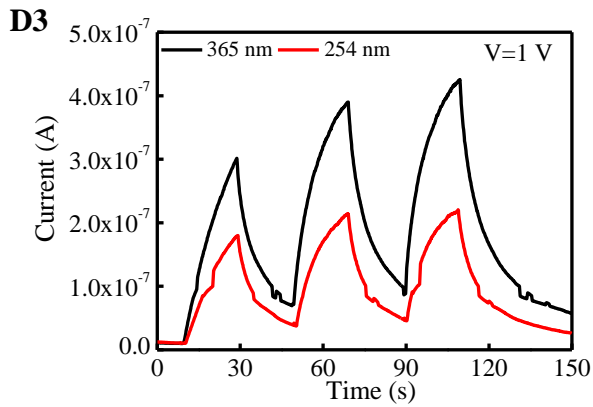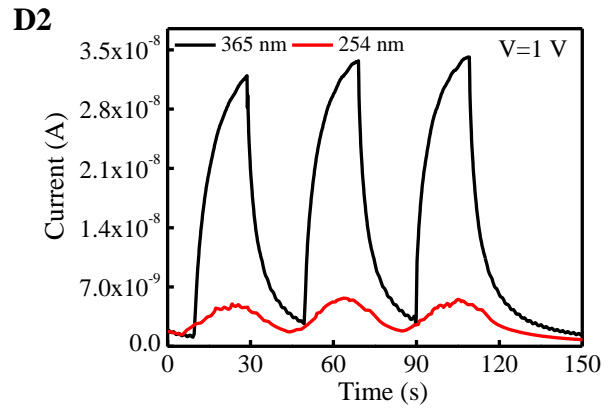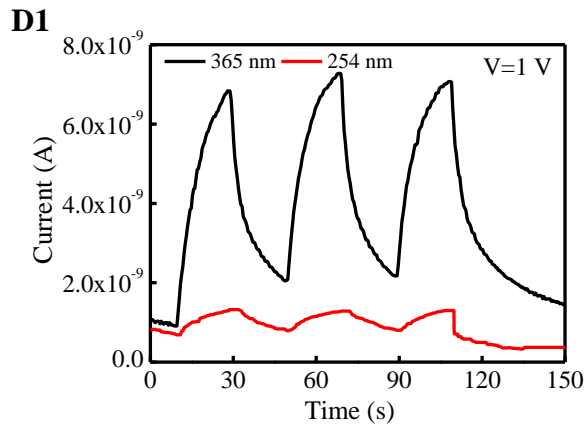
Figure 3.11. Transient photoresponse of the devices D1, D2, D3, D4 under 365 nm and 254 nm light illumination.
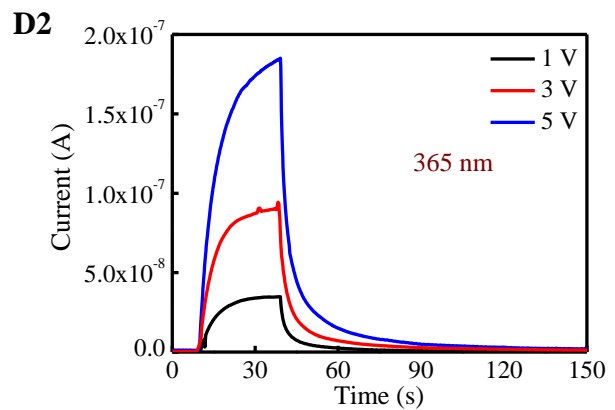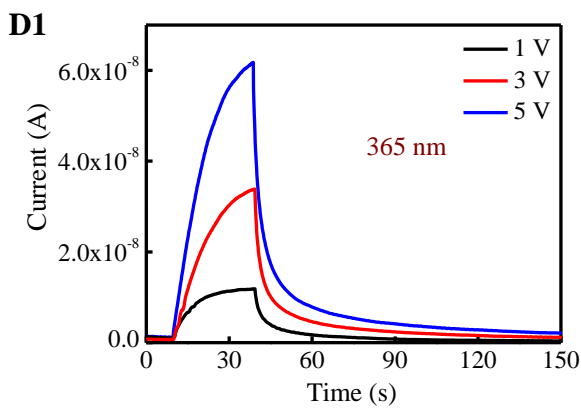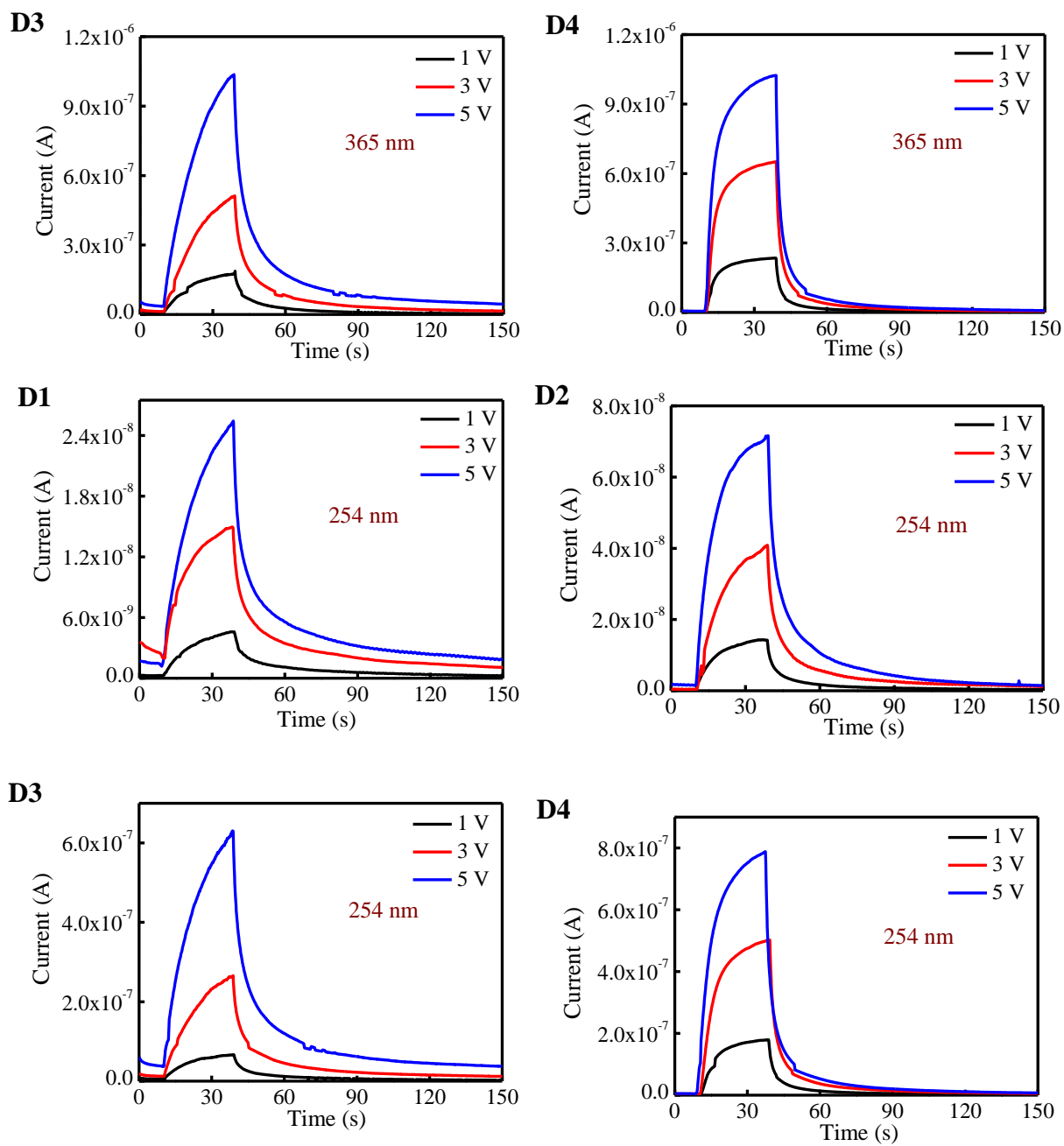
Figure 3.12. Transient photoresponse of the devices D1, D2, D3, D4 under 365 nm and 254 nm light illumination at different bias voltages.

To study the effect of time on the morphology, optical and photoresponse properties of face-down ZnO nanorods the growth time is increased from 5 h to 7 h and 9 h. Since face-down sample with ZnO nanoparticle film exhibited better performance, devices with 7 h grown ZnO nanorods with and without ZnO film (D9 and D10) and 9 h grown nanorods with and without ZnO film (D11 and D12) were fabricated. IV characteristics and transient photoresponse of the devices under 365 nm and 254 nm light illumination were measured and the results are summarized in Table 3.3. IV characteristics are shown in Figure 3.13 and transient photoresponse at 1 V is shown in Figure 3.14. On-off ratio of D10 is higher than that of D9 and D12 is higher than that of D11 under 365 nm and 254 nm light illumination due to the surface passivation effect. In all cases, the rise and fall times were reduced upon ZnO film deposition. R and D of D10 are higher than those of D9. The R and D values are increasing with growth time from 5 h to 7 h. After that, the density of defect states is increasing and R and D values are reduced. The lengths of the nanorods are increasing with growth time and after the deposition of ZnO nanoparticle film the morphology of the face-down samples are changing. It will affect the device performance. For 5 h grown samples the morphology is not affected by the ZnO nanoparticle film deposition. So, D4 exhibited fast response with better UV detecting performance.
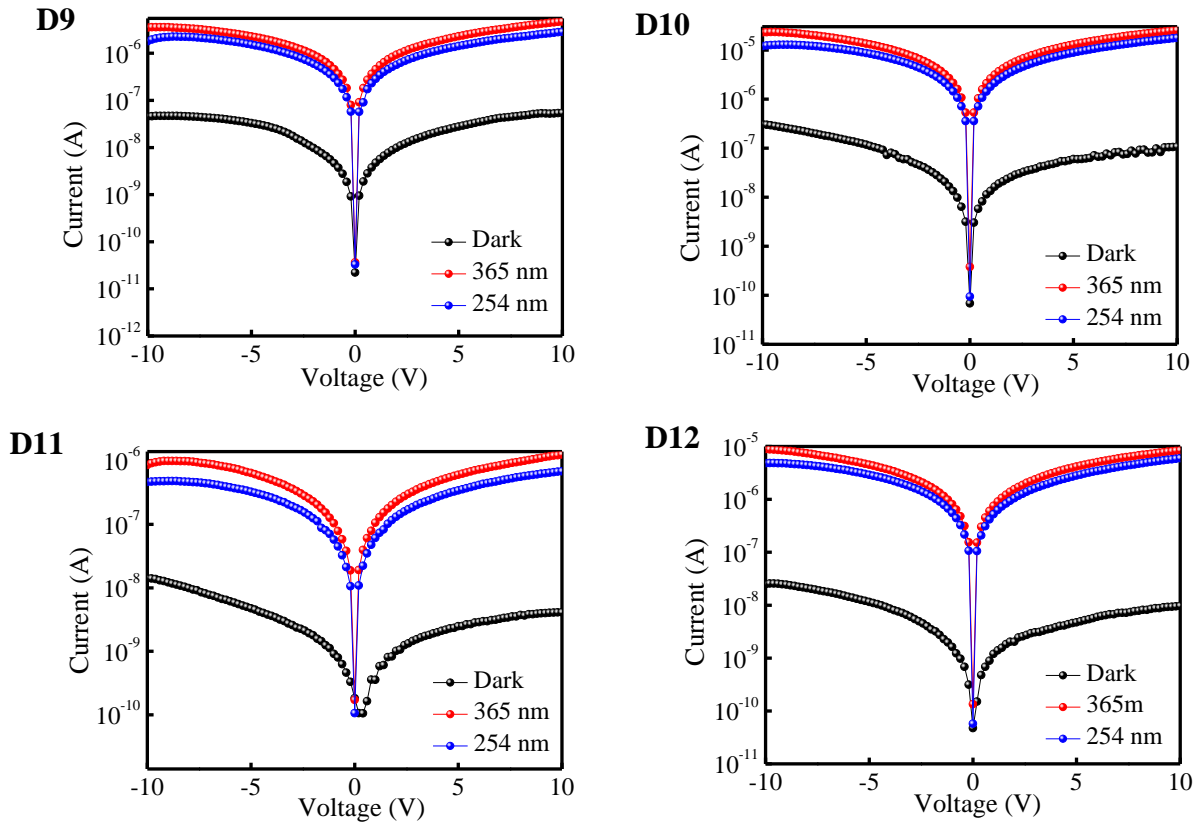
Figure 3.13. IV characteristics of D9, D10, D11 and D12 under dark, 365 nm and 254 nm light illumination.
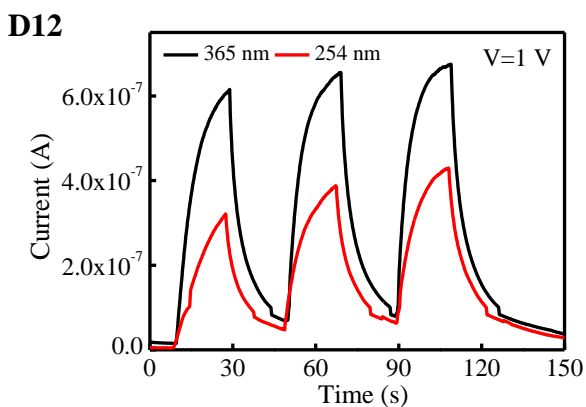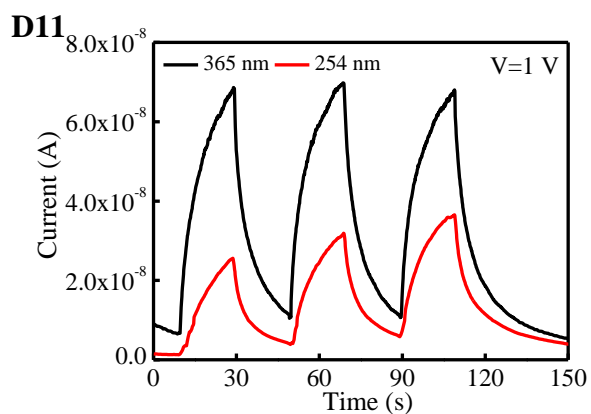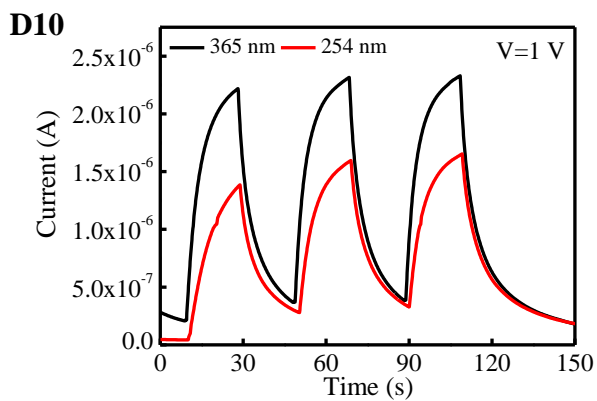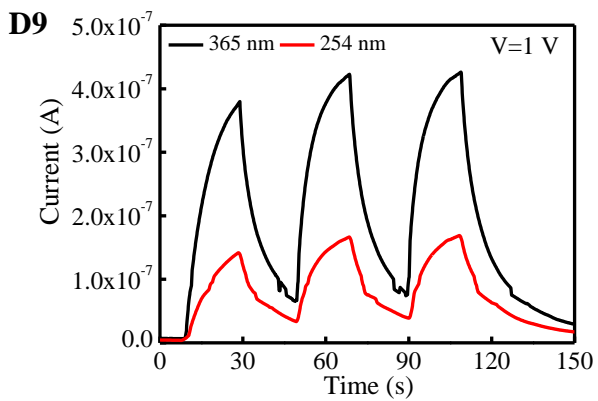
Figure 3.14. Transient photoresponse of D9, D10, D11 and D12 365 nm and 254 nm light illumination at 1 V.

Device	On-off ratio	Rise time (s)	Fall time (s)	Responsivity (mA/W)	Detectivity (Jones)
365 nm					
D2- Face-down ZnO nanorod, 5 h	2.35×10^2	12.50	14.06	7.92	6.83×10^{10}
D4- Face-down ZnO nanorod+ZnO film, 5 h	2.13×10^2	10.42	11.98	88.48	2.17×10^{11}
D9-Face-down ZnO nanorod, 7 h	96.68	20.04	49.41	91.43	1.48×10^{11}
D10-Face-down ZnO nanorod+ZnO film, 7 h	1.95×10^2	15.90	27.97	528.02	5.08×10^{11}
D11-Face-down ZnO nanorod, 9 h	2.97×10^2	20.15	23.85	21.28	1.26×10^{11}
D12-Face-down ZnO nanorod+ZnO film, 9 h	6.32×10^2	16.45	13.71	152.56	4.92×10^{11}
254 nm					
D2- Face-down ZnO nanorod, 5 h	48.70	16.45	24.67	0.83	7.20×10^9
D4- Face-down ZnO nanorod+ZnO film, 5 h	1.72×10^2	12.50	16.15	36.88	9.07×10^{10}
D9-Face-down ZnO nanorod, 7 h	60.71	15.08	86.65	29.48	4.78×10^{10}
D10-Face-down ZnO nanorod+ZnO film, 7 h	1.32×10^2	12.61	32.57	184.65	1.77×10^{11}
D11-Face-down ZnO nanorod, 9 h	1.70×10^2	21.39	37.84	6.31	3.73×10^{10}
D12-Face-down ZnO nanorod+ZnO film, 9 h	4.35×10^2	17.72	16.16	54.21	1.75×10^{11}

Table 3.3. Performance parameters of D9 to D12. Data for D2 and D4 are again given here for comparison.

To further improve the device performance of face-up samples, the face-up ZnO nanorods grown at 5 h are deposited on interdigitated ITO coated substrates. D13 was fabricated with channel width and length 30 mm and 150 μm respectively. IV characteristics and transient photoresponse were measured under 365 nm and 254 nm light illumination and the results are summarized in Table 3.4. IV characteristics and transient photoresponse measured at 1 V are shown in Figure 3.15a and 3.15b. The device exhibited an on-off ratio of 1.50×10^3 and 1.25×10^3 under 365 nm and 254 nm light illumination respectively. The device exhibited fast photodetection performance with rise and fall times of 1.88 s and 6.39 s under 365 nm light

illumination and 1.69 s and 8.91 s under 254 nm light illumination. The device exhibited detectivity of 4.20×10^{11} Jones and LDR of 62.01 dB at 1 V under 365 nm. The better performance of these devices may be due to the ITO film which gives a uniform contact to the all rods compared to a thermally evaporated top contact. This is evident from the higher photocurrent which is 2 orders higher for 365 nm and 3 orders higher for 254 nm compared to the respective performances of D1.
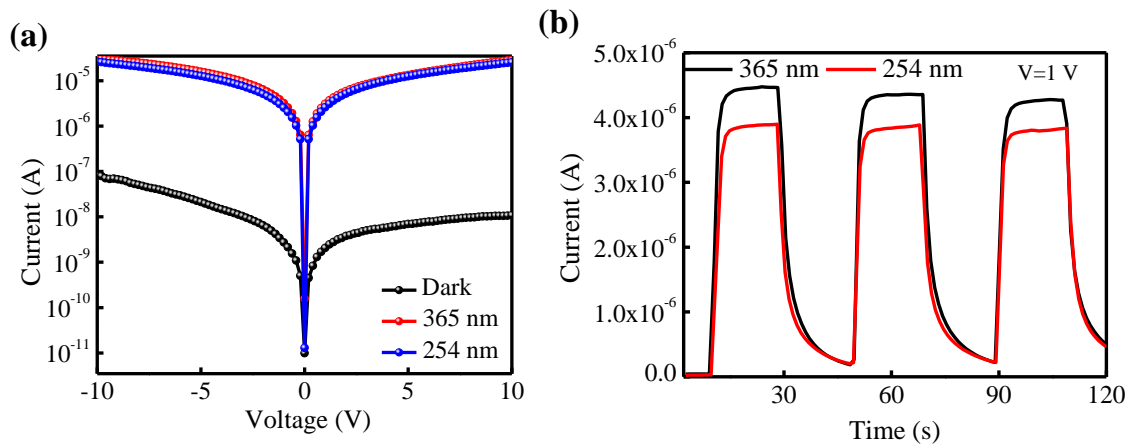
Figure 3.15. (a) IV characteristics of D13 under dark, 365 nm and 254 nm illumination (b) Transient photoresponse of D13 at 1 V under 365 nm and 254 nm illumination.

Device	On-off ratio	Rise time (s)	Fall time (s)	Responsivity (mA/W)	Detectivity (Jones)
365 nm					
D13	1.50×10^3	1.88	6.39	55.60	4.20×10^{11}
254 nm					
D13	1.25×10^3	1.69	8.91	23.90	1.81×10^{11}

Table 3.4. Performance parameters of D13.

3.5 Conclusions

Vertically and randomly oriented ZnO nanorods were synthesized and characterized. Face-down configuration yields ZnO nanorods preferentially oriented along the (002) direction. The surface states present in the samples were passivated by coating thin layers of Al_2O_3, TiO_2, nafion and ZnO nanoparticle film. The devices were fabricated in photoconductor configuration using ZnO nanorods with and without passivation. The morphology of the face-down sample is not affected by ZnO thin film deposition. The response time of the devices measured at 1 V was reduced upon the deposition of the ZnO film as a surface passivation layer. The rise time of the face-down sample with ZnO thin film was reduced by 24.01% and fall time by 34.53% under 254 nm light illumination. The passivated devices exhibited better performance when illuminated by 254 nm and 365 nm UV light from the front side. The device with homojunction created by depositing a thin layer of ZnO nanoparticles on face-down sample exhibited fast response with better UV detection properties compared to all other devices due to the preferentially and uniformly arranged ZnO nanorods with lesser surface states. Effect of growth time on the photoresponse properties was studied by changing the growth time to be 5 h, 7 h and 9 h. As the growth time increases the length of the nanorods and the defect states are increasing. For 7 h and 9 h samples, after the deposition of ZnO nanoparticle film, the morphology is changed and it affects the device performance. the 5 h grown sample exhibited better performance with fast response. The device fabricated on interdigitated ITO with face-up sample, D13, exhibited an on-off ratio of 1.50×10^3 , rise and fall times of 1.88 s and 6.39 s, detectivity of 4.20×10^{11} Jones responsivity of 55.60 mA/W and LDR of 62.01 dB at 1 V under 365 nm light illumination.

3.6 References

1. Sang, L., Liao, M. & Sumiya, M. A Comprehensive Review of Semiconductor Ultraviolet Photodetectors: From Thin Film to One-Dimensional Nanostructures. *Sensors* **13**, 10482–10518 (2013).

2. Hou, Y., Mei, Z. & Du, X. Semiconductor ultraviolet photodetectors based on ZnO and Mg x Zn 1− x O. *J. Phys. D. Appl. Phys.* **47**, 283001 (2014).

3. Zhang, T., Yu, J., Deng, Y., Tian, N. & Gao, P. Fast response ultraviolet photodetectors based on solution-processed ZnO nanocrystals. *Sci. China Technol. Sci.* **58**, 1328–1332 (2015).

4. Zhang, X. *et al.* Giant UV photoresponse of a GaN nanowire photodetector through effective Pt nanoparticle coupling. *J. Mater. Chem. C* **5**, 4319–4326 (2017).

5. Wu, Y. *et al.* Ultraviolet light sensitive In-doped ZnO thin film field effect transistor printed by inkjet technique. *Phys. status solidi* **208**, 206–209 (2011).

6. Liu, Y. *et al.* Ultraviolet detectors based on epitaxial ZnO films grown by MOCVD. *J. Electron. Mater.* **29**, 69–74 (2000).

7. Li, L., Gu, L., Lou, Z., Fan, Z. & Shen, G. ZnO Quantum Dot Decorated Zn_2SnO_4 Nanowire Heterojunction Photodetectors with Drastic Performance Enhancement and Flexible Ultraviolet Image Sensors. *ACS Nano* **11**, 4067–4076 (2017).

8. Djurišić, A. B., Ng, A. M. C. & Chen, X. Y. ZnO nanostructures for optoelectronics: Material properties and device applications. *Prog. Quantum Electron.* **34**, 191–259 (2010).

9. Deka Boruah, B. Zinc oxide ultraviolet photodetectors: rapid progress from conventional to self-powered photodetectors. *Nanoscale Adv.* **1**, 2059–2085 (2019).

10. Li, Y. *et al.* Full-solution processed all-nanowire flexible and transparent ultraviolet photodetectors. *J. Mater. Chem. C* **6**, 11666–11672 (2018).

11. Zhang, Y., Ram, M. K., Stefanakos, E. K. & Goswami, D. Y. Synthesis, Characterization, and Applications of ZnO Nanowires. *J. Nanomater.* **2012**, 1–22 (2012).

12. Butanovs, E. *et al.* Fast-Response Single-Nanowire Photodetector Based on ZnO/WS_2 Core/Shell Heterostructures. *ACS Appl. Mater. Interfaces* **10**, 13869–13876 (2018).

13. Bahariqushchi, R. *et al.* Free carrier enhanced depletion in ZnO nanorods decorated with bimetallic AuPt nanoclusters. *Nanoscale* **12**, 19213–19222 (2020).

14. Nasiri, N., Jin, D. & Tricoli, A. Nanoarchitechtonics of Visible-Blind Ultraviolet Photodetector Materials: Critical Features and Nano-Microfabrication. *Adv. Opt. Mater.* **1800580**, 1800580 (2018).

15. Guo, Z. *et al.* Visible and ultraviolet light alternative photodetector based on ZnO nanowire/n-Si heterojunction. *Appl. Phys. Lett.* **93**, 163501 (2008).

16. Huang, H. *et al.* Zero-biased near-ultraviolet and visible photodetector based on ZnO nanorods/n-Si heterojunction. *Appl. Phys. Lett.* **94**, 063512 (2009).

17. Yang, Y., Guo, W., Qi, J., Zhao, J. & Zhang, Y. Self-powered ultraviolet photodetector

based on a single Sb-doped ZnO nanobelt. *Appl. Phys. Lett.* **97**, 223113 (2010).

18. Ji, L. W. *et al.* Ultraviolet photodetectors based on selectively grown ZnO nanorod arrays. *Appl. Phys. Lett.* **94**, 2012–2015 (2009).

19. Hassan, J. J. *et al.* High sensitivity and fast response and recovery times in a ZnO nanorod array/ p -Si self-powered ultraviolet detector. *Appl. Phys. Lett.* **101**, 261108 (2012).

20. Abdulrahman, A. F. *et al.* Fabrication and Characterization of High-Quality UV Photodetectors Based ZnO Nanorods Using Traditional and Modified Chemical Bath Deposition Methods. *Nanomaterials* **11**, 677 (2021).

21. Tian, C. *et al.* Performance enhancement of ZnO UV photodetectors by surface plasmons. *ACS Appl. Mater. Interfaces* **6**, 2162–2166 (2014).

22. Alsultany, F. H., Hassan, Z. & Ahmed, N. M. A high-sensitivity, fast-response, rapid-recovery UV photodetector fabricated based on catalyst-free growth of ZnO nanowire networks on glass substrate. *Opt. Mater. (Amst).* **60**, 30–37 (2016).

23. Qin, L., Shing, C., Sawyer, S. & Dutta, P. S. Enhanced ultraviolet sensitivity of zinc oxide nanoparticle photoconductors by surface passivation. *Opt. Mater. (Amst).* **33**, 359–362 (2011).

24. Vasudevan, A., Jung, S. & Ji, T. On the Responsivity of UV Detectors Based on Selectively Grown ZnO Nanorods. *IEEE Sens. J.* **12**, 1317–1325 (2012).

25. Ates, E. S., Kucukyildiz, S. & Unalan, H. E. Zinc Oxide Nanowire Photodetectors with Single-Walled Carbon Nanotube Thin-Film Electrodes. *ACS Appl. Mater. Interfaces* **4**, 5142–5146 (2012).

26. Ko, Y. H., Nagaraju, G. & Yu, J. S. Fabrication and Optimization of Vertically Aligned ZnO Nanorod Array-Based UV Photodetectors via Selective Hydrothermal Synthesis. *Nanoscale Res. Lett.* **10**, 323 (2015).

27. Lam, K.-T. *et al.* High-Sensitive Ultraviolet Photodetectors Based on ZnO Nanorods/CdS Heterostructures. *Nanoscale Res. Lett.* **12**, 31 (2017).

28. Shaikh, S. K., Ganbavale, V. V., Mohite, S. V., Patil, U. M. & Rajpure, K. Y. ZnO nanorod based highly selective visible blind ultra-violet photodetector and highly sensitive NO_2 gas sensor. *Superlattices Microstruct.* **120**, 170–186 (2018).

29. Sun, W.-C., Yeh, Y.-C., Ko, C.-T., He, H. & Chen, M.-J. Improved characteristics of near-band-edge and deep-level emissions from ZnO nanorod arrays by atomic-layer-deposited Al_2O_3 and ZnO shell layers. *Nanoscale Res. Lett.* **6**, 556 (2011).

30. Chen, C., He, H., Lu, Y., Wu, K. & Ye, Z. Surface Passivation Effect on the Photoluminescence of ZnO Nanorods. *ACS Appl. Mater. Interfaces* **5**, 6354–6359 (2013).

31. Lin, C.-C., Chen, H.-P., Liao, H.-C. & Chen, S.-Y. Enhanced luminescent and electrical properties of hydrogen-plasma ZnO nanorods grown on wafer-scale flexible substrates. *Appl. Phys. Lett.* **86**, 183103 (2005).

32. Zhong, P., Ma, X. & Xi, H. Passivating ZnO Surface States by C_{60} Pyrrolidine Tris-Acid for Hybrid Solar Cells Based on Poly(3-hexylthiophene)/ZnO Nanorod Arrays. *Polymers (Basel).* **10**, 4 (2017).

33. Liu, K. W., Chen, R., Xing, G. Z., Wu, T. & Sun, H. D. Photoluminescence characteristics

of high quality ZnO nanowires and its enhancement by polymer covering. *Appl. Phys. Lett.* **96**, 023111 (2010).

34. Ali, A. *et al.* Enhanced band edge luminescence of ZnO nanorods after surface passivation with ZnS. *Phys. E Low-dimensional Syst. Nanostructures* **103**, 329–337 (2018).

35. Lin, T. N. *et al.* Influence of pulsed laser annealing on the optical properties of ZnO nanorods. *Phys. status solidi* **209**, 1461–1466 (2012).

36. Yao, B., Feng, L., Cheng, C., Loy, M. M. T. & Wang, N. Tailoring the luminescence emission of ZnO nanostructures by hydrothermal post-treatment in water. *Appl. Phys. Lett.* **96**, 223105 (2010).

37. Liu, M., Nam, C.-Y., Black, C. T., Kamcev, J. & Zhang, L. Enhancing Water Splitting Activity and Chemical Stability of Zinc Oxide Nanowire Photoanodes with Ultrathin Titania Shells. *J. Phys. Chem. C* **117**, 13396–13402 (2013).

38. Nandanapalli, K. R. & Mudusu, D. Surface Passivated Zinc Oxide (ZnO) Nanorods by Atomic Layer Deposition of Ultrathin ZnO Layers for Energy Device Applications. *ACS Appl. Nano Mater.* **1**, 4083–4091 (2018).

39. Bie, Y. Q. *et al.* Self-Powered, Ultrafast, Visible-Blind UV Detection and Optical Logical Operation based on ZnO/GaN Nanoscale p-n Junctions. *Adv. Mater.* **23**, 649–653 (2011).

40. Jin, Z., Gao, L., Zhou, Q. & Wang, J. High-performance flexible ultraviolet photoconductors based on solution-processed ultrathin ZnO/Au nanoparticle composite films. *Sci. Rep.* **4**, 4268 (2015).

41. Wang, Y. *et al.* Temperature-dependence studies of organolead halide perovskite-based metal/semiconductor/metal photodetectors. *RSC Adv.* **7**, 20206–20211 (2017).

42. Lee, K. *et al.* Improved dynamic properties of ZnO-based photo-transistor with polymer gate dielectric by ultraviolet treatment. *J. Phys. D. Appl. Phys.* **41**, 135102 (2008).

43. Yu, J. *et al.* ZnO-based ultraviolet avalanche photodetectors. *J. Phys. D. Appl. Phys.* **46**, 305105 (2013).

44. Xu, Z. *et al.* Photoconductive UV Detectors Based on ZnO Films Prepared by Sol-Gel Method. *J. Sol-Gel Sci. Technol.* **36**, 223–226 (2005).

45. Jin, Z., Gao, L., Zhou, Q. & Wang, J. High-performance flexible ultraviolet photoconductors based on solution-processed ultrathin ZnO/Au nanoparticle composite films. *Sci. Rep.* **4**, 4268 (2015).

46. Ahn, S. E. *et al.* Photoresponse of sol-gel-synthesized ZnO nanorods. *Appl. Phys. Lett.* **84**, 5022–5024 (2004).

47. Li, Q. H., Gao, T., Wang, Y. G. & Wang, T. H. Adsorption and desorption of oxygen probed from ZnO nanowire films by photocurrent measurements. *Appl. Phys. Lett.* **86**, 123117 (2005).

48. Bera, A. & Basak, D. Photoluminescence and Photoconductivity of ZnS-Coated ZnO Nanowires. *ACS Appl. Mater. Interfaces* **2**, 408–412 (2010).

49. Weng, W. Y., Chang, S. J., Hsu, C. L., Hsueh, T. J. & Chang, S. P. A Lateral ZnO Nanowire Photodetector Prepared on Glass Substrate. *J. Electrochem. Soc.* **157**, K30 (2010).

50. Chitara, B., Panchakarla, L. S., Krupanidhi, S. B. & Rao, C. N. R. UV Photodetectors Based on ZnO Nanorods: Role of Defect-Concentration. *Jpn. J. Appl. Phys.* **50**, 100206 (2011).

51. Sarkar, S. & Basak, D. Defect controlled ultra high ultraviolet photocurrent gain in Cu-doped ZnO nanorod arrays: De-trapping yield. *Appl. Phys. Lett.* **103**, 041112 (2013).

52. Liu, Y. H. *et al.* Visible-Blind Photodetectors With Mg-Doped ZnO Nanorods. *IEEE Photonics Technol. Lett.* **26**, 645–648 (2014).

53. Akhtarianfar, S. F., Khayatian, A., Shakernejad, R., Almasi-Kashi, M. & Hong, S. W. Improved sensitivity of UV sensors in hierarchically structured arrays of network-loaded ZnO nanorods via optimization techniques. *RSC Adv.* **7**, 32316–32326 (2017).

54. Poornajar, M., Marashi, P., Haghshenas Fatmehsari, D. & Kolahdouz Esfahani, M. Synthesis of ZnO nanorods via chemical bath deposition method: The effects of physicochemical factors. *Ceram. Int.* **42**, 173–184 (2016).

55. Cao, B. & Cai, W. From ZnO Nanorods to Nanoplates: Chemical Bath Deposition Growth and Surface-Related Emissions. *J. Phys. Chem. C* **112**, 680–685 (2008).

56. Wang, M., Kim, E. J., Hahn, S. H., Park, C. & Koo, K.-K. Controlled Crystal Growth and Crystallite Orientation in ZnO Films/Nanorods Prepared by Chemical Bath Deposition: Effect of Solvent. *Cryst. Growth Des.* **8**, 501–506 (2008).

57. Hanna, B., Manuraj, M., Surendran, K. P. & Unni, K. N. N. Opto-electronic properties of solution-processed zinc oxide thin films: role of solvents and doping. *J. Mater. Sci. Mater. Electron.* **31**, 13570–13577 (2020).

58. Gaddam, V., Kumar, R. R., Parmar, M., Nayak, M. M. & Rajanna, K. Synthesis of ZnO nanorods on a flexible Phynox alloy substrate: influence of growth temperature on their properties. *RSC Adv.* **5**, 89985–89992 (2015).

59. Hanna, B., Surendran, K. P. & Narayanan Unni, K. N. Low temperature-processed ZnO thin films for p–n junction-based visible-blind ultraviolet photodetectors. *RSC Adv.* **8**, 37365–37374 (2018).

60. Shivanna, R., Rajaram, S. & Narayan, K. S. Interface engineering for efficient fullerene-free organic solar cells. *Appl. Phys. Lett.* **106**, 123301 (2015).

61. Chen, Y.-C., Cheng, H.-Y., Yang, C.-F. & Hsieh, Y.-T. Investigation of the Optimal Parameters in Hydrothermal Method for the Synthesis of ZnO Nanorods. *J. Nanomater.* **2014**, 1–6 (2014).

62. Holzwarth, U. & Gibson, N. The Scherrer equation versus the 'Debye-Scherrer equation'. *Nat. Nanotechnol.* **6**, 534–534 (2011).

63. Yogamalar, N. R. & Chandra Bose, A. Burstein–Moss shift and room temperature near-band-edge luminescence in lithium-doped zinc oxide. *Appl. Phys. A* **103**, 33–42 (2011).

64. Malik, G., Jaiswal, J., Mourya, S. & Chandra, R. Optical and other physical properties of hydrophobic ZnO thin films prepared by dc magnetron sputtering at room temperature. *J. Appl. Phys.* **122**, 143105 (2017).

65. Zhang, H. *et al.* Characterization and modeling of a ZnO nanowire ultraviolet photodetector with graphene transparent contact. *J. Appl. Phys.* **114**, 234505 (2013).

66.   Kim, Y. *et al.* Formation of a functional homo-junction interface through ZnO atomic layer passivation: Enhancement of carrier mobility and threshold voltage in a ZnO nanocrystal field effect transistor. *J. Alloys Compd.* **804**, 213–219 (2019).

67.   Zayed, M. *et al.* Effect of Morphology and Plasmonic on Au/ZnO Films for Efficient Photoelectrochemical Water Splitting. *Nanomaterials* **11**, 2338 (2021).

68.   Foo, K. L., Kashif, M., Hashim, U. & Ali, M. E. Sol–gel derived ZnO nanoparticulate films for ultraviolet photodetector (UV) applications. *Optik (Stuttg).* **124**, 5373–5376 (2013).

69.   Li, Y., Valle, F. Della, Simonnet, M., Yamada, I. & Delaunay, J.-J. High-performance UV detector made of ultra-long ZnO bridging nanowires. *Nanotechnology* **20**, 045501 (2009).

70.   Prades, J. D. *et al.* The effects of electron–hole separation on the photoconductivity of individual metal oxide nanowires. *Nanotechnology* **19**, 465501 (2008).

Visible-blind ultraviolet photodetectors using polymer/ZnO nanocomposite thin films
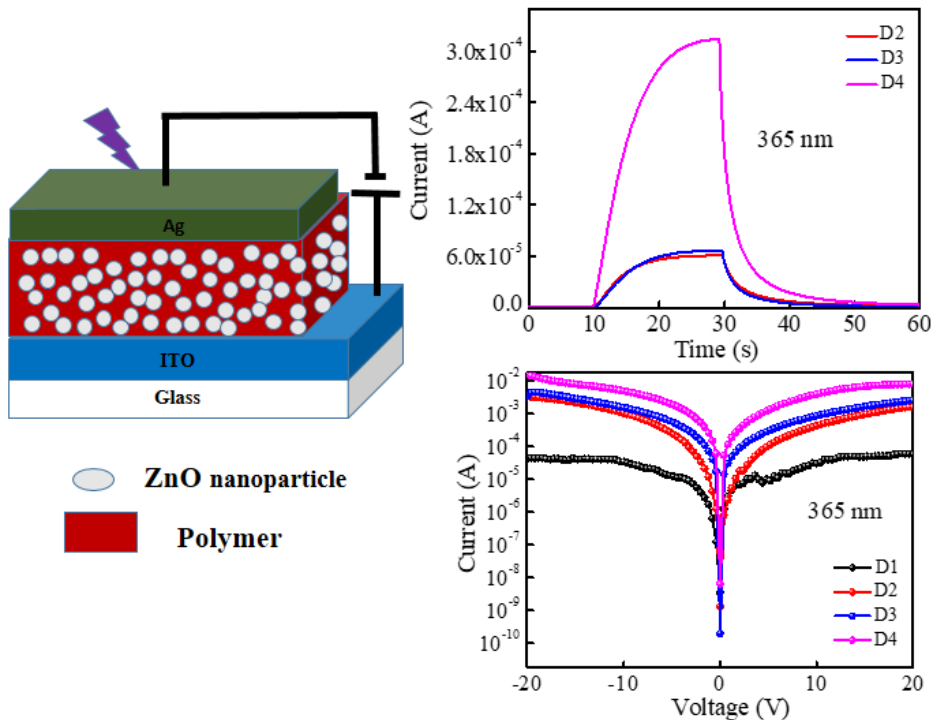
4.1 Abstract

We report the fabrication and characterization of polymer/zinc oxide (ZnO) nanocomposite based visible-blind UV photodetectors. UV photodetectors based on nanocomposites of ZnO with three polymers poly(methyl methacrylate) (PMMA), polystyrene (PS) and poly(vinylidene difluoride-trifluoroethylene (P(VDF-TrFE)) were prepared by physical mixing method. P(VDF-TrFE)/ZnO nanocomposite-based device exhibited the best performance possibly due to its ferroelectric property. Then we studied the influence of the concentration of ZnO nanoparticles in P(VDF-TrFE) by preparing thin films of the latter with 0.5 wt%, 1wt% and 5 wt% ZnO nanoparticles. The films were characterized by atomic force microscopy (AFM), X-

ray diffraction (XRD), fourier transform- infrared spectroscopy (FTIR) and UV-Visible absorption spectroscopy. XRD and FTIR studies confirmed the formation of the β phase of P(VDF-TrFE) in pristine polymer films and P(VDF-TrFE)/ZnO nanocomposites. Effect of electrode materials on the photodetector performance of nanocomposites was studied by using ITO bottom electrode and top electrode with either Al, Ag or Au. The device with Ag showed the best performance. Hence photodetector measurements were carried out using ITO and Ag electrodes varying the ZnO concentration in the polymer nanocomposite. Electrical response of the detector to 365 nm and 254 nm UV light illumination was studied and P(VDF-TrFE)/5 wt% ZnO nanocomposite with top Ag electrode exhibited the best performance with on-off ratio, 1.4×10^4; responsivity, 14.43 A/W; linear dynamic range, 83.09 dB and detectivity, 2.27×10^{13} Jones under 365 nm light illumination at 2 V biasing. Ferroelectric polarization mechanism of P(VDF-TrFE) and the choice of electrode play an important role in separating the charge carriers upon UV illumination. Finally the influence of morphology of ZnO was studied by synthesizing ZnO nanorods and nanoflowers and characterizing photodetectors based on P(VDF-TrFE)/1 wt% ZnO nanorod and P(VDF-TrFE)/1 wt% ZnO nanoflower composites.

4.2 Introduction

In the last few years, UV photodetectors are getting increased attention due to their potential applications in pollution monitoring systems, satellite communication systems, diagnosis, flame detection, missile warning etc.[1] ZnO, TiO$_2$, GaN, diamond, SiC etc. are the commonly used materials for the fabrication of UV photodetectors.[2,3] Among them zinc oxide (ZnO) is getting more attention due to its relatively large exciton binding energy, wide direct band gap, non-toxicity, low cost, various synthetic methods, high stability etc.[4–6] Also, different morphologies of ZnO can be easily synthesized by cost-effective techniques.[7] Though ZnO-based devices exhibit high photoconductivity gain, they show rather long response and recovery times due to the persistent photoconductivity (PPC) effect produced by the surface states and

defects.[8] These also lead to the visible emission and thus limit their applications in UV selective spectral response. Polymer/ZnO composite systems are recently getting more attention due to their applications in pressure sensors, photodetectors, supercapacitors, medical devices, food packaging systems, coatings, water treatment etc.[9,10] It is found that the polymer properties could be enhanced by the addition of inorganic nanofillers into the polymer matrix and their properties are considerably different from those of the pristine polymers.[11] A polymer nanocomposite can be defined as a system containing nanofillers of size less than 100 nm in at least any one dimension and these nanofillers act as dopants to enhance the properties of polymers by the quantum confinement effect.[10] The properties of the polymer/ZnO nanocomposite film can be modified by varying the size and morphology of the ZnO nanoparticles.[12] In turn, the properties of the polymer matrix can influence the nanocomposite properties. Polymer nanocomposites can be prepared either by physical or chemical mixing methods. In physical mixing method, the nanoparticles and polymer matrix are connected by van der-Waals or Lewis acid-base interaction and in the case of chemical mixing method, strong interaction takes place between the nanoparticles and the polymer matrix.[10]

Polymer/ZnO nanocomposite is a good choice for fabricating flexible UV photodetectors with high photoresponsivity, sensitivity and external quantum efficiency. Park et al. fabricated UV photodetectors based on PVK/ZnO quantum dots modified by graphene layer, which exhibited good performance with on/off ratio of 10^8 at 0.4 V under 365 nm light illumination.[13] In 2016, Kang et al. fabricated a solution-processable UV photodetector based on ZnO/PVK nanocomposite as the photoactive layer and found that the exciton binding energy of the polymer nanocomposite was low and the photogenerated excitons could be easily separated and collected at the respective electrodes. The device exhibited fast response and on/off ratio of 10^3.[14] Later, in 2017, Joseph et al. fabricated a UV-A photodetector based on ZnO/PVA nanocomposite. In this work, they studied the structural, electrical and optical properties of PVA and ZnO/PVA

nanocomposite. The photodetector exhibited a rise time of 1.017 s and a long recovery time of 602.2 s.[15] Patra et al. fabricated a polymer/ZnO nanocomposite based UV photodetector. In this work, they used spherical ZnO nanoparticles of size 50 nm as the filler and PVDF and PVP as the polymer matrices. The ZnO/PVDF device exhibited a response time of 40 s and ZnO/PVP device exhibited a response time of 0.167 s.[9] UV photodiodes based on ZnO/PVA nanocomposite modified by graphene quantum dots were fabricated by Majlesara et al. in 2019. The device exhibited a responsivity of 26.8 A/W and photocurrent of 1.07 µA at 365 nm light illumination. The response time of the device with ZnO/PVA nanocomposite without modification is too long, which is improved upon modification by graphene quantum dots.[16] Mitra et al. studied the negative photoresponse in ZnO/PEDOT:PSS nanocomposite under UV and visible light. They found that the conductance of the device is decreased by the trapping of holes in the PEDOT:PSS channel by the electrons generated upon illumination in the ZnO nanoparticles. The device exhibited a long response time due to the large junction capacitance produced by the charges trapped at the ZnO nanoparticle surface.[17] The polymer/ZnO nanocomposite is the best option to achieve flexible, transparent and high photoresponsivity UV photodetectors.

The polymer matrix affects the optoelectronic properties of the nanocomposite and hence the choice of the polymer is very important in photodetector applications. In this work, we have selected three polymers, poly(methyl methacrylate) (PMMA), polystyrene (PS) and poly(vinylidene difluoride-trifluoroethylene (P(VDF-TrFE)). PMMA and PS are both thermoplastic polymers with many similar physical properties. PMMA has several applications in optics, medical technologies and aesthetics whereas PS is widely used for packaging. Impact strength and tensile strength are better for PMMA. P(VDF-TrFE) is a ferroelectric polymer which has many promising applications in the electronic industry. All the three polymers are fairly transparent in the visible and thus can be used for fabricating visible-blind photodetectors. In this work, we synthesized PMMA/ZnO, PS/ZnO and P(VDF-TrFE)/ ZnO nanocomposites by

physical mixing method and the UV photodetectors were fabricated in ITO/ polymer/ZnO nanocomposite/ M structure, where M could be Ag, Au or Al.

P(VDF-TrFE) is a good choice due to its structural flexibility, low cost, stability and high piezoelectricity.[18] P(VDF-TrFE) is a copolymer of PVDF and depending on the position of F atoms, P(VDF-TrFE) exists in different crystalline phases such as α, β, γ, δ and ε.[19] The β phase exhibits better ferroelectric, optical and electrical properties.[20] The addition of ZnO nanoparticle into the P(VDF-TrFE) matrix can improve its optical and electrical properties by an interfacial interaction between the P(VDF-TrFE) and ZnO nanoparticles.[12]

Realizing this potential, P(VDF-TrFE) and ZnO combinations have been employed in different device applications. ZnO-based field-effect transistor functioning as non-volatile memory element has been reported with P(VDF-TrFE) as the gate dielectric.[21] Piezoelectric properties of P(VDF-TrFE) are reported to be enhanced by the addition of ZnO nanoparticles.[22] Filamentary resistive switching has been observed in P(VDF-TrFE)/ZnO nanocomposite film. It is reported that conduction paths are formed along the Zn-rich/F-deficient regions.[23] Although the P(VDF-TrFE)/ZnO nanocomposite thin films have been investigated for piezoelectric and memory applications, studies of the same for UV-photodetectors are rare in literature. ZnO nanowires deposited on an aligned P(VDF-TrFE) nanofiber film have shown promise as a UV detector. Wang et al. have reported a field-effect transistor based on ZnO nanosheets with P(VDF-TrFE) as the gate dielectric.[24] This device showed very high on-off ratio and responsivity. However, it employed a coercive field of about 20 V to suppress the dark current. Also, a reverse gate voltage was required to bring back the off state once the on state has been achieved by the exposure to UV radiation. ZnO nanowires deposited on an aligned P(VDF-TrFE) nanofiber film have shown promise as a UV detector. The directionality and fabrication time of the electrospun film are the critical parameters here.[25] Self-powered flexible photodetectors were fabricated by combining photogating, piezo-phototronic and ferroelectric properties by

introducing a thin film of P(VDF-TrFE)/ZnO nanocomposite in the device structure.[26] It modulates the charge carrier transport behaviour at the interface by the internal electric field produced by UV light illumination. The device exhibited better performance with a responsivity of 419 mA/W and detectivity of 9.7×10^{12} Jones under 325 nm illumination.

UV photodetectors can be fabricated in different configurations. Metal semiconductor metal (MSM) photodetectors fabricated based on ZnO showed excellent photodetection properties.[27–29] Fast response, low capacitance per unit area and high photoresponsivity are the advantages of MSM photodetectors.[30] Their fabrication techniques are simple and easy for large scale integration. There are two types of MSM photodetectors. Planar MSM photodetectors and vertical MSM photodetectors. Planar MSM photodetectors consist of a semiconductor with interdigitated electrodes lying on its surface and the semiconductor layer is directly exposed to light. In vertical MSM photodetectors the semiconductor layer is sandwiched between two metal electrodes. The top electrode should be sufficiently thin to transmit the light into the semiconductor layer. Compared to planar MSM photodetectors, it is easy to control the distance between the two electrodes of vertical MSM photodetectors. It helps to improve the response speed by reducing the parasitic capacitance of the device.[31] However, the applications of conventional MSM detectors are limited due to its high dark current, slow response and low responsivity.[32] The performance of the device depends on the active layer thickness and properties of the material. Therefore, it is necessary to develop a method to fabricate high performance UV photodetectors to meet the practical applications.

Here, polymer/ZnO nanocomposite based photodetectors were fabricated in MSM configuration. Since, P(VDF-TrFE)/ ZnO nanocomposite-based UV photodetector exhibited better performance, we studied the structural and electrical properties for various wt% of ZnO nanoparticles in the P(VDF-TrFE) polymer matrix. The effect of electrode material on the photoresponse property was studied by employing Au, Ag and Al as the electrode material. The

device with Ag as the top electrode exhibited better performance. In order to study the effect of morphology of ZnO on the device performance P(VDF-TrFE)/ZnO nanorod and P(VDF-TrFE)/ZnO nanoflower nanocomposites-based UV detectors were fabricated.

4.3 Experimental

4.3.1 Synthesis of PMMA/ ZnO nanocomposite and preparation of thin films

80 mg of PMMA was dissolved in 1 ml toluene and stirred at 50 ^{0}C for 12 h. ZnO nanoparticles were synthesized by precipitation method. The synthesis and characterization of ZnO nanoparticles have been done as in chapter 2.[33] 5 wt % of ZnO nanoparticles were added to this solution and sonicated for 1 h. Then this solution was spin coated on ITO coated glass substrates and annealed at 120 ^{0}C for 1 h.

4.3.2 Synthesis of PS/ ZnO nanocomposite and preparation of thin films

100 mg of PS was dissolved in toluene and stirred at room temperature for 3 h. 5 wt% of ZnO nanoparticles were added to this solution and sonicated for 1 h. This solution was spin coated on ITO coated glass substrates and annealed at 120 ^{0}C for 1 h.

4.3.3 Synthesis of P(VDF-TrFE)/ ZnO nanocomposite and preparation of thin films

100 mg of P(VDF-TrFE) (VDF-70 mol%, TrFe-30 mol%) was dissolved in 1 ml methyl ethyl ketone and stirred at room temperature for 2 h [34]. The ZnO nanoparticles of different concentrations such as 0.5 wt%, 1 wt%, 5 wt% were added to the P(VDF-TrFE) solution. ZnO concentration above 5 wt% led to agglomeration and non-uniformities in the film. The solutions were then sonicated for 1 h. These solutions were spin-coated on ITO coated glass substrates and then annealed at 120 ^{0}C for 2 h to form the β phase [35].

4.3.4 Synthesis of P(VDF-TrFE)/ ZnO nanorods nanocomposite and preparation of thin films.

25 mM zinc nitrate hexahydrate (25 mmol) was dissolved in 100 ml DI water and 25 mM hexamethylenetetramine (HMTA) was dissolved in 100 ml DI water. Both the solutions were mixed and stirred at room temperature for 30 minutes.[36] The mixture was placed in an oven at 90° C for 5 h. After 5 h, the solution was allowed to cool down to room temperature and the product was washed with DI water by centrifugation. Finally the product was annealed at 200° C for 2 h in air. 1 wt% of ZnO nanorods were added to the P(VDF-TrFE) solution and sonicated for 1 h. This solution was spin-coated on ITO coated glass substrates and then annealed at 120 ^{0}C for 2 h.

4.3.5 Synthesis of P(VDF-TrFE)/ ZnO nanoflower nanocomposite and preparation of thin films

20 ml aqueous solution of sodium hydroxide (NaOH) was added to the 20 ml aqueous solution of zinc acetate dihydrate at room temperature. White precipitate was formed and it was transferred to a teflon lined stainless steel autoclave. The autoclave was kept at 70 ^{0}C for 24 h. After cooled to room temperature, the white precipitate was washed with methanol by centrifugation and dried at 70 ^{0}C. 1 wt% of ZnO nanoflowers were added to the P(VDF-TrFE) solution and sonicated for 1 h. This solution was spin-coated on ITO coated glass substrates and then annealed at 120 ^{0}C for 2 h.

4.3.6 Characterization of polymer/ZnO nanocomposite thin films

Optical properties of the polymer/ZnO nanocomposites were studied by Fluorolog Spectrofluorometer, HORIBA Jobin Yvon and PerkinElmer UV/VIS/NIR Spectrometer, Lambda 950. The surface morphology of the ZnO nanostructures and nanocomposites were investigated by Bruker AFM, high resolution transmission electron microscope (HRTEM), FEI

Tecnai 30, G2S-TWIN and Carl Zeiss scanning electron microscope (SEM) Germany with EDS. Crystalline properties of the nanocomposites were studied from X-ray diffraction (XRD) patterns measured by XPert-PRO Scan Diffractometer with Cu Kα (λ=1.5406 Å) radiation from 20^0 to 80^0 scanning range and FTIR spectra measured by IR Prestige-21 FTIR Spectrophotometer, Shimadzu. The thicknesses of the films were measured by the Bruker stylus profilometer.

4.3.7 Fabrication of the devices

The device structure is shown in Figure 4.1. For photoresponse studies, ITO/PMMA/5 wt% ZnO/Ag, ITO/PS/5 wt% ZnO/Ag and ITO/P(VDF-TrFE)/5 wt% ZnO/Ag devices were fabricated. Since, P(VDF-TrFE)/5 wt% ZnO nanocomposite based device exhibited better performance, ITO/ P(VDF-TrFE)/Ag, ITO/ P(VDF-TrFE)/0.5 wt% ZnO/Ag, ITO/ P(VDF-TrFE)/ 1 wt% ZnO/Ag were fabricated to study the effect of concentration of ZnO nanoparticles on device performance. In all devices, the thickness of the active layer was approximately 680 ± 10 nm and the active area was 2 mm^2. The thickness of the films was optimized by spin coating the solutions at different RPM.
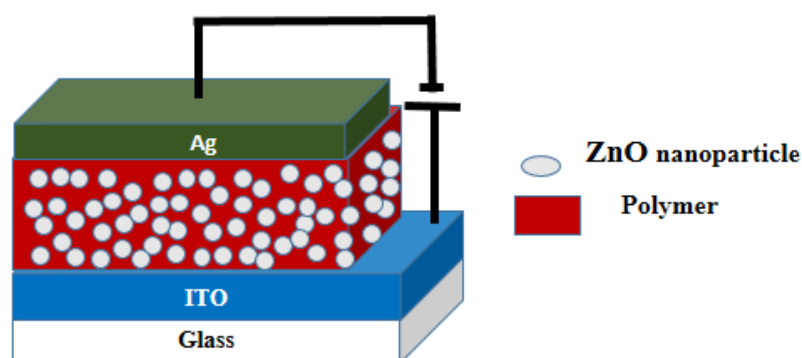
Figure 4.1. Schematic diagram of the device.

The bottom electrode (ITO) had a thickness of 150 nm, while the top electrode, which was thermally evaporated, had a thickness of 100 nm. The effect of electrode material on the photoresponse property P(VDF-TrFE)/ZnO nanocomposite was studied by replacing the electrode material Ag of the device ITO/ P(VDF-TrFE)/5wt% ZnO/Ag by Al or Au and comparing the performance.

The effect of morphology of ZnO on the device performance was studied by fabricating ITO/ P(VDF-TrFE)/5wt% ZnO nanorod /Ag and ITO/ P(VDF-TrFE)/5wt% ZnO nanoflower/Ag devices and compared with ITO/ P(VDF-TrFE)/5wt% ZnO nanoparticle/Ag.

4.3.8 Characterization of devices

The current-voltage characteristics and transient photoresponse of the devices were studied with Keithley 2400 source meter and 6 W ENF 260C Spectroline UV Lamp with 365 nm and 254 nm wavelengths with peak UV intensity 350 $\mu W/cm^2$ and 390 $\mu W/cm^2$ at a distance of 15cm for UV-A and UV-C radiation respectively. The capacitance-voltage (C-V) measurements were done with Keithley 4200A SCS Parameter Analyzer. Spectral response measurements were carried out by using a 350 W Xenon lamp coupled to a Newport monochromator and chopped at 40 Hz using a light chopper blade as a light source and a power meter to measure the intensity of light at each wavelength.

4.4 Results and Discussion

4.4.1 Characterization of ZnO nanoparticles

The TEM and SEM images of the ZnO nanoparticles are shown in Figure 4.2. The nanoparticles are in spherical shape with particle size 20 nm. Figure 4.2(c) shows the EDS spectra in which strong Zn and O peaks are observed. The amount of Zn and O present in the sample are shown in the table in inset. It indicates that only Zn and O elements are present in the sample without the presence of any impurities.

(a)

(b)

(c)

Element	Weight%	Atomic%
O K	37.44	70.97
Zn K	62.56	29.03
Totals	100.00	
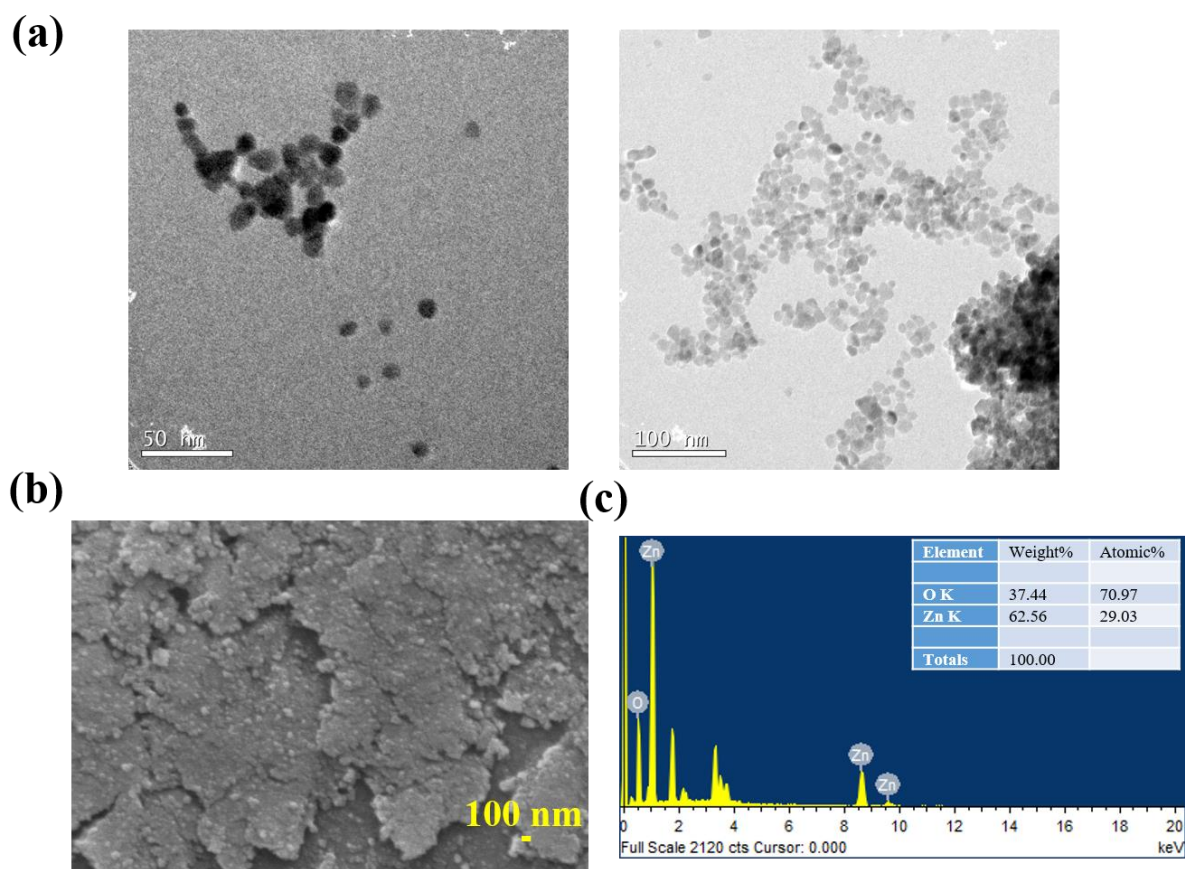
Figure 4.2. (a) TEM images of ZnO nanoparticles (b) SEM images of ZnO nanoparticles (c) EDS spectra of ZnO nanoparticles.

4.4.2 Optical properties of polymer/ZnO nanocomposite thin films

The optical properties of the polymer/ZnO nanocomposite films were studied by means of UV-Visible absorption spectroscopy and PL spectroscopy. The UV visible absorption spectra and PL spectra of PMMA/ 5wt% ZnO, PS/5 wt% ZnO and P(VDF-TrFE)/5 wt% ZnO nanocomposite films are shown in Figure 4.3. The thin films of P(VDF-TrFE), PMMA and PS showed negligible absorption in the UV region. After the addition of ZnO nanoparticles to the polymer matrix the absorption in the UV region is significantly enhanced for all the three polymers. P(VDF-TrFE)/5 Wt% ZnO nanocomposite film showed higher absorbance in the UV region and all three films are transparent in the visible region, which makes them good candidates for visible-blind UV detectors. There are two peaks observed in PL spectra of polymer/ZnO

composite films. One peak observed near 370 nm is due to the near band edge emission and the other observed in the visible state is due to the defect states in ZnO.[37] The intensity of defect emission is very high compared to the near band edge emission in a ZnO nanoparticle thin film. In polymer/ZnO nanocomposite films the intensity of near band edge emission is higher than that of visible emission. Thus, the polymer matrix seems to have passivated these defects and the visible emission is suppressed in the PL spectra of the polymer nanocomposite films as shown in Figure 4.3c.
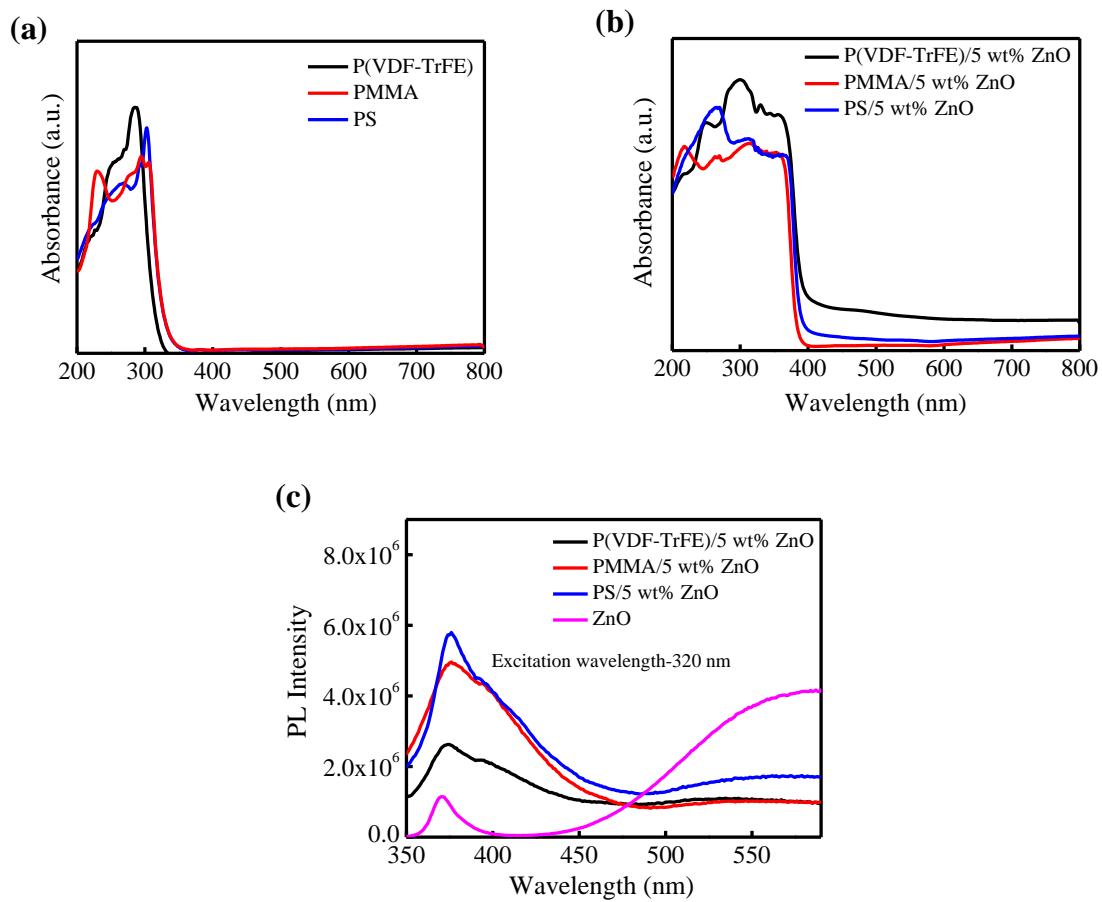
Figure 4.3. (a) UV visible absorption spectra of PMMA, PS, P(VDF-TrFE) thin films (b) UV visible absorption spectra of PMMA/ 5wt% ZnO, PS/5 wt% ZnO and P(VDF-TrFE)/5 wt% ZnO nanocomposite films (c) PL spectra of ZnO nanoparticles, PMMA/ 5 wt% ZnO, PS/5 wt% ZnO and P(VDF-TrFE)/5 wt% ZnO nanocomposite films.

4.4.3 Photodetector measurements

There are three spectral regions in the UV spectrum of electromagnetic radiation such as, UV-A ranging from 400 nm-320 nm, UV-B ranging from 320 nm-280 nm and UV-C ranging from 280 nm-10 nm. These radiations have both advantages and disadvantages in human life and therefore the detection of UV radiation becomes very important for the very existence of human life. IV characteristics of ITO/PMMA/5 wt% ZnO/Ag, ITO/PS/5 wt% ZnO/Ag and ITO/P(VDF-TrFE)/5 wt% ZnO/Ag devices under dark, 365 nm light illumination at an intensity of 1.24 mW/cm^2 and 10^3 under 254 nm light illumination at an intensity of 2.4 mW/cm^2 is shown in Figure 4.4. The devices were exposed to UV light from both sides, i.e, from the glass/ITO side (bottom side) and the metal electrode side (top side). Typical photoresponse for 365 nm and 254 nm of ITO/P(VDF-TrFE)/5 wt% ZnO/Ag when exposed from the bottom side is shown in Figure 4.5a. The photoresponse to 254 nm when exposed from the bottom side is extremely weak. Glass/ITO absorbs in the UV region, and it is more severe for 254 nm, which may be a reason for the diminished performance of the detector in this wavelength.[38] While the device being exposed from the top, the UV transmission of the metal electrode becomes important. The top electrode does allow partial transmission of 365 nm and 254 nm though the latter is much weaker.[38] Hence, the results of UV exposure from the top side only are discussed hereafter.

The ITO/P(VDF-TrFE)/5 wt% ZnO/Ag device exhibited better performance under 365 nm illumination due to the ferroelectric nature of P(VDF-TrFE). The performance parameters of the devices at 2 V are summarized in Table 4.1. It is found that the performance of the device depends on the choice of the polymer. PMMA /ZnO nanocomposite based devices exhibited poor performance compared to other two devices. At 2 V the responsivity of P(VDF-TrFE)/ZnO nanocomposite was 14.43 A/W and that of PS/ZnO nanocomposite was 0.64 A/W and PMMA/ZnO nanocomposite was 0.02 A/W. The more insulating nature of PMMA may be a reason for the lower performance. P(VDF-TrFE)/ZnO-based devices exhibited higher values of

D and LDR. The ferroelectric property of P(VDF-TrFE) could be associated with the improved device performance with the same. The ferroelectric property of P(VDF-TrFE) helps to improve the device performance. It has been reported that a field of 10^5 V/m is enough to polarize P(VDF-TrFE)/perovskite bulk heterojunction.[18] In our case, the applied bias of 2 V causes a field of 10^6 V/m and this generates a built-in potential. Under UV illumination, the nanoparticles absorb the radiation and generate electron-hole pairs. The built-in-potential generated due to the polarization effect helps separate the electron-hole pairs.[18] The holes move to the negatively biased electrode and electrons, to the positively biased electrode causing the photocurrent.

Another interesting observation is the presence of a short-circuit current for these polymer/ZnO devices. For the PMMA/ZnO and PS/ZnO devices, the minimum dark current is not at 0 V. This could be due to interfacial polarization originated by the polarization field. However, this feature is absent in the P(VDF-TrFE)/ZnO device where the minimum current is observed at 0 V for dark and photocurrents. We believe that the ferroelectric character of the P(VDF-TrFE) leads to higher molecular spatial ordering which compensates for the interfacial polarization. The ferroelectric nature of P(VDF-TrFE)/ZnO nanocomposite was confirmed from C-V measurements by fabricating Ag/P(VDF-TrFE)/5 wt% ZnO/Ag device. The C-V curve of the P(VDF-TrFE)/5 wt% ZnO nanocomposite is shown in Figure 4.5b. The hysteresis behaviour in the C-V curve shows the ferroelectric polarization in P(VDF-TrFE)/5 wt % ZnO nanocomposite[39].
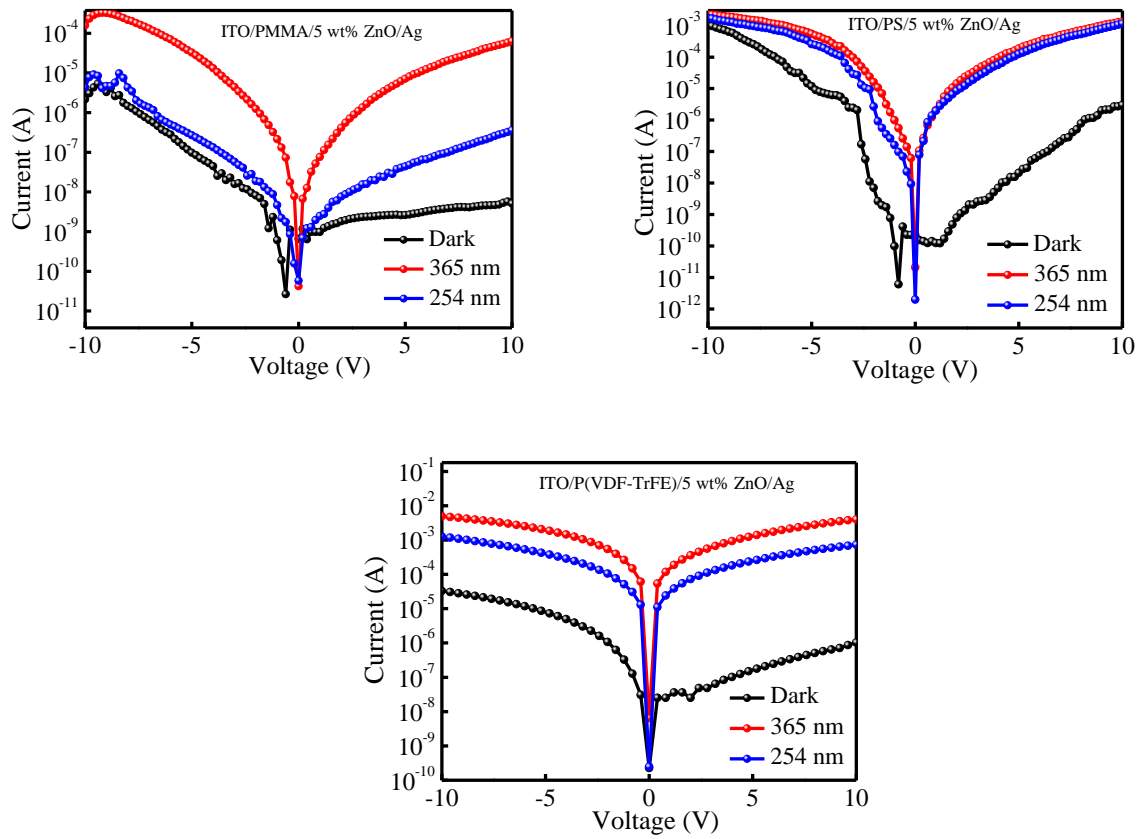
Figure 4.4. IV characteristics of ITO/PMMA/ 5wt% ZnO/Ag, ITO/PS/5 wt% ZnO/Ag and ITO/P(VDF-TrFE)/5 wt% ZnO/Ag devices.
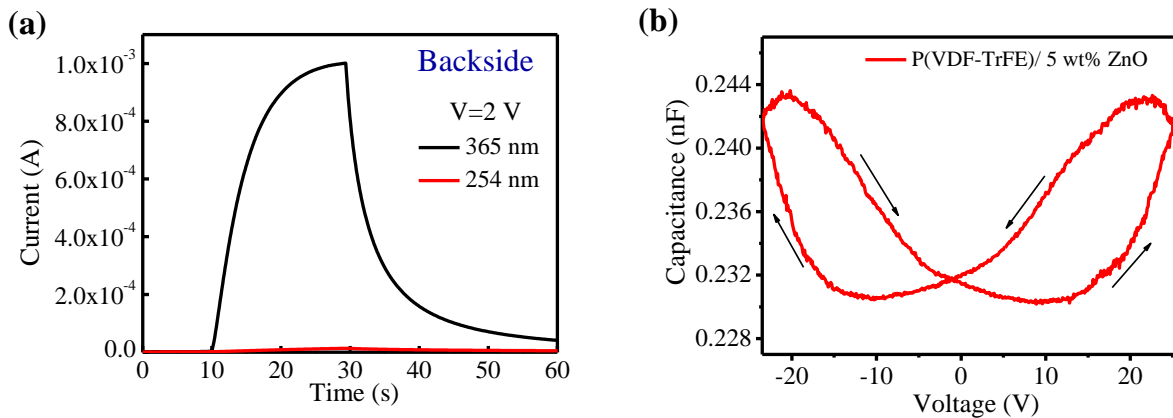
Figure 4.5. (a) Transient photoresponse of P(VDF-TrFE)/5 wt% of ZnO illuminated from bottom side under 365 nm and 254 nm light illumination at 2 V (b) C-V curve of P(VDF-TrFE)/5 wt% of ZnO nanocomposite film.

Transient photoresponse of the devices are shown in Figure 4.6. ITO/P(VDF-TrFE)/5 wt% ZnO/Ag device exhibited faster response compared to other two polymer nanocomposite devices under 365 nm light illumination. The device showed a rise time of 9.37 s and a fall time of 6.91 s.
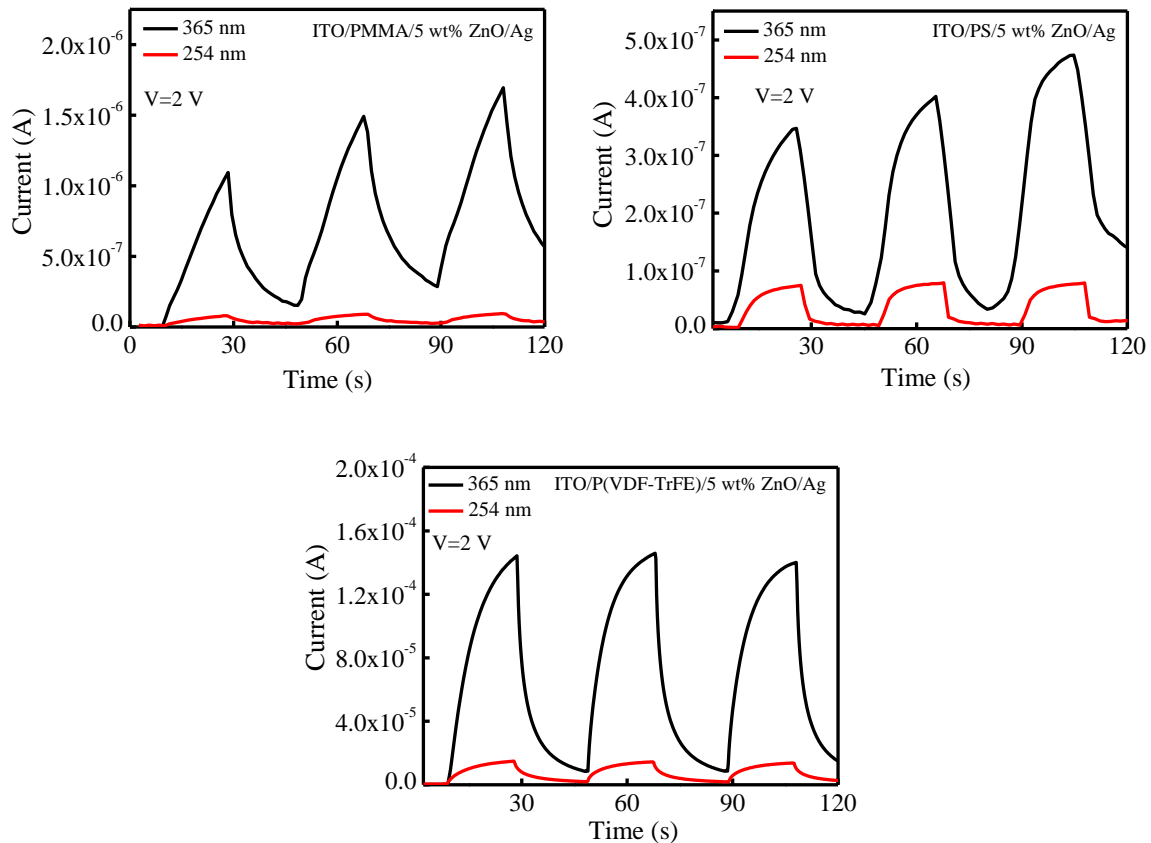
Figure 4.6. Transient photoresponse of ITO/PMMA/5 wt% ZnO/Ag, ITO/PS/5 wt% ZnO/Ag and ITO/P(VDF-TrFE)/5 wt% ZnO/Ag devices. The biasing voltage for all devices is kept at 2 V.

Since, P(VDF-TrFE)/5 wt% ZnO nanocomposite based device exhibited better performance, ITO/ P(VDF-TrFE)/Ag, ITO/ P(VDF-TrFE)/0.5 wt% ZnO/Ag and ITO/ P(VDF-TrFE)/ 1 wt% ZnO/Ag devices were fabricated to study the effect of concentration of ZnO nanoparticles on device performance.

Device	Photocurrent (A)	On-off ratio	Rise time (s)	Fall time (s)	Responsivity (A/W)	Detectivity (Jones)	LDR (dB)
365 nm							
ITO/PMMA/ 5 wt% ZnO/Ag	4.13×10^{-7}	2.5×10^{2}	14.57	45.69	0.016	1.02×10^{11}	47.98
ITO/PS/5 wt% ZnO/Ag	1.58×10^{-5}	2.2×10^{3}	12.36	10.18	0.638	1.89×10^{12}	66.96
ITO/P(VDF-TrFE)/5 wt% ZnO/Ag	3.58×10^{-4}	1.40×10^{4}	9.37	6.91	14.43	2.27×10^{13}	83.09
254 nm							
ITO/PMMA/ 5 wt% ZnO/Ag	7.64×10^{-8}	4.3	14.67	66.83	1.24×10^{-4}	7.69×10^{8}	13.32
ITO/PS/5 wt% ZnO/Ag	2.67×10^{-6}	3.75×10^{2}	10.05	9.37	0.0554	1.64×10^{11}	51.50
ITO/P(VDF-TrFE)/5 wt% ZnO/Ag	7.22×10^{-5}	2.80×10^{3}	12.47	14.61	1.50	1.98×10^{12}	68.94

Table 4.1. Summary of performance parameters of polymer/ZnO nanocomposite devices.

4.4.4 Characterization of P(VDF-TrFE) /ZnO nanocomposite thin films

AFM images of the P(VDF-TrFE)/ZnO nanocomposite films with different concentrations of ZnO nanoparticles are shown in Figure 4.7. The RMS surface roughness values are given in Table 4.2. It can be seen that the addition of ZnO nanoparticles to the P(VDF-TrFE) polymer does not affect the fibrillar morphology of the polymer much, though the agglomeration of ZnO nanoparticle increases with an increase in the concentration of the same. The suspension bonds and unsaturated bonds present on the surface of ZnO nanoparticles, having activity are not stable and they combine with other atoms to become stable.[20] So, the higher surface activity and surface area of the ZnO nanoparticles are the reasons for the clustering of nanoparticles.
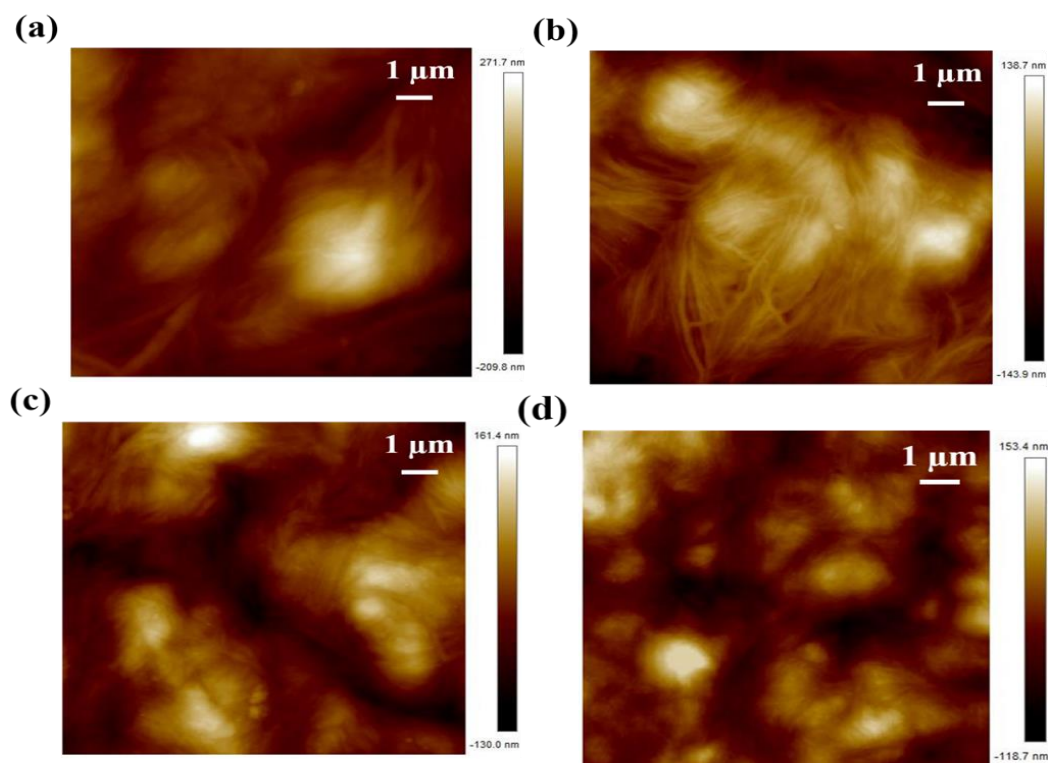
Figure 4.7. AFM images of (a) P(VDF-TrFE) film. (b) P(VDF-TrFE)/0.5 wt% ZnO nanocomposite film (c) P(VDF-TrFE)/1 wt% ZnO nanocomposite film and (d) P(VDF-TrFE)/5 wt% ZnO nanocomposite film.

The crystalline and structural properties of P(VDF-TrFE) film and the nanocomposite films were studied using XRD and FTIR spectroscopy. XRD pattern is shown in Figure 4.8. The XRD peaks observed near 20^0 correspond to the (110) and (200) planes and the peaks observed near 41^0 correspond to the (201) and (111). These are the characteristic peaks of the β phase of the P(VDF-TrFE) matrix.[40] The remaining peaks correspond to the (100), (002), (101), (102), (110), (103) and (112) planes of the ZnO nanoparticles in agreement with the standard card JCPDS 36-1451. From the XRD pattern, it is clear that the crystalline structure of P(VDF-TrFE) is not affected by the addition of ZnO nanoparticles. The weakening of the intensity of the peak observed near 20^0 with the increase in the concentration of ZnO nanoparticles indicates the loss of crystallinity of P(VDF-TrFE) films, which may be due to the agglomeration of ZnO nanoparticles. The % of crystallinity of the β phase in the samples is calculated using the area under the major peak around 20^0 and summarized in Table 4.2.
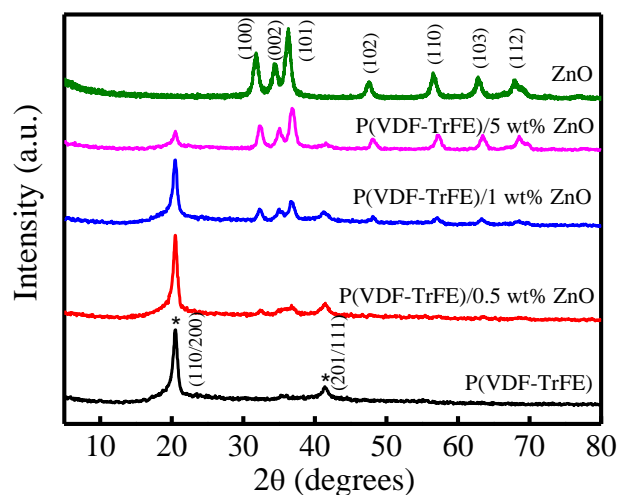
Figure 4.8. XRD pattern of P(VDF-TrFE), ZnO and P(VDF-TrFE)/ZnO nanocomposite films. The XRD peaks of P(VDF-TrFE) is represented by *

Sample	RMS surface roughness (nm)	Crystallinity of β phase (%)
P(VDF-TrFE)	56.8	57.15
P(VDF-TrFE)/0.5 wt% ZnO	44.3	57.02
P(VDF-TrFE)/1 wt% ZnO	44.3	49.50
P(VDF-TrFE)/5 wt% ZnO	37.8	33.58

Table 4.2. The RMS surface roughness values and the crystallinity of β phase in P(VDF-TrFE) and P(VDF-TrFE)/ZnO nanocomposite.

FTIR measurements of the samples were performed to confirm crystalline phase and the FTIR spectra are shown in Figure 4.9. The peaks observed at 510 cm⁻¹, 843 cm⁻¹, 882 cm⁻¹, 1285 cm⁻¹, 1400 cm⁻¹ and 1430 cm⁻¹ confirmed the formation of β phase of P(VDF-TrFE).[41] The peaks at 510 cm⁻¹, 843 cm⁻¹ and 1430 cm⁻¹ may belong to both β and γ phases. However, if 1234 cm⁻¹ is absent then the peaks at 510 cm⁻¹ and 843 cm⁻¹ correspond to β phase only as per previous reports.[42] Also, the peak observed near 1285 cm⁻¹ is the characteristic peak of β phase.[41] The peak observed near 1430 cm⁻¹ can be used to characterize both β and γ phases. However, it can be seen that it is absent in all the films with ZnO. Hence we believe that the presence of γ phase

can be ruled out in our samples. The addition of ZnO nanoparticles does not seem to change the β crystalline phase of P(VDF-TrFE). However, it can be seen that the β phase content is decreasing with the addition of ZnO. Both these observations agree with the findings from XRD. The peaks at 510 cm^{-1} and 1430 cm^{-1} are observed due to the CH$_2$ and CF$_2$ bending vibrations.[43] Symmetric stretching vibrations of CF$_2$ and C-C bonds are represented by the peak observed at 843 cm^{-1}.[12] The peak observed near 882 cm^{-1} corresponds to the rocking of C-C skeleton vibration.[44] The peak at 1285 cm^{-1} is due to the mixed vibrations of CH$_2$ rocking and CF$_2$ asymmetric stretching vibrations.[45] The wagging vibration of CH$_2$ and the bending vibration of CF$_2$ are indicated by the peak at 1400 cm^{-1}.[45]
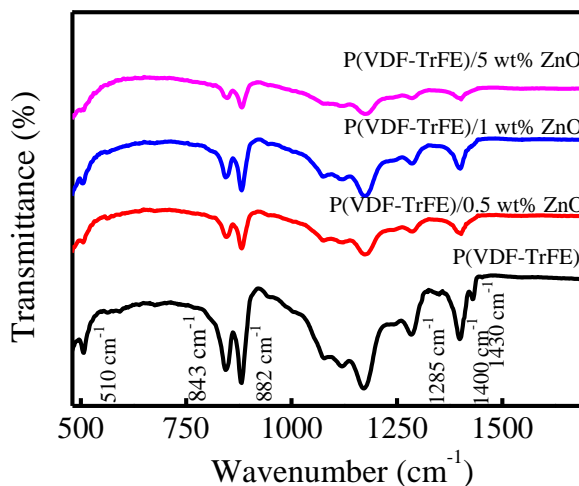
Figure 4.9. FTIR spectra of P(VDF-TrFE) and P(VDF-TrFE)/ZnO nanocomposite films.

The optical properties of the polymer nanocomposite films were studied by means of UV-Visible absorption and PL spectroscopy. The absorption spectra of the samples are shown in Figure 4.10a. The absorbance of P(VDF-TrFE) in the UV region is negligible, which is enhanced with the addition of ZnO nanoparticles. The P(VDF-TrFE)/ZnO nanocomposite films show an absorption peak at 360 nm. The intensity of UV absorption increases with the increase in the concentration of ZnO nanoparticles. The P(VDF-TrFE)/ZnO nanocomposite films are

transparent in the visible region and can be used for spectral selective UV photodetector applications. In other words, they are visible-blind. Figure 4.10b shows the PL spectra of ZnO nanoparticles and P(VDF-TrFE)/ZnO nanocomposites. The intensity of visible emission in ZnO nanoparticles is suppressed in nanocomposites and near band edge emission is enhanced. i.e., the polymer can passivate the surface defects of ZnO. As we will see later, this has important ramifications with regard to the rise time and fall time as well as the visible-blind property of the P(VDF-TrFE)/ZnO nanocomposite based UV photodetectors.
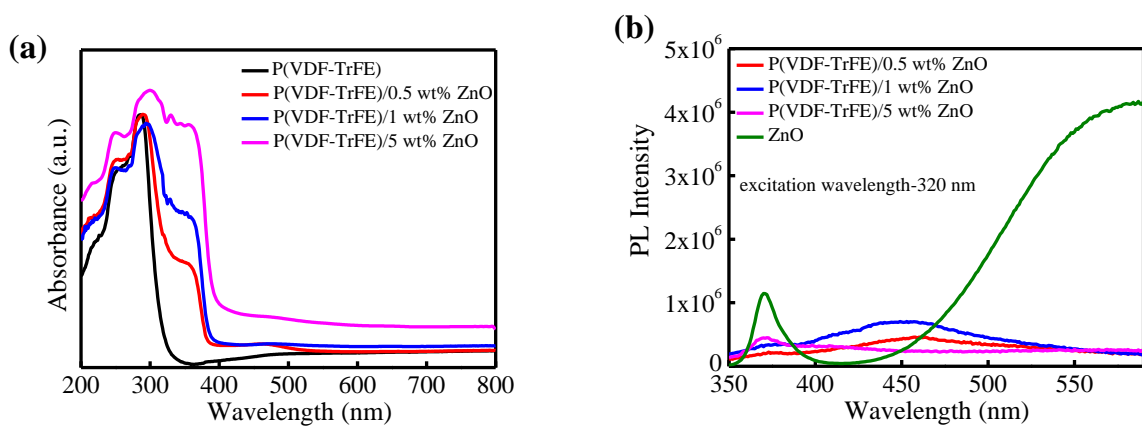
Figure 4.10. (a) UV-Visible absorbance spectra of P(VDF-TrFE) and P(VDF-TrFE)/ZnO nanocomposite films (b) PL spectra of ZnO and P(VDF-TrFE)/ZnO nanocomposite films.

4.4.5 Photodetector measurements

IV characteristics of the devices with Ag top electrode under dark, 365 nm and 254 nm light illumination are shown in Figure 4.10. ITO/P(VDF-TrFE)/Ag device exhibited very low response under UV illumination. The nanocomposite based devices exhibited very good performance with on-off ratio in the order of 10^4 under 365 nm and 254 nm light illumination. It is found that the photocurrent increases with the ZnO concentration. D1 is the ITO/P(VDF-TrFE)/Ag, D2 is the ITO/P(VDF-TrFE)/0.5 wt% ZnO/Ag, D3 is the ITO/P(VDF-TrFE)/1 wt% ZnO/Ag and D4 is the ITO/P(VDF-TrFE)/5 wt% ZnO/Ag device. The values of on–off ratio of

the devices at 2 V are summarized in Table 4.3. The order of on-off ratio was the same for all the nanocomposite devices under 365 nm UV illumination. These devices had very good breakdown strength as they did not fail even at 20 V.
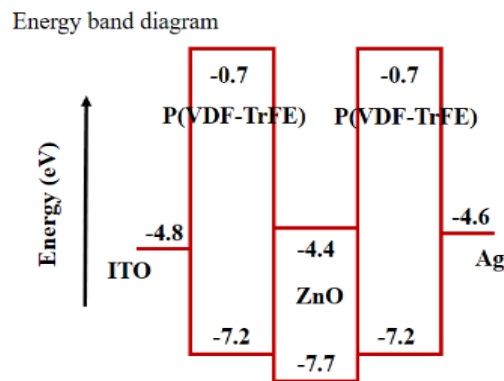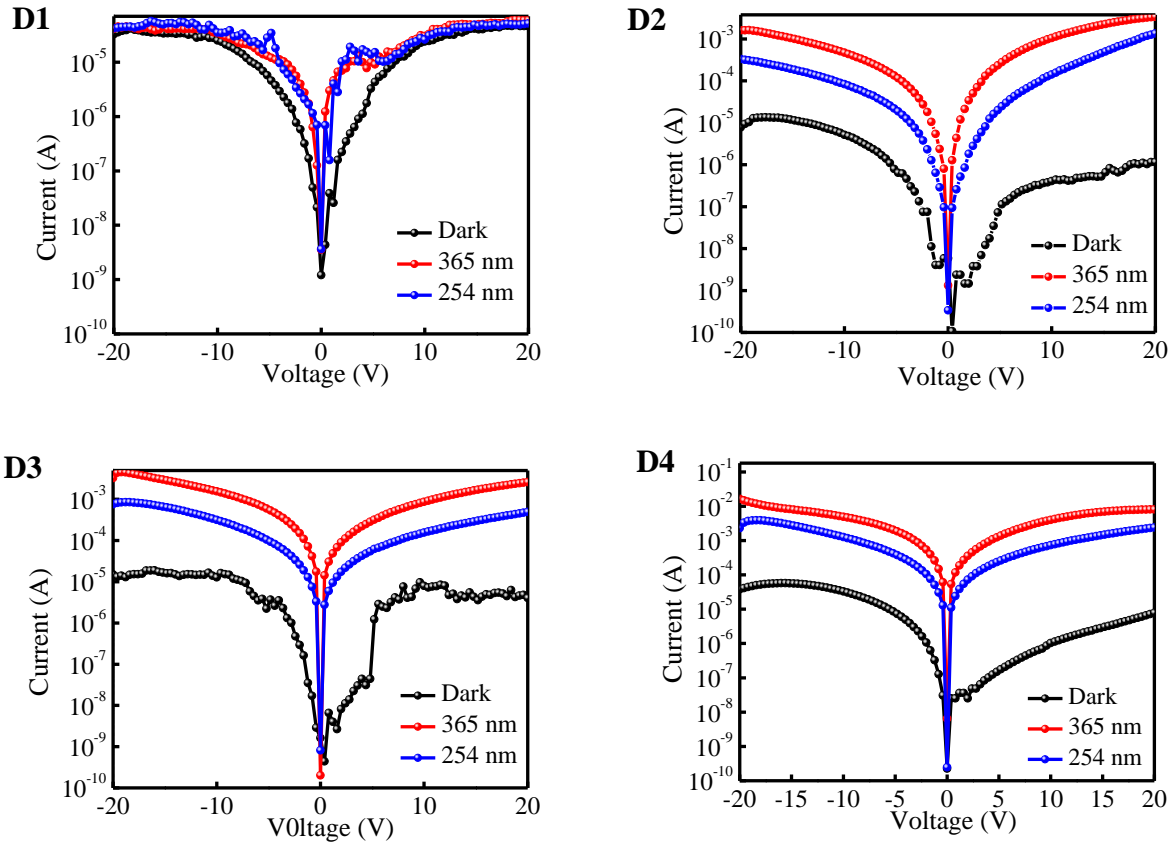
Figure 4.11. IV characteristics of D1, D2, D3 and D4 measured under dark, 365 nm and 254 nm light illumination and energy band diagram of the device.

In agreement with the UV-visible absorption data, these photodetectors did not show any response to RGB LEDs confirming that they are indeed visible-blind.

The results of the transient photoresponse measurements are shown in Figure 4.12. Rise time and fall times were measured for all the devices and the values are summarized in Table 4.3. D4 exhibited faster performance compared to D2 and D3 under 365 nm and 254 nm UV illumination. The comparison of photocurrent and transient photoresponse of the devices under 365 nm and 254 nm light illumination are shown in Figure 4.13.
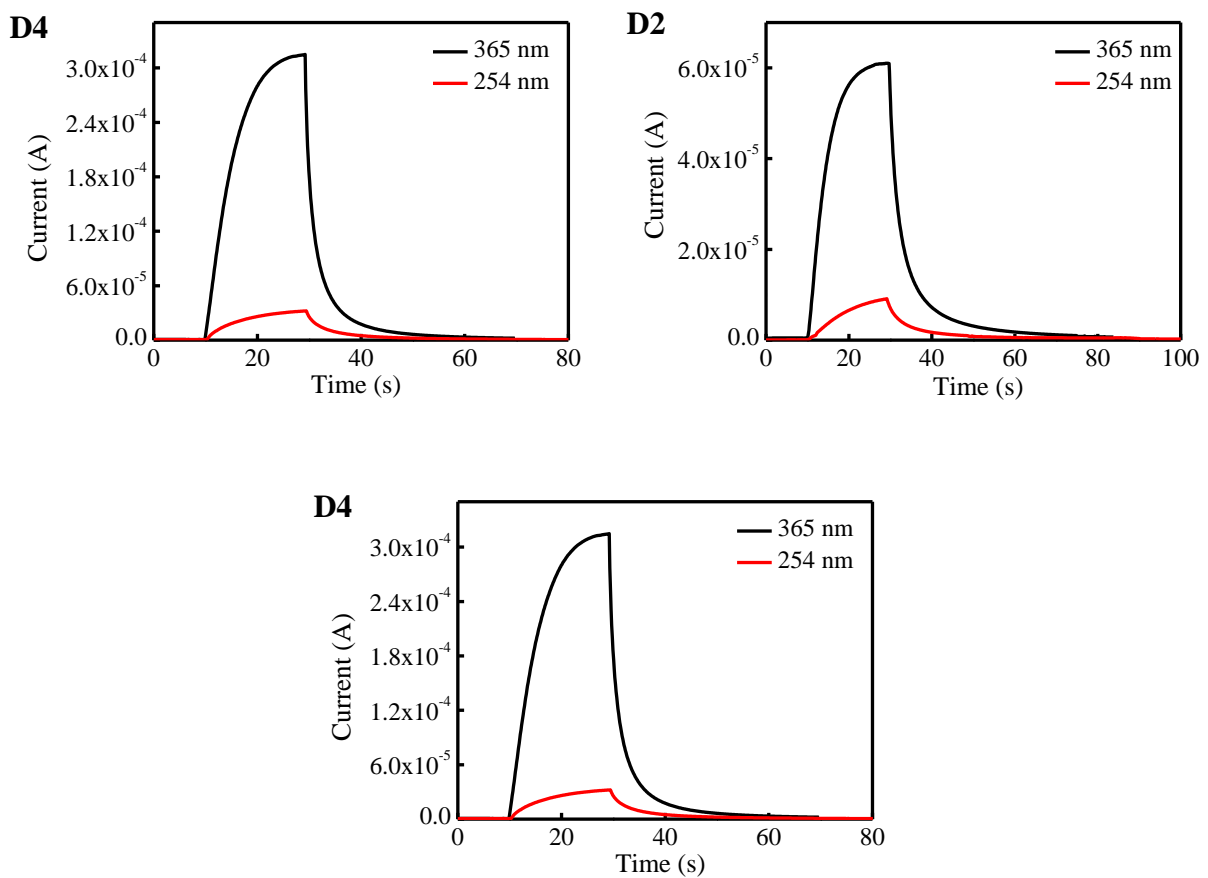
Figure 4.12. Transient photoresponse of the device D2, D3 and D4 measured at 2 V under 365 nm and 254 nm light illumination.

143
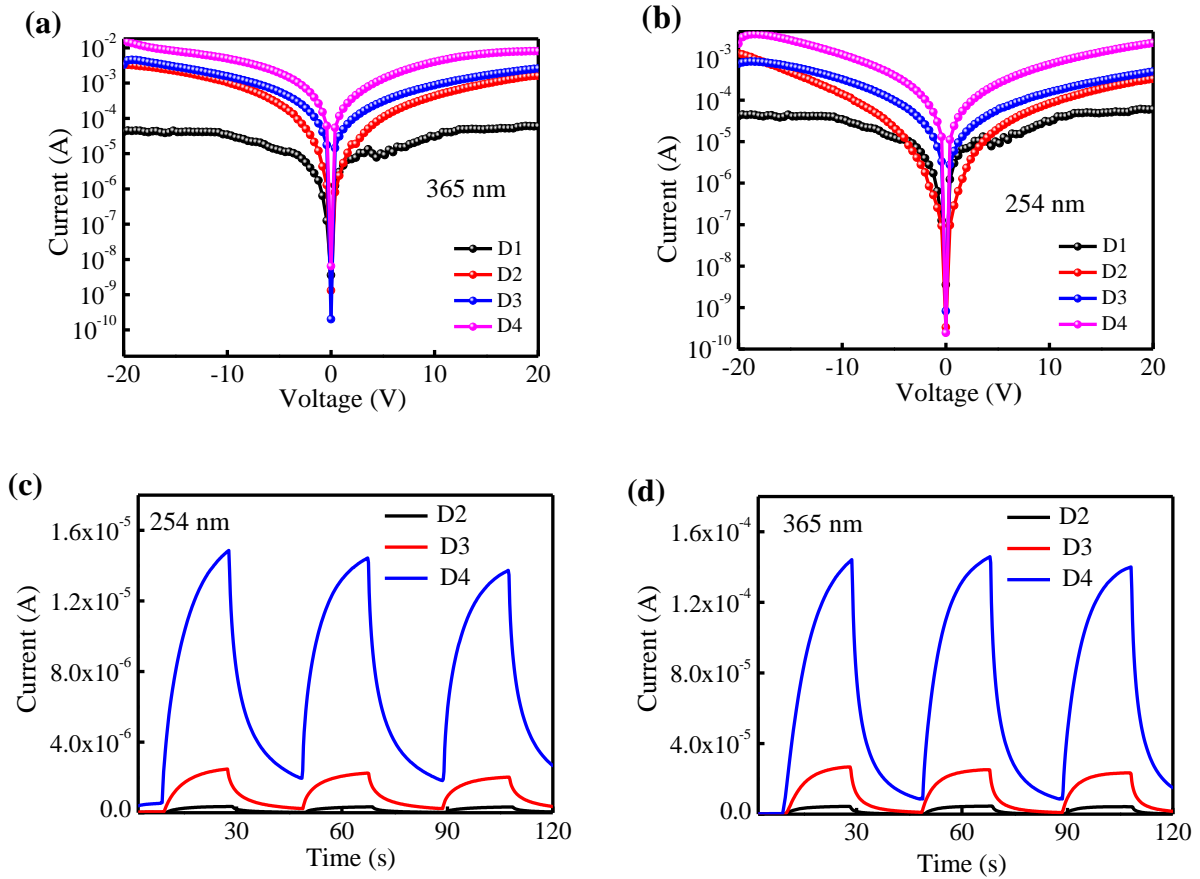
Figure 4.13. (a) Comparison of photocurrent under 365 nm (b) Comparison of photocurrent under 254 nm (c) Comparison of transient photoresponse under 365 nm at 2 V and (d) Comparison of transient photoresponse under 254 nm at 2 V.

The calculated LDR values of the devices are summarized in Table 4.3. The values of LDR of the devices are better than similar devices fabricated based on high-cost materials and by expensive fabrication techniques.[46,47]

The values of responsivity and detectivity are summarized in Table 4.3. It is found that the values of responsivity and detectivity increase with ZnO concentration. The highest value of responsivity, 14.43 A/W and detectivity, 2.27×10^{13} Jones are obtained for the device D4 under 365 nm light illumination. D4 exhibited better performance with more than 50 times enhancement in responsivity under 365 nm compared to D1. An on-off ratio of 10^5 has been reported for electron depleted ZnO-based UV detectors.[48] However, it required a biasing of 5 V

and had very high values of rise and fall times. It may be noted that decorating ZnO with NiO nanoparticles helped bring down the rise and fall times below 10s.[49] The ferroelectric nature of our nanocomposite helps in attaining on-off ratio of 10^4 at 2 V while keeping the rise and fall times below 10s. Surface passivation of ZnO by the polymer seems to reduce the surface defects and improves the rise and fall times. It is also interesting to note that the EQE corresponding to the highest responsivity is 4903%. Here we need to consider many factors. First, P(VDF-TrFE) is reported to support hole transport [50]. It has also been reported that in PVDF, hole injection is preferred when high work function electrodes are used [51]. The energy level diagram of the P(VDF:TrFE): ZnO photodetector is given in Figure 4.11.

Device	On-off ratio	Rise time (s)	Fall time (s)	Responsivity (A/W)	Detectivity (Jones)	LDR (dB)
365 nm						
D1	31.19	-	-	0.27	1.43×10^{11}	29.88
D2	2.30×10^4	8.44	11.16	1.37	9.01×10^{12}	87.23
D3	1.09×10^4	9.09	8.62	3.63	1.01×10^{13}	80.17
D4	1.40×10^4	9.37	6.91	14.43	2.27×10^{13}	83.09
254 nm						
D1	46.23	-	-	0.21	1.11×10^{11}	33.29
D2	1.20×10^3	13.05	19.19	0.03	2.47×10^{11}	61.58
D3	2.10×10^3	11.18	20.06	0.36	9.99×10^{11}	66.44
D4	2.80×10^3	12.47	14.61	1.50	1.98×10^{12}	68.94

Table 4.3. Summary of performance parameters of devices under 365 nm and 254 nm illumination at 2 V.

When UV light is absorbed by ZnO, electron-hole pairs are created. Some holes may migrate to the HOMO of P(VDF-TrFE) due to the favourable energy level. But electrons could be trapped by the surface defects of ZnO and that is why we do not see an appreciable current. In other words, our photodetector does not work in self-powered mode. When we apply a bias to the electrodes, in addition to the exposure of UV light, the positive electrode (anode) energy levels are pushed down relative to the negative electrode (cathode) energy levels and some band bending happens in both P(VDF-TrFE) and ZnO. Anode can more easily inject holes into

P(VDF-TrFE) which can move through the P(VDF-TrFE) matrix. The photogenerated electrons get trapped by the surface defects of ZnO and if ZnO nanoparticles are available in the immediate vicinity to the electrodes, the injection barrier of holes gets further reduced due to this negative charge [52]. This injection current is subsumed in the photocurrent that we measure and that is why the EQE exceeds 100%.
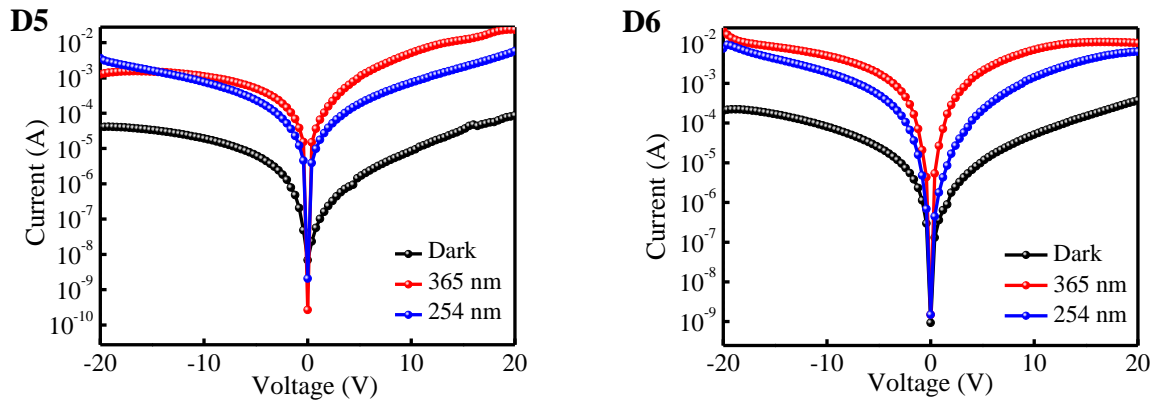
Figure 4.14. IV characteristics of the devices with Al and Au top electrodes measured under dark, 365 nm and 254 nm light illumination.
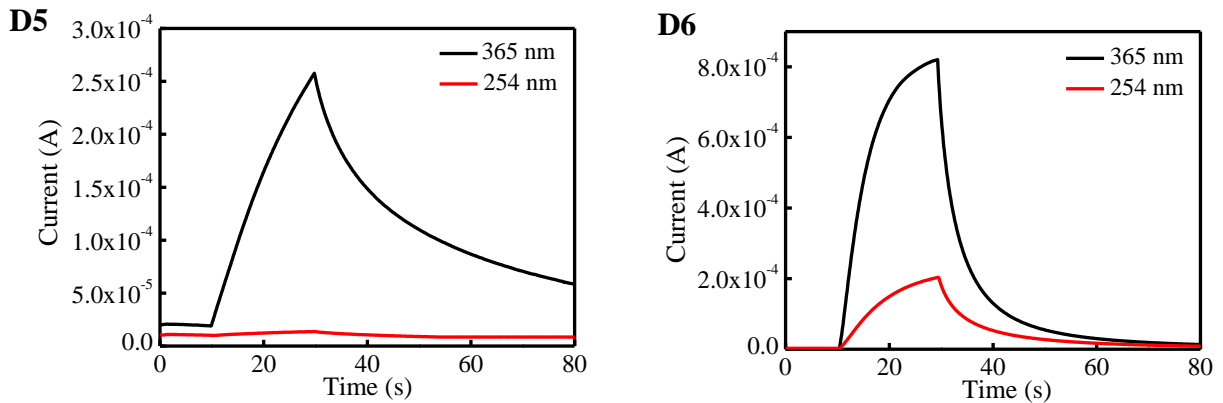
Figure 4.15. Transient photoresponse of the devices with Al and Au top electrodes measured at 2 V under 365 nm and 254 nm light illumination.

Device	Dark current (A)	Photo current (A)	On-off ratio	Rise time (s)	Fall time (s)	Responsivity (A/W)	Detectivity (Jones)	LDR (dB)
365 nm								
D4	2.50×10^{-8}	3.57×10^{-4}	1.43×10^{4}	9.37	6.91	14.43	2.27×10^{13}	83.09
D5	2.35×10^{-7}	1.56×10^{-4}	6.64×10^{2}	10.04	98.47	6.3	3.25×10^{12}	56.46
D6	1.76×10^{-6}	2.85×10^{-4}	1.62×10^{2}	10.14	14.94	11.4	2.15×10^{12}	45.25
254 nm								
D4	2.50×10^{-8}	7.22×10^{-5}	2.89×10^{3}	12.47	14.61	1.50	1.98×10^{12}	68.94
D5	2.35×10^{-7}	3.84×10^{-5}	1.63×10^{2}	15.02	>100	0.79	4.10×10^{11}	44.26
D6	1.76×10^{-6}	1.69×10^{-5}	9.60	13.16	25.50	0.31	5.94×10^{10}	19.63

Table 4.4. Summary of performance parameters of devices with Ag, Al and Au top electrodes under 365 nm and 254 nm illumination at 2 V.

To study the effect of different electrode materials on the performance of photodetectors, we fabricated devices with different top electrodes and compared the device performances. Since D4 exhibited better performance, we fabricated devices with Al and Au electrodes with the rest of the device design identical to D4. D5 is ITO/P(VDF-TrFE)/5 wt% ZnO/Al device and D6 is ITO/P(VDF-TrFE)/5 wt% ZnO/Au. The results are summarized in Table 4.4.

ITO/P(VDF-TrFE)/5 wt% ZnO/Ag device exhibited better performance with an on-off ratio 1.4×10^{4}; responsivity 14.43 A/W; and fast response under 365 nm light illumination. This device showed the highest photocurrent and the lowest dark current. ITO/P(VDF-TrFE)/5 wt% ZnO/Al showed responsivity of 6.3 A/W, but it showed a very large value for fall time. When Al is deposited on the P(VDF-TrFE)/0.5 wt% ZnO nanocomposite surface, the chances of its chemical reaction with the atoms on the nanocomposite surface are enhanced. Kochervinkii et

al. have studied the effect of top electrode material on the properties of P(VDF-TrFE).[53] They found that there are defects such as oxygen-containing groups and those due to chemical addition, present on the surface of the polymer. These defects interact with the Al particles due to the latter's low work function and form Al_2O_3 and Al_xF_y.[53] These new functional groups form a low conductivity layer on the surface and affect device performance. Under 254 nm light illumination also ITO/P(VDF-TrFE)/5 wt% ZnO/Ag device exhibited better performance. The differences in the performance of the devices are due to the difference in the work function of the electrode materials.[54] The IV characteristics of D5 and D6 are shown in Figure 4.14 and the transient photoresponse is shown in Figure 4.15. The device with Ag top electrode exhibited maximum value of photocurrent, responsivity, detectivity, LDR and on-off ratio and exhibited minimum value of dark current, rise time and fall time at 365 nm and 254 nm light illumination. ZnO is a well-known electron transport material and P(VDF-TrFE) has been reported to be supporting hole current.[51] Thus, the choice of these materials is very useful for realizing high photoresponse.

The effect of morphology of ZnO on the photoresponse properties were studied by additionally fabricating ITO/P(VDF-TrFE)/1 wt% ZnO nanorods/Ag (D7) and ITO/P(VDF-TrFE)/1 wt% ZnO nanoflowers/Ag (D8).

4.4.6 Characterization of ZnO nanorods

The morphology of ZnO nanorods were studied by SEM and TEM. The SEM and TEM images are shown in Figure 4.16a and 4.16b. The length of the nanorods slightly varies with average length around 7 μm. HMTA plays an important role in the formation of ZnO nanorods. It regulates the pH of the solution and promotes rod like growth of ZnO nanostructures. The hydroxyl ions formed by the thermal degradation of HMTA react with Zn^{2+} ions to form ZnO.[55] The SEM and TEM images are in agreement with each other. It is confirmed by the EDS spectra that only Zn and O elements are present in the sample as shown in Figure 4.16c. The weight

percentages of Zn and O elements in the sample are given in the inset table. The XRD pattern of ZnO nanorods is shown in Figure 4.16d. All the XRD peaks were identified in the recorded range of 2θ with the standard card JCPDS 36-1451. It confirmed the hexagonal wurtzite structure of ZnO nanorods and crystallite size is found to be 71.36 nm.
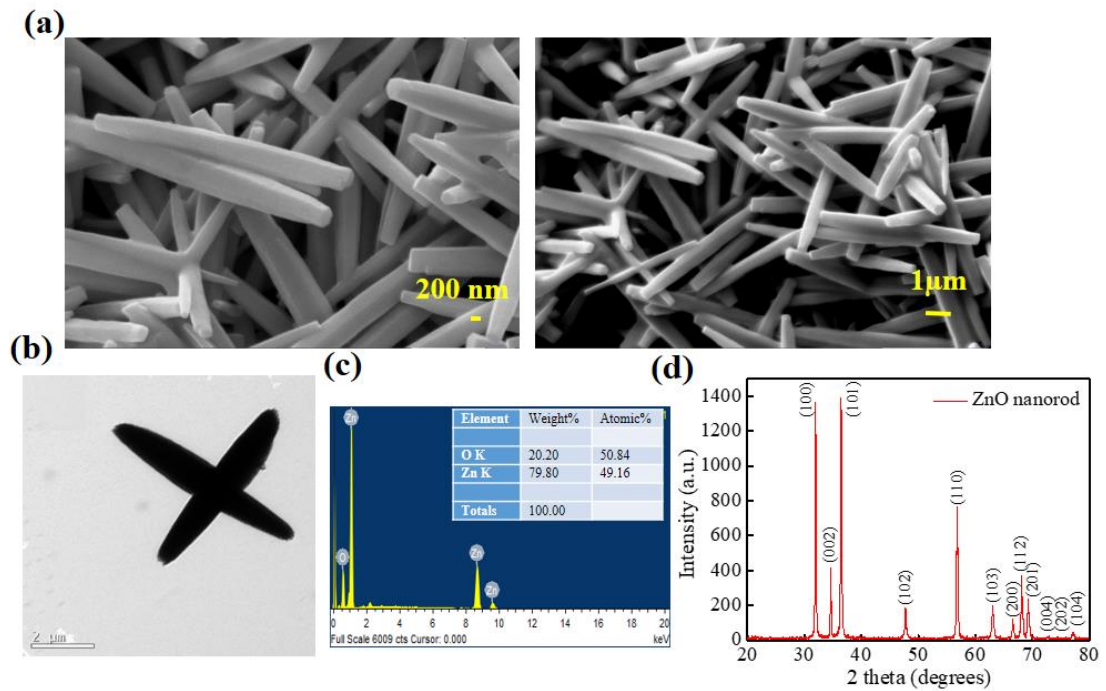
Figure 4.16. (a) SEM images of ZnO nanorods (b) TEM images of ZnO nanorods (c) EDS spectra of ZnO nanorods and (d) XRD pattern of ZnO nanorods.

4.4.7 Characterization of ZnO nanoflowers
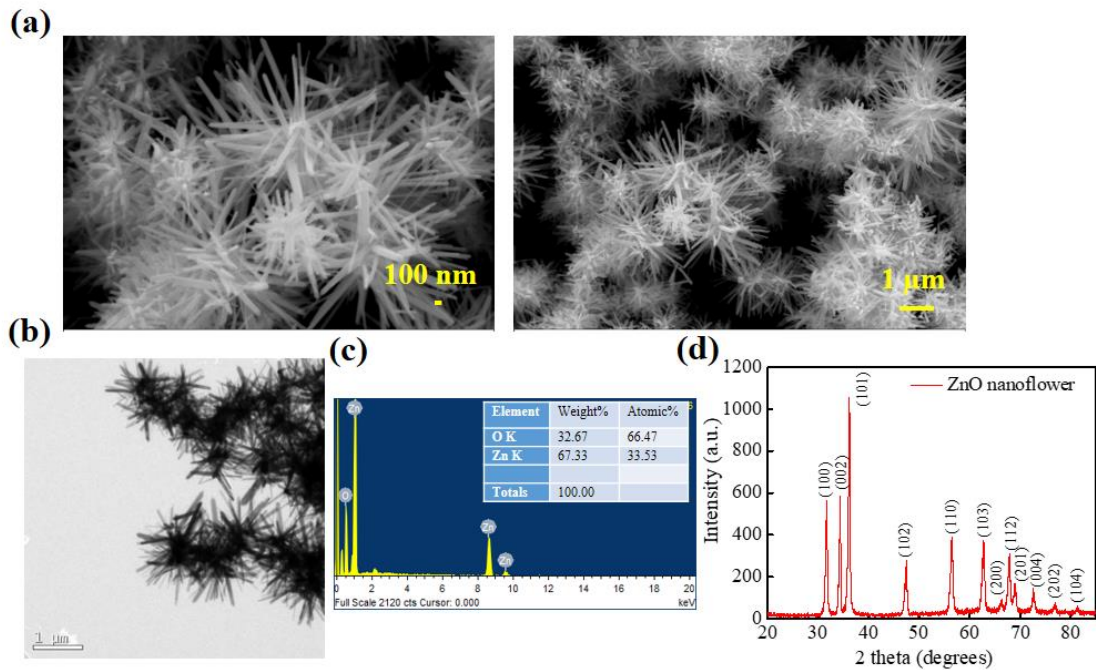
Figure 4.17. (a) SEM images of ZnO nanoflowers (b) TEM images of ZnO nanoflowers (c) EDS spectra of ZnO nanoflowers and (d) XRD pattern of ZnO nanoflowers.

SEM and TEM images of ZnO nanoflowers are shown in Figure 4.17a and 17b. The flower like morphology of ZnO can be easily seen in TEM and SEM images. ZnO nanoflowers consist of several ZnO nanorods originating from a single centre. The nanorods form a flower shape to reduce the surface energy. The purity of the chemical composition is determined by EDS spectra shown in Figure 4.17c. The sample contains no impurity with strong peaks corresponding to Zn and O. XRD pattern shown in Figure 4.17d confirmed the hexagonal wurtzite structure and the crystallite size is found to be 65.24 nm.

4.4.8 Characterization of P(VDF-TrFE)/ 1 wt% ZnO nanorods and P(VDF-TrFE)/1 wt% ZnO nanoflowers

SEM images of the nanocomposites are shown in Figure 4.18. The ZnO nanorods and nanoflowers are uniformly dispersed in the polymer. The addition of ZnO nanorods and nanoflowers are not affecting the morphology of P(VDF-TrFE) similar to that of P(VDF-TrFE)/ZnO nanoparticle composite.

(a)   **(b)**
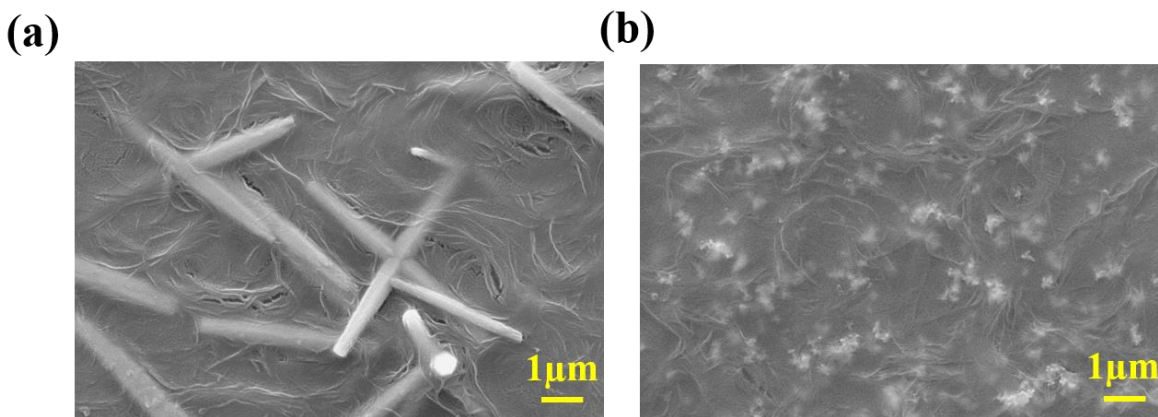
Figure 4.18. (a) SEM image of P(VDF-TrFE)/1 wt% ZnO nanorod (b) SEM image of P(VDF-TrFE)/1 wt% ZnO nanoflower.

Absorption and PL spectra of P(VDF-TrFE)/ 1wt% ZnO nanostructures are shown in Figure 4.19a and 4.19b. P(VDF-TrFE)/1 wt% ZnO nanoparticles showed maximum absorption in the UV region. All nanocomposites are transparent in the visible region and are suitable for visible-blind photodetection applications. In the PL spectra, it is clear that the intensity of near band edge emission is higher than that of visible emission due to defects in all nanocomposites. It indicates that the surface defects and trap states present in ZnO nanostructures are effectively passivated by P(VDF-TrFE).
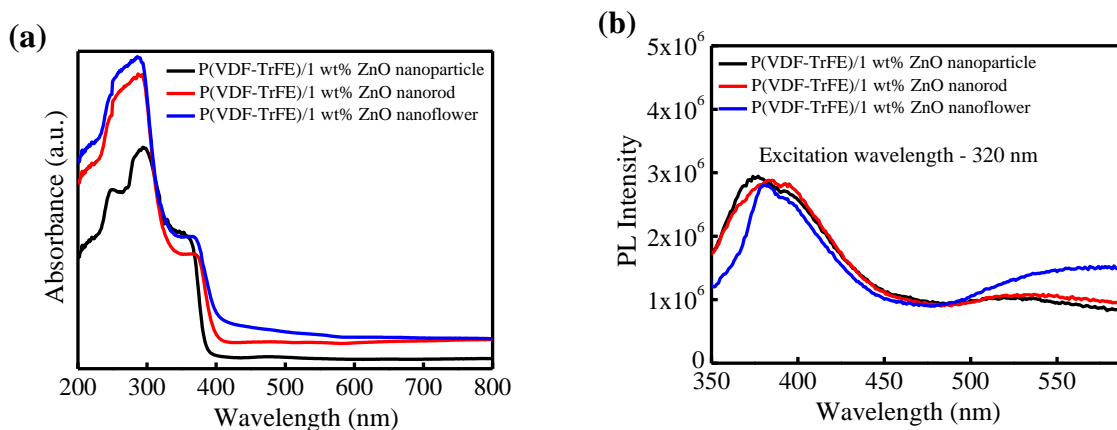
Figure 4.19. (a) Absorption spectra of P(VDF-TrFE) 1 wt% ZnO nanostructures (b) PL spectra of P(VDF-TrFE) 1 wt% ZnO nanostructures.

4.4.9 Photodetector measurements of ITO/P(VDF-TrFE)1 wt% ZnO nanostructures/Ag

IV characteristics of the devices, ITO/ P(VDF-TrFE)1 wt% ZnO nanoparticles/Ag (D3), ITO/ P(VDF-TrFE)1 wt% ZnO nanorods/Ag (D7), ITO/ P(VDF-TrFE)1 wt% ZnO nanoflowers/Ag (D8) under dark, 365 nm and 254 nm light illumination are shown in Figure 4.11 and in Figure 4.20. The performance parameters are summarized in Table 4.5. It is found that the device D8 exhibited low dark current and maximum value of on-off ratio of 4.48×10^5 at 0 V under 365 nm light illumination. The morphology of ZnO nanostructures plays a significant role in the device performance. D7 and D8 are self-powered when illuminated with 365 nm and 254 nm. ZnO nanorods exhibit high surface to volume ratio and long conduction path[56] and compared to ZnO nanoparticles and nanorods, ZnO nanoflowers show high surface to volume ratio and large surface area. They can increase the light travelling path and thereby increase the light absorption efficiency.[57] This feature makes them suitable for high performance photodetection applications. A bridging network is formed between ZnO nanorods in D5 and between nanoflowers in D6 and this provides a continuous path for the electrons to flow. This bridging network makes the devices self-powered.

Transient photoresponse of the devices under 365 nm and 254 nm are shown in Figure 4.21. Compared to D7 and D8, D3 exhibited fast response. Responsivity, Detectivity and LDR values were calculated and summarized in Table 4.5. D8 is self-powered with a responsivity of 4.2 mA/W, detectivity of 2.18×10^{12} and LDR of 113.03 under 365 nm. So, P(VDF-TrFE)/ZnO nanoflower nanocomposites are suitable for the fabrication of high performance self-powered UV photodetectors. Spectral response measurements of D7 and D8 confirmed that they are visible-blind and they can be used for UV selective applications. Results of spectral response measurements are shown in Figure 4.22.
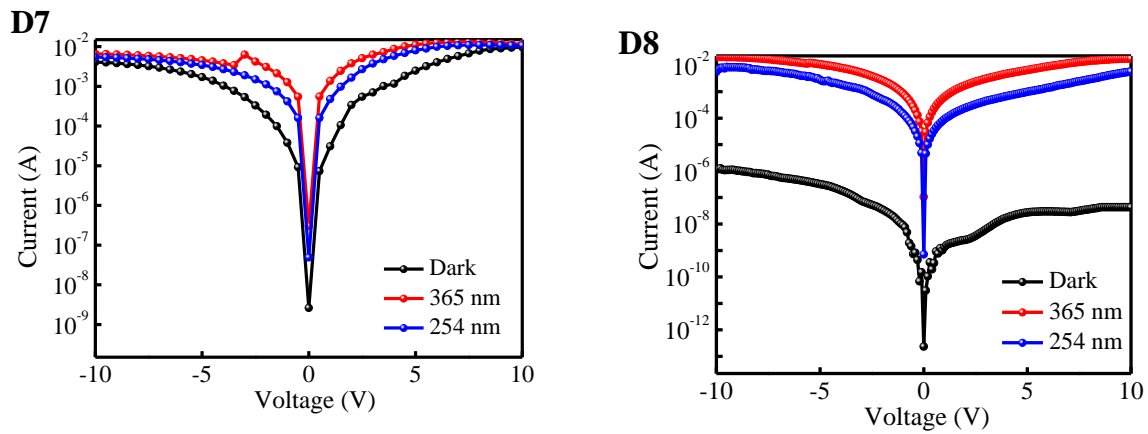
Figure 4.20. IV characteristics of D7 and D8.
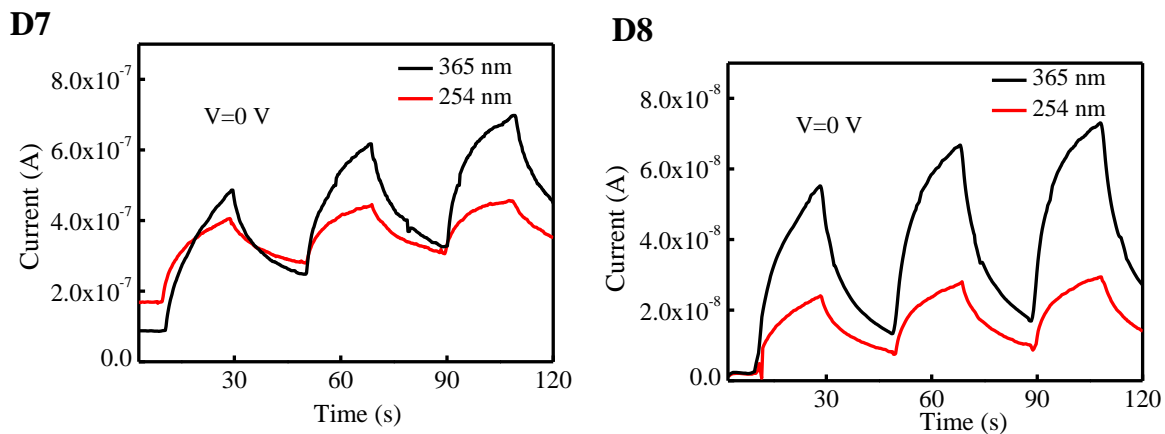
Figure 4.21. Transient photoresponse of D7 and D8.
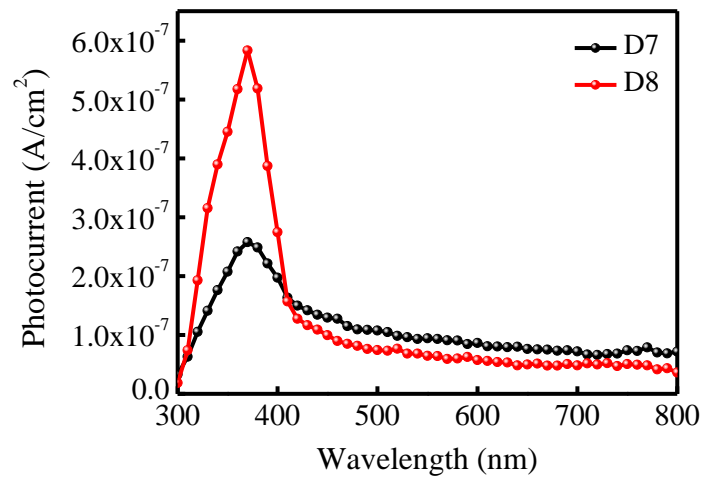
Figure 4.22. Spectral response of D7 and D8.

Device	On-off ratio	Rise time (s)	Fall time (s)	Responsivity (A/W)	Detectivity (Jones)	LDR (dB)
365 nm						
D3-ITO/P(VDF-TrFE)/1 wt% ZnO nanoparticle/Ag at 1 V	1.2×10^4	7.31	6.76	1.974	7.78×10^{12}	81.72
D7-ITO/P(VDF-TrFE)/1 wt% ZnO nanorod/Ag at 0 V	1.1×10^2	-	-	0.012	5.96×10^{10}	41.18
At 1 V	44.78	-	-	54.43	2.45×10^{12}	33.02
D8-ITO/P(VDF-TrFE)/1 wt% ZnO nanoflower/Ag at 0 V	4.48×10^5	13.74	63.35	0.0042	2.18×10^{12}	113.03
At 1 V	4.15×10^5	20.69	40.76	25.17	1.62×10^{14}	112.37
254 nm						
D3-ITO/P(VDF-TrFE)/1 wt% ZnO nanoparticle/Ag at 1 V	2.3×10^3	7.62	15.85	0.198	7.84×10^{11}	67.52
D7-ITO/P(VDF-TrFE)/1 wt% ZnO nanorod/Ag at 0 V	18.65	-	-	0.001	5.23×10^9	25.41
At 1 V	15.51	-	-	9.32	4.19×10^{11}	23.81
D8-ITO/P(VDF-TrFE)/1 wt% ZnO nanoflower/Ag at 0 V	3.04×10^3	12.90	82.86	1.48×10^{-5}	7.67×10^9	69.68
At 1 V	5.99×10^4	22.32	175.58	1.87	1.21×10^{13}	95.55

Table 4.5. Performance parameters of D3, D7 and D8.

4.5 Conclusions

PMMA/ZnO, PS/ZnO and P(VDF-TrFE)/ ZnO nanoparticle nanocomposites were synthesized and photoresponse properties were studied. P(VDF-TrFE)/ZnO nanocomposite devices exhibited better performance and the effect of concentration of ZnO on the device performance was studied by varying ZnO concentration in the polymer matrix. The surface morphology and structural, optical and crystalline properties of P(VDF-TrFE)/ZnO nanocomposites thin films have been studied and the formation of the β crystalline phase has been confirmed by XRD and FTIR spectra. It is seen that the % of crystallinity decreases and UV absorption increases with ZnO concentration. The photoresponse properties have been studied with ITO as the bottom electrode and Ag, Au or Al as the top electrode. The choice of the top electrode and ZnO concentration show a profound influence on the UV photodetector performance. P(VDF-TrFE)/5 wt% ZnO nanocomposite based UV photodetector with Ag top electrode exhibited best performance with a responsivity, 14.43 A/W; detectivity, 2.27×10^{13} Jones; LDR, 83.09 dB and on-off ratio, 1.43×10^4 under 365 nm light illumination at 2 V. The built-in field due to polarization of P(VDF-TrFE) helps in separating the electron-hole pair formed in ZnO upon UV irradiation. The UV absorption, responsivity and detectivity are increasing with the increase in ZnO concentration. The effect of morphology of ZnO nanostructure in the polymer matrix was studied by fabricating UV detectors based on P(VDF-TrFE)/1 wt% ZnO nanorod and P(VDF-TrFE)/ 1 wt% ZnO nanoflower composites. These devices were self-powered due to the long conduction path and high surface to volume ratio of ZnO nanorods and nanoflowers. The results indicate the feasibility of fabrication of low-cost, self-powered, flexible and highly sensitive visible-blind UV photodetectors with P(VDF-TrFE)/ZnO nanocomposites.

4.6 References

1. Guo, X. *et al.* Solution processable organic/inorganic hybrid ultraviolet photovoltaic detector. *AIP Adv.* **6**, 055318 (2016).

2. Bie, Y. Q. *et al.* Self-Powered, Ultrafast, Visible-Blind UV Detection and Optical Logical Operation based on ZnO/GaN Nanoscale p-n Junctions. *Adv. Mater.* **23**, 649–653 (2011).

3. Son, D. I., Yang, H. Y., Kim, T. W. & Park, W. Il. Transparent and flexible ultraviolet photodetectors based on colloidal ZnO quantum dot/graphene nanocomposites formed on poly(ethylene terephthalate) substrates. *Compos. Part B Eng.* **69**, 154–158 (2015).

4. Hanna, B., Manuraj, M., Surendran, K. P. & Unni, K. N. N. Opto-electronic properties of solution-processed zinc oxide thin films: role of solvents and doping. *J. Mater. Sci. Mater. Electron.* **31**, 13570–13577 (2020).

5. Deka Boruah, B. Zinc oxide ultraviolet photodetectors: rapid progress from conventional to self-powered photodetectors. *Nanoscale Adv.* **1**, 2059–2085 (2019).

6. Najib, S. *et al.* Tailoring morphology to control defect structures in ZnO electrodes for high-performance supercapacitor devices. *Nanoscale* **12**, 16162–16172 (2020).

7. Fan, Z. & Lu, J. G. Zinc Oxide Nanostructures: Synthesis and Properties. *J. Nanosci. Nanotechnol.* **5**, 1561–1573 (2005).

8. Tian, C. *et al.* Performance enhancement of ZnO UV photodetectors by surface plasmons. *ACS Appl. Mater. Interfaces* **6**, 2162–2166 (2014).

9. Patra, S. *et al.* ZnO polymer composite based visible blind UV photo detector. *Mater. Res. Bull.* **101**, 240–245 (2018).

10. Ponnamma, D. *et al.* Synthesis, optimization and applications of ZnO/polymer nanocomposites. *Mater. Sci. Eng. C* **98**, 1210–1240 (2019).

11. Han, J. *et al.* Highly Sensitive Impact Sensor Based on PVDF-TrFE/Nano-ZnO Composite Thin Film. *Sensors* **19**, 830 (2019).

12. Tan, K. S., Gan, W. C., Velayutham, T. S. & Majid, W. H. A. Pyroelectricity enhancement of PVDF nanocomposite thin films doped with ZnO nanoparticles. *Smart Mater. Struct.* **23**, 125006 (2014).

13. Yang, H. Y., Son, D. I., Kim, T. W., Lee, J. M. & Park, W. Il. Enhancement of the photocurrent in ultraviolet photodetectors fabricated utilizing hybrid polymer-ZnO quantum dot nanocomposites due to an embedded graphene layer. *Org. Electron.* **11**, 1313–1317 (2010).

14. Lee, S.-W. *et al.* Low Dark-Current, High Current-Gain of PVK/ZnO Nanoparticles Composite-Based UV Photodetector by PN-Heterojunction Control. *Sensors* **16**, 74 (2016).

15. Mathen, J. J. *et al.* Transparent ZnO–PVA binary composite for UV-A photo detector: optical, electrical and thermal properties followed by laser induced fluorescence. *J. Mater. Sci. Mater. Electron.* **28**, 7190–7203 (2017).

16. Mousavi, S. S., Sajad, B. & Majlesara, M. H. Fast response ZnO/PVA nanocomposite-based photodiodes modified by graphene quantum dots. *Mater. Des.* **162**, 249–255 (2019).

17. G, H. *et al.* Negative photoresponse in ZnO–PEDOT:PSS nanocomposites and photogating effects. *Nanoscale Adv.* **1**, 2435–2443 (2019).

18. Cao, F., Tian, W., Meng, L., Wang, M. & Li, L. Ultrahigh-Performance Flexible and Self-Powered Photodetectors with Ferroelectric P(VDF-TrFE)/Perovskite Bulk Heterojunction. *Adv. Funct. Mater.* **29**, 1808415 (2019).

19. Karumuthil, S. C., Rajeev, S. P. & Varghese, S. Poly(vinylidene fluoride-trifluoroethylene)-ZnO Nanoparticle Composites on a Flexible Poly(dimethylsiloxane) Substrate for Energy Harvesting. *ACS Appl. Nano Mater.* **2**, 4350–4357 (2019).

20. Li, J. *et al.* Enhanced piezoelectric output of the PVDF-TrFE/ZnO flexible piezoelectric nanogenerator by surface modification. *Appl. Surf. Sci.* **463**, 626–634 (2019).

21. Park, C. H., Lee, K. H., Lee, B. H., Sung, M. M. & Im, S. Channel/ferroelectric interface modification in ZnO non-volatile memoryTFT with P(VDF-TrFE)polymer. *J. Mater. Chem.* **20**, 2638–2643 (2010).

22. Dodds, J. S., Meyers, F. N. & Loh, K. J. Piezoelectric Characterization of PVDF-TrFE Thin Films Enhanced With ZnO Nanoparticles. *IEEE Sens. J.* **12**, 1889–1890 (2012).

23. Kim, T. Y. *et al.* Ferroelectric-mediated filamentary resistive switching in P(VDF-TrFE)/ZnO nanocomposite films. *Phys. Chem. Chem. Phys.* **20**, 16176–16183 (2018).

24. Wang, P. *et al.* Ferroelectric Localized Field-Enhanced ZnO Nanosheet Ultraviolet Photodetector with High Sensitivity and Low Dark Current. *Small* **14**, 1800492 (2018).

25. Kang, D. H., Kim, N. K. & Kang, H. W. High efficient photo detector by using ZnO nanowire arrays on highly aligned electrospun PVDF-TrFE nanofiber film. *Nanotechnology* **30**, 365303 (2019).

26. Shen, T. *et al.* Ultrahigh-Performance Self-Powered Flexible Photodetector Driven from Photogating, Piezo-Phototronic, and Ferroelectric Effects. *Adv. Opt. Mater.* **8**, 1901334 (2020).

27. He, Y. *et al.* Study of the photoconductive ZnO UV detector based on the electrically floated nanowire array. *Sensors Actuators A Phys.* **181**, 6–12 (2012).

28. Singh, S. *et al.* A study of hydrothermally grown ZnO nanorod-based metal-semiconductor-metal UV detectors on glass substrates. *Nanomater. Nanotechnol.* **7**, 184798041770214 (2017).

29. Young, S.-J. *et al.* Flexible Ultraviolet Photodetectors Based on One-Dimensional Gallium-Doped Zinc Oxide Nanostructures. *ACS Appl. Electron. Mater.* **2**, 3522–3529 (2020).

30. Liu, K., Sakurai, M. & Aono, M. ZnO-Based Ultraviolet Photodetectors. *Sensors* **10**, 8604–8634 (2010).

31. Shi, L. *et al.* Status and Outlook of Metal–Inorganic Semiconductor–Metal Photodetectors. *Laser Photon. Rev.* **15**, 2000401 (2021).

32. Al-Khalli, N. & Debbar, N. Performance enhancement of ZnO-based MSM photodiodes by optimizing structure parameters. *Int. J. Numer. Model. Electron. Networks, Devices*

Fields **32**, e2519 (2019).

33. Hanna, B., Surendran, K. P. & Narayanan Unni, K. N. Low temperature-processed ZnO thin films for p–n junction-based visible-blind ultraviolet photodetectors. *RSC Adv.* **8**, 37365–37374 (2018).

34. C K, S., Valiyaneerilakkal, U., Singh, K. & Varghese, S. Device level optimization of poly(vinylidene fluoride-trifluoroethylene)–zinc oxide polymer nanocomposite thin films for ferroelectric applications. *J. Appl. Phys.* **118**, 204102 (2015).

35. Arshad, A. N. *et al.* Dielectric and Structural Properties of Poly(vinylidene fluoride) (PVDF) and Poly(vinylidene fluoride-trifluoroethylene) (PVDF-TrFE) Filled with Magnesium Oxide Nanofillers. *J. Nanomater.* **2019**, 1–12 (2019).

36. Gaddam, V., Kumar, R. R., Parmar, M., Nayak, M. M. & Rajanna, K. Synthesis of ZnO nanorods on a flexible Phynox alloy substrate: influence of growth temperature on their properties. *RSC Adv.* **5**, 89985–89992 (2015).

37. Zhang, H. *et al.* Characterization and modeling of a ZnO nanowire ultraviolet photodetector with graphene transparent contact. *J. Appl. Phys.* **114**, 234505 (2013).

38. Hanna, B., Pillai, L. R., Rajeev, K., Surendran, K. P. & Unni, K. N. N. Visible-blind UV photodetectors using a polymer/ZnO nanocomposite thin film. *Sensors Actuators A Phys.* **338**, 113495 (2022).

39. Jung, S.-W. Nonvolatile Ferroelectric P(VDF-TrFE) Memory Transistors Based on Inkjet-Printed Organic Semiconductor. *ETRI J.* **35**, 734–737 (2013).

40. Wang, F., Kong, Y., Liu, Z. & Zhu, H. All-organic Poly(butyl methacrylate)/Poly(vinylidenefluoride-trifluoroethylene) Dielectric Composites with Higher Permittivity and Low Dielectric Loss for Energy Storage Application. *Polym. Plast. Technol. Eng.* **56**, 526–534 (2017).

41. Chen, S., Yao, K., Tay, F. E. H. & Chew, L. L. S. Comparative investigation of the structure and properties of ferroelectric poly(vinylidene fluoride) and poly(vinylidene fluoride-trifluoroethylene) thin films crystallized on substrates. *J. Appl. Polym. Sci.* **116**, 3331–3337 (2010).

42. Cai, X., Lei, T., Sun, D. & Lin, L. A critical analysis of the α, β and γ phases in poly(vinylidene fluoride) using FTIR. *RSC Adv.* **7**, 15382–15389 (2017).

43. Habibur, R. M., Yaqoob, U., Muhammad, S., Uddin, A. S. M. I. & Kim, H. C. The effect of RGO on dielectric and energy harvesting properties of P(VDF-TrFE) matrix by optimizing electroactive β phase without traditional polling process. *Mater. Chem. Phys.* **215**, 46–55 (2018).

44. Xia, K. *et al.* Research on the effect of spin-coating process on ferroelectric phase of PVDF-TrFE/ZnO film. in *2016 Symposium on Piezoelectricity, Acoustic Waves, and Device Applications (SPAWDA)* 248–252 (IEEE, 2016).

45. Augustine, R. *et al.* Electrospun poly(vinylidene fluoride-trifluoroethylene)/zinc oxide nanocomposite tissue engineering scaffolds with enhanced cell adhesion and blood vessel formation. *Nano Res.* **10**, 3358–3376 (2017).

46. Song, W. *et al.* High-performance self-powered UV-Vis-NIR photodetectors based on horizontally aligned GaN microwire array/Si heterojunctions. *J. Mater. Chem. C* **5**,

11551–11558 (2017).

47. Guo, F., Xiao, Z. & Huang, J. Fullerene Photodetectors with a Linear Dynamic Range of 90 dB Enabled by a Cross-Linkable Buffer Layer. *Adv. Opt. Mater.* **1**, 289–294 (2013).

48. Nasiri, N., Bo, R., Wang, F., Fu, L. & Tricoli, A. Ultraporous Electron-Depleted ZnO Nanoparticle Networks for Highly Sensitive Portable Visible-Blind UV Photodetectors. *Adv. Mater.* **27**, 4336–4343 (2015).

49. Nasiri, N., Bo, R., Fu, L. & Tricoli, A. Three-dimensional nano-heterojunction networks: a highly performing structure for fast visible-blind UV photodetectors. *Nanoscale* **9**, 2059–2067 (2017).

50. Hanna, A. N., Bhansali, U. S., Khan, M. A. & Alshareef, H. N. Characterization of current transport in ferroelectric polymer devices. *Org. Electron.* **15**, 22–28 (2014).

51. Xia, F. & Zhang, Q. M. Schottky emission at the metal polymer interface and its effecton the polarization switching of ferroelectric poly(vinylidenefluoride-trifluoroethylene) copolymer thin films. *Appl. Phys. Lett.* **85**, 1719–1721 (2004).

52. Guo, F. *et al.* A nanocomposite ultraviolet photodetector based on interfacial trap-controlled charge injection. *Nat. Nanotechnol.* **7**, 798–802 (2012).

53. Kochervinskii, V. V., Chubunova, E. V. & Bedin, S. A. An effect of electrode material on pinning layer characteristics and depolarization field in polymer ferroelectrics. *J. Appl. Phys.* **124**, 064102 (2018).

54. Zhou, W. *et al.* Electrode effect on high-detectivity ultraviolet photodetectors based on perovskite oxides. *J. Appl. Phys.* **114**, 224503 (2013).

55. Strano, V. *et al.* Double Role of HMTA in ZnO Nanorods Grown by Chemical Bath Deposition. *J. Phys. Chem. C* **118**, 28189–28195 (2014).

56. Zhang, Y., Ram, M. K., Stefanakos, E. K. & Goswami, D. Y. Synthesis, Characterization, and Applications of ZnO Nanowires. *J. Nanomater.* **2012**, 1–22 (2012).

57. Gedamu, D. *et al.* Rapid Fabrication Technique for Interpenetrated ZnO Nanotetrapod Networks for Fast UV Sensors. *Adv. Mater.* **26**, 1541–1550 (2014).

SUMMARY AND FUTURE SCOPE OF WORK

We have developed a room temperature-processable ZnO film, fabricated UV-detectors using different configurations and tried to address the challenges of self-powering of the devices and passivation of the surface defects with various techniques. Also, we have made an attempt to correlate the morphology of the ZnO nanostructures with the performance of the UV detector. In chapter 2, self-powered and low temperature processable UV detectors were fabricated based on organic-inorganic hybrid heterojunction. The defects in the ZnO thin films were passivated by a thin layer of TiO_2. The device performance is optimized by varying the thickness of the organic layer. Different organic layers were used in the device structure to study the spectral response properties. In chapter 3, low operating voltage UV photodetectors based on ZnO nanorods were fabricated in photoconductor configuration. Different morphologies of ZnO nanorods were synthesized by facing the substrate in different orientations in the growth solution. The defects in ZnO nanorods were passivated by using the surface passivation layer. The effect of growth time on electrical, optical and photoresponse properties of nanorods were studied. In chapter 4, UV photodetectors based on ZnO nanoparticle/polymer nanocomposites were fabricated. The defects present in the ZnO nanoparticles were passivated by the polymer coating and the device exhibited better performance at low bias voltages. ZnO nanorod/polymer and ZnO nanoflower/polymer nanocomposites were synthesized and photoresponse properties were studied.

In summary, out of the various design strategies, organic-inorganic hybrid heterojunction based devices are the suitable choice to fabricate visible-blind, fast response, self-powered and flexible UV detectors. ZnO nanoparticle/P(VDF-TrFE) nanocomposite based devices showed excellent photoresponse with maximum on-off ratio at 2 V. The ZnO nanoflower/P(VDF-TrFE) nanocomposite based devices are self-powered due to the formation of bridging network between ZnO nanoflowers. ZnO nanorod based devices showed good photoresponse properties. But they exhibited long response and decay times due to the presence of defects.

In future, printed self-powered and wearable UV sensors can be fabricated by developing screen printable ink formulations from ZnO nanoparticles. Multiband response photodetectors from UV to IR region can be fabricated using organic-inorganic hybrid heterojunction. The properties of polymer/ZnO nanocomposite can be varied by changing the concentration and morphology of ZnO and by changing the choice of the polymer and its processing. The device performance can be further improved by using different metal oxides and different device configurations of ZnO nanostructures. Eventually, these may lead to high efficiency early missile warning systems and fire detection systems

ABSTRACT

Name of the Student: **Ms. Hanna B.**

Registration No. : 10PP16J39007

Faculty of Study: Physical Sciences

Year of Submission: 2022

AcSIR academic centre/CSIR Lab: CSIR-National Institute for Interdisciplinary Science and Technology (CSIR-NIIST)

Name of the Supervisor(s): Dr. K. N. Narayanan Unni & Dr. K. P. Surendran

Title of the thesis: **Studies on visible-blind ultraviolet photodetectors with low voltage operation using zinc oxide nanostructures**

Chapter 1 gives the fundamental ideas of the working mechanism and different types of UV photodetectors and the challenges in device fabrication. A brief overview of the developments in this area with particular focus on ZnO-based UV photodetectors is given. It also outlines the challenges in ZnO-based, self-powered, flexible and wearable UV detector fabrication.

Chapter 2 Gives the details of fabrication of a self-powered p-n junction photodiode based on annealing-free ZnO thin films prepared from ZnO nanoparticles and N,N′-Di(1-naphthyl)-N,N′-diphenyl-(1,1′-biphenyl)-4,4′-diamine (NPB). At zero bias, the device exhibited responsivity of 0.017 A/W, external quantum efficiency (EQE) of 5.68%, an on-off ratio more than 10^3 and linear dynamic range (LDR) of 63 dB. A high built-in potential at the ZnO/NPB interface could be the reason for this performance at zero bias. The rise and fall times were 156 ms and 319 ms respectively. The device performance was optimized by varying the thickness of the NPB layer. The device with 30 nm thick NPB film exhibited better performance. Further, different organic materials were used for device fabrication. The properties of the organic layer influence the spectral response properties of the devices. The device with NPB as an organic layer exhibited the best performance for a UV detector.

Chapter 3 Deals with the fabrication and characterization of visible-blind ultraviolet (UV) photodetectors based on ZnO nanorods fabricated on glass substrates in planar photoconductor configuration with Au electrodes. Nanorods of different morphologies were obtained by placing the seed layer coated substrate in the growth solution in face-up or face-down configurations during chemical bath deposition. The intensity of defect emission due to surface states was higher than that of the near band edge emission (NBE) in both cases. The defect emission was substantially controlled by forming a homojunction of the nanorods with a thin layer of ZnO nanoparticles as a surface passivation layer deposited by spin coating. The response time of the devices measured at 1 V was reduced upon the deposition of the ZnO film as a surface passivation layer. The rise time of the face-down sample with ZnO thin film was reduced by 24.01% and fall time by 34.53% under 254 nm light illumination. Nanorods were grown for different growth durations to study the effect of growth time on the structural and photoresponse properties of the device. The device having face-down ZnO nanorods with the passivation film exhibited the best transient photoresponse at 365 nm and 254 nm UV illumination. The rise and fall times of the face-down ZnO nanorods were improved by depositing the nanorods on the interdigitated ITO coated substrates. The device exhibited an on-off ratio of 1.50×10^3, rise and fall times of 1.88 s and 6.39 s, detectivity of 4.20×10^{11} Jones responsivity of 55.60 mA/W and LDR of 62.01 dB at 1 V under 365 nm light illumination.

Chapter 4 Describes the fabrication and characterization of polymer/ZnO nanocomposite based visible-blind UV photodetectors. UV photodetectors based on nanocomposites of ZnO with three polymers, poly(methyl methacrylate) (PMMA), polystyrene (PS) and poly(vinylidene difluoride-trifluoroethylene (P(VDF-TrFE)) were prepared by physical mixing method. P(VDF-TrFE)/ZnO nanocomposite-based device exhibited the best performance possibly due to its ferroelectric property. Then we studied the influence of the concentration of ZnO nanoparticles in P(VDF-TrFE) by preparing thin films of the latter with 0.5 wt%, 1wt% and 5 wt% ZnO nanoparticles. Effect of electrode materials on the photodetector performance of nanocomposites was studied by using ITO bottom electrode and top electrode with either Al, Ag or Au. The device with Ag showed the best performance. Electrical response of the detector to 365 nm and 254 nm UV light illumination was studied and P(VDF-TrFE)/5 wt% ZnO nanocomposite with top Ag electrode exhibited the best performance with on-off ratio, 1.4×10^4; responsivity, 14.43 A/W; linear dynamic range, 83.09 dB and detectivity, 2.27×10^{13} Jones under 365 nm light illumination at 2 V biasing. Ferroelectric polarization mechanism of P(VDF-TrFE) and the choice of electrode play an important role in separating the charge carriers upon UV illumination. Finally the influence of morphology of ZnO was studied by synthesizing ZnO nanorods and nanoflowers and characterizing photodetectors based on P(VDF-TrFE)/1 wt% ZnO nanorod and P(VDF-TrFE)/1 wt% ZnO nanoflower composites.

List of publications

Details of publications emanating from the thesis work

Published

1. **Hanna B**, Lekshmi R Pillai, Kavya Rajeev, Surendran K P and Narayanan Unni K N "Visible-blind UV photodetectors using a polymer/ZnO nanocomposite thin film", Sensors Actuators A Physical, 2022, 338, 113495

2. **Hanna B**, Surendran K P and Narayanan Unni K N, "Opto-electronic properties of solution-processed zinc oxide thin films: role of solvents and doping", journal of materials science: materials in electronics, 2020, 31, 13570-13577

3. **Hanna B**, Surendran K P and Narayanan Unni K N, "Low temperature-processed ZnO thin films for p-n junction based visible blind ultraviolet photodetectors", RSC Advances, 2018,8,37365

Manuscripts submitted/under preparation

4. **Hanna B**, Surendran K P and Narayanan Unni K N, "Ultraviolet photodetectors based on ZnO nanorods: effect of oriented growth and surface passivation" (Under preparation)

5. **Hanna B**, Surendran K P and Narayanan Unni K N, "Broadband photodetectors based on organic-inorganic hybrid heterojunction using annealing-free ZnO thin films" (Under preparation)

6. **Hanna B**, Surendran K P and Narayanan Unni K N, "Polymer/ZnO nanocomposite-based ultraviolet photodetectors: influence of nanomorphology of ZnO" (Under preparation)

List of conference presentations

1. Ultraviolet photodetectors based on ZnO nanorods synthesized by chemical bath deposition method. **Hanna B**, K. P. Surendran and K. N. Narayanan Unni. A poster presented in ICEM-14 at CSIR- NIIST, Thiruvananthapuram on 2020, 5-7 February

2. Ultraviolet photodetectors based on ZnO nanorods. **Hanna B**, K. P. Surendran and K. N. Narayanan Unni. A poster presented in ICAFM at CSIR- NIIST, Thiruvananthapuram on 2019, 9-10 December

3. Ultraviolet photodetectors based on zinc oxide: dependence on morphology, **Hanna B**, K. P. Surendran and K. N. Narayanan Unni A paper presented at 31st Kearala Science Congress at Fatima Matha National College,   Kollam on 2019, 2-3 February

4. ZnO nanoflower/ Carbon Nanotube Nanocomposite Electrodes for Supercapacitors, **Hanna B**, Manuraj Mohan, K. P. Surendran, R. B. Rakhi and K. N. Narayanan Unni. A poster presented at National Conference on Emerging Trends in Science Technology & Application of Electron Microscope (STAEM)-2018 at CSIR-National Institute for Interdisciplinary Science and Technology (NIIST), Thiruvananthapuram on 2018, 19-21 December.

5. Annealing-free ZnO nanocomposite thin films for ultraviolet photodetectors, **Hanna B**, K. P. Surendran and K. N. Narayanan Unni. A poster presented at International Symposium on Functional Materials (ISFM-2018): Energy and Biomedical Applications organized by IIT Kanpur, UIC USA and PU Chandigargh at Hotel Shivalik View on 2018, 14-16 April

6. Ultraviolet photodetector based on NPB/ZnO nanoparticle heterojunction, **Hanna B** and K. N. Narayanan Unni. A paper presented at National Conference on Luminescence and its Applications at CSIR-National Institute for Interdisciplinary Science and Technology (NIIST), Thiruvananthapuram on 2018, 14-16 February

7. Studies on p-doped ZnO thin films prepared by sol-gel technique, **Hanna B**, Manuraj M and K. N. Narayanan Unni. A poster presented at 8th East Asia Symposium on Functional Dyes and Advanced Materials (EAS 8) at CSIR-National Institute for Interdisciplinary Science and Technology (NIIST), Thiruvananthapuram on 2017, 20-22 September

Visible-blind UV photodetectors using a polymer/ZnO nanocomposite thin film

B. Hanna [a,c], Lekshmi R. Pillai [d], Kavya Rajeev [a,c], K.P. Surendran [b,c], K.N.N. Unni [a,c,*]

[a] *Photosciences and Photonics Section, Chemical Sciences and Technology Division, CSIR-National Institute for Interdisciplinary Science and Technology, Thiruvananthapuram 695019, Kerala, India*
[b] *Functional Materials Section, Materials Science and Technology Division, CSIR-National Institute for Interdisciplinary Science and Technology, Thiruvananthapuram 695019, Kerala, India*
[c] *Academy of Scientific and Innovative Research (AcSIR), Ghaziabad 201002, India*
[d] *Department of Physics, T K Madhava Memorial College, Nangiarkulangara 690513, India*

ARTICLE INFO

ABSTRACT

We report the fabrication and characterization of visible-blind UV photodetectors using thin films of polymer/zinc oxide (ZnO) nanocomposites. Polymer-ZnO nanocomposites based on three polymers, poly(methyl methacrylate)(PMMA), polystyrene(PS) and poly(vinylidene difluoride-trifluoroethylene(P(VDF-TrFE)) were studied. The electrical response of the detectors to 365 nm and 254 nm UV light illumination was probed. P(VDF-TrFE)/ZnO nanocomposite-based device exhibited the best performance compared to the other devices, possibly due to its ferroelectric property. Further, we prepared P(VDF-TrFE)/ZnO nanocomposite with different wt% of ZnO nanoparticles and characterized them by atomic force microscopy (AFM), X-ray diffraction (XRD), fourier transform- infrared spectroscopy (FTIR), UV-Visible absorption spectroscopy, and Photoluminescence (PL). XRD and FTIR studies confirmed the formation of the β phase of P(VDF-TrFE) in pristine polymer films and their nanocomposites. The influence of the top electrode material on the photodetector performance of nanocomposites was studied. P(VDF-TrFE)/5 wt% ZnO nanocomposite with Ag top electrode exhibited the best performance with on-off ratio, 1.4×10^4; responsivity, 14.43 A/W; linear dynamic range, 83.09 dB and detectivity, 2.27×10^{13} jones under 365 nm light illumination. The ferroelectric polarization mechanism of P(VDF-TrFE) and the choice of electrode play an important role in the performance of the devices.

1. Introduction

UV photodetectors have been getting increased attention in the last few years due to their potential applications in pollution monitoring systems, satellite communication systems, flame detection, missile warning, etc. [1]. ZnO, TiO$_2$, GaN, diamond, SiC, etc., are the commonly used materials for fabricating UV photodetectors. Among them, ZnO is popular due to its relatively large exciton binding energy, wide direct bandgap, non-toxicity, low cost, versatility in synthetic methods, high stability, etc. [2,3]. Also, different morphologies of ZnO can be easily synthesized by cost-effective techniques [4]. Many research groups have reported UV photodetectors based on ZnO [5–8]. Graphene nanodot arrays/ZnO hybrid UV detector exhibited better performance than a ZnO-based device with a responsivity of 22.55 mA/W and rise and fall

time of 2.5 s and 11 s, respectively [9]. Ning et al. reported transparent and self-powered UV photodetector based on crossed ZnO nanofiber array homojunction. The device showed an on-off ratio of 10^4 and rise and fall time of 3.90 s and 4.71 s, respectively [10]. ZnO/NiO heterojunction-based device exhibited maximum responsivity of 0.415 mA/W, rise time of 7.5 s, and fall time of 4.8 s [11]. Organic/inorganic core-shell photodetectors fabricated by depositing p-type conducting polyaniline on ZnO microwire array showed fast response with a responsivity of 0.56 mA/W at zero bias [12]. Though ZnO-based devices exhibit high photoconductivity gain, they show extended response and recovery times due to the persistent photoconductivity (PPC) effect produced by the surface states and defects [13]. These also lead to visible emission and thus limit their applications in UV selective spectral response. Polymer/ZnO composite systems are becoming attractive due

* Corresponding author at: Photosciences and Photonics Section, Chemical Sciences and Technology Division, CSIR-National Institute for Interdisciplinary Science and Technology, Thiruvananthapuram 695019, Kerala, India.
E-mail address: unni@niist.res.in (K.N.N. Unni).

to their applications in pressure sensors, photodetectors, super-capacitors, medical devices, food packaging systems, coatings, water treatment, etc. [14,15]. It is found that the polymer properties could be altered by the addition of inorganic nanofillers into the polymer matrix [16]. A polymer nanocomposite can be defined as a system containing nanofillers of a size less than 100 nm in at least one dimension. These nanofillers act as dopants to enhance the properties of polymers by the quantum confinement effect [15]. The properties of the polymer/ZnO nanocomposite film can be modified by varying the size and morphology of the ZnO nanoparticles [17]. The properties of the polymer matrix, in turn, can influence the nanocomposite properties. Polymer nano-composites can be prepared either by physical or chemical mixing methods. In the physical mixing method, the nanoparticles and polymer matrix are connected by van der-Waal's or Lewis acid-base interaction. In the case of the chemical mixing method, strong interaction occurs between the nanoparticles and the polymer matrix due to the chemical reaction between them [15].

Polymer/ZnO nanocomposite is a good choice for fabricating flexible UV photodetectors. Park et al. fabricated UV photodetectors based on PVK/ZnO quantum dots modified by graphene layer, which exhibited good performance with an on/off ratio of 10^8 at 0.4 V under 365 nm light illumination [18]. In 2016, Kang et al. fabricated a solution-processable UV photodetector based on ZnO/PVK nano-composite. The device exhibited a fast response and on/off ratio of 10^3 [19]. Later, in 2017, Joseph et al. fabricated a UV-A photodetector based on ZnO/PVA nanocomposite. The photodetector exhibited a rise time of 1.017 s and a long recovery time of 602.2 s [20]. Patra et al. fabricated a PVDF and PVP-based polymer/ZnO nanocomposite-based UV photode-tector. The ZnO/PVDF device exhibited a response time of 40 s, and ZnO/PVP device exhibited a response time of 0.167 s [14]. UV photo-diodes based on ZnO/PVA nanocomposite modified by graphene quantum dots were fabricated by Majlesara et al. in 2019 [21]. The device exhibited a responsivity of 26.8 A/W and a photocurrent of 1.07 μA at 365 nm light illumination. The response time of the device with ZnO/PVA nanocomposite without modification is too long, which is improved upon modification by graphene quantum dots [21]. Mitra et al. studied the negative photoresponse in ZnO/PEDOT: PSS nano-composite under UV and visible light [22]. They found that the conductance of the device is decreased by the trapping of holes in the PEDOT: PSS channel by the electrons generated upon illumination in the ZnO nanoparticles. The device exhibited a long response time due to the large junction capacitance produced by the charges trapped at the ZnO nanoparticle surface [22].

The polymer matrix affects the optoelectronic properties of the nanocomposite, and hence the choice of the polymer is crucial in photodetector applications. In this work, we have selected three poly-mers, poly(methyl methacrylate)(PMMA), polystyrene(PS) and poly (vinylidene difluoride-trifluoroethylene(P(VDF-TrFE)). PMMA and PS are both thermoplastic polymers with many similar physical properties. PMMA has several optics, medical technologies, and aesthetic applica-tions, whereas PS is widely used for packaging. Impact strength and tensile strength are better for PMMA. P(VDF-TrFE) is a ferroelectric polymer with many promising applications in the electronic industry. All three polymers are fairly transparent in the visible and thus can be used for fabricating visible blind photodetectors. In this work, we syn-thesized PMMA/ZnO, PS/ZnO, and P(VDF-TrFE)/ ZnO nanocomposites by the physical mixing method, and the UV photodetectors were fabri-cated in ITO/ polymer/ZnO nanocomposite/ M structure, where M could be Ag, Au or Al.

2. Experimental

The experimental procedure for the synthesis and characterization of PMMA/ZnO, PS/ZnO, and P(VDF-TrFE)/ ZnO nanocomposites and de-vice fabrication is given in Supplementary Information.

## 3. Results and discussions

3.1. Optical properties of polymer/ZnO nanocomposite thin films

The optical properties of the polymer/ZnO nanocomposite films were studied using UV-Visible absorption spectroscopy. The UV visible absorption spectra of polymer/ZnO nanocomposite films are shown in Fig. 1, and absorption spectra of different polymer films are shown in ESI Fig. S1. P(VDF-TrFE)/5 wt% ZnO nanocomposite film showed higher absorbance in the UV region 300–400 nm, and all three films were transparent in the visible region. It is well-known that the surface defects of ZnO lead to emission in the visible region. The polymer matrix seems to have passivated these defects, and the visible emission is suppressed in the PL spectra of the polymer nanocomposite films, as shown in ESI Fig. S2.

3.2. Photodetector measurements

The devices were exposed to UV light from both sides, i.e, from the glass/ITO side (bottom side) and the metal electrode side (top side). Typical photoresponse for 365 nm and 254 nm when exposed from the bottom side is shown in Fig. S3 in the Supplementary Information. The photoresponse to 254 nm when exposed from the bottom side is extremely weak. Glass/ITO absorbs in the UV region, and it is more severe for 254 nm, which may be a reason for the diminished perfor-mance of the detector in this wavelength. The transmission spectrum of glass/ITO is shown in Fig. S4 of the Supplementary Information. It can be seen that the transmission of 254 nm is very weak. While the device being exposed from the top, the UV transmission of the metal electrode becomes important. The transmission spectrum of Fig. 0.100 nm Ag film on quartz has been given in Fig. S5, Supplementary Information. We can see that the electrode does allow partial transmission of 365 nm and 254 nm though the latter is much weaker. Hence, the results of UV exposure from the top side only are discussed hereafter.

IV characteristics of ITO/PMMA/5 wt% ZnO/Ag, ITO/PS/5 wt% ZnO/Ag and ITO/P(VDF-TrFE)/5 wt% ZnO/Ag devices under dark, 365 nm light illumination at an intensity of 1.24 mW/cm^2 and under 254 nm light illumination at an intensity of 2.4 mW/cm^2 are shown in Fig. 2. The ITO/P(VDF-TrFE)/5 wt% ZnO/Ag device performed better under 365 nm illumination. The performance parameters of the devices at 2 V are summarized in Table 1. It is found that the performance of the device depends on the choice of the polymer. At 2 V, the responsivity of P(VDF-TrFE)/ZnO nanocomposite was 14.43 A/W; that of PS/ZnO nanocomposite was 0.64 A/W, and that of PMMA/ZnO nanocomposite was 0.02 A/W. The more insulating nature of PMMA may be a reason for
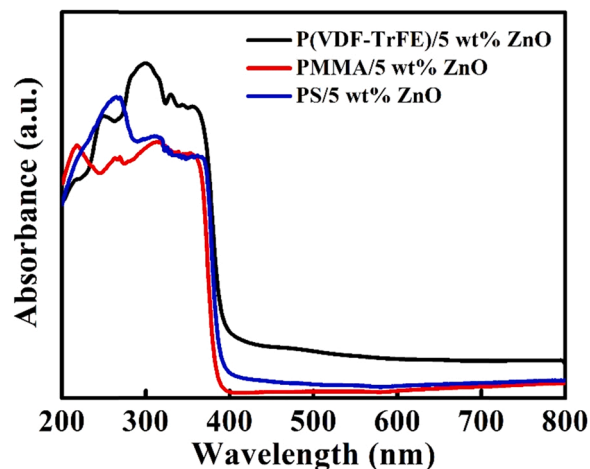
Fig. 1. UV visible absorption spectra of PMMA/ 5 wt% ZnO, PS/5 wt% ZnO, and P(VDF-TrFE)/5 wt% ZnO nanocomposite films.
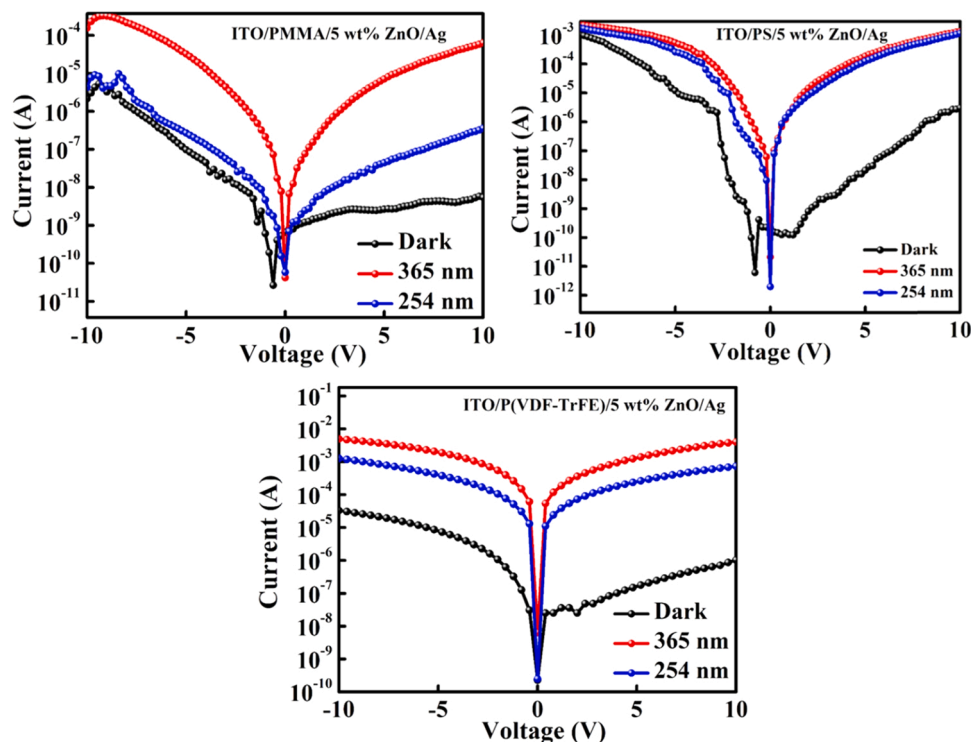
Fig. 2. IV characteristics of ITO/PMMA/ 5 wt% ZnO/Ag, ITO/PS/5 wt% ZnO/Ag and ITO/P(VDF-TrFE)/5 wt% ZnO/Ag devices.

Table 1
Summary of performance parameters of polymer/ZnO nanocomposite devices.

Device	Photocurrent (A)	On-off ratio	Rise time (s)	Fall time (s)	Responsivity (A/W)	Detectivity (jones)	LDR (dB)
365 nm							
ITO/PMMA/5 wt% ZnO/Ag	4.13×10^{-7}	2.5×10^2	14.57	45.69	0.016	1.02×10^{11}	47.98
ITO/PS/5 wt% ZnO/Ag	1.58×10^{-5}	2.2×10^3	12.36	10.18	0.638	1.89×10^{12}	66.96
ITO/P(VDF-TrFE)/5 wt% ZnO/Ag	3.579×10^{-4}	1.40×10^4	9.37	6.91	14.43	2.27×10^{13}	83.09
254 nm							
ITO/PMMA/5 wt% ZnO/Ag	7.64×10^{-8}	4.3	14.67	66.83	1.24×10^{-4}	7.69×10^8	13.32
ITO/PS/5 wt% ZnO/Ag	2.67×10^{-6}	3.75×10^2	10.05	9.37	0.0554	1.64×10^{11}	51.50
ITO/P(VDF-TrFE)/5 wt% ZnO/Ag	7.224×10^{-5}	2.80×10^3	12.47	14.61	1.50	1.98×10^{12}	68.94

the lower performance. The ferroelectric property of P(VDF-TrFE) could be associated with improved device performance. It has been reported that a field of 10^5 V/m is enough to polarize P(VDF-TrFE)/perovskite bulk heterojunction [23]. In our case, the applied bias of 2 V causes a field of 10^6 V/m, which generates a built-in potential. Under UV illumination, the nanoparticles absorb the radiation and generate electron-hole pairs. The built-in potential generated due to the polarization effect helps separate the electron-hole pairs [23]. The holes move to the negatively biased electrode and electrons to the positively biased electrode causing the photocurrent.

Another interesting observation is the presence of a short-circuit current for these polymer/ZnO devices. For the PMMA/ZnO and PS/ZnO devices, the minimum dark current is not at 0 V. This could be due to interfacial polarization originated by the polarization field. However, this feature is absent in the P(VDF-TrFE)/ZnO device, where the minimum current is observed at 0 V for dark and photocurrents. We believe that the ferroelectric character of the P(VDF-TrFE) leads to higher molecular spatial ordering, which compensates for the interfacial polarization. The ferroelectric nature of P(VDF-TrFE)/ZnO nanocomposite was confirmed from C-V measurements by fabricating Ag/P(VDF-TrFE)/5 wt% ZnO/Ag device. C-V curve of the P(VDF-TrFE)/5 wt% ZnO nanocomposite is shown in Fig. 3. The hysteresis behavior in the C-V curve indicates the ferroelectric polarization [24]. Such characteristic
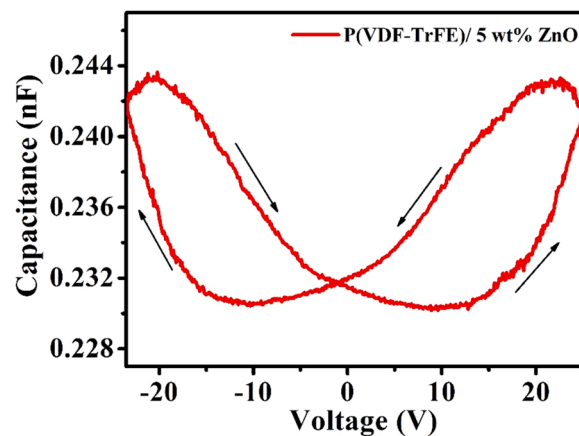

Fig. 3. C-V curve of P(VDF-TrFE)/5 wt% of ZnO nanocomposite film.

butterfly-shaped CV loops have been reported for P(VDF-TrFE) [25].

The transient photoresponse of the devices is shown in Fig. 4. ITO/P(VDF-TrFE)/5 wt% ZnO/Ag device exhibited a fast response compared to the other two polymer nanocomposite devices under 365 nm light
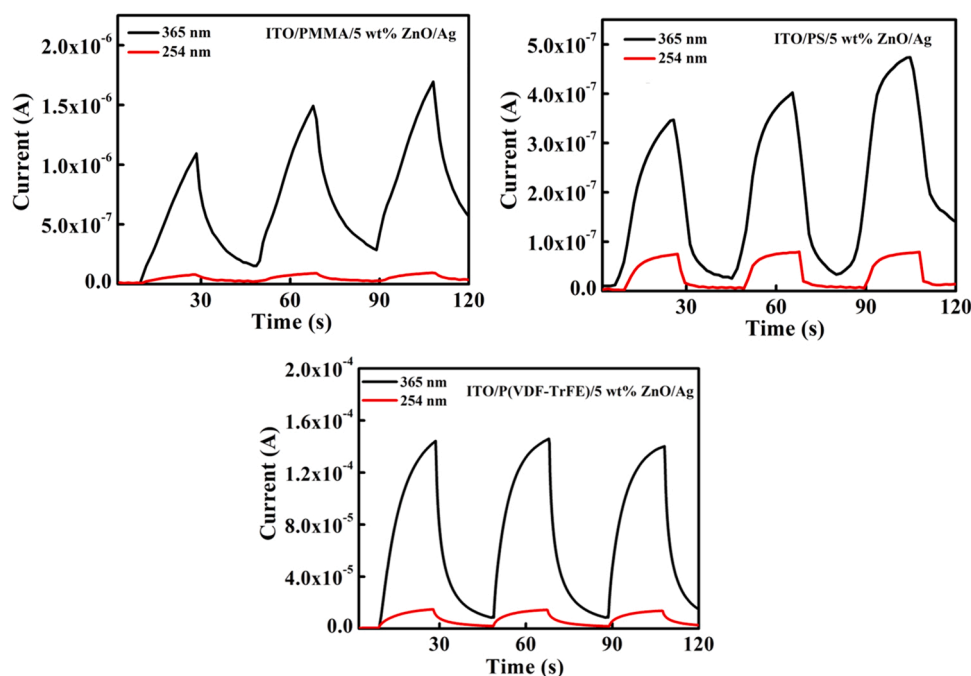
Fig. 4. Transient photoresponse of ITO/PMMA/ 5 wt% ZnO/Ag, ITO/PS/5 wt% ZnO/Ag and ITO/P(VDF-TrFE)/5 wt% ZnO/Ag devices. The biasing voltage for all devices is kept at 2 V.

illumination. The device showed a rise time of 9.37 s and a fall time of 6.91 s

P(VDF-TrFE) is a good choice due to its structural flexibility, low cost, stability, and high piezoelectricity [23]. P(VDF-TrFE) is a copolymer of PVDF and depending on the position of F atoms, P(VDF-TrFE) exists in different crystalline phases such as α, β, γ, δ and ε [26]. The β phase exhibits better ferroelectric, optical, and electrical properties [27]. The addition of ZnO nanoparticles into the P(VDF-TrFE) matrix can improve its optical and electrical properties by an interfacial interaction between the P(VDF-TrFE) and ZnO nanoparticles [17].

Realizing this potential, P(VDF-TrFE) and ZnO combinations have been employed in different device applications such as field-effect transistors, piezoelectric devices, and memory elements [28–30]. However, studies of the same for UV-photodetectors are rare in literature. ZnO nanowires deposited on an aligned P(VDF-TrFE) nanofiber film have shown promise as a UV detector. The directionality and fabrication time of the electrospun film are the critical parameters here [31]. Wang et al. have reported a field-effect transistor based on ZnO nanosheets with P(VDF-TrFE) as the gate dielectric [32]. This device showed a very high on-off ratio and responsivity. However, it employed a coercive field of about 20 V to suppress the dark current. Also, a reverse gate voltage was required to bring back the off-state once the on-state has been achieved by the exposure to UV radiation.

Since P(VDF-TrFE)/5 wt% ZnO nanocomposite-based device exhibited better performance, we further studied P(VDF-TrFE): ZnO nanocomposites in detail with different wt% of ZnO. We decided to explore lower concentrations of ZnO as concentrations higher than 5 wt % led to bad quality films.

3.3. Characterization of P(VDF-TrFE) /ZnO nanocomposite thin films

3.3.1. Surface morphology

AFM images of the P(VDF-TrFE)/ZnO nanocomposite films with different concentrations of ZnO nanoparticles are shown in ESI Fig. S6. The RMS surface roughness values are given in Table 2. It can be seen that the addition of ZnO nanoparticles to the P(VDF-TrFE) polymer does not affect the fibrillar morphology of the polymer much. However, the agglomeration of ZnO nanoparticle increases with an increase in

Table 2
The RMS surface roughness values and the crystallinity of β phase in P(VDF-TrFE) and P(VDF-TrFE)/ZnO nanocomposite.

Sample	RMS surface roughness (nm)	The crystallinity of the β phase (%)
P(VDF-TrFE)	56.8	57.15
P(VDF-TrFE)/0.5 wt% ZnO	44.3	57.02
P(VDF-TrFE)/1 wt% ZnO	44.3	49.50
P(VDF-TrFE)/5 wt% ZnO	37.8	33.58

concentration. The suspension bonds and unsaturated bonds present on the surface of ZnO nanoparticles, having activity, are not stable, and they combine with other atoms to become stable [27]. So, the higher surface activity and surface area of the ZnO nanoparticles are the reasons for the clustering of nanoparticles.

3.3.2. Structural properties

The crystalline and structural properties of P(VDF-TrFE) film and the nanocomposite films were studied using XRD and FTIR spectroscopy. XRD pattern is shown in Fig. 5. The XRD peaks observed near 20^0 correspond to the (110) and (200) planes, and the peaks observed near 41^0 correspond to the (201) and (111) planes. These are the characteristic peaks of the β phase of the P(VDF-TrFE) matrix [33]. The peaks correspond to the (100), (002), (101), (102), (110), (103), and (112) planes of the ZnO nanoparticles in agreement with the standard card JCPDS 36-1451. From the XRD pattern, it is clear that the crystalline structure of P(VDF-TrFE) is not affected by the addition of ZnO nanoparticles. The weakening of the intensity of the peak observed near 20^0 with the increase in the concentration of ZnO nanoparticles indicates the loss of crystallinity of P(VDF-TrFE) films, which may be due to the agglomeration of ZnO nanoparticles. The % of crystallinity of the β phase in the samples is calculated using the area under the prominent peak around 20^0, and the values are summarized in Table 2.

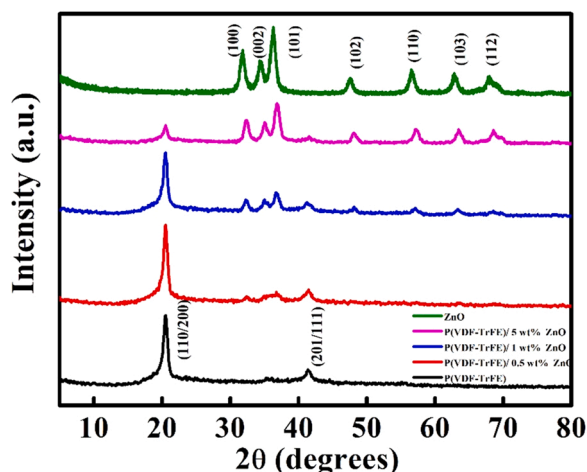FTIR measurements of the samples were performed to confirm the

Fig. 5. XRD pattern of P(VDF-TrFE), ZnO, and P(VDF-TrFE)/ZnO nanocomposite films.

crystalline phase, and the corresponding spectra are shown in Fig. 6. The peaks observed at 510 cm^{-1}, 843 cm^{-1}, 882 cm^{-1}, 1285 cm^{-1}, 1400 cm^{-1} and 1430 cm^{-1} confirmed the formation of β phase of P(VDF-TrFE) [34]. The peaks at 510 cm^{-1}, 843 cm^{-1}, and 1430 cm^{-1} may belong to both β and γ phases. However, if 1234 cm^{-1} is absent, the peaks at 510 cm^{-1} and 843 cm^{-1} correspond to the β phase only as per previous reports [35]. Also, the peak observed near 1285 cm^{-1} is the characteristic peak of the β phase [34]. The peak observed near 1430 cm^{-1} can be used to characterize both β and γ phases. However, it can be seen that it is absent in all the films with ZnO. Hence we believe that the presence of the γ phase can be ruled out in our samples. The addition of ZnO nanoparticles does not seem to change the β crystalline phase of P (VDF-TrFE). However, it can be seen that the β phase content is decreasing with the addition of ZnO. Both these observations agree with the findings from XRD. The peaks at 510 cm^{-1} and 1430 cm^{-1} are observed due to the CH$_2$ and CF$_2$ bending vibrations [36]. Symmetric stretching vibrations of CF$_2$ and C-C bonds are represented by the peak observed at 843 cm^{-1} [17]. The peak observed near 882 cm^{-1} corresponds to the rocking of C-C skeleton vibration [37]. The peak at 1285 cm^{-1} is due to the mixed vibrations of CH$_2$ rocking and CF$_2$ asymmetric stretching vibrations [38]. The wagging vibration of CH$_2$ and the bending vibration of CF$_2$ are indicated by the peak at 1400 cm^{-1} [38].

3.3.3. Optical properties
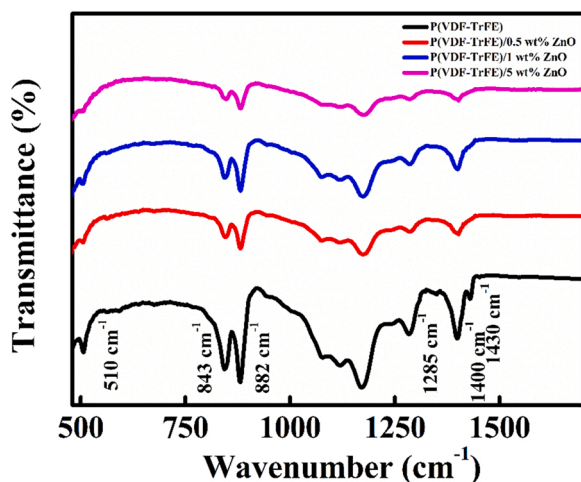
The absorption spectra of the samples are shown in Fig. 7. The absorbance of P(VDF-TrFE) in the UV region is negligible, which is enhanced with the addition of ZnO nanoparticles. The P(VDF-TrFE)/ ZnO nanocomposite films show an absorption peak at 360 nm. The intensity of UV absorption increases with the increase in the concentration of ZnO nanoparticles. The P(VDF-TrFE)/ZnO nanocomposite films are transparent in the visible region and can be used for spectral selective UV photodetector applications. In other words, they are visible-blind. The polymer can passivate the surface defects of ZnO. Such passivation has significant ramifications concerning the rise time and fall time, as well as the visible blind property of the P(VDF-TrFE)/ZnO nanocomposite-based UV photodetectors.

3.4. Photodetector measurements

IV characteristics of the devices, ITO/P(VDF-TrFE)/x wt% ZnO/Ag, under 365 nm and 254 nm light illumination are shown in Fig. 8, where x is 0, 0.5, 1, and 5 for devices D1, D2, D3, and D4 respectively. The dark characteristics of all the devices are shown together in ESI Fig. S7. ITO/P (VDF-TrFE)/Ag device exhibited a feeble response under UV illumination. The nanocomposite-based devices exhibited excellent performance with the on-off ratio of 10^4 under 365 nm and 10^3 under 254 nm light illumination.

It is found that the photocurrent increases with the ZnO concentration. The values of the on-off ratio of the devices at 2 V are summarized in the Table 3. The order of on-off ratio was the same for all the nanocomposite devices under 365 nm UV illumination. These devices had outstanding breakdown strength as they did not fail even at 20 V.

In agreement with the UV–visible absorption data, these photodetectors did not respond to RGB LEDs, confirming that they are visible blind.

The results of the transient photoresponse measurements at 2 V are shown in ESI Fig. S8, and the comparison of cyclic photoresponse of all the devices under 365 nm and 254 nm are shown in ESI Fig. S9. Minor variation in the maximum photocurrent upon each exposure is seen due to the minor differences in the manually adjusted exposure time. However, this is negligible as the standard deviation for the maximum photocurrent, for example, is only 0.079 × 10^{-4} A for D4. Rise and fall times were measured for all the devices, and the values are summarized in Table 3. D4 exhibited faster performance than D2 and D3 under 365 nm and 254 nm UV illumination. The photoresponse measurements done in a.c. rooms with lower humidity and normal rooms with higher humidity did not show any appreciable difference. P(VDF-TrFE) films show excellent hydrophobicity [39]. Hence, humidity is not expected to
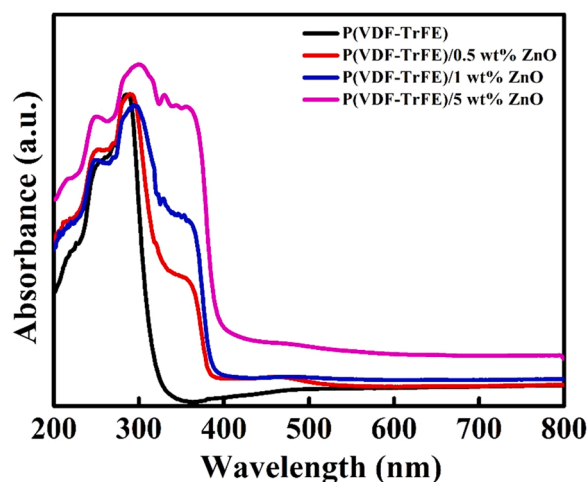

Fig. 6. FTIR spectra of P(VDF-TrFE) and P(VDF-TrFE)/ZnO nanocomposite films.

Fig. 7. UV-Visible absorbance spectra of P(VDF-TrFE) and P(VDF-TrFE)/ZnO nanocomposite films.
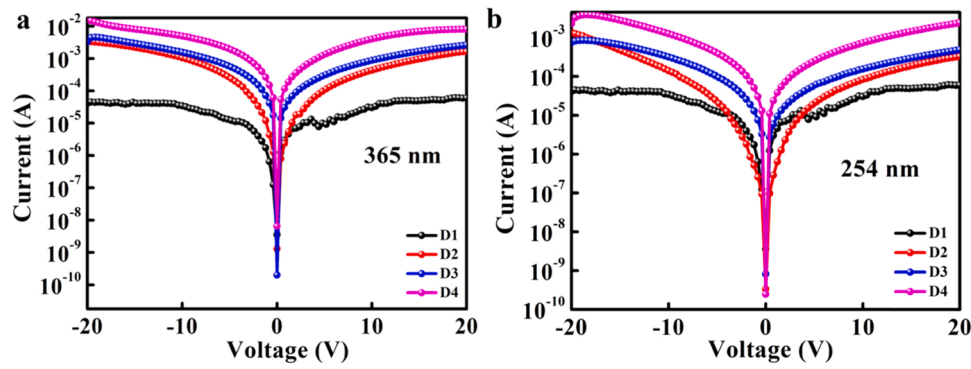
Fig. 8. IV characteristics of D1, D2, D3, and D4 measured under 365 nm and 254 nm light illumination.

Table 3
Summary of performance parameters of devices under 365 nm and 254 nm illumination at 2 V.

Device	On-off ratio	Rise time (s)	Fall time (s)	Responsivity (A/W)	Detectivity (jones)	LDR (dB)
365 nm						
D1	31.19	–	–	0.27	1.43×10^{11}	29.88
D2	2.30×10^{4}	8.44	11.16	1.37	9.01×10^{12}	87.23
D3	1.09×10^{4}	9.09	8.62	3.63	1.01×10^{13}	80.17
D4	1.40×10^{4}	9.37	6.91	14.43	2.27×10^{13}	83.09
254 nm						
D1	46.23	–	–	0.21	1.11×10^{11}	33.29
D2	1.20×10^{3}	13.05	19.19	0.03	2.47×10^{11}	61.58
D3	2.10×10^{3}	11.18	20.06	0.36	9.99×10^{11}	66.44
D4	2.80×10^{3}	12.47	14.61	1.50	1.98×10^{12}	68.94

Table 4
Summary of performance parameters of devices with Ag, Al, and Au top electrodes under 365 nm and 254 nm illumination at 2 V.

Device	Dark current (A)	Photocurrent (A)	On-off ratio	Rise time (s)	Fall time (s)	Responsivity (A/W)	Detectivity (jones)	LDR (dB)
365 nm								
ITO/P(VDF-TrFE)/5 wt% ZnO/Ag	2.50×10^{-8}	3.57×10^{-4}	1.43×10^{4}	9.37	6.91	14.43	2.27×10^{13}	83.09
ITO/P(VDF-TrFE)/5 wt% ZnO/Al	2.35×10^{-7}	1.56×10^{-4}	6.64×10^{2}	10.04	98.47	6.3	3.25×10^{12}	56.46
ITO/P(VDF-TrFE)/5 wt% ZnO/Au	1.76×10^{-6}	2.85×10^{-4}	1.62×10^{2}	10.14	14.94	11.4	2.15×10^{12}	45.25
254 nm								
ITO/P(VDF-TrFE)/5 wt% ZnO/Ag	2.50×10^{-8}	7.22×10^{-5}	2.89×10^{3}	12.47	14.61	1.50	1.98×10^{12}	68.94
ITO/P(VDF-TrFE)/5 wt% ZnO/Al	2.35×10^{-7}	3.84×10^{-5}	1.63×10^{2}	15.02	>100	0.79	4.10×10^{11}	44.26
ITO/P(VDF-TrFE)/5 wt% ZnO/Au	1.76×10^{-6}	1.69×10^{-5}	9.60	13.16	25.50	0.31	5.94×10^{10}	19.63

have a profound influence on the properties of these detectors. The high melting point of P(VDF-TrFE)~250⁰ C guarantees that there should not be any degradation with temperature. Since our ZnO is not doped, we do not expect the carrier concentration to vary much with temperature. It has been previously reported that the carrier concentration of ZnO does not vary much with the temperature [40].

Linear dynamic range (LDR) is an important parameter to characterize the performance of a photodetector, and it is given by Eq. (1),

$$LDR = 20 \; log \frac{I_{max}}{I_{min}} \qquad (1)$$

where I_{min} is the dark current and I_{max} is the photocurrent. The calculated LDR values of the devices are summarized in Table 3. The values of LDR of the devices are better than similar devices fabricated based on high-cost materials and by expensive fabrication techniques [41,42].

The responsivity of the devices, which is the ratio of the photocurrent to the incident optical power P_o, was calculated by using the Eq. (2),

$$R = \frac{I_{light} \; - \; I_{dark}}{P_o} \qquad (2)$$

From responsivity, detectivity can be calculated by Eq. (3),

$$D = \frac{R}{\sqrt{2qJ_d}} \qquad (3)$$

where J_d is the dark current density and q is the electron charge. It is expressed in jones, and it is the measure of the sensitivity of a device. The values of responsivity and detectivity are summarized in Table 3. It is found that the values of responsivity and detectivity increase with ZnO concentration. The highest value of responsivity, 14.43 A/W, and detectivity, 2.27×10^{13} jones, are still for the device D4 under 365 nm

light illumination. D4 exhibited better performance with more than 50 times enhancement in responsivity under 365 nm than D1. An on-off ratio of 10^5 has been reported for electron-depleted ZnO-based UV detectors [43]. However, it required a biasing of 5 V and had very high rise and fall times values. It may be noted that decorating ZnO with NiO nanoparticles helped decrease the rise and fall times below 10 s [44]. Our nanocomposite's ferroelectric nature helps attain an on-off ratio of 10^4 at 2 V while keeping the rise and fall times below 10 s. Surface passivation of ZnO by the polymer seems to reduce the surface defects and improve the rise and fall times. It is also interesting to note that the EQE corresponding to the highest responsivity is 4903%. Here we need to consider many factors. First, P(VDF-TrFE) is reported to support hole transport [45]. It has also been reported that in PVDF, hole injection is preferred when high work function electrodes are used [46]. The energy level diagram of the P(VDF:TrFE): ZnO photodetector is given in Fig. S10, Supplementary Information.

When UV light is absorbed by ZnO, electron-hole pairs are created. Some holes may migrate to the HOMO of P(VDF-TrFE) due to the favorable energy level. But electrons could be trapped by the surface defects of ZnO and that is why we do not see an appreciable current. In other words, our photodetector does not work in self-powered mode. When we apply a bias to the electrodes, in addition to the exposure of UV light, the positive electrode(anode) energy levels are pushed down relative to the negative electrode (cathode) energy levels and some band bending happens in both P(VDF-TrFE) and ZnO. Anode can more easily inject holes into P(VDF-TrFE) which can move through the P(VDF-TrFE) matrix. The photogenerated electrons get trapped by the surface defects of ZnO and if ZnO nanoparticles are available in the immediate vicinity to the electrodes, the injection barrier of holes gets further reduced due to this negative charge [47]. This injection current is subsumed in the photocurrent that we measure and that is why the EQE exceeds 100%.

To study the effect of different electrode materials on the performance of photodetectors, we fabricated devices with different top electrodes and compared the device performances. Since D4 exhibited relatively better performance, we fabricated devices with Al and Au electrodes with the rest of the device design identical to D4. The performance of the devices with Al and Au top electrodes is inferior to that with Ag top electrodes. ITO/P(VDF-TrFE)/5 wt% ZnO/Al showed responsivity of 6.3 A/W, but it showed a huge value for fall time. When Al is deposited on the P(VDF-TrFE)/0.5 wt% ZnO nanocomposite surface, the chances of its chemical reaction with the atoms on the nanocomposite surface are enhanced. Kochervinkii et al. have studied the effect of top electrode material on the properties of P(VDF-TrFE) [48]. They found that there are defects such as oxygen-containing groups and those due to chemical additives present on the surface of the polymer. These defects interact with the Al particles due to the latter's low work function and form Al_2O_3 and Al_xF_y [48]. These new functional groups form a low conductivity layer on the surface and affect device performance. Under 254 nm light illumination also, ITO/P(VDF-TrFE)/5 wt% ZnO/Ag device exhibited better performance. The IV characteristics of the

ITO/P(VDF-TrFE)/5 wt% ZnO/Au and ITO/P(VDF-TrFE)/5 wt% ZnO/Al devices are shown in Fig. 9, and the transient photoresponse is shown in Fig. 10. As shown in Fig. 11, the Al device does not reach saturation, whereas the Au device shows almost saturation in the same time interval. This may be due to the low conductivity layer formed at the Al/polymer interface due to the reaction between defects such as oxygen-containing groups on the polymer surface and Al. The device with Ag top electrode exhibited a maximum value of photocurrent, responsivity, detectivity, LDR, and on-off ratio. It exhibited a minimum dark current value, rise time, and fall time at 365 nm and 254 nm light illumination. ZnO is a known electron transport material, and P (VDF-TrFE) has been reported to be supporting hole current [46]. Thus, the choice of these materials is very useful for realizing high photoresponse. The image of the fabricated device is shown in Fig. S11.

4. Conclusion

PMMA/ZnO, PS/ZnO, and P(VDF-TrFE)/ ZnO nanocomposites were synthesized, and photoresponse properties were studied. The polymer matrix effectively suppresses the surface defects of ZnO. P(VDF-TrFE)/ ZnO nanocomposite device exhibited better photoresponse due to the higher absorption in the UV region and probably the ferroelectric nature. The effect of ZnO concentration on device performance was studied by varying ZnO concentration in the polymer matrix. The surface morphology and structural, optical, and crystalline properties of P(VDF-TrFE)/ZnO nanocomposites thin films have been studied, and the formation of the β crystalline phase has been confirmed by XRD and FTIR spectra. It is seen that the % of crystallinity decreases, and UV absorption increases with ZnO concentration. The photoresponse properties have been studied with ITO as the bottom electrode and Ag, Au, or Al as the top electrode. The choice of the top electrode and ZnO concentration show a profound influence on the UV photodetector performance. P (VDF-TrFE)/5 wt% ZnO nanocomposite based UV photodetector with Ag top electrode exhibited the best performance with responsivity, 14.43 A/W; detectivity, 2.27×10^{13} jones; LDR, 83.09 dB and on-off ratio, 1.43×10^4 under 365 nm light illumination at 2 V. The built-in field due to polarization of P(VDF-TrFE) helps separate the electron-hole pair formed in ZnO upon UV irradiation. The UV absorption, responsivity, and detectivity increase with the increase in ZnO concentration. The results indicate the fabrication feasibility of low-cost, flexible, and highly sensitive visible blind UV photodetectors with P(VDF-TrFE)/ZnO nanocomposites.

CRediT authorship contribution statement

Hanna B: Investigation, Formal analysis, Writing – original draft, Visualization. **Lekshmi R Pillai:** Investigation, Validation. **Kavya Rajeev:** Investigation, Validation. **K P Surendran:** Writing – review & editing, Supervision. **K N Narayanan Unni:** Conceptualization, Methodology, Writing – review & editing, Supervision, Funding acquisition.
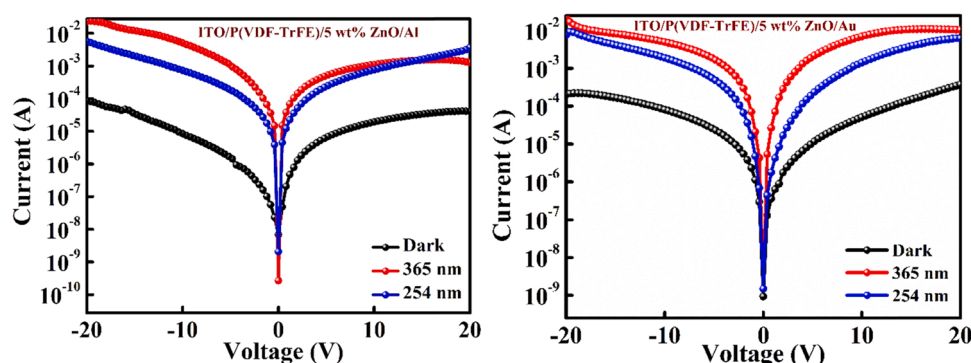
Fig. 9. IV characteristics of the devices with Al and Au top electrodes measured under dark, 365 nm, and 254 nm light illumination.
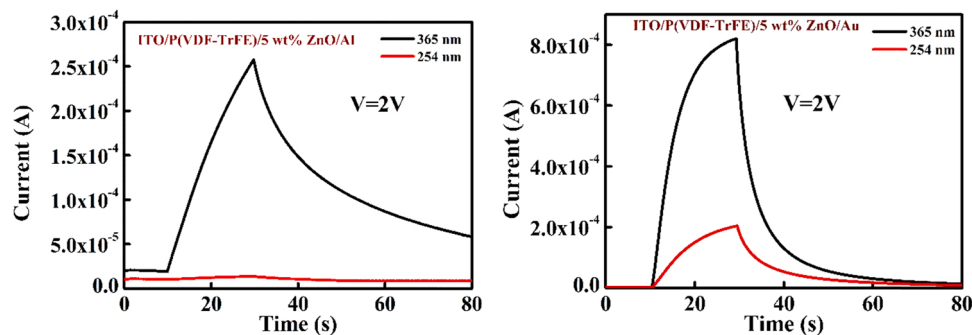
Fig. 10. Transient photoresponse of the devices with Al and Au top electrodes measured at 2 V under 365 nm and 254 nm light illumination. The biasing voltage for all devices is kept at 2 V.

Declaration of Competing Interest

The authors declare that they have no known competing financial interests or personal relationships that could have appeared to influence the work reported in this paper.

Acknowledgements

Appendix A. Supporting information

Supplementary data associated with this article can be found in the online version at doi:10.1016/j.sna.2022.113495.

References

[1] P.R. Jubu, F.K. Yam, Development and characterization of MSM UV photodetector based on gallium oxide nanostructures, Sens. Actuators A Phys. 312 (2020), 112141, https://doi.org/10.1016/j.sna.2020.112141.

[2] B. Hanna, M. Manuraj, K.P. Surendran, K.N.N. Unni, Opto-electronic properties of solution-processed zinc oxide thin films: role of solvents and doping, J. Mater. Sci. Mater. Electron. 31 (2020) 13570–13577, https://doi.org/10.1007/s10854-020-03913-7.

[3] E.Y. Shaba, J.O. Jacob, J.O. Tijani, M.A.T. Suleiman, A critical review of synthesis parameters affecting the properties of zinc oxide nanoparticle and its application in wastewater treatment, Appl. Water Sci. 11 (2021) 48, https://doi.org/10.1007/s13201-021-01370-z.

[4] H. Vahdat Vasei, S.M. Masoudpanah, M. Habibollahzadeh, Different morphologies of ZnO via solution combustion synthesis: the role of fuel, Mater. Res. Bull. 125 (2020), 110784, https://doi.org/10.1016/j.materresbull.2020.110784.

[5] K. Hu, F. Teng, L. Zheng, P. Yu, Z. Zhang, H. Chen, X. Fang, Binary response Se/ZnO p-n heterojunction UV photodetector with high on/off ratio and fast speed, Laser Photon. Rev. 11 (2017), 1600257, https://doi.org/10.1002/lpor.201600257.

[6] B. Zhao, F. Wang, H. Chen, L. Zheng, L. Su, D. Zhao, X. Fang, An ultrahigh responsivity (9.7 mA W −1) self-powered solar-blind photodetector based on individual ZnO–Ga2O3 heterostructures, Adv. Funct. Mater. 27 (2017), 1700264, https://doi.org/10.1002/adfm.201700264.

[7] B. Hanna, K.P. Surendran, K.N.Narayanan Unni, Low temperature-processed ZnO thin films for p–n junction-based visible-blind ultraviolet photodetectors, RSC Adv. 8 (2018) 37365–37374, https://doi.org/10.1039/C8RA07312K.

[8] W. Ouyang, J. Chen, Z. Shi, X. Fang, Self-powered UV photodetectors based on ZnO nanomaterials, Appl. Phys. Rev. 8 (2021), 031315, https://doi.org/10.1063/5.0058482.

[9] R. Tang, S. Han, F. Teng, K. Hu, Z. Zhang, M. Hu, X. Fang, Size-controlled graphene nanodot arrays/ZnO hybrids for high-performance UV photodetectors, Adv. Sci. 5 (2018), 1700334, https://doi.org/10.1002/advs.201700334.

[10] Y. Ning, Z. Zhang, F. Teng, X. Fang, Novel transparent and self-powered UV photodetector based on crossed ZnO nanofiber array homojunction, Small 14 (2018), 1703754, https://doi.org/10.1002/smll.201703754.

[11] Z. Zhang, Y. Ning, X. Fang, From nanofibers to ordered ZnO/NiO heterojunction arrays for self-powered and transparent UV photodetectors, J. Mater. Chem. C 7 (2019) 223–229, https://doi.org/10.1039/C8TC05877F.

[12] Y. Chen, L. Su, M. Jiang, X. Fang, Switch type PANI/ZnO core-shell microwire heterojunction for UV photodetection, J. Mater. Sci. Technol. 105 (2022) 259–265, https://doi.org/10.1016/j.jmst.2021.07.031.

[13] S. Park, N.-K. Cho, B.J. Kim, S.Y. Jeong, I.K. Han, Y.S. Kim, S.J. Kang, Reducing the persistent photoconductivity effect in zinc oxide by sequential surface ultraviolet ozone and annealing treatments, ACS Appl. Electron. Mater. 1 (2019) 2655–2663, https://doi.org/10.1021/acsaelm.9b00623.

[14] S. Patra, A. Ray, A. Roy, P. Sadhukhan, S. Pujaru, U.K. Ghorai, R. Bhar, S. Das, ZnO polymer composite based visible blind UV photo detector, Mater. Res. Bull. 101 (2018) 240–245, https://doi.org/10.1016/j.materresbull.2018.01.041.

[15] D. Ponnamma, J. Cabibihan, M. Rajan, S.S. Pethaiah, K. Deshmukh, J.P. Gogoi, S.K. K. Pasha, M.B. Ahamed, J. Krishnegowda, B.N. Chandrashekar, A.R. Polu, C. Cheng, Synthesis, optimization and applications of ZnO/polymer nanocomposites, Mater. Sci. Eng. C 98 (2019) 1210–1240, https://doi.org/10.1016/j.msec.2019.01.081.

[16] J. Han, D. Li, C. Zhao, X. Wang, J. Li, X. Wu, Highly sensitive impact sensor based on PVDF-TrFE/Nano-ZnO composite thin film, Sensors 19 (2019) 830, https://doi.org/10.3390/s19040830.

[17] K.S. Tan, W.C. Gan, T.S. Velayutham, W.H.A. Majid, Pyroelectricity enhancement of PVDF nanocomposite thin films doped with ZnO nanoparticles, Smart Mater. Struct. 23 (2014), 125006, https://doi.org/10.1088/0964-1726/23/12/125006.

[18] H.Y. Yang, D.I. Son, T.W. Kim, J.M. Lee, W.Il Park, Enhancement of the photocurrent in ultraviolet photodetectors fabricated utilizing hybrid polymer-ZnO quantum dot nanocomposites due to an embedded graphene layer, Org. Electron. 11 (2010) 1313–1317, https://doi.org/10.1016/j.orgel.2010.04.009.

[19] S.-W. Lee, S.-H. Cha, K.-J. Choi, B.-H. Kang, J.-S. Lee, S.-W. Kim, J.-S. Kim, H.-M. Jeong, S.-A. Gopalan, D.-H. Kwon, S.-W. Kang, Low dark-current, high current-gain of PVK/ZnO nanoparticles composite-based UV photodetector by PN-heterojunction control, Sensors 16 (2016) 74, https://doi.org/10.3390/s16010074.

[20] J.J. Mathen, J. Madhavan, A. Thomas, A.J. Edakkara, J. Sebastian, G.P. Joseph, Transparent ZnO–PVA binary composite for UV-A photo detector: optical, electrical and thermal properties followed by laser induced fluorescence, J. Mater. Sci. Mater. Electron. 28 (2017) 7190–7203, https://doi.org/10.1007/s10854-017-6400-1.

[21] S.S. Mousavi, B. Sajad, M.H. Majlesara, Fast response ZnO/PVA nanocomposite-based photodiodes modified by graphene quantum dots, Mater. Des. 162 (2019) 249–255, https://doi.org/10.1016/j.matdes.2018.11.037.

[22] H.G. Vempati S., K.N. Prajapati, K. Bandopadhyay, V. Kalathingal, J. Mitra, Negative photoresponse in ZnO–PEDOT:PSS nanocomposites and photogating effects, Nanoscale Adv. 1 (2019) 2435–2443, https://doi.org/10.1039/C9NA00116F.

[23] F. Cao, W. Tian, L. Meng, M. Wang, L. Li, Ultrahigh-performance flexible and self-powered photodetectors with ferroelectric P(VDF-TrFE)/perovskite bulk heterojunction, Adv. Funct. Mater. 29 (2019), 1808415, https://doi.org/10.1002/adfm.201808415.

[24] S.-W. Jung, Nonvolatile ferroelectric P(VDF-TrFE) memory transistors based on inkjet-printed organic semiconductor, ETRI J. 35 (2013) 734–737, https://doi.org/10.4218/etrij.13.0212.0280.

[25] Y.-J. Doh, D.-C. Yi, Nonvolatile memory devices based on few-layer graphene films, Nanotechnology 21 (2010), 105204, https://doi.org/10.1088/0957-4484/21/10/105204.

[26] S.C. Karumuthil, S.P. Rajeev, S. Varghese, Poly(vinylidene fluoride-trifluoroethylene)-ZnO nanoparticle composites on a flexible poly (dimethylsiloxane) substrate for energy harvesting, ACS Appl. Nano Mater. 2 (2019) 4350–4357, https://doi.org/10.1021/acsanm.8b02248.

[27] J. Li, C. Zhao, K. Xia, X. Liu, D. Li, J. Han, Enhanced piezoelectric output of the PVDF-TrFE/ZnO flexible piezoelectric nanogenerator by surface modification, Appl. Surf. Sci. 463 (2019) 626–634, https://doi.org/10.1016/j.apsusc.2018.08.266.

[28] C.H. Park, K.H. Lee, B.H. Lee, M.M. Sung, S. Im, Channel/ferroelectric interface modification in ZnO non-volatile memoryTFT with P(VDF-TrFE)polymer, J. Mater. Chem. 20 (2010) 2638–2643, https://doi.org/10.1039/B921732K.

[29] J.S. Dodds, F.N. Meyers, K.J. Loh, Piezoelectric characterization of PVDF-TrFE thin films enhanced with ZnO nanoparticles, IEEE Sens. J. 12 (2012) 1889–1890, https://doi.org/10.1109/JSEN.2011.2182043.

[30] T.Y. Kim, G. Anoop, Y.J. Son, S.H. Kim, E. Lee, J.Y. Jo, Ferroelectric-mediated filamentary resistive switching in P(VDF-TrFE)/ZnO nanocomposite films, Phys.

Chem. Chem. Phys. 20 (2018) 16176–16183, https://doi.org/10.1039/C8CP02024H.

[31] D.H. Kang, N.K. Kim, H.W. Kang, High efficient photo detector by using ZnO nanowire arrays on highly aligned electrospun PVDF-TrFE nanofiber film, Nanotechnology 30 (2019), 365303, https://doi.org/10.1088/1361-6528/ab2278.

[32] P. Wang, Y. Wang, L. Ye, M. Wu, R. Xie, X. Wang, X. Chen, Z. Fan, J. Wang, W. Hu, Ferroelectric localized field-enhanced ZnO nanosheet ultraviolet photodetector with high sensitivity and low dark current, Small 14 (2018), 1800492, https://doi.org/10.1002/smll.201800492.

[33] F. Wang, Y. Kong, Z. Liu, H. Zhu, All-organic poly(butyl methacrylate)/poly (vinylidenefluoride-trifluoroethylene) dielectric composites with higher permittivity and low dielectric loss for energy storage application, Polym. Plast. Technol. Eng. 56 (2017) 526–534, https://doi.org/10.1080/03602559.2016.1233257.

[34] S. Chen, K. Yao, F.E.H. Tay, L.L.S. Chew, Comparative investigation of the structure and properties of ferroelectric poly(vinylidene fluoride) and poly(vinylidene fluoride-trifluoroethylene) thin films crystallized on substrates, J. Appl. Polym. Sci. 116 (2010) 3331–3337, https://doi.org/10.1002/app.31794.

[35] X. Cai, T. Lei, D. Sun, L. Lin, A critical analysis of the α, β and γ phases in poly (vinylidene fluoride) using FTIR, RSC Adv. 7 (2017) 15382–15389, https://doi.org/10.1039/C7RA01267E.

[36] R.M. Habibur, U. Yaqoob, S. Muhammad, A.S.M.I. Uddin, H.C. Kim, The effect of RGO on dielectric and energy harvesting properties of P(VDF-TrFE) matrix by optimizing electroactive β phase without traditional polling process, Mater. Chem. Phys. 215 (2018) 46–55, https://doi.org/10.1016/j.matchemphys.2018.05.010.

[37] K. Xia, Y. Li, J. Li, B. Xie, C. Zhao, J. Han, Research on the effect of spin-coating process on ferroelectric phase of PVDF-TrFE/ZnO film, in: Proceedings of the Symp. Piezoelectricity, Acoust. Waves, Device Appl., IEEE, 2016, 248–252. 〈https://doi.org/10.1109/SPAWDA.2016.7829998〉.

[38] R. Augustine, P. Dan, A. Sosnik, N. Kalarikkal, N. Tran, B. Vincent, S. Thomas, P. Menu, D. Rouxel, Electrospun poly(vinylidene fluoride-trifluoroethylene)/zinc oxide nanocomposite tissue engineering scaffolds with enhanced cell adhesion and blood vessel formation, Nano Res. 10 (2017) 3358–3376, https://doi.org/10.1007/s12274-017-1549-8.

[39] T.Q. Trung, S. Ramasundaram, S.W. Hong, N.-E. Lee, Flexible and Transparent nanocomposite of reduced graphene oxide and P(VDF-TrFE) copolymer for high thermal responsivity in a field-effect transistor, Adv. Funct. Mater. 24 (2014) 3438–3445, https://doi.org/10.1002/adfm.201304224.

[40] D. Saha, A.K. Das, R.S. Ajimsha, P. Misra, L.M. Kukreja, Effect of disorder on carrier transport in ZnO thin films grown by atomic layer deposition at different temperatures, J. Appl. Phys. 114 (2013), 043703, https://doi.org/10.1063/1.4815941.

[41] W. Song, X. Wang, H. Chen, D. Guo, M. Qi, H. Wang, X. Luo, X. Luo, G. Li, S. Li, High-performance self-powered UV-Vis-NIR photodetectors based on horizontally aligned GaN microwire array/Si heterojunctions, J. Mater. Chem. C 5 (2017) 11551–11558, https://doi.org/10.1039/C7TC04184E.

[42] F. Guo, Z. Xiao, J. Huang, Fullerene photodetectors with a linear dynamic range of 90 db enabled by a cross-linkable buffer layer, Adv. Opt. Mater. 1 (2013) 289–294, https://doi.org/10.1002/adom.201200071.

[43] N. Nasiri, R. Bo, F. Wang, L. Fu, A. Tricoli, Ultraporous electron-depleted ZnO nanoparticle networks for highly sensitive portable visible-blind UV photodetectors, Adv. Mater. 27 (2015) 4336–4343, https://doi.org/10.1002/adma.201501517.

[44] N. Nasiri, R. Bo, L. Fu, A. Tricoli, Three-dimensional nano-heterojunction networks: a highly performing structure for fast visible-blind UV photodetectors, Nanoscale 9 (2017) 2059–2067, https://doi.org/10.1039/C6NR08425G.

[45] A.N. Hanna, U.S. Bhansali, M.A. Khan, H.N. Alshareef, Characterization of current transport in ferroelectric polymer devices, Org. Electron. 15 (2014) 22–28, https://doi.org/10.1016/j.orgel.2013.10.009.

[46] F. Xia, Q.M. Zhang, Schottky emission at the metal polymer interface and its effecton the polarization switching of ferroelectric poly(vinylidenefluoride-trifluoroethylene) copolymer thin films, Appl. Phys. Lett. 85 (2004) 1719–1721, https://doi.org/10.1063/1.1786364.

[47] F. Guo, B. Yang, Y. Yuan, Z. Xiao, Q. Dong, Y. Bi, J. Huang, A nanocomposite ultraviolet photodetector based on interfacial trap-controlled charge injection, Nat. Nanotechnol. 7 (2012) 798–802, https://doi.org/10.1038/nnano.2012.187.

[48] V.V. Kochervinskii, E.V. Chubunova, S.A. Bedin, An effect of electrode material on pinning layer characteristics and depolarization field in polymer ferroelectrics, J. Appl. Phys. 124 (2018), 064102, https://doi.org/10.1063/1.5028563.

Hanna B. obtained her Bachelor's Degree in Physics from St. Dominic's college, Kanjirappally (affiliated to Mahatma Gandhi University, Kerala, India) in 2012. She completed her Master's Degree in Physics with specialization in Condensed Matter Physics from Central University, Pondicherry, India in 2014. She is currently pursuing her Ph.D. in Physics at National Institute for Interdisciplinary Science and Technology (NIIST) and Academy of Scientific and Innovative Research (AcSIR), Council of Scientific and Industrial Research (CSIR).

Lekshmi R. Pillai completed her Bachelor's Degree in Physics in 2017 from N. S. S. College Pandalam, Kerala, India. She obtained her Master's Degree in Physics from T. K. Madhava Memorial College, Nangiarkulangara, India in the year 2019. Currently she is pursuing a Degree in Education from Kerala University College of Teacher Education, University of Kerala, India.

Kavya Rajeev obtained her Bachelor's Degree in Physics from Nirmalagiri College, Kuthuparamba (affiliated to Kannur University, Kerala, India) in 2016 and Master's Degree in Physics from Pondicherry University in 2018. She is currently pursuing her Ph. D. in Physics at CSIR-NIIST and AcSIR, CSIR.

Dr. K. P. Surendran is a Principal Scientist with Materials Science and Technology Division of CSIR-NIIST, Thiruvananthapuram, India. He is also an Associate Professor with AcSIR, CSIR. In 2005, he received his doctorate in Physics from Kerala University, India. After post-doctoral stints at Indian Institute of Science, Bengaluru; Aveiro and Coimbra Universities in Portugal, he joined IFW Dresden as Alexander von Humboldt fellow. From 2012 onwards he is working with CSIR-NIIST. His current research interests include functional inks for printed electronics, 2D materials, lead free piezoelectric nanogenerators, EMI shielding materials, low temperature cofired ceramics and printed antennas. He has authored 85 papers and 3 patents.

Dr. K. N. Narayanan Unni obtained his Ph D in 2001 in Physics from Mahatma Gandhi University, India. After post-doctoral stints at Indian Institute of Technology Bombay and University of Angers, France, he joined Samtel Color Ltd, New Delhi in 2005 and became the Team Leader of OLED Display Unit in 2008. Later he joined Indian Institute of Technology Kanpur as a Principal Research Engineer. In 2013, he joined CSIR and currently he is a Senior Principal Scientist and Head of the Photosciences and Photonics Section with CSIR-NIIST and a Professor with AcSIR, CSIR. His main area of research is organic and hybrid electronics.

Opto-electronic properties of solution-processed zinc oxide thin films: role of solvents and doping

B. Hanna, M. Manuraj, K. P. Surendran & K. N. Narayanan Unni

ONLINE
FIRST

Springer

Springer

Opto-electronic properties of solution-processed zinc oxide thin films: role of solvents and doping

B. Hanna[1,2] · M. Manuraj[1] · K. P. Surendran[2,3] · K. N. Narayanan Unni[1,2]

Abstract

Undoped zinc oxide (ZnO) and nitrogen-doped zinc oxide (NZO) thin films were prepared on transparent conducting oxide-coated glass substrates by employing sol–gel technique. The effect of different solvents and nitrogen doping on the optical, structural, and electrical properties was investigated by UV–visible absorption spectroscopy, atomic force microscopy (AFM), X-ray diffraction (XRD), profilometry, and Hall effect studies. ZnO films yielded transmittance above 85% and the bandgap of ZnO thin films decreased with doping. XRD pattern confirmed hexagonal wurtzite structure of ZnO. NZO thin films were found to be in the nano-thin film phase with thickness of 40 nm. Hall effect studies yielded carrier concentration of 1.2×10^{15} cm^{-3} and 2.03×10^{14} cm^{-3}, respectively, for undoped and doped ZnO thin films. The changes in vibrational modes of ZnO due to nitrogen doping were detected using Fourier transform infrared (FTIR) analysis. It was found that p-type doping, leading to an improved surface morphology, led to a reduction in optical bandgap and an increased charge carrier mobility. The choice of the solvent was found to have a profound influence on the surface morphology, optical bandgap, tail states distribution, and charge carrier mobility.

1 Introduction

Transparent conducting films have a wide range of applications in optoelectronic devices. Low resistivity, high transmittance in the visible range, and high stability against heat are the important and highly desired properties of transparent conducting films [1]. Most of the transparent conducting oxides such as indium tin oxide (ITO), fluorine-doped Tin Oxide (FTO), etc., have high cost, low stability to H$_2$

✉ K. N. Narayanan Unni
unni@niist.res.in

1 Photosciences and Photonics Section, Chemical Sciences and Technology Division, CSIR-National Institute for Interdisciplinary Science and Technology, Thiruvananthapuram, Kerala 695019, India

2 Academy of Scientific and Innovative Research (AcSIR), Ghaziabad 201002, India

3 Functional Materials Section, Materials Science and Technology Division, CSIR-National Institute for Interdisciplinary Science and Technology, Thiruvananthapuram, Kerala 695019, India

plasma, and toxicity. On the other hand, zinc oxide (ZnO) is a low-cost and comparatively stable material with high transmission [2–4]. ZnO is a wide direct bandgap semiconductor which finds application in thin film transistors [5], light emitting diodes [6], solar cells [7, 8], sensors [9], photodetectors [10], and in photocatalysis [11]. Most of the optoelectronic applications require high carrier mobility and consequently, doping of ZnO becomes essential. ZnO thin films are prepared by various deposition techniques such as sputtering [12], chemical vapor deposition (CVD) [13], pulsed laser deposition (PLD) [14], molecular beam epitaxy (MBE) [15], spray pyrolysis [16], sol–gel process [17–19], etc. Compared to other methods, sol–gel process is a simple, low-cost, and effective method to produce high-quality thin films. In addition, it is easy to control the composition and to fabricate large-area thin films. Although sol–gel process is an easier technique for fabricating thin films, there are certain critical factors influencing the physical, optical and electronic properties of ZnO thin films. These factors include pre-annealing temperature, post-annealing temperature and film thickness. Since ZnO is intrinsically n-type semiconductor, one of the major challenges in the development of ZnO-based optoelectronic devices is to get an efficient p-type ZnO [18]. Recently researchers have been working on p-type ZnO by doping with different elements (N, N–Al,

Li, As, Na, P and K) using various techniques [19–24]. Because of nitrogen's low ionization energy, ionic radius comparable with oxygen, ease of handling, low toxicity, and source-abundance, it can be considered as the most promising dopant [25, 26]. Although solution processing has been established as an effective and simple technique for ZnO thin film fabrication, the very same attractive features need to be maintained while we fabricate p-doped ZnO thin films by solution processing. Precursor solvent is reported to play an important role in defining the opto-electrical properties of spin-coated transparent conducting ZnO:Ga thin films [27]. Similarly, the molar ratio of the precursor is also important. It is important to understand the behavior of the doped film in the nano-thin film regime (less than 50 nm). However, detailed studies on the optoelectronic properties of ZnO nano-thin film prepared by solution processing with special emphasis on the effect of solvents and electrical doping are scarce in literature. In the present work, we have attempted to dope ZnO with nitrogen through a solution processing technique and to study the optical and electrical properties of the doped films, keeping the molar ratio of the precursor material, zinc acetate dihydrate ($Zn(CH_3COO)_2.2H_2O$) constant. Thickness of the film is another critical factor and most of the previous reports deal with thicker ZnO films as given in the electronic supplementary material while we report on the p-type doping effect on a nano-thin film of ZnO, which is having a thickness of 40 nm.

2 Experimental

In this work, we prepared both doped and undoped ZnO by sol–gel process and thin films were deposited by spin-coating. Two different 0.5 molar solutions of undoped ZnO were prepared using 2-methoxyethanol and isopropyl alcohol as solvents. In both cases, zinc acetate and monoethanolamine were used as the solute and stabilizing agent, respectively. The solutions were named as ZnO-1 (2-methoxyethanol), ZnO-2 (isopropyl alcohol). ZnO-1 was stirred for 12 h at 60 °C. ZnO-2 was stirred for 2 h at 60 °C and aged at room temperature for 24 h. The solutions were spin-coated on ultrasonically cleaned and subsequently UV-ozone-treated ITO-coated glass substrates at 1500 rpm and the films were annealed at 170 °C for 1 h in air.

N-doped ZnO (NZO) nano-thin films were prepared by adding ammonium acetate as the dopant precursor to ZnO-1. The solution was stirred for 2 h at 60 °C and aged at room temperature for 72 h. The solution was spin coated at 1500 rpm on ultrasonically cleaned and subsequently UV-ozone-treated FTO-coated glass substrates. The samples were annealed at 250 °C for 10 min and the process was repeated for 8 times to get the required thickness. The thin films were post-heated at 500 °C for 1.5 h in the N_2

atmosphere. In all the three samples, the molar ratio of $Zn(CH_3COO)_2.2H_2O$ is kept constant at 0.5.

Optical properties of the doped and undoped ZnO thin films were studied by using PerkinElmer UV/VIS/NIR Spectrometer, Lambda 950. Surface morphology of the thin films were investigated by Bruker AFM. Bruker Stylus Profilometer was used for the thickness measurements. X-ray diffraction (XRD) patterns were recorded by XPert-PRO Scan Diffractometer with Cu Kα ($\lambda = 1.5406$ Å) radiation from 20° to 60° scanning range. Hall effect measurements were done using physical property measurement system (PPMS) from Quantum Design, in a van der Pauw configuration with 1×1 cm^2 sample size. Fourier transform infrared (FTIR) spectra of doped and undoped thin films were measured by IR Prestige-21 Fourier Transform Infrared Spectrophotometer, Shimadzu.

3 Results and discussion

All our measurements have been done at RT. Temperature might not appreciably affect the p-type conductivity because the film is annealed at 500 °C during the film preparation stage. The process conditions have been optimized for a good quality film and we do understand that any variation in the process conditions may have a profound influence on the conductivity of doped ZnO films as previously reported [15, 28, 29].

3.1 Optical properties

Figure 1 shows the UV–visible transmission spectra of ZnO thin films. ZnO films yielded transmittance above 85%. From the transmittance spectra, it is clear that the UV absorption edge was red shifted upon nitrogen doping. The interference fringes in the transmission spectra are indicative of the high surface quality and homogeneity of the films [30].

The values of the energy bandgap of both doped and undoped ZnO were measured from the Tauc's plot by employing the relation,

$$\alpha h\nu = A\left(h\nu - E_g\right)^n, \tag{1}$$

where α is an absorption coefficient, A is the proportionality constant, $h\nu$ is the incident energy, and E_g is the bandgap of the material [31]. Since ZnO is a direct bandgap semiconductor [32], value of n is given by 1/2. Figure 2 shows the Tauc's plot of doped and undoped ZnO. The optical bandgap of ZnO-1, ZnO-2, and NZO are summarized in Table 1. The results suggest that the optical bandgap of NZO shows slightly lower value than that of the pure ZnO. The value of energy bandgap of ZnO-2 is smaller than that of ZnO-1. The difference in the bandgap of ZnO thin films in different
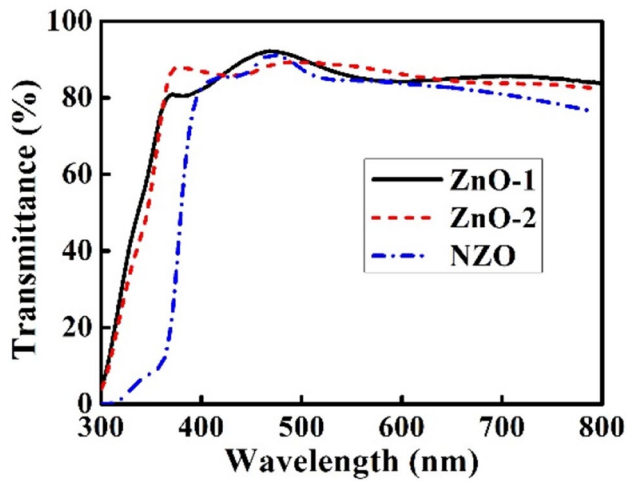
Fig. 1 UV-visible transmission spectra of doped and undoped ZnO thin films

solvents is due to the dependence of microstructure and morphology of the film on the solvent, which would change the interatomic interactions and thereby the optical properties of the thin films [33].

The relation between absorption coefficient and photon energy near band edge is given by the Urbach relation [34],

$$\alpha = \alpha_0 \exp\left(h\nu/E_u\right), \tag{2}$$

where α_0 is a constant and E_u is the width of the localized states or Urbach energy. The Urbach energy of the ZnO thin films can be measured from the slope of the graph plotted between $\ln(\alpha)$ and $h\nu$. Figure 3 shows the plot of $\ln(\alpha)$ vs. $h\nu$. The values of Urbach energy of doped and undoped ZnO thin films are given in Table 1. We found that Urbach energy decreases upon doping and that of ZnO-2 is smaller than ZnO-1. This implies that more defect levels are introduced when we use 2-methoxyethanol as solvent. The decrease in the Urbach energy in NZO indicates the decrease in the defect states of thin films.
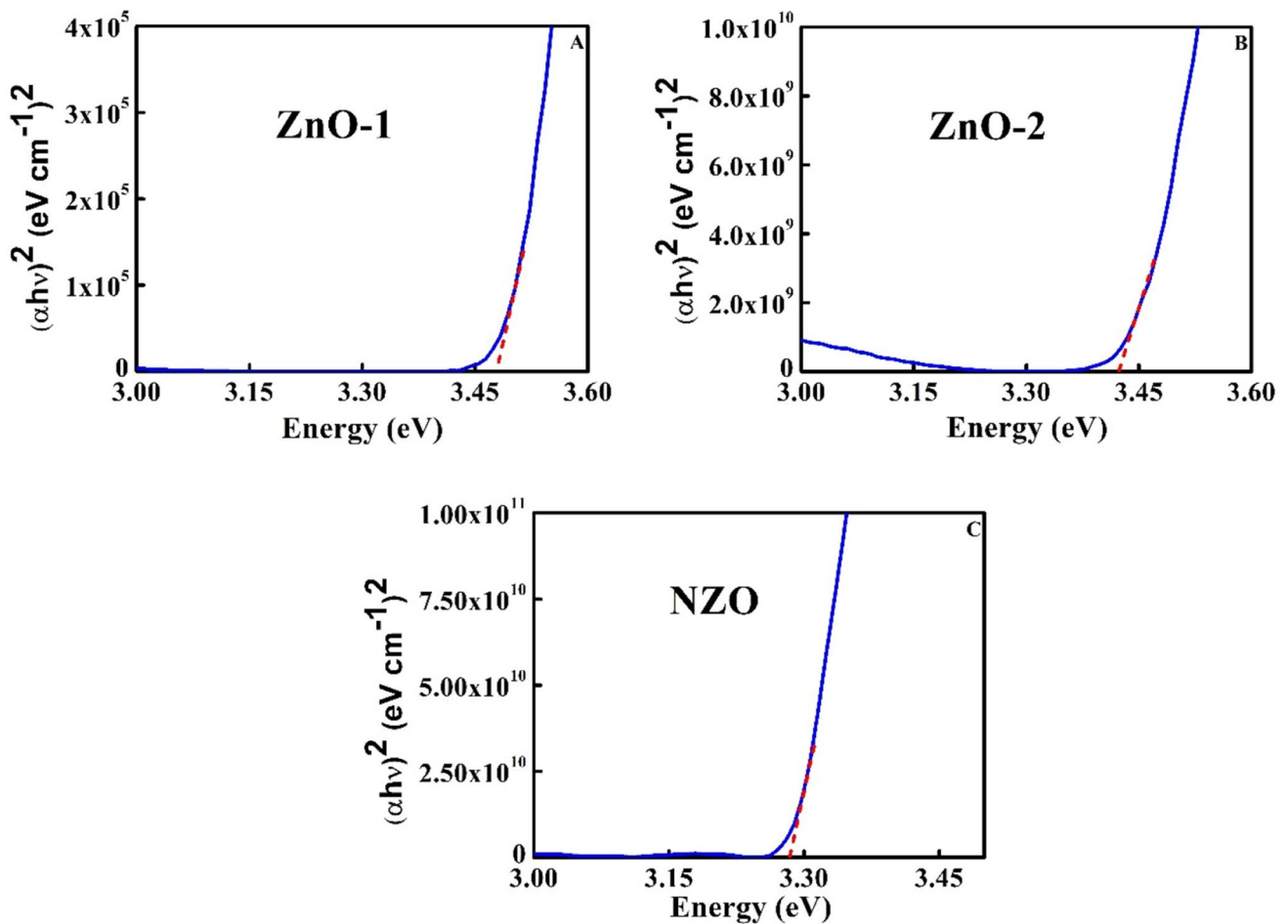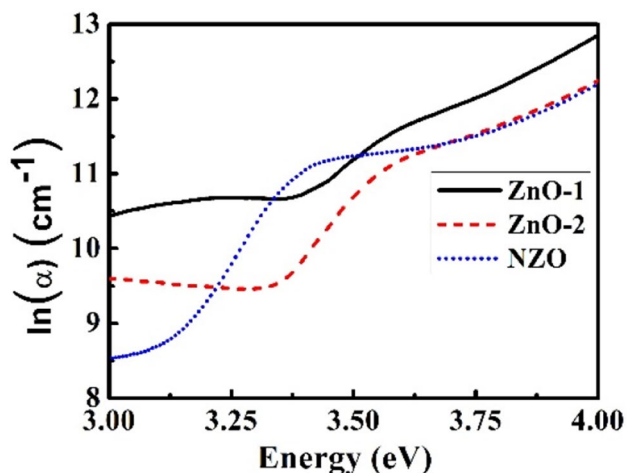

Fig. 2 Tauc's plot for **a** ZnO-1, **b** ZnO-2, **c** NZO thin films

Table 1 Values of optical energy bandgap and Urbach energy of ZnO-1, ZnO-2 and NZO thin films

Sample	Energy bandgap (eV)	Urbach energy (eV)
ZnO-1	3.47	0.308
ZnO-2	3.42	0.217
NZO	3.29	0.129

Fig. 3 Urbach plot of ZnO-1, ZnO-2, and NZO thin films

3.2 Morphological and structural properties

AFM images of doped and undoped ZnO thin films obtained by tapping mode are shown in Fig. 4. AFM study reveals that nitrogen doping increases the average grain size and enhances the surface roughness of the thin films. The properties of the ZnO thin film surface, i.e., the surface roughness, grain size, and RMS values are strongly affected by the choice of solvents used for the preparation of ZnO thin films [32, 35]. From the AFM images, it is evident that for ZnO-2, the RMS values are greater than that of ZnO-1. High-quality thin films have been obtained for ZnO-1 and hence we decided to use only ZnO-1 for p-type doping studies. The RMS values of NZO are greater than that of ZnO-1. The RMS values of ZnO-1, ZnO-2, and NZO are given in the Table 2. The grain size of ZnO-2 looks larger probably due to the agglomeration. The thickness of the doped and undoped ZnO thin films was measured by stylus profilometer. The thickness values are 60 nm, 100 nm, and 40 nm for ZnO-1, ZnO-2, and NZO, respectively. The difference in thickness of ZnO-1 and ZnO-2 is due to the difference in the solubility of the precursor materials in the solvents, since molar ratio is fixed in all the cases. To get an appreciable thickness, the spin-coating process was repeated 8 times. It is understood that these process variations might have added to the RMS surface roughness of these films.

The crystal structure analysis of these thin films was done by using XRD. The XRD patterns of ZnO thin films are shown in Fig. 5. For undoped ZnO-1, (002) and (110) peaks were obtained and for ZnO-2, (002), (101), and (110) peaks were observed. For NZO, (100), (002), (101), (102), and (110) peaks were observed. The results are summarized in the Table 3. All the XRD peaks were identified with the standard card JCPDS 36-1451 in the recorded range of 2θ. It is concluded that the thin films are crystallized in hexagonal wurtzite structure and there was no preferential growth orientation [36].

The crystallite size D was calculated using Scherrer's relation given in Eq. (3),

$$D = \frac{K\lambda}{\beta \cos\theta}, \tag{3}$$

where K is a constant, λ is the X-ray wavelength and β is the full width at half maximum (FWHM) [37]. The results suggest that there is a shift in the (002) and (110) planes of ZnO-1 and NZO due to the difference in the ionic radii of O and N. Ionic radii of N is greater than that of O [38]. N substituting O will produce a strain in the crystal and causes shift in XRD peaks to higher or lower angles [38]. The XRD patterns show that both the undoped ZnO thin films prepared with the solvents, 2-methoxyethanol, and isopropyl alcohol exhibit the highest intensity XRD peak on the (002) plane located at 33.4°. However, NZO thin film exhibits the highest intensity XRD peak on the (101) plane located at 36.632°. Therefore, the crystallite size along the plane (002) was calculated for ZnO-1 and ZnO-2 and that of NZO was calculated along (101) plane [31]. The crystallite size of the films is summarized in Table 2. The results show that the crystallite size and thickness of ZnO-1 is smaller than that of ZnO-2 which could be due to the higher viscosity of isopropyl alcohol compared with 2-methoxyethanol. This indicates that 2-methoxyethanol is a better solvent and its fast drying characteristics of ZnO precursor layers, leads to more compact assembly of smaller crystals with less pinholes on annealing. The results are in agreement with findings from the AFM studies. Preferential crystallite orientation can be determined from texture coefficient (TC) and it is given by [39],

$$TC = \frac{\frac{I(hkl)}{I_0(hkl)}}{\frac{1}{N}\sum_n \frac{I(hkl)}{I_0(hkl)}}, \tag{4}$$

where $I(hkl)$ is the measured intensity of the peak, $I_0(hkl)$ is the relative intensity of the plane from JCPDS data, and N is the number of reflections. TC of ZnO-1, ZnO-2,, and NZO were calculated. Highest value of TC was obtained for (002) plane in ZnO-1 and ZnO-2. This means that more number of crystallites are oriented along (002) plane. But for NZO,
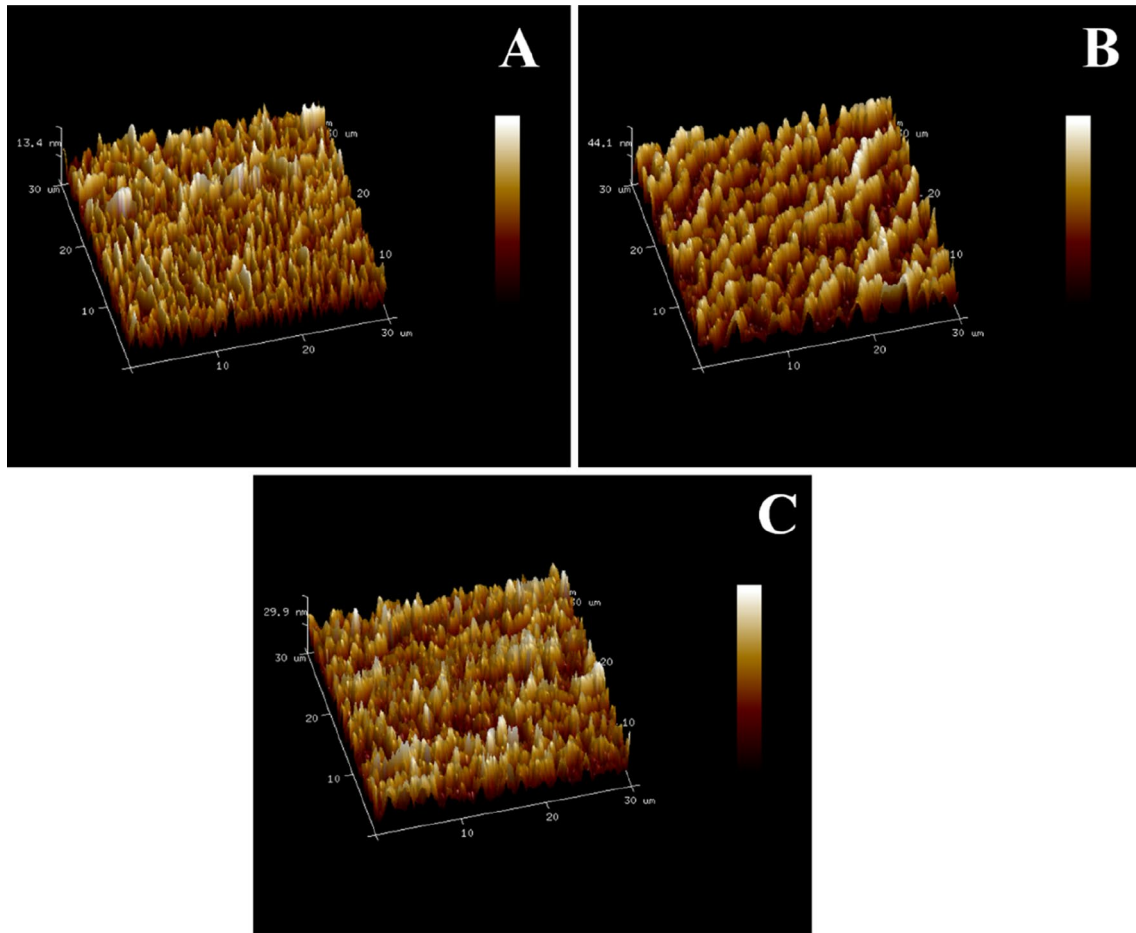
Fig. 4 AFM images of ZnO thin films. **a** ZnO-1, **b** ZnO-2, **c** NZO

Table 2 Values of RMS surface roughness and crystallite size of ZnO-1, ZnO-2, and NZO

Sample	RMS surface roughness (nm)	Crystallite size (nm)
ZnO-1	70.4	15.6
ZnO-2	105	21.8
NZO	81.3	27.6

Fig. 5 XRD pattern of ZnO-1, ZnO-2, and NZO

highest value of *TC* was obtained for (110) plane. TC of (002) plane of NZO film was less than that of the (002) plane of ZnO-1. When doped with nitrogen, the preferential crystallite orientation changes and the crystallites are randomly oriented. This increases the surface roughness of the film. The values of *I/II* and TC of all the planes ZnO-1, ZnO-2, and NZO are summarized in Table 3.
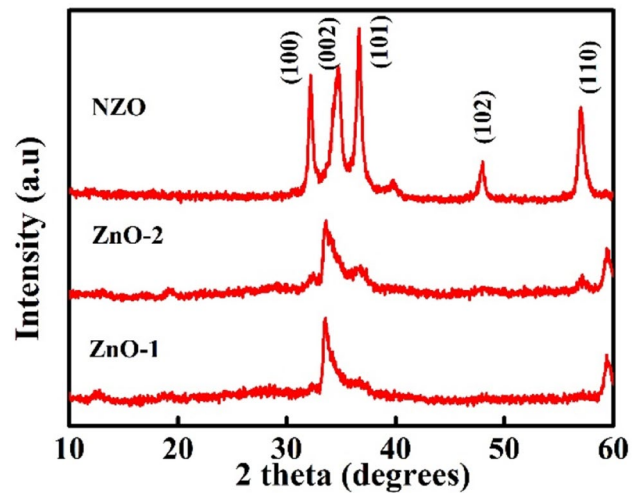
Table 3 The structure parameters obtained from XRD studies on ZnO-1, ZnO-2, and NZO

Sample	Number of peaks	Peak position (2θ)	(hkl)	d spacing (Å)	FWHM	I/I_0	TC
ZnO-1	1	33.444	002	2.677	0.554	2.272	1.07
	2	59.502	110	1.600	0.554	1.963	0.927
ZnO-2	1	33.465	002	2.675	0.396	2.272	2.120
	2	36.759	101	2.442	0.950	0.214	0.200
	3	57.062	110	1.612	0.950	0.720	0.673
NZO	1	32.154	100	2.781	0.396	1.220	0.938
	2	34.729	002	2.580	0.356	1.713	1.310
	3	36.632	101	2.451	0.316	1.000	0.768
	4	47.912	102	1.897	0.475	0.807	0.666
	5	56.914	110	1.616	0.277	1.763	1.350

Table 4 Values of carrier concentration, conductivity, mobility, and carrier type of doped and undoped ZnO thin films

Sample	Carrier Concentration (n/p) (/cm^3)	Conductivity (σ) (S/cm)	Mobility (μ) (cm^2/Vs)	Carrier type
ZnO-1 (ITO contact)	1.2×10^{15}	1.05×10^{-5}	0.05	n
ZnO-2 (ITO contact)	4.84×10^{15}	6.77×10^{-5}	0.08	n
NZO (ITO/Pt contact)	2.03×10^{14}	7.35×10^{-6}	0.23	p

3.3 Electrical properties

The electrical and electronic properties of the thin films were studied by two probe measurement and Hall effect. We calculated the conductivity from two probe measurement and carrier concentration from Hall effect method. The values of conductivity, carrier concentration, carrier type, and mobility of doped and undoped ZnO thin films are listed in Table 4. Inherent n-type conductivity of ZnO-1 and ZnO-2 is due to the native point defects in the ZnO thin films [18]. The interstitial H-atoms form bonds with O and Zn and these act as a shallow donor level and contribute to the n-type conductivity [18]. In NZO, N is substituted for O and this acts as deep acceptor level and contributes to the p-type conductivity [18]. The conductivity of ZnO-1, ZnO-2, and NZO was measured by two probe method by using ITO contacts and that of NZO was found to be one order less. Low conductivity of NZO is due to the high injection barrier for holes when ITO contact is used. Hence Pt contacts were deposited over ITO using PT-1 platinum paste (Dyesol) and we found that the conductivity has increased from 4.67×10^{-7} S/cm (ITO contact) to 7.35×10^{-6} S/cm (ITO/Pt contact). Basically, ZnO is a n-type semiconductor and when doped with N, it passivates all the donor levels and this increases the hole concentration [40]. This is the reason why carrier concentration of NZO (holes) appears to be less than that of ZnO-1 and ZnO-2 (electrons). However, the increased mobility and the change of sign of the majority carrier give evidence to the p-type doping.
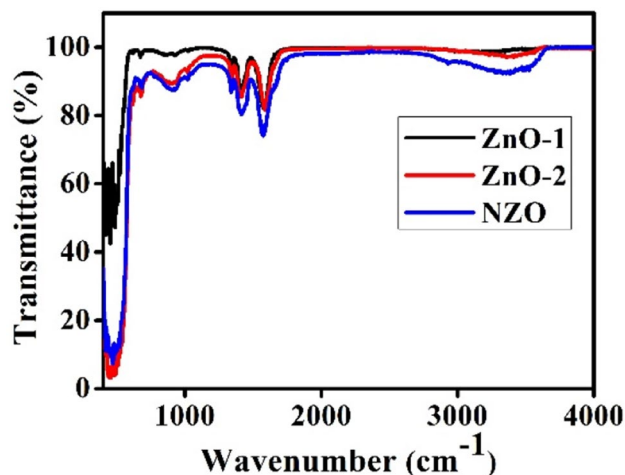
Fig. 6 FTIR spectra of doped and undoped ZnO thin films

3.4 FTIR analysis

To understand the presence of molecular species in the doped and undoped samples and to find the effect of doping on the vibrational modes of undoped ZnO, FTIR measurements were done from 400 to 4000/cm at room temperature. FTIR spectra of doped and undoped samples are shown in Fig. 6. Absorption peaks observed below 1000/cm correspond to interatomic vibrations of metal oxides [17]. The absorption bands between 480 and 580/cm are due to Zn–O stretching mode [38]. The peak observed near 900/cm corresponds to the hydrogen substituted at the oxygen site

bound to the lattice Zn site (i.e., Zn–H) [41]. The oxygen replaced by hydrogen may act as a shallow donor level and contributes to the n-type conductivity of undoped ZnO. The absorption bands near 1330/cm, 1400/cm, and 1570/cm were observed for doped and undoped samples and correspond to symmetric and asymmetric stretching vibrations of C=O group [42]. Small variations in the IR peak positions in the region 1000–1500/cm are due to the effect of solvent and N doping. The peak at 2930/cm was observed only for NZO, indicating the presence of N in the NZO [43]. The absorption peak near 3400/cm is due to the O–H stretching mode [44] and it becomes more symmetrical with nitrogen doping.

4 Conclusions

We have fabricated doped and undoped ZnO thin films by a relatively facile process through sol–gel technology. P-type doping was done which improved the surface morphology of the film and resulted in a reduction in the value of bandgap. P-doped ZnO was in the nano-thin film form with thickness 40 nm. The thin films were crystalline with crystallite sizes, 15.6 nm, 21.8 nm, and 27.6 nm for ZnO-1, ZnO-2, and NZO, respectively. Mobility values of 0.05 cm^2/Vs, 0.08 cm^2/Vs, and 0.23 cm^2/Vs were obtained for ZnO-1, ZnO-2, and NZO, respectively. The inherent n-type behavior of ZnO-1 and ZnO-2 is due to the H substituted at the O site and that is proved by FTIR measurements. As a p–n junction of ZnO is a pre-requisite for several optoelectronic applications, the results are relevant for flexible and transparent electronics, based on solution-processed ZnO.

References

1. S. Lany, A. Zunger, Phys. Rev. Lett. **98**, 045501 (2007)
2. M. Zhao, F. Shang, J. Lv, Y. Song, F. Wang, Z. Zhou, G. He, M. Zhang, X. Song, Z. Sun, Y. Wei, X. Chen, Nanoscale Res. Lett. **9**, 485 (2014)
3. X. Duan, C. Li, L. Fu, Y. Wu, G. Chen, K. Xu, L. Shao, P. Yang, Z. Yu, P. Ding, H. Ma, Y. Li, Y. Du, Superlattices Microstruct. **128**, 30 (2019)
4. E.T. Seid, F.B. Dejene, J. Mater. Sci. Mater. Electron. **30**, 11833 (2019)
5. S. Thiemann, M. Gruber, I. Lokteva, J. Hirschmann, M. Halik, J. Zaumseil, A.C.S. Appl, Mater. Interfaces **5**, 1656 (2013)
6. A. Ghorai, S. Bayan, N. Gogurla, A. Midya, S.K. Ray, A.C.S. Appl, Mater. Interfaces **9**, 558 (2017)
7. J. Wei, Z. Yin, S.C. Chen, Q. Zheng, A.C.S. Appl, Mater. Interfaces **9**, 6186 (2017)
8. D. Barpuzary, A.S. Patra, J.V. Vaghasiya, B.G. Solanki, S.S. Soni, M. Qureshi, A.C.S. Appl, Mater. Interfaces **6**, 12629 (2014)
9. G. Algün, N. Akçay, J. Mater. Sci.: Mater. Electron. **30**, 16124 (2019)
10. B. Hanna, K. P. Surendran, K.N. Narayanan Unni, RSC Adv. **8**, 37365 (2018)
11. A. Di Mauro, M.E. Fragalà, V. Privitera, G. Impellizzeri, Mater. Sci. Semicond. Process. **69**, 44 (2017)
12. A. Barhoumi, L. Yang, N. Sakly, H. Boughzala, G. Leroy, J. Gest, J.-C. Carru, S. Guermazi, Eur. Phys. J. Appl. Phys. **62**, 20302 (2013)
13. S.-H. Park, J.-W. Park, S.-M. Yang, K.-H. Kim, N.-M. Hwang, J. Phys. Chem. C **119**, 25047 (2015)
14. M. Girtan, M. Kompitsas, R. Mallet, I. Fasaki, Eur. Phys. J. Appl. Phys. **51**, 33212 (2010)
15. M. Suja, S.B. Bashar, M.M. Morshed, J. Liu, A.C.S. Appl, Mater. Interfaces **7**, 8894 (2015)
16. I. Chaki, A. Belayachi, T. El Bahraoui, M. Regragui, M. Abd-Lefdil, Eur. Phys. J. Appl. Phys. **68**, 30301 (2014)
17. M.F. Khan, A.H. Ansari, M. Hameedullah, E. Ahmad, F.M. Husain, Q. Zia, U. Baig, M.R. Zaheer, M.M. Alam, A.M. Khan, Z.A. AlOthman, I. Ahmad, G.M. Ashraf, G. Aliev, Sci. Rep. **6**, 27689 (2016)
18. A. Janotti, C. G. Van de Walle, Rep. Prog. Phys. **72**, 126501 (2009)
19. M. Dutta, T. Ghosh, D. Basak, J. Electron. Mater. **38**, 2335 (2009)
20. M. Hjiri, M.S. Aida, O.M. Lemine, L. El Mir, Mater. Sci. Semicond. Process. **89**, 149 (2019)
21. L.-W. Weng, W.-Y. Uen, S.-M. Lan, S.-M. Liao, T.-N. Yang, C.-H. Wu, H.-F. Hong, W.-Y. Ma, C.-C. Shen, Appl. Surf. Sci. **277**, 1 (2013)
22. L. Yue, Z. Zhang, Y. Ma, W. Zhang, J. Nanomater. **2016**, 1 (2016)
23. B. Panigrahy, D. Bahadur, RSC Adv. **2**, 6222 (2012)
24. W. Jun, Y. Yintang, Mater. Lett. **62**, 1899 (2008)
25. H. Nian, S.H. Hahn, K.-K. Koo, E.W. Shin, E.J. Kim, Mater. Lett. **63**, 2246 (2009)
26. Y.J. Zeng, Z.Z. Ye, W.Z. Xu, B. Liu, Y. Che, L.P. Zhu, B.H. Zhao, Mater. Lett. **61**, 41 (2007)
27. A.K. Srivastava, J. Kumar, Mater. Chem. Phys. **162**, 436 (2015)
28. U. Chaitra, M.G. Mahesha, D. Kekuda, K.M. Rao, Appl. Phys. A **125**, 394 (2019)
29. T.K. Pathak, V. Kumar, L.P. Purohit, Phys. E Low-Dimensional Syst. Nanostructures **74**, 551 (2015)
30. J. George, K.S. Joseph, B. Pradeep, T.I. Palson, Phys. Status Solidi **106**, 123 (1988)
31. M.K. Jayaraj, A. Antony, M. Ramachandran, Bull. Mater. Sci. **25**, 227 (2002)
32. P. Raghu, C. S. Naveen, J. Shailaja, and H. M. Mahesh, in *AIP Conf. Proc.* (2016), p. 020469
33. K.L. Foo, M. Kashif, U. Hashim, W.-W. Liu, Ceram. Int. **40**, 753 (2014)
34. F. Urbach, Phys. Rev. **92**, 1324 (1953)
35. Q. Liang, F. Qiao, X. Cui, X. Hou, Mater. Sci. Semicond. Process. **89**, 154 (2019)
36. S.W. Xue, X.T. Zu, W.L. Zhou, H.X. Deng, X. Xiang, L. Zhang, H. Deng, J. Alloys Compd. **448**, 21 (2008)
37. P. Scherrer, Math.-Phys. Kl **2**, 98 (1918)
38. R. Kumari, A. Sahai, N. Goswami, Prog. Nat. Sci. Mater. Int. **25**, 300 (2015)
39. T. Srinivasulu, K. Saritha, K.T.R. Reddy, Mod. Electron. Mater. **3**, 76 (2017)
40. D.P. Norton, Y.W. Heo, M.P. Ivill, K. Ip, S.J. Pearton, M.F. Chisholm, T. Steiner, Mater. Today **7**, 34 (2004)
41. K. Senthilkumar, M. Tokunaga, H. Okamoto, O. Senthilkumar, Y. Fujita, Appl. Phys. Lett. **97**, 091907 (2010)
42. F.S. Ghoreishi, V. Ahmadi, M. Samadpour, J. Nanostruct. **3**, 453 (2014)

43. B.M. Keyes, L.M. Gedvilas, X. Li, T.J. Coutts, J. Cryst. Growth **281**, 297 (2005)
44. M.N. Kamalasanan, S. Chandra, Thin Solid Films **288**, 112 (1996)
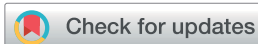
Low temperature-processed ZnO thin films for p–n junction-based visible-blind ultraviolet photodetectors

Hanna B.,[ab] Surendran K. P. [ID][ac] and Narayanan Unni K. N. [ID] *[ab]

Ultraviolet (UV) photodetectors have drawn extensive attention due to their numerous applications in both civilian and military areas including flame detection, UV sterilization, aerospace UV monitoring, missile early warning, and ultraviolet imaging. Zinc oxide (ZnO)-based UV detectors exhibit remarkable performance; however, many of them are not visible-blind, and the fabrication techniques involve a high-temperature annealing step. Here, we fabricated a p–n junction photodiode based on annealing-free ZnO thin films prepared from ZnO nanoparticles and *N,N'*-di(1-naphthyl)-*N,N'*-diphenyl-(1,1'-biphenyl)-4,4'-diamine (NPB). NPB was chosen due to its transparent nature in the visible region and high hole mobility. The ZnO nanoparticles and thin films were characterized by UV-visible absorption spectroscopy, atomic force microscopy (AFM), scanning electron microscopy (SEM), dynamic light scattering (DLS) particle size analysis, Fourier-transform infrared (FTIR) spectroscopy, photoluminescence spectroscopy, XRD and profilometry. The device exhibited responsivity of 0.037 A/W and an external quantum efficiency (EQE) of 12.86% at 5 V bias under 360 nm illumination. In addition, with no biasing, the device exhibited an on−off ratio of more than 10^3 and a linear dynamic range (LDR) of 63 dB. A high built-in potential at the ZnO/NPB interface could be the reason for this performance at zero bias. The rise and fall times were 156 ms and 319 ms, respectively. The results suggest that a visible-blind UV photodetector with acceptable performance can be fabricated using annealing-free ZnO films, which may lead to the realization of flexible detectors due to the low-temperature processes involved.

Introduction

Ultraviolet (UV) detectors have great importance for the survival and development of humankind since excessive exposure to UV radiation causes skin cancer, damage to the immune system and acceleration of the aging process. UV photodetectors are optoelectronic devices that find a wide range of applications in different areas such as radiation detection, UV imaging, pollution monitoring, and space communications.[1] Silicon and photomultiplier tube (PMT)-based UV photodetectors have received greater attention due to their high sensitivity, high signal-to-noise ratio and high responsivity. However, PMTs need high operating voltages and an ultra-high vacuum environment, and silicon photodetectors require filters to stop higher wavelength radiation during their operation.[2] To circumvent these

limitations, UV photodetectors are presently fabricated based on wide bandgap semiconductors such as ZnO,[3–6] GaN,[7] TiO₂,[8] diamond,[9] and SiC.[10] Among them, ZnO is the most suitable material for the fabrication of UV photodetectors due to its attractive properties such as high radiation tolerance, high break down voltage, low toxicity, high transparency, low cost, high electron mobility, large exciton binding energy (60 meV), high refractive index and versatile synthetic methods.[11] These synthetic methods include molecular beam epitaxy (MBE), pulsed laser deposition (PLD), sputtering, chemical vapor deposition (CVD), and solution processing. Compared to all other techniques, solution processing is a simple and low-cost technique to produce high-quality thin films.

UV photodetectors can be fabricated in different configurations such as a p–n junction photodiode, photoconductor, avalanche photodiode, phototransistor, metal semiconductor metal (MSM) photodiode, Schottky photodiode, and p–i–n photodiode. Tian *et al.* fabricated an MSM photodetector based on ZnO thin films deposited by sputtering. The responsivity of the device increased from 0.836 to 1.306 A W⁻¹ due to surface plasmon resonance of Pt nanoparticles coated over the surface of the device.[12] Moreover, p–n junction photodetectors are found to have low dark current and a fast response; they can also operate without any applied bias. The formation of

ᵃAcademy of Scientific and Innovative Research (AcSIR), CSIR-NIIST Campus, Thiruvananthapuram 695019, India. E-mail: unni@niist.res.in

ᵇPhotosciences and Photonics Section, Chemical Sciences and Technology Division, CSIR-National Institute for Interdisciplinary Science and Technology, Thiruvananthapuram-695019, Kerala, India

ᶜFunctional Materials Section, Materials Science and Technology Division, CSIR-National Institute for Interdisciplinary Science and Technology, Thiruvananthapuram-695019, Kerala, India

a nanoscale heterojunction between p-NiO and n-ZnO nano-wires by annealing at 600 °C can enhance the photogain of the detector because it increases the surface band bending and charge separation efficiency of photogenerated carriers.[13] Since the processing temperature is very high, we cannot use this technique for the fabrication of flexible photodetectors. Lee *et al.* fabricated a deep UV photodetector based on amorphous gallium oxide (GaO_x) films grown by a high-cost atomic layer deposition technique (ALD).[14] Here, we fabricated a low-cost and low-temperature processable organic–inorganic hybrid UV photodetector that can respond to both near and deep UV wavelengths. A p–n junction formed between organic and inorganic materials has the advantages of low cost, large optical absorption bandwidth, large area fabrication, low-temperature processability, selective spectral response, mechanical flexibility and high sensitivity[15,16] since it combines the unique properties of both organic and inorganic semiconductors. In addition, p–n junction photodiodes might work with applied zero bias. In 2016, Ranjith *et al.* reported ZnO nanorod/PEDOT:PSS hybrid heterojunction-based and ZnO nanorod-based UV photodetectors and compared the results.[17] They found that photocurrent, sensitivity and responsivity of ZnO nanorod/PEDOT:PSS hybrid devices are higher than that of ZnO nanorod-based devices. This observation was explained based on the fact that the photoinduced charge separation efficiency of the organic–inorganic hybrid device is higher.

Another important requisite for UV detectors is the ability to be visible-blind. n-ZnO/p-Si heterostructures are reported to be suitable for UV photodetectors;[18] however, the photoresponse to visible light needs to be addressed. A photodetector based on n-ZnO/insulator-MgO/p-Si grown by Molecular Beam Epitaxy (MBE) has been shown to be visible-blind.[19] However, simpler fabrication techniques are required for low-cost manufacturing.

Recently, flexible photodetectors have gained considerable attention because of their potential applications in spacecrafts, future paper displays and wearable and portable devices.[20] ZnO thin films prepared by the sol–gel process require high annealing temperatures to produce high-quality films with high electron mobility.[21] Hence, this technique is not suitable for the fabrication of flexible devices. ZnO thin films prepared from ZnO nanoparticle dispersion can be a good alternative to the sol–gel process.

The above discussion indicates the need for developing a UV photodetector that can work with zero applied bias and be processed at low temperatures; also, it should be visible-blind. We have attempted to address these challenges in the present study.

Herein, we fabricated a UV photodetector based on an organic–inorganic heterojunction formed between ZnO nanoparticles and *N,N*′-di(1-naphthyl)-*N,N*′-diphenyl-(1,1′-biphenyl)-4,4′-diamine (NPB). NPB has been widely used as a hole transporting material for organic light-emitting diodes. We have selected NPB because of its excellent film-forming properties, high hole mobility and transparent nature in the visible region.[22] This technique is suitable for the fabrication of flexible UV photodetectors as it avoids a high-temperature annealing step.

Experimental

Annealing-free ZnO thin film preparation

Annealing-free ZnO thin films were prepared from ZnO nano-particle dispersion by a method similar to the one reported by Alem *et al.*[23] Zinc acetate dihydrate (1.475 g) was dissolved in 62.5 ml of methanol under reflux; 0.74 g of KOH was dissolved in 32.5 ml of methanol and this solution was then added to the first solution dropwise using a syringe. The resultant mixture was refluxed under Ar for 6 h and a white precipitate was formed. Subsequently, this precipitate was washed twice with methanol and the nanoparticles were separated through centrifugation. The nanoparticles were dispersed in chloroform and filtered through 0.2 μm PTFE filter. Then, propylamine was added to keep the solution stable and homogeneous. This solution was spin-coated at 3000 rpm and no further plasma treatment or thermal annealing was required. The ZnO film-coated substrates were kept under low vacuum (10^{-1} torr) overnight to evaporate the solvent completely.

Characterization of ZnO

The optical properties of the annealing-free ZnO thin films were studied using a Fluorolog Spectrofluorimeter, HORIBA Jobin Yvon and PerkinElmer UV/VIS/NIR Spectrometer, Lambda 950. The surface morphology of the ZnO thin films before and after TiO_2 deposition was investigated with Bruker AFM. The surface morphologies of annealing-free ZnO thin film and synthesized ZnO nanoparticles were recorded with a Carl Zeiss scanning electron microscope (SEM), Germany. A Bruker Stylus Profilometer was used for thickness measurements. The size of the nanoparticles was measured using the dynamic light scattering (DLS) method at 25 °C with Malvern Zetasizer Nano Zs. X-ray diffraction (XRD) patterns were recorded with an XPert-PRO Scan Diffractometer with Cu Kα ($\lambda = 1.54060$ Å) radiation from 20° to 70° scanning range. Fourier-transform infrared (FTIR) spectra of the ZnO nanoparticles were measured with an IR prestige-21 FTIR Spectrophotometer, Shimadzu.

Device fabrication

The structure of the fabricated device is shown in Fig. 1(a) and the device fabrication procedure is shown in Fig. 1(b). Annealing-free ZnO thin films were deposited by spin coating on ultrasonically cleaned and subsequently UV–ozone-treated ITO-coated glass substrates at 3000 rpm. Also, 0.15 M TiO_2 solution was prepared by dissolving 55 μl of titanium diisopropoxide bis(acetylacetonate) in 1 ml of isopropyl alcohol. This solution was deposited on the ZnO layer as a surface passivation layer and annealed at 125 °C for 1 h. NPB was thermally evaporated as a hole transporting layer. Finally, an Ag anode (100 nm) was thermally evaporated.

Characterization of the UV photodetector

The current–voltage characteristics and transient photoresponse of the device were studied with a Keithley 2400 source meter and 6 W ENF 260C Spectroline UV Lamp with 365 nm and
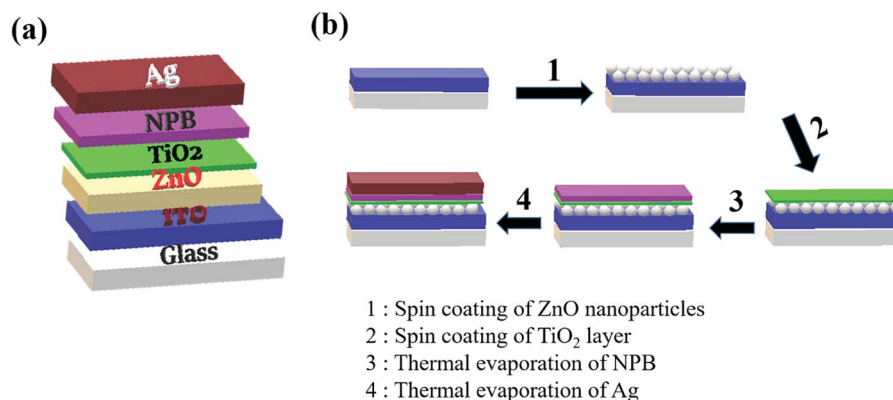
Fig. 1 (a) Device structure of the photodetector. (b) Schematic diagram depicting steps of device fabrication.

254 nm wavelengths. Spectral response measurements were carried out using a 250 W xenon lamp coupled to a Newport monochromator and chopped at 40 Hz using a light chopper blade as a light source.

Results and discussions

Characterization of ZnO

The surface morphology of the annealing-free ZnO thin films was imaged using atomic force microscopy (AFM). Fig. 2 shows the AFM image of a ZnO thin film obtained through tapping mode with 1 μm and 500 nm scanning ranges before and after

TiO_2 deposition. The nanoparticles were spherical in shape. Thicknesses of the ZnO and TiO_2 thin films were determined using profilometry. The RMS surface roughness values of ZnO thin films before and after TiO_2 deposition are summarized in the Table 1. The RMS surface roughness of ZnO was low in areas where a compact ZnO layer was formed. However, there were some areas where the depth was higher and this probably led to a greater value for RMS roughness when we selected a large area for the estimation of the same. However, the RMS surface roughness decreased on TiO_2 deposition due to the improvement in film quality. The particle size of the ZnO nanoparticles from AFM image was found to be less than 50 nm. The fact that
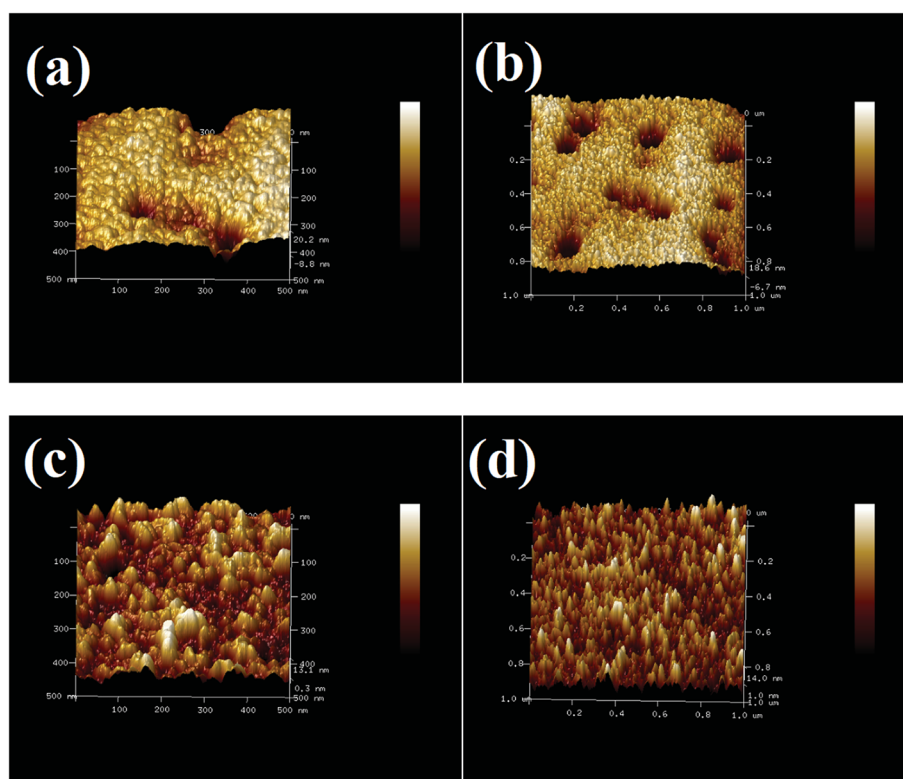

Fig. 2 AFM images of annealing-free ZnO thin films before and after TiO_2 deposition: (a) and (b) before TiO_2 deposition; (c) and (d) after TiO_2 deposition.

...

Table 1 RMS surface roughness values of ZnO thin films before and after TiO$_2$ deposition

Sample	RMS surface roughness (scanning range 500 nm)	RMS surface roughness (scanning range 1 μm)
ZnO	6.98 nm	7.07 nm
ZnO + TiO$_2$	3.66 nm	3.71 nm

the RMS surface roughness increases only incrementally for longer scan ranges is an indication of the quality and uniformity of the film.

The SEM images of the ZnO thin film and synthesized ZnO nanoparticles recorded with a magnification of ×50k are shown in Fig. 3.

The structural properties of ZnO nanoparticles were studied using XRD and FTIR spectroscopy. The XRD pattern of the ZnO nanoparticles is shown in Fig. 4(a). The (100), (002), (101) (102), (110), (103) and (112) peaks were observed. All the XRD peaks were identified with the standard card JCPDS 36-1451 in the recorded range of 2θ. It was confirmed that the ZnO nanoparticles have a hexagonal wurtzite structure. We calculated the crystallite size for the most intense peak by using Debye Scherrer's formula[24]

$$D = \frac{K\lambda}{\beta \cos \theta} \quad (1)$$

where K is a constant, λ is the X-ray wavelength and β is the full width at half maximum intensity (FWHM). The crystallite size is found to be 15.1 nm. The XRD pattern of a ZnO thin film with and without passivation layer is shown in Fig. 4(b). It can be seen that there is hardly any change in the XRD data. This indicates that TiO$_2$ is amorphous and does not affect the crystallinity of ZnO in any manner. The NPB thin film deposited by thermal evaporation is considered to be amorphous.[25] During the deposition of NPB, we did not anneal the film or heat the substrate; thus, there is no effect on the crystalline properties of ZnO.

To understand the presence of molecular species in the prepared samples, FTIR studies were conducted within the range from 400 cm^{-1} to 4000 cm^{-1} at room temperature. FTIR spectra of ZnO nanoparticles are shown in Fig. 5. Absorption bands below 1000 cm^{-1} are due to interatomic vibrations of metal oxides.[26] The absorption bands observed between 480 cm^{-1} and 580 cm^{-1} correspond to the Zn–O stretching mode.[27] The n-type conductivity of undoped ZnO is due to the presence of impurities such as hydrogen (H), which is present in almost all growth environments. The interstitial H bonding with oxygen (O) and H substituted for O in ZnO can act as
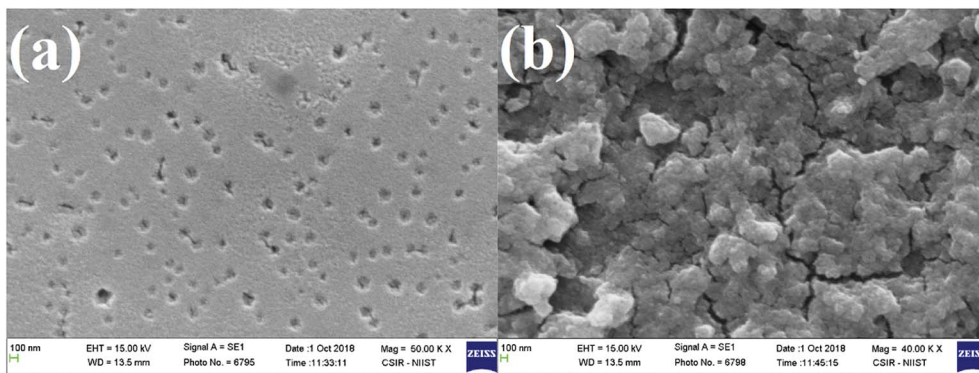
Fig. 3 (a) SEM image of annealing-free ZnO thin film. (b) SEM image of synthesized ZnO nanoparticles.
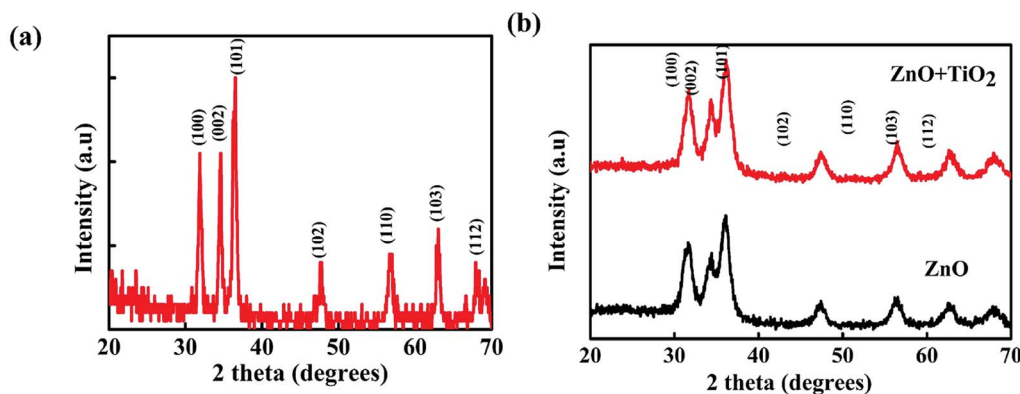
Fig. 4 (a) XRD pattern of ZnO nanoparticles. (b) XRD patterns of ZnO thin films before and after TiO$_2$ deposition.
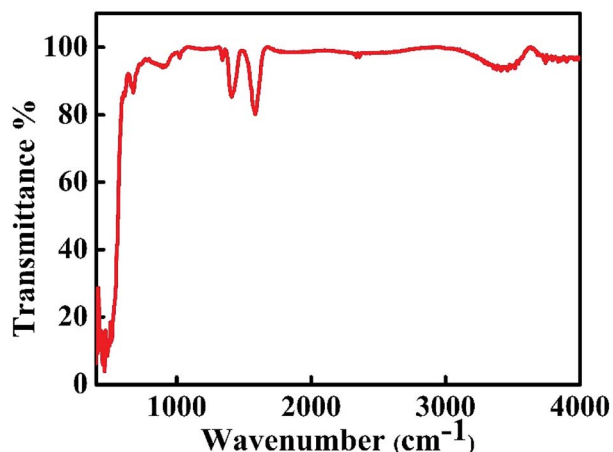
Fig. 5 FTIR spectra of ZnO nanoparticles.

shallow donor levels and contribute to n-type conductivity. Substitutional H is more stable than interstitial H. The peak near 900 cm^{-1} is related to the hydrogen substituted at the oxygen site bound to the lattice Zn site (*i.e.*, Zn–H).[28] The peak near 900 cm^{-1} is related to the hydrogen substituted at the oxygen site bound to the lattice Zn site (*i.e.*, Zn–H). The IR peaks around 1330 cm^{-1}, 1400 cm^{-1} and 1570 cm^{-1} are observed due to symmetric and asymmetric stretching vibrations of C=O group.[29] The absorption band near 3400 cm^{-1} corresponds to the O–H stretching mode.[21]

DLS measurements were carried out at 632.8 nm with a He–Ne gas laser at an angle of 175°. The mean diameter of the nanoparticles was 51 nm.

The optical properties of ZnO thin films were studied by using photoluminescence (PL) and UV-visible absorption spectroscopy. The transmittance spectra of ZnO thin film before and after TiO$_2$ deposition are shown in Fig. 6(a). The films yielded transmittance above 85% in the visible region before and after TiO$_2$ deposition, and it can be seen that the transparent nature of ZnO is not affected by TiO$_2$ deposition. This is highly desirable as the transparent nature of ZnO is very important for several optoelectronic applications. The value of the energy band gap of ZnO thin film can be calculated from the Tauc's plot using the relation

$$\alpha h\nu = A(h\nu - E_g)^n \tag{2}$$

where α is absorption coefficient, A is the proportionality constant, $h\nu$ is the incident energy and E_g is the band gap of the material.[30] Since ZnO is reported to be a direct band gap semiconductor,[31] the value of n is taken to be 1/2 and then, the eqn (2) becomes

$$(\alpha h\nu) = A(h\nu - E_g)^{1/2} \tag{3}$$

Fig. 6(b) shows the Tauc's plot of ZnO thin film, and we estimated the band gap to be 3.34 eV. The relation between

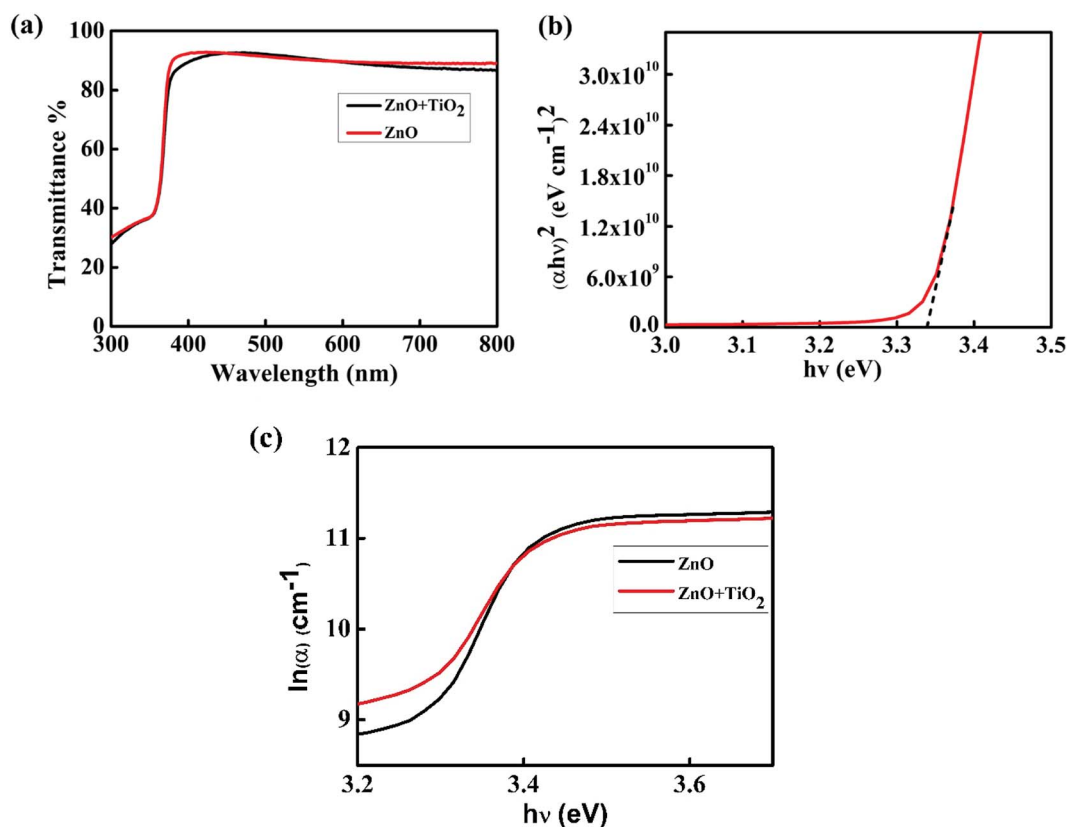**Fig. 6** (a) Transmittance spectra, (b) Tauc's plot, and (c) Urbach plot of ZnO thin film with and without a TiO$_2$ film.
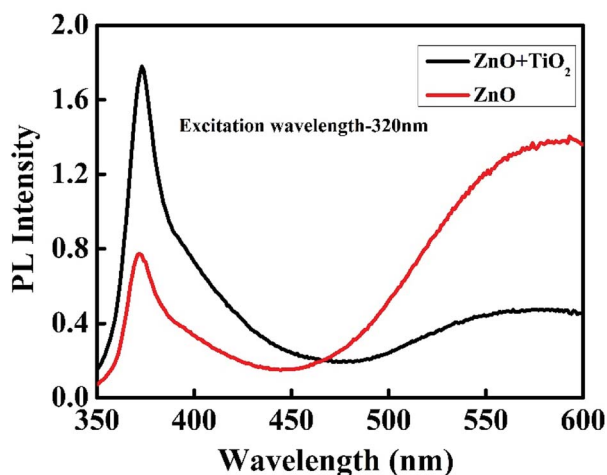
Fig. 7   PL spectra of ZnO thin films before and after TiO_2 deposition.

absorption coefficient and photon energy near the band edge is given by

$$\alpha = \alpha_0 \exp(h\nu/E_u) \qquad (4)$$

where α_0 is a constant and E_u is the width of localized states known as the Urbach energy.[32] The Urbach energy of the ZnO thin film can be calculated from the slope of the curve plotted between $\ln(\alpha)$ and $h\nu$. Fig. 6(c) shows the plot of $\ln(\alpha)$ *vs.* $h\nu$.[33] The value of the Urbach energy of ZnO thin film before TiO_2 deposition is 0.877 eV and that after TiO_2 deposition is 0.651 eV. We found that Urbach energy of annealing-free ZnO thin films decreases upon TiO_2 deposition. The decrease in the Urbach energy implies reduction in defects after TiO_2 deposition.

The PL spectra of ZnO thin film excited at 320 nm are shown in Fig. 7. The peak at 370 nm is due to the near band edge emission and the other near 585 nm is due to the oxygen vacancy defect.[34] To passivate the defect, a very thin layer of TiO_2 is deposited as a surface passivation layer.[35] From the PL spectrum of ZnO after TiO_2 deposition, it is clear that the intensity of UV emission is enhanced and that of visible emission is suppressed due to decrease in the defect density.

The enhancement in UV emission is due to fluorescence resonance energy transfer (FRET) between TiO_2 and ZnO thin film, and the reduction in the intensity of the visible emission is due to the surface passivation effect because of the covering by TiO_2 layer.[35]

Characterization of UV photodetector

The UV radiation spectrum is divided into UV-A (400–320 nm), UV-B (320–280 nm) and UV-C (280–10 nm) regions; UV radiation with wavelength greater than 280 nm can reach the Earth's surface. Overexposure to UV-A and UV-B may result in skin cancer, erythema, premature ageing, burns, *etc.* UV-C radiation is important for inter-satellite communications. For these reasons, we fabricated a UV photodetector that can detect both UV-A and UV-C radiations. The IV characteristics of the device under dark and 365 nm light illumination at intensity of 1.24 mW cm^{-2} and 254 nm light illumination at intensity of 2.4 mW cm^{-2} are shown in Fig. 8(a). Upon UV illumination, ZnO and NPB absorb UV light and generate electron–hole pairs. These electron–hole pairs dissociate into electron and holes by the built-in potential at the organic–inorganic heterojunction. These electrons and holes are collected by the electrodes and thus, a photocurrent is produced. The dark current of the device is 10.2 nA; the photocurrent of the device under 365 nm light illumination is 15 μA and that under 254 nm light illumination is 0.64 μA. The on–off ratio of the device at 365 nm light illumination is 1.5×10^3 and at 254 nm light illumination, the value is 62. Fig. 8(b) shows the transient photoresponse of the device under 365 nm and 254 nm light illuminations at 0 V with a step size of 10 s. From the transient photoresponse, we calculated a rise time and fall time for the device; the device exhibited a rise time of 156 ms and fall time of 319 ms.

We measured the IV characteristics and transient photoresponse with increasing intensity of illumination at 365 nm. We observed an increase in the photocurrent with an increase in the intensity of illumination. Fig. 9(a) and (b) and show the IV characteristics and transient photoresponse with increase in the intensity of radiation, and Fig. 9(c) shows the transient photoresponse with increasing intensity.
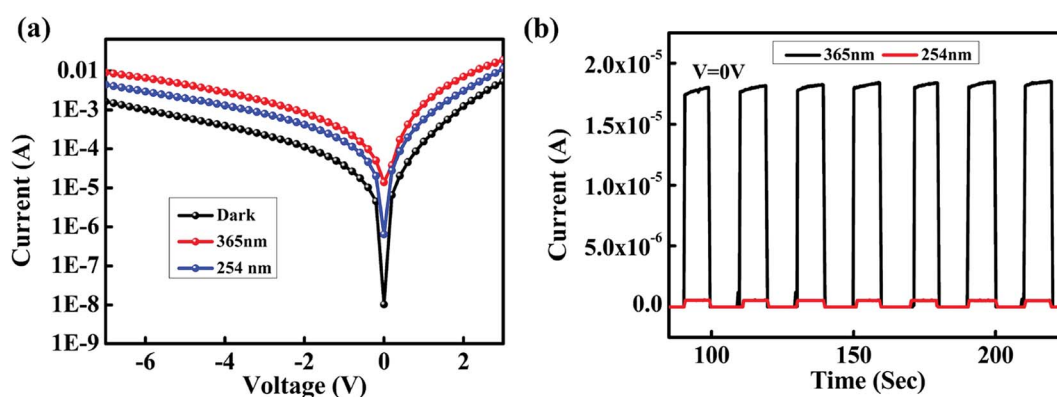

Fig. 8   (a) IV characteristics of the photodetector under dark, 365 nm and 254 nm light illumination. (b) Transient photoresponse under 365 nm and 254 nm light illumination at 0 V.
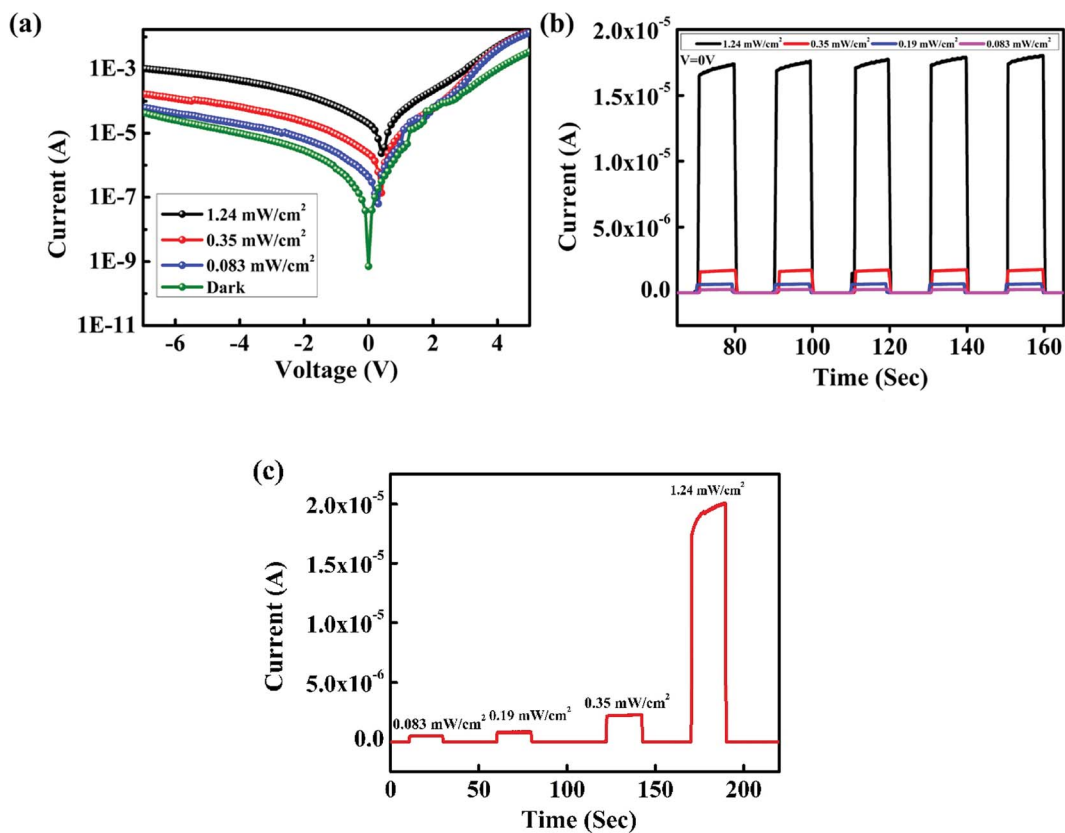
Fig. 9 (a) IV characteristics of the photodetector at different UV (365 nm) intensities and (b) transient photoresponses under 365 nm light illumination at different intensities. (c) Transient photoresponse with increasing intensity.
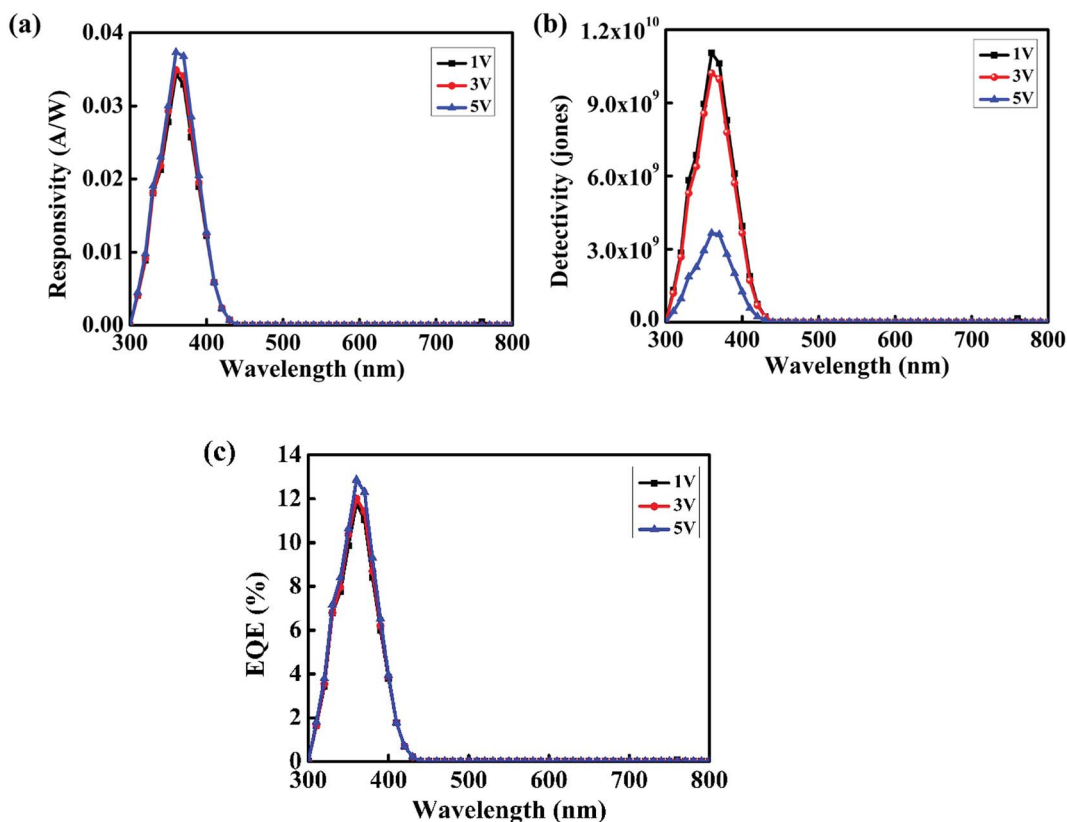

Fig. 10 (a) Spectral response. (b) Detectivity *vs.* wavelength. (c) EQE *vs.* wavelength.

Table 2 Responsivity, EQE and detectivity values of the device at different bias voltages

Bias voltage	Responsivity (A W^{-1})	EQE (%)	Detectivity (jones)
1 V	0.034	11.81	1.11×10^{10}
3 V	0.035	12.02	1.02×10^{10}
5 V	0.037	12.86	3.66×10^9

Spectral response measurements were carried out within 300 nm to 800 nm wavelength range using an incident photon to current efficiency (IPCE) measurement system. The spectral response of the device at different bias voltages is shown in Fig. 10(a). From spectral response measurements, it is clear that the device is completely visible-blind and suitable for applications requiring selective UV detection. The maximum response is obtained for 360 nm. The shoulder around 350 nm can be due to absorption by NPB.[36] Responsivity is defined as the ratio of the photocurrent to the incident optical power, and it can be calculated using eqn (5):[37]

$$R = \frac{I}{P_0} \tag{5}$$

Here, I is the photocurrent and P_0 is the incident optical power. We calculated the responsivity at bias values of 1 V, 2 V and 3 V and found that the responsivity increases with an increase in the bias voltage. Detectivity is expressed in the units of jones and is used to characterize the sensitivity of the device. The higher the detectivity, the more sensitive the device will be to a particular wavelength range. From the responsivity, we calculated the detectivity of the device using the relation[38]

$$D = \frac{R}{\sqrt{2qJ_d}} \tag{6}$$

where J_d is the dark current density and q is the charge of an electron. At a potential of 1 V, the device exhibited maximum detectivity of 1.11×10^{10} jones. Fig. 10(b) shows the plot of detectivity vs. wavelength. The number of electron–hole pairs generated per incident photon is defined as the external quantum efficiency and it is given by eqn (7):[37]

$$\eta = \frac{\text{No of electron} - \text{hole pairs generated}}{\text{No of incident photons}} \tag{7}$$

$$\eta = \frac{\dfrac{I}{q}}{\dfrac{P_0}{h\nu}} \tag{8}$$

Then, responsivity is calculated as follows:

$$R = \frac{I}{P_0} = \frac{q\eta}{h\nu} = \frac{q\eta\lambda}{hc} \tag{9}$$

This indicates that the responsivity varies with the wavelength λ.[39] Fig. 10(c) shows the variation of external quantum efficiency with wavelength. The device exhibited maximum responsivity of 0.037 A W^{-1} and external quantum efficiency of 12.86% at 360 nm illumination at 5 V. The values of responsivity, detectivity and external quantum efficiency at different bias voltages at 360 nm are summarized in Table 2.

These values are indeed promising when we compare them with recent results for p–n junction-based UV detectors with ZnO. A comparison is given in Table 3.

Another important parameter to evaluate the performance of a photodetector is the linear dynamic range (LDR) or the range of current over which the response is linear; it is given by eqn (10), where $I_{\min}$ is the dark current and $I_{\max}$ is the photocurrent.

$$\text{LDR} = 20 \log\left(\frac{I_{\min}}{I_{\max}}\right) \tag{10}$$

LDR of the device is 63 dB. This value is comparable with the LDR value of UV photodetectors fabricated based on InGaAs (66 dB).[51] It is very interesting to note that a UV photodetector based on ZnO fabricated from a simple and cost-effective fabrication technique yields an LDR value that is quite similar to that of the one fabricated using energy intensive techniques. We believe that this is an important step in fabricating flexible photodetectors.

Table 3 Comparison of the performance of our UV detector with recent reports for ZnO-based p–n junction photodetectors

Structure	Responsivity (mA W^{-1})	Detectivity (jones)	On/off ratio	Rise/decay times (ms)	Reference
p–n junction arrays of ZnO nanofibers	1	—	10^2 at 2 V	3900/4710	40
Al/PFO/ZnO/ITO	40 at 2 V	3×10^{10}	—	—	41
ITO/ZnO/PEDOT:PSS/Au	13	—	—	200	42
ITO/H:VZnO/PEDOT:PSS/Ag	2.65	5.25×10^{10}	—	23/26	43
ITO/n-ZnO nanorods/i-ZnO/p-GaN	138.9	—	73.3 at −4 V	1000	44
n-ZnO/p-GaN	450	—	—	—	45
n-ZnO/p-NiO/Ni	2050	—	21.3 at −3.5 V	18 100	46
ZnO/Sb-doped ZnO nanowire	—	—	26.5 at −0.1 V	30	47
ITO/NiO/ZnO/Ti/Au	190 at 1.2 V	3.8×10^{12}	—	—	48
ZnO/PANI	—	—	—	12 000	49
p-Si/n-ZnO/Al	75	6.44×10^9	1115 at 2 V	—	50
ITO/ZnO/TiO$_2$/NPB/Ag	37	3.66×10^9	10^3 at 0 V	156/319	Present work

Conclusions

We fabricated a low-temperature-processable and visible-blind UV photodetector based on an NPB/ZnO nanoparticle heterojunction, which can work at zero applied bias. The ZnO thin films did not require any annealing and were transparent in the visible region. The device exhibited responsivity of 0.037 A W^{-1} and EQE of 12.86% at 5 V under 360 nm light illumination. The rise and fall times were 156 ms and 319 ms, respectively. We observed an increase in the photocurrent with increasing intensity of radiation. The results suggest that a UV photodetector with promising performance can be fabricated using annealing-free ZnO films, which may lead to the development of flexible detectors.

Conflicts of interest

There are no conflicts to declare.

Acknowledgements

References

1 L. Sang, M. Liao and M. Sumiya, *Sensors*, 2013, **13**, 10482–10518.

2 K. Liu, M. Sakurai and M. Aono, *Sensors*, 2010, **10**, 8604–8634.

3 Z. Bai, X. Chen, X. Yan, X. Zheng, Z. Kang and Y. Zhang, *Phys. Chem. Chem. Phys.*, 2014, **16**, 9525–9529.

4 Y. H. Ko, G. Nagaraju and J. S. Yu, *Nanoscale Res. Lett.*, 2015, **10**, 323.

5 L. Qin, C. Shing, S. Sawyer and P. S. Dutta, *Opt. Mater.*, 2011, **33**, 359–362.

6 Z. Jin, L. Gao, Q. Zhou and J. Wang, *Sci. Rep.*, 2015, **4**, 4268.

7 M. Mishra, A. Gundimeda, S. Krishna, N. Aggarwal, L. Goswami, B. Gahtori, B. Bhattacharyya, S. Husale and G. Gupta, *ACS Omega*, 2018, **3**, 2304–2311.

8 Y. Xie, L. Wei, G. Wei, Q. Li, D. Wang, Y. Chen, S. Yan, G. Liu, L. Mei and J. Jiao, *Nanoscale Res. Lett.*, 2013, **8**, 188.

9 S. Salvatori, M. Rossi, F. Scotti, G. Conte, F. Galluzzi and V. Ralchenko, *Diamond Relat. Mater.*, 2000, **9**, 982–986.

10 A. Aldalbahi, E. Li, M. Rivera, R. Velazquez, T. Altalhi, X. Peng and P. X. Feng, *Sci. Rep.*, 2016, **6**, 23457.

11 V. A. Coleman and C. Jagadish, in *Zinc Oxide Bulk, Thin Films and Nanostructures*, Elsevier, 2006, pp. 1–20.

12 C. Tian, D. Jiang, B. Li, J. Lin, Y. Zhao, W. Yuan, J. Zhao, Q. Liang, S. Gao, J. Hou and J. Qin, *ACS Appl. Mater. Interfaces*, 2014, **6**, 2162–2166.

13 J. R. D. Retamal, C.-Y. Chen, D.-H. Lien, M. R. S. Huang, C.-A. Lin, C.-P. Liu and J.-H. He, *ACS Photonics*, 2014, **1**, 354–359.

14 S. H. Lee, S. Bin Kim, Y. Moon, S. M. Kim, H. J. Jung, M. S. Seo, K. M. Lee, S. Kim and S. W. Lee, *ACS Photonics*, 2017, **4**, 2937–2943.

15 B. Guo, G. Wu, H. Chen and M. Wang, *Org. Electron.*, 2016, **29**, 13–21.

16 J. Ha, S. Yoon, J. Lee and D. S. Chung, *Nanotechnology*, 2016, **27**, 095203.

17 K. S. Ranjith and R. T. Rajendra Kumar, *Nanotechnology*, 2016, **27**, 095304.

18 L.-C. Chen and C.-N. Pan, *Eur. Phys. J.: Appl. Phys.*, 2008, **44**, 43–46.

19 T. C. Zhang, Y. Guo, Z. X. Mei, C. Z. Gu and X. L. Du, *Appl. Phys. Lett.*, 2009, **94**, 113508.

20 T. Q. Trung, V. Q. Dang, H.-B. Lee, D.-I. Kim, S. Moon, N.-E. Lee and H. Lee, *ACS Appl. Mater. Interfaces*, 2017, **9**, 35958–35967.

21 M. N. Kamalasanan and S. Chandra, *Thin Solid Films*, 1996, **288**, 112–115.

22 L. G. Wang, J. J. Zhu, X. L. Liu and L. F. Cheng, *J. Electron. Mater.*, 2017, **46**, 5546–5552.

23 S. Alem, J. Lu, R. Movileanu, T. Kololuoma, A. Dadvand and Y. Tao, *Org. Electron.*, 2014, **15**, 1035–1042.

24 L. Qin, C. Shing and S. Sawyer, *IEEE Electron Device Lett.*, 2011, **32**, 51–53.

25 Z. Wang, J. Wang, G. Shi, C. Xu, Z. Hou, Y. Zuo and L. Xi, *J. Nanosci. Nanotechnol.*, 2017, **17**, 3829–3834.

26 M. I. Khan, K. A. Bhatti, R. Qindeel, N. Alonizan and H. S. Althobaiti, *Results Phys.*, 2017, **7**, 651–655.

27 R. Kumari, A. Sahai and N. Goswami, *Prog. Nat. Sci.: Mater. Int.*, 2015, **25**, 300–309.

28 K. Senthilkumar, M. Tokunaga, H. Okamoto, O. Senthilkumar and Y. Fujita, *Appl. Phys. Lett.*, 2010, **97**, 091907.

29 F. S. Ghoreishi, V. Ahmadi and M. Samadpour, *J. Nanostruct.*, 2014, **3**, 453–459.

30 T. K. Pathak, V. Kumar and L. P. Purohit, *Physica E Low Dimens. Syst. Nanostruct.*, 2015, **74**, 551–555.

31 P. Raghu, C. S. Naveen, J. Shailaja and H. M. Mahesh, in *AIP Conference Proceedings*, 2016, vol. 1728, p. 020469.

32 Y. Kim and J.-Y. Leem, *J. Nanosci. Nanotechnol.*, 2016, **16**, 5186–5189.

33 R. C. Rai, *J. Appl. Phys.*, 2013, **113**, 153508.

34 A. Gadallah and M. M. El-Nahass, *Adv. Condens. Matter Phys.*, 2013, **2013**, 1–11.

35 L. Xu, *Chin. Opt. Lett.*, 2009, **7**, 953–955.

36 Z. Wei, Y. Jun-Sheng, H. Jiang, J. Ya-Dong, Z. Qing and C. Kang-Li, *Chin. Phys. B*, 2010, **19**, 047802.

37 R. D. Jansen-van Vuuren, A. Armin, A. K. Pandey, P. L. Burn and P. Meredith, *Adv. Mater.*, 2016, **28**, 4766–4802.

38 J. Yu and N. Tian, *Phys. Chem. Chem. Phys.*, 2016, **18**, 24129–24133.

39 E. Monroy, F. Omn s and F. Calle, *Semicond. Sci. Technol.*, 2003, **18**, R33–R51.

40 Y. Ning, Z. Zhang, F. Teng and X. Fang, *Small*, 2018, **14**, 1703754.

41 X. Guo, L. Tang, J. Xiang, R. Ji, K. Zhang, S. K. Lai, J. Zhao, J. Kong and S. P. Lau, *AIP Adv.*, 2016, **6**, 055318.

42 N. Hernandez-Como, G. Rivas-Montes, F. J. Hernandez-Cuevas, I. Mejia, J. E. Molinar-Solis and M. Aleman, *Mater. Sci. Semicond. Process.*, 2015, **37**, 14–18.

43 B. Deka Boruah and A. Misra, *ACS Appl. Mater. Interfaces*, 2016, **8**, 18182–18188.

44 L. Zhang, F. Zhao, C. Wang, F. Wang, R. Huang and Q. Li, *Electron. Mater. Lett.*, 2015, **11**, 682–686.

45 M. Ding, D. Zhao, B. Yao, Z. Li and X. Xu, *RSC Adv.*, 2015, **5**, 908–912.

46 Y. H. Ko, G. Nagaraju and J. S. Yu, *Nanoscale*, 2015, **7**, 2735–2742.

47 Y. Wang, Y. Chen, W. Zhao, L. Ding, L. Wen, H. Li, F. Jiang, J. Su, L. Li, N. Liu and Y. Gao, *Nano-Micro Lett.*, 2017, **9**, 11.

48 M. R. Hasan, T. Xie, S. C. Barron, G. Liu, N. V. Nguyen, A. Motayed, M. V. Rao and R. Debnath, *APL Mater.*, 2015, **3**, 106101.

49 H. Wang, G. Yi, X. Zu, P. Qin, M. Tan and H. Luo, *Mater. Lett.*, 2016, **162**, 83–86.

50 P. Hazra, S. K. Singh and S. Jit, *Journal of Semiconductor Technology and Science*, 2014, **14**, 117–123.

51 X. Gong, M. Tong, Y. Xia, W. Cai, J. S. Moon, Y. Cao, G. Yu, C.-L. Shieh, B. Nilsson and A. J. Heeger, *Science*, 2009, **325**, 1665–1667.